

Novel Monocarboxylate Transporter 1 and 4 Inhibitors:
***In Vitro* and *In Vivo* Studies as Potential Anticancer**
Agents

A THESIS

SUBMITTED TO THE FACULTY OF

UNIVERSITY OF MINNESOTA

BY

SHIRISHA JONNALAGADDA

IN PARTIAL FULFILLMENT OF THE REQUIREMENTS

FOR THE DEGREE OF

DOCTOR OF PHILOSOPHY

Venkatram R. Merreddy

APRIL 2019

© Shirisha Jonnalagadda 2019

ACKNOWLEDGEMENTS

I would like to express my appreciation and sincere gratitude to Dr. Venkatram R. Mereddy, my thesis advisor, for his valuable advice, continuous support and expert guidance towards my personal and professional development. I am also thankful to him for his awesome support over the years in my development as a scientist.

Furthermore, I would like to express my deepest gratitude to Dr. Lester Drewes for his mentorship and guidance during my entire Ph.D. work. I also take this opportunity to thank Mary Sneve and Zachary Blankenheim from Dr. Drewes's group for their technical help in some of the experiments.

I am highly thankful to Dr. Teresa Rose-Hellekant for her help in training me in establishing tumor models, surgical procedures and other *in vivo* techniques. My sincere thanks to Dr. Jon Holy for training in some of the molecular biology and fluorescence methods.

I am grateful to Dr. Viktor Zhdankin for his constant support and encouragement during my M.S. and Ph.D. at UMD.

I would also like to thank all faculty and staff in College of Pharmacy, Department of Chemistry and Biochemistry, School of Medicine, and Integrated Biosciences for the knowledge and help they have provided me during my M.S. and Ph.D.

I would especially like to thank my husband Sravan Jonnalagadda for helping and guiding me through my Ph.D. and his constant support in my life.

I would like to acknowledge Departments of Chemistry and Biochemistry, College of Pharmacy, Integrated Biosciences, DOD-BCRP, Whiteside Clinical Research Institute, University of Minnesota, Randy Shaver Cancer Research Community for the financial support of my thesis work.

I thank Grady Nelson, Lucas Solano, Conor Ronayne, Tanner Schumacher, Zachary Gardner and all the present and past lab members for their incessant support for the past few years.

Lastly, I would like to thank my parents and sisters for their encouragement in my studies.

ABSTRACT

Shirisha Jonnalagadda, *Novel Monocarboxylate Transporter 1 and 4 Inhibitors: In Vitro and In Vivo Studies as Potential Anticancer Agents*, Doctor of Philosophy (Integrated Biosciences), University of Minnesota.

The primary goal of my research project is to develop novel drug candidates that target cancer cell glycolysis and oxidative phosphorylation via MCT1 and/or MCT4 inhibition for the treatment of cancers. We have discovered several candidate compounds based on CHC and coumarin templates with low nanomolar potency. The current research is innovative because the compounds presented in this thesis are among the very first to be used as dual monocarboxylate transporters 1 and 4 inhibitors (MCT1 and MCT4) for cancer treatment. These dual MCT1 and MCT4 inhibitors have low cell proliferation inhibition and are well tolerated in mice at high dosages. These inhibitors have been tested in *in vivo* tumor models and these studies indicate significant tumor growth inhibition in MCT1 expressing WiDr, 4T1-luc2 and GL261-luc2 and MCT4 expressing MDA-MB-231 xenograft/syngraft models. Our recently discovered highly potent dual MCT1 and MCT4 inhibitors are easy to synthesize, generally non-toxic, water soluble, and effective in arresting the tumor growth *in vivo* as single agents as well as in combination with clinical drugs. The impact of this project will be an enhanced, and improved anticancer agents and a longer and better quality of life for cancer patients with MCT1 and/or MCT4 expressing cancers. As MCT1 and/or MCT4 are expressed in a wide variety of cancers, these inhibitors can also be used as a broad-spectrum anticancer agents for the treatment of solid tumors.

TABLE OF CONTENTS

Acknowledgements.....	i
Abstract.....	ii
Table of contents.....	iii
List of schemes.....	xiv
List of figures.....	xvi
List of tables.....	xxii
List of abbreviations.....	xxiv
CHAPTER 1: Introduction.....	1
1.1 Evolution of hallmarks of cancer: A focus on tumor metabolism.....	1
1.2 Glycolysis and its relation to Warburg effect.....	2
1.3 Reverse Warburg effect in cancer cells.....	4
1.4 Monocarboxylic acid transporters and their importance in metabolism...6	
1.5 MCT1 expression in cancers.....	8
1.6 MCT4 expression in cancers.....	9
1.7 Triple negative breast cancer and MCT4.....	10
1.8 Significance of caveolin-1 in TNBC.....	13
1.9 Metabolic plasticity in cancer.....	15
1.10 Other processes involved in cancer cell survival.....	17
1.10.1 Oxidative stress and reactive oxygen species.....	17
1.10.2 Autophagy.....	19

1.10.3	Glutaminolysis.....	20
1.11	MCT1 inhibitors reported in the literature.....	21
1.11.1	α -Cyano-4-hydroxy cinnamic acid (CHC).....	21
1.11.2	Disodium 4,4'-diisothiocyanatostilbene-2,2'-disulfonate....	24
1.11.3	Quercetin and Ionidamine.....	25
1.11.4	Gabapentin enacarbil.....	26
1.11.5	3-Bromopyruvic acid (3-BPA) and its analog NEO218.....	27
1.11.6	AstraZeneca's AZD3965 and ARC155858.....	28
1.11.7	Substituted pteridine diones and triones.....	29
1.11.8	Coumarin derivatives 7AAC1 and 7AAC2.....	30
1.11.9	Pyrazole methylpropanoic acid derivatives.....	31
1.12	Conclusions.....	32
1.13	Thesis objective and hypothesis.....	33

CHAPTER 2: Structure-activity relationship studies of α -cyano-4-		
hydroxycinnamic acid: Discovery of novel drug candidates with		
	improved MCT1 inhibition properties.....	35
2.1	Structural modification of CHC.....	35
2.1.1	Structural modification of CHC via Knoevenagel condensation.....	36
2.1.2	Synthesis of electron withdrawing group containing CHC derivatives 2.1a-2.1e.....	37

2.1.3	Synthesis of electron donating group containing CHC derivatives 2.1f-2.1i.....	38
2.1.4	Synthesis of 4-alkyl substituted CHC derivatives 2.1j-2.1m	39
2.1.5	Evaluation of compounds 2.1a-2.1m for MCT1 inhibition using ¹⁴ C-lactate uptake assay.....	40
2.2	Synthesis of N,N-dialkyl CHC derivatives.....	44
2.2.1	Synthesis of N,N-dialkyl CHC derivatives 2.2a and 2.2b	45
2.2.2	Evaluation of N,N-dialkyl CHC derivatives 2.2a and 2.2b for MCT1 inhibition.....	46
2.2.3	Synthesis of N,N-dialkyl CHC derivatives 2.2c-2.2j	47
2.2.4	Synthesis of N,N-dialkyl CHC derivatives 2.2k and 2.2l ...	49
2.2.5	Synthesis of N,N-diphenyl CHC derivative 2.2m	51
2.2.6	Evaluation of N,N-dialkyl CHC derivatives 2.2c-2.2m for MCT1 inhibition.....	52
2.3	Discussion.....	57
2.4	Conclusions.....	60

CHAPTER 3: Structure-activity relationship studies of *N,N*-dialkyl/diaryl

o-substituted CHC derivatives as MCT1 inhibitors: *In vitro* and *in vivo*

studies as potential anticancer agents.....	61
---	----

3.1 Synthesis of N,N-dialkyl o-methoxy CHC derivatives 3a-3g	61
3.1.1 Synthesis of N,N-dialkyl o-methoxy CHC derivatives 3h and 3i	64
3.1.2 Synthesis of N,N-diphenyl o-methoxy CHC derivative 3j ...	66
3.1.3 Synthesis of N,N-dialkyl o-allyloxy CHC derivative 3k	67
3.2 Evaluation of N,N-dialkyl/diaryl o-substituted CHC derivatives 3a-3k for MCT1 inhibition properties: Results and discussion.....	68
3.3 Cell proliferation/cytotoxicity study of compounds 3a-3k : Results and discussion.....	73
3.3.1 Cell proliferation inhibition of compounds 3a-3k using MTT assay.....	73
3.3.2 Cytotoxicity evaluation of compounds 3a-3k using SRB assay.....	76
3.4 Cell proliferation inhibition of test compounds in various cancer cell lines under hypoxic conditions using MTT assay: Results and discussion...	81
3.5 Cell cycle analysis of compound 3j in WiDr and MDA-MB-231 cell lines: Results and discussion.....	83
3.6 Systemic toxicity evaluation of N,N-dialkyl/diaryl o-methoxy CHC derivatives 3h-3k in CD-1 mice: Results and discussion.....	88
3.7 In vivo anticancer efficacy studies using lead candidate compounds: Results and discussion.....	92

3.7.1	Anticancer efficacy of compounds 3b and 3j in MCT1 expressing WiDr flank model.....	92
3.7.2	Chemoprevention study of compound 3j in MCT1 expressing WiDr flank model.....	95
3.7.3	Anticancer efficacy of lead candidate compound 3j in syngeneic 4T1-luc2 flank model.....	97
3.8	Evaluation of compound 3j for pharmacokinetic parameters: Results and discussion.....	100
3.9	Conclusions.....	102

CHAPTER 4:	Structure-activity relationship studies of 7- <i>N,N</i> -dialkyl 3-carboxy coumarins as MCT1 inhibitors: <i>In vitro</i> and <i>in vivo</i> studies as potential anticancer agents.....	103
4.1	Synthesis of 7- <i>N,N</i> -dialkyl 3-carboxy coumarin derivatives 4a and 4b	103
4.1.1	Synthesis of 7- <i>N,N</i> -dialkyl 3-carboxy coumarin derivatives 4c-4g	106
4.1.2	Synthesis of 7- <i>N,N</i> -dialkyl 3-carboxy coumarin derivative 4h	108
4.1.3	Synthesis of 7- <i>N,N</i> -diphenyl 3-carboxy coumarin derivative 4i	109

4.2 Evaluation of 7-N,N-dialkyl/diaryl carboxy coumarins 4a-4i for MCT1 inhibition: Results and discussion.....	110
4.3 Cell proliferation inhibition of compounds 4a-4i in GL261-luc2 and MDA-MB-231 cell lines using MTT assay: Results and discussion.....	115
4.4 Cell cycle analysis of compound 4g in MDA-MB-231 cell line: Results and discussion.....	117
4.5 In vitro protein binding, Caco-2 permeability and metabolic stability studies: Results and discussion.....	118
4.5.1 Protein binding studies of compounds 3g, 3h, 3j, 3k and 4g in human plasma.....	120
4.5.2 Caco-2 permeability studies of compounds 3g, 3h, 3j, 3k and 4g	121
4.5.3 Metabolic stability assay in mouse and human liver microsomes using compounds 3g, 3h, 3j, 3k and 4g	124
4.6 Systemic toxicity evaluation of the lead candidate compound 4g in CD-1 mice: Results and discussion.....	128
4.7 Anticancer efficacy of lead compound 4g in a glioblastoma tumor model: Results and discussion.....	130
4.8 Conclusions.....	133

CHAPTER 5: Evaluation of N,N-dialkyl/diaryl o-substituted CHC derivatives and 7-N,N-dialkyl/diaryl 3-carboxy coumarins as MCT4 inhibitors:	
In vitro and in vivo studies as potential anticancer agents.....	134
5.1 Evaluation of compounds 3a-3k and 4a-4i for MCT4 inhibition in MDA-MB-231 cell line: Results and discussion.....	134
5.2 Effect of lead compounds 3j and 4g on glycolysis and mitochondrial OxPhos.....	142
5.2.1 Glycolysis stress test in MDA-MB-231 and WiDr cell lines using 3j and 4g	144
5.2.2 Glycolysis stress test in 4T1 cell line using 3j and 4g	153
5.2.3 Mitochondrial stress test in MDA-MB-231 and WiDr cell lines using 3j and 4g	155
5.2.4 Mitochondrial stress test in 4T1 cell line using 3j	166
5.2.5 Glycolysis stress test in MDA-MB-231 and WiDr cell lines using 3b and 3j	168
5.2.6 Mitochondrial stress test in MDA-MB-231 and WiDr cell lines using 3b and 3j	171
5.3 Florescence microscopy study of compound 3j in MDA-MB-231 and WiDr cell lines.....	176
5.4 Anticancer efficacy of lead candidate compounds in MDA-MB-231-luc tumor xenograft models.....	179
5.4.1 Anticancer efficacy of compound 3j in MDA-MB-231-luc	

tumor xenograft model.....	180
5.4.2 Anticancer efficacy of compound 3j compared to doxorubicin in MDA-MB-231-luc tumor xenograft model.....	182
5.4.3 Anticancer efficacy of compound 3j at a higher dosage in MDA-MB-231-luc flank model.....	184
5.4.4 Anticancer efficacy of the lead candidate compound 4g in MDA-MB-231-luc tumor model.....	186
5.5 In vitro and in vivo evaluation of reverse Warburg effect in TNBC MDA-MB-231.....	188
5.5.1 Optimization of seeding concentration of cells for co-culture of 3T3 MEFs WT and 3T3 MEFs KO fibroblasts with MDA-MB-231 cell line.....	188
5.5.2 Cell proliferation inhibition of compounds 3h-3k in MDA-MB-231, and co-cultures with 3T3 MEF WT and 3T3 MEF KO under normal conditions.....	191
5.5.3 Cell proliferation inhibition of compounds 3h-3k in MDA-MB-231, and co-cultures with 3T3 MEF WT and 3T3 MEF KO under hypoxic conditions.....	192
5.6 Anticancer efficacy of lead MCT inhibitor 3j in MDA-MB-231-luc based orthotopic models.....	193
5.6.1 Anticancer efficacy of lead MCT inhibitor 3j in MDA-MB-231-luc orthotopic model.....	194

5.6.2 Anticancer efficacy of lead MCT inhibitor 3j in MDA-MB-231-luc orthotopic model co-injected with 3T3 MEF WT cells.....	195
5.6.3 Anticancer efficacy of lead MCT inhibitor 3j in MDA-MB-231-luc orthotopic model co-injected with 3T3 MEF KO cells.....	197
5.7 Conclusions.....	201
CHAPTER 6: Experimental procedures and spectral characterization.....	203
6.1 Chemicals and methods of compound characterization.....	203
6.2 Cell lines and culture conditions.....	204
6.3 Representative synthesis of (E)-2-cyano-3-(4-fluorophenyl)acrylic acid 2.1a	206
6.4 Representative synthesis of (E)-2-cyano-3-(4-methoxyphenyl)acrylic acid 2.1f	207
6.5 Representative synthesis of (E)-2-cyano-3-(4-methylphenyl)acrylic acid 2.1j	208
6.6 Representative synthesis of (E)-2-cyano-3-(4-(dipropylamino)phenyl) acrylic acid 2.2c	209
6.7 Representative synthesis of (E)-2-cyano-3-(4-(dipropylamino) -2-methoxyphenyl) acrylic acid 3a	210

6.8 Synthesis of (E)-3-(2-(allyloxy)-4-(diethylamino)phenyl)	
-2-cyanoacrylic acid 3k	212
6.9 Representative procedure for the synthesis of 7-(dipropylamino)	
-2-oxo-2H-chromene-3-carboxylic acid 4c	213
6.10 Spectral characterization of synthesized compounds.....	215
6.11 Western blot of RBE4, MDA-MB-231, WiDr and 4T1-luc2 cell lines.	253
6.12 MCT1 inhibition using ¹⁴ C-lactate uptake assay.....	254
6.13 MCT4 inhibition using ¹⁴ C-lactate uptake assay.....	255
6.14 Sulforhodamine-B assay.....	256
6.15 MTT assay.....	257
6.16 MTT assay in hypoxic conditions.....	258
6.17 Cell cycle analysis using propidium iodide.....	259
6.18 Ethical considerations for animal studies.....	260
6.19 General procedure for systemic toxicity evaluation.....	261
6.20 Anticancer efficacy of compound 3j in MCT1 expressing WiDr	
flank model.....	262
6.21 Chemoprevention study of compound 3j in MCT1 expressing	
WiDr flank model.....	263
6.22 Anticancer efficacy of MCT1 inhibitor in 4T1-luc2 flank model.....	263
6.23 Evaluation of pharmacokinetic parameters in CD-1 mice.....	264
6.24 Protein binding studies.....	267

6.25 Caco-2 permeability studies.....	267
6.26 Microsomal stability studies.....	268
6.27 Seahorse XFe96 [®] assessment of glycolysis and mitochondrial Respiration.....	269
6.28 Florescence microscopy study.....	270
6.29 Anticancer efficacy in MDA-MB-231-luc flank xenograft tumor model.....	271
6.30 Anticancer efficacy of lead MCT inhibitor 3j in MDA-MB-231-luc orthotopic model.....	272
6.31 Anticancer efficacy of lead MCT inhibitor 3j in MDA-MB-231-luc orthotopic model co-injected with 3T3 MEF WT cells.....	272
6.32 Anticancer efficacy of lead MCT inhibitor 3j in MDA-MB-231-luc orthotopic model co-injected with 3T3 MEF KO cells.....	273
6.33 Statistical analysis.....	273
References.....	274
Appendix.....	282

LIST OF SCHEMES

Scheme 2a: Synthesis of CHC derivatives 2.1a-2.1e with electron withdrawing groups at <i>para</i> position.....	37
Scheme 2b: Synthesis of CHC derivatives 2.1f-2.1i with electron donating group a <i>para</i> position.....	38
Scheme 2c: Synthesis of CHC derivatives 2.1j-2.1m with alkyl group substitutions at <i>para</i> position.....	39
Scheme 2d: Synthesis of (<i>E</i>)-2-cyano-3-(4-(dimethylamino)phenyl)acrylic acid 2.2a and (<i>E</i>)-2-cyano-3-(4-(diethylamino)phenyl)acrylic acid 2.2b	45
Scheme 2e: Synthesis of (<i>E</i>)-2-cyano-3-(4-(dialkylamino)phenyl)acrylic acids 2.2c-2.2j	48
Scheme 2f: Synthesis of (<i>E</i>)-2-cyano-3-(4-(pyrrolidin-1-yl)phenyl)acrylic acid 2.2k and (<i>E</i>)-2-cyano-3-(4-(piperidin-1-yl)phenyl)acrylic acid 2.2l	50
Scheme 2g: Synthesis of (<i>E</i>)-2-cyano-3-(4-(diphenylamino)phenyl)acrylic acid 2.2m	51
Scheme 2h: Structure-activity relationship studies on cyanoacrylic acid unit...	58
Scheme 3a: Synthesis of (<i>E</i>)-2-cyano-3-(4-(dialkylamino)-2-methoxyphenyl) acrylic acids 3a-3g	63

Scheme 3b: Synthesis of (<i>E</i>)-2-cyano-3-(2-methoxy-4-(pyrrolidin-1-yl)phenyl)acrylic acid 3h and (<i>E</i>)-2-cyano-3-(2-methoxy-4-(piperidin-1-yl)phenyl)acrylic acid 3i	65
Scheme 3c: Synthesis of (<i>E</i>)-2-cyano-3-(4-(diphenylamino)-2-methoxyphenyl)acrylic acid 3j	66
Scheme 3d: Synthesis of (<i>E</i>)-3-(2-(allyloxy)-4-(diethylamino)phenyl)-2-cyanoacrylic acid 3k	67
Scheme 4a: Synthesis of 7-(dimethylamino)-2-oxo-2H-chromene-3-carboxylic acid 4a and 7-(diethylamino)-2-oxo-2H-chromene-3-carboxylic acid 4b	105
Scheme 4b: Synthesis of 7-(dialkylamino)-2-oxo-2H-chromene-3-carboxylic acids 4c-4g	107
Scheme 4c: Synthesis of 2-oxo-7-(pyrrolidin-1-yl)-2H-chromene-3-carboxylic acid 4h	108
Scheme 4d: Synthesis of 7-(diphenylamino)-2-oxo-2H-chromene-3-carboxylic acid 4i	109

LIST OF FIGURES

Figure 1a: Important hallmarks of cancer and their characteristics.....	1
Figure 1b: Metabolic symbiosis and Warburg effect in cancer cells.....	3
Figure 1c: Stromal-epithelial metabolic coupling and reverse Warburg effect....	5
Figure 1d: Inhibition of MCT1 and/or MCT4 leads to a decrease in tumor growth.	7
Figure 1e: Breast cancer is classification based on the receptor status.....	10
Figure 1f: Tumor heterogeneity and metabolic plasticity in cancer cells.....	16
Figure 1g: Structure of CHC.....	21
Figure 1h: Structures of MCT1 inhibitors DIDS, quercetin, lonidamine and gabapentin enacarbil.....	24
Figure 1i: Structures of 3-bromopyruvic acid and NEO218.....	27
Figure 1j: Structures of AZD3965 and AR-C158858.....	28
Figure 1k: Structures of substituted pteridine trione and diones.....	29
Figure 1l: Structures of aminocarboxy coumarins 7ACC1 and 7ACC2.....	30
Figure 1m: Representative example of 2-((1-(2-chlorobenzyl)-5-(3-substituted phenyl)-1H-pyrazol-3-yl)methoxy)-2-methylpropanoic acid.....	31
Figure 2a: Possible positions on CHC for structure-activity relationship studies...	35
Figure 2b: Knoevenagel condensation reaction.....	36
Figure 2c: Western blot analysis of MCT1 and MCT4 expressions in RBE4, MDA-MB-231, 4T1-luc2, and WiDr cell lines.....	40
Figure 2d: MCT1 IC ₅₀ of CHC derivatives 2.1a-2.1e	41

Figure 2e: MCT1 IC ₅₀ of CHC derivatives 2.1f-2.1i	42
Figure 2f: MCT1 IC ₅₀ of CHC derivatives 2.1j-2.1m	43
Figure 2g: Replacement of OH group with <i>N,N</i> -dialkyl group in CHC.....	44
Figure 2h: MCT1 IC ₅₀ (nM) of <i>N,N</i> -dialkyl CHC derivatives 2.2a-2.2m in RBE4 cell line.	53
Figure 2h: Proposed modification of <i>ortho</i> position of <i>N,N</i> -dialkyl CHC derivative with a methoxy group.....	49
Figure 2i: Structure-activity relationship and MCT1 inhibition of <i>N,N</i> -dialkyl CHC derivatives.....	59
Figure 3a: Proposed modification of <i>ortho</i> position of <i>N,N</i> -dialkyl CHC derivative with a methoxy group.....	61
Figure 3b: MCT1 inhibition of <i>N,N</i> -dialkyl/diaryl <i>o</i> -substituted cyanoacetic acids 3a-3k in RBE4 cell line.	69
Figure 3c: Optimized structural features required for potent MCT1 inhibition.....	72
Figure 3d: Cell cycle analysis of compound 3j at 1X and 2X of the IC ₅₀ concentration of in WiDr cell line.	84
Figure 3e: Cell cycle analysis of MDA-MB-231 cell line treated with lead compound 3j	85
Figure 3f: Lead candidate compounds 3h-3k for further <i>in vivo</i> studies.....	88
Figure 3g: Systemic toxicity study of compounds in CD-1 mice.....	90

Figure 3h: 1,4-addition and reversibility of cyanocinnamic acid based MCT1 inhibitors.....	91
Figure 3i: Anticancer efficacy of lead compounds in a WiDr flank model.....	94
Figure 3j: Chemoprevention of lead compounds in a WiDr flank model.....	96
Figure 3k: Anticancer efficacy of lead compounds in a 4T1-luc2 flank model....	98
Figure 3l: Pharmacokinetic time-concentration profile in CD-1 mice.....	100
Figure 4a: CHC and coumarin derivatives.....	103
Figure 4b: Structures of the biologically active coumarin derivatives.....	104
Figure 4c: MCT1 inhibition of <i>N,N</i> -dialkyl/diaryl 3-carboxy coumarins 4a-4i in RBE4 cell line.	111
Figure 4d: Cell cycle analysis of compound 4g at IC ₅₀ concentration in MDA-MB-231 cell line.....	118
Figure 4e: Lead molecules chosen for further <i>in vitro</i> studies.....	119
Figure 4f: Body weight changes in systemic toxicity study of compound 4g in CD-1 mice.	128
Figure 4g: 1,4-addition and reversibility of carboxy coumarin based MCT1 inhibitors.....	129
Figure 4h: Anticancer efficacy of lead compound 4g in a GL261-luc2 flank model.....	131
Figure 5a: MCT4 IC ₅₀ (nM)* of <i>N,N</i> -dialkyl/diaryl <i>o</i> -methoxy CHC derivatives 3a-3k in MDA-MB-231 cell line.....	137

Figure 5b: Lead compounds evaluated for extracellular flux analysis using Seahorse XFe96 based GST and MST.....	143
Figure 5c: Glycolysis stress test profiles in MDA-MB-231 cell line using compound 3j, 4g, CHC and AZD3965 at 10 and 30 μ M concentrations.....	146
Figure 5d: Glycolysis stress test profiles in WiDr cell line using compound 3j, 4g, CHC and AZD3965 at 10 and 30 μ M concentrations.....	147
Figure 5e: Effect of compounds 3j , 4g , CHC and AZD on glycolysis.....	148
Figure 5f: Effect of compounds 3j , 4g , CHC and AZD on glycolytic capacity....	150
Figure 5g: Effect of compounds 3j , 4g , CHC and AZD on glycolytic reserve....	152
Figure 5h: Glycolysis stress test of compounds 3j and 4g in 4T1 cell line.....	154
Figure 5i: Mitochondrial stress test profiles in MDA-MB-231 cell line using compound 3j, 4g, CHC and AZD3965 at 10 and 30 μ M concentrations.....	157
Figure 5j: Mitochondrial stress test profiles in WiDr cell line using compound 3j, 4g, CHC and AZD3965 at 10 and 30 μ M concentrations.....	158
Figure 5k: Effect of compounds 3j , 4g , CHC and AZD on maximal respiration...	159
Figure 5l: Effect of compounds 3j , 4g , CHC and AZD on ATP production.....	161
Figure 5m Effect of compounds 3j , 4g , CHC and AZD on proton leak.....	163
Figure 5n: Effect of compounds 3j , 4g , CHC and AZD on spare respiratory capacity.....	165
Figure 5o: Mitochondrial stress test of compound 3j in 4T1 cell line.....	167
Figure 5p: Glycolysis stress test of compounds 3b and 3j in MDA-MB-231 cell line.....	169

Figure 5q: Glycolysis stress test of compounds 3b and 3j in WiDr cell line.....	170
Figure 5r: Mitochondrial stress test of compounds 3b and 3j in MDA-MB-231 cell line.....	172
Figure 5s: Mitochondrial stress test of compounds 3b and 3j in WiDr cell line.....	173
Figure 5t: Representative fluorescence microscopy images of MDA-MB-231 cells treated with compound 3j and labeled with mitotracker red.....	177
Figure 5u: Representative fluorescence microscopy images of WiDr cells treated with compound 3j and labeled with mitotracker red.	178
Figure 5v: Tumor growth inhibition study with compound 3j in MDA-MB-231-luc tumor xenograft model.	181
Figure 5w: Anticancer efficacy with compound 3j and doxorubicin in MDA-MB-231-luc tumor xenograft model.	183
Figure 5x: <i>In vivo</i> anticancer efficacy study using compound 3j in MDA-MB-231 xenograft model.	185
Figure 5y: Anticancer efficacy of lead compound 4g in MDA-MB-231-luc flank model.....	187
Figure 5z: Determination of optimal seeding concentration of 3T3 MEFs cells....	189
Figure 5aa: Determination of optimal seeding concentration of MDA-MB-231 cells with 3T3 MEFs cells.	190

Figure 5ab: <i>In vivo</i> anticancer efficacy study in MDA-MB-231-luc orthotopic model.	194
Figure 5ac: <i>In vivo</i> anticancer efficacy study in MDA-MB-231-luc + 3T3 MEF WT orthotopic model.....	196
Figure 5ad: <i>In vivo</i> anticancer efficacy study in MDA-MB-231-luc + 3T3 MEF KO orthotopic model.....	198
Figure 5ae: Tumor growth in control groups on day-24 after tumor inoculation in MDA-MB-231-luc, MDA-MB-231-luc co-injected with 3T3 MEF WT, and MDA-MB-231-luc co-injected with 3T3 MEF KO.....	200

LIST OF TABLES

Table 2a: MCT1 IC ₅₀ (nM)* of <i>N,N</i> -dialkyl CHC derivatives 2.2a-2.2m in RBE4 cell line.....	54
Table 3a: MCT1 IC ₅₀ (nM)* of <i>N,N</i> -dialkyl/diaryl <i>o</i> -substituted CHC derivatives 3a-3k in RBE4 cell line.....	70
Table 3b: MTT assay IC ₅₀ * values of <i>N,N</i> -dialkyl <i>o</i> -methoxy CHC derivatives in 4T1-luc2 and GL261-luc2, WiDr and MDA-MB-231 cell lines.....	75
Table 3c: SRB assay IC ₅₀ * values of <i>N,N</i> -dialkyl <i>o</i> -methoxy CHC derivatives in 4T1-luc2 and GL261-luc2, WiDr and MDA-MB-231 cell lines.....	77
Table 3d: MTT assay IC ₅₀ * values of <i>N,N</i> -dialkyl <i>o</i> -methoxy CHCs in 4T1-luc2, GL261-luc2 and MDA-MB-231 cell lines in hypoxic conditions.....	82
Table 4a: MCT1 IC ₅₀ (mM)* of 7- <i>N,N</i> -dialkyl/aryl carboxy coumarins 4a-4i in RBE4 cell line.....	112
Table 4b: MTT assay IC ₅₀ * values of 7- <i>N,N</i> -dialkyl/diaryl carboxy coumarins 4a-4i in GL261-luc2 and MDA-MB-231 cell lines.....	115
Table 4c: <i>In vitro</i> protein binding studies (protein binding: plasma, human).....	120
Table 4d: A-B Caco-2 permeability studies of compounds 3g, 3h, 3j, 3k and 4g ...	122
Table 4e: B-A Caco-2 permeability studies of compounds 3g, 3h, 3j, 3k and 4g ...	123
Table 4f: Metabolic stability in human liver microsomes for compounds 3g, 3h, 3j, 3k and 4g	125

Table 4g: Metabolic stability in mouse liver microsomes for compounds 3g, 3h, 3j, 3k and 4g	126
Table 5a: MCT4 IC ₅₀ (nM)* of <i>N,N</i> -dialkyl/diaryl <i>o</i> -methoxy CHC derivatives 3a-3k in MDA-MB-231 cell line.....	138
Table 5b: MTT assay IC ₅₀ * values of compounds 3h-3k in MDA-MB-231, and co-cultures with 3T3 MEF WT and 3T3 MEF KO under normal conditions....	191
Table 5c: MTT assay IC ₅₀ * values of compounds 3h-3k in MDA-MB-231, and co-cultures with 3T3 MEF WT and 3T3 MEF KO under hypoxic conditions.....	192
Table 6a: HPLC conditions of analyte and internal standard (diazepam).....	265

LIST OF ABBREVIATIONS

ATP	adenosine triphosphate
MCT	monocarboxylic acid transporter
SLC16	solute carrier 16
kDa	kilo Dalton
OxPhos	oxidative phosphorylation
ER	estrogen receptor
HER-2	human epidermal growth factor-2
TNBC	triple negative breast cancer
PR	progesterone receptor
Cav	caveolin
ROS	reactive oxygen species
RNS	reactive nitrogen species
HIF-1 α	hypoxia inducing factor
NF- κ B	nuclear factor kappa-light-chain-enhancer
DNA	deoxyribonucleic acid
GLS	glutaminase
GDH	glutamate dehydrogenase
α KG	α -ketoglutarate
CHC	α -Cyano-4-hydroxy cinnamic acid
μ mol	micromoles
LLc	Lewis lung carcinoma

mM	millimolar
CAM	chicken chorioallantoic membrane
DIDS	disodium 4,4'-diisothiocyanatostilbene-2,2'-disulfonate
IC ₅₀	inhibition of 50% of the activity or cell growth
K _i	inhibitor constant
VDAC	voltage-dependent anion channel
MPC	mitochondrial pyruvate carrier
FDA	food and drug administration
3-BPA	3-bromopyruvic acid
mg/Kg	dosage in milligram per kilogram of mouse
NSG	NOD/LtSz-scid IL-2R γ null mice
RBE4	rat brain endothelial 4 cell line
F	fluoro
Br	bromo
CN	cyano functional group
NO ₂	nitro functional group
CH ₃ CN	acetonitrile
NH ₄ Ac	ammonium acetate
dpm	disintegrations per minute
OH	hydroxy functional group
DMF	<i>N,N</i> -dimethylformamide
POCl ₃	phosphorus (V) oxychloride

R-Br	alkyl/aryl bromide
H ₂ O	water
Bu ₄ NI	tetra- <i>n</i> -butyl ammonium iodide
CNCH ₂ COOH	cyanoacetic acid
HBr	hydrobromic acid
H ₂ SO ₄	sulfuric acid
PBr ₃	phosphorous tribromide
nM	nanomolar
SEM	standard error of the mean
SAR	structure-activity relationship
K ₂ CO ₃	potassium carbonate
SRB	sulforhodamine-B
MTT	3-(4,5-dimethylthiazol-2-yl)-2,5-diphenyltetrazolium bromide
MEM	minimum essential medium
DMEM	Dulbecco's minimum essential medium
PI	propidium iodide
FCM	flow cytometry
acetyl CoA	acetyl coenzyme A
DMSO	dimethyl sulfoxide
ip	intraperitoneal
bid	twice a day
qd	once a day

CYP	cytochrome P450 enzyme
PBS	phosphate buffered saline
EtOH	ethanol
NaOH	sodium hydroxide
BBr ₃	boron tribromide
HEPES	(4-(2-hydroxyethyl)-1-piperazineethanesulfonic acid)
GST	glycolysis stress test
MST	mitochondrial stress test
ECAR	extracellular acidification rate
OCR	oxygen consumption rate
mpH	milli pH
pmol	pico moles
AZD	AZD3965
FCCP	carbonyl cyanide-4-(trifluoromethoxy)phenylhydrazone
ETC	electron transport chain
Dox	doxorubicin
WT	wild type
KO	knock out
¹ H NMR	Proton (¹ H) nuclear magnetic resonance spectrum
¹³ C NMR	Carbon (¹³ C) nuclear magnetic resonance spectrum
HRMS	high resolution mass spectrometer
FBS	fetal bovine serum

ATCC	American type cell culture
TLC	thin layer chromatography
HCl	hydrochloric acid
Hz	Hertz
MHz	Mega Hertz
<i>J</i>	Coupling constant
CDCl ₃	deuterated chloroform
mA	milli amperes
PBST	phosphate buffered saline with Tween 20

CHAPTER 1: Introduction

1.1 Evolution of hallmarks of cancer: A focus on tumor metabolism

Hanahan and Weinberg summarized the evolution of major hallmarks of cancer in 2000 and updated them in 2011 to incorporate new developments in cancer research (Figure 1a).^{1,2} It has been widely accepted by research community to target these hallmarks for therapeutic intervention to prevent, treat and eliminate cancer.³ Mutational events, multiple signaling pathways, and highly heterogeneous nature are some of the important characteristics of cancer cells which are responsible for tumorigenesis. It is also clear from several key studies that many of the altered signaling pathways are related to tumor cell metabolism and these alterations seem to be critical for malignant transformation of tumor cells.⁴ Based on these studies, alteration in cellular metabolism has become an important hallmark of cancer and a very attractive target to explore cancer therapeutics.

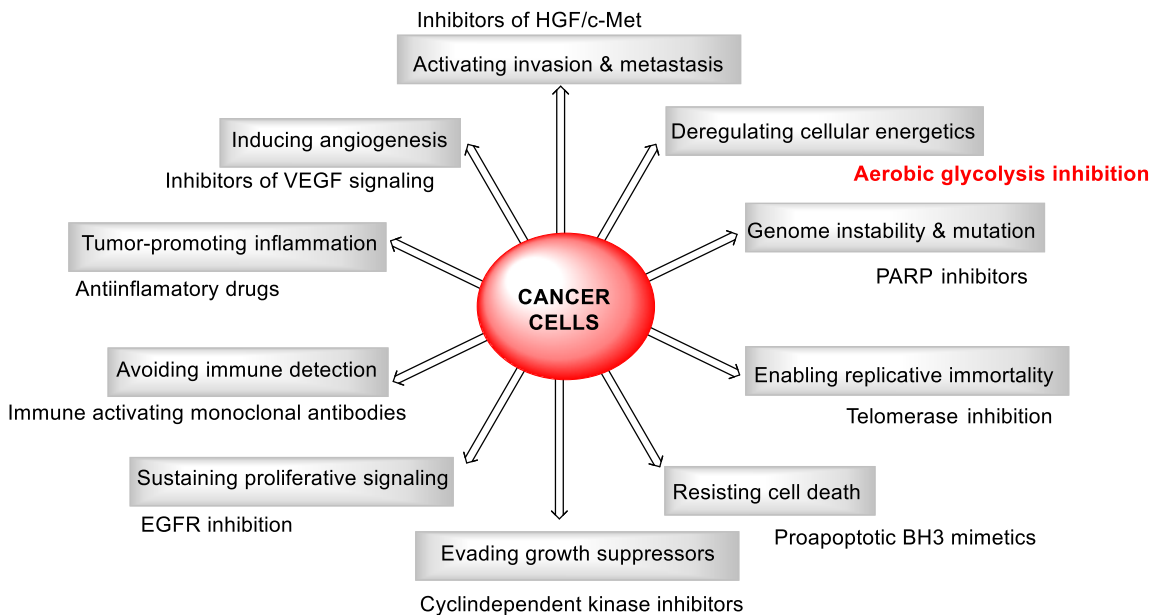


Figure 1a: Important hallmarks of cancer and their characteristics²

1.2 Glycolysis and its relation to Warburg effect

Some of the important cellular metabolic pathways for generation of energy include aerobic glycolysis, mitochondrial oxidative phosphorylation (OxPhos), glutaminolysis, fatty acid metabolism, etc. Adaptation of glycolysis is a critical survival mechanism for many advanced stage tumors.⁵ Glycolysis is a process of metabolism which involves the conversion of glucose to lactate and pyruvate. Tumors contain oxygen rich (aerobic) and oxygen deficient (hypoxic) regions. In tumor hypoxia, cancer cells consume large quantities of glucose which results in the production of lactic acid and pyruvic acid as by-products. Glycolysis is a very inefficient process as just two moles of ATP are produced per one mole of glucose, but it occurs at a rapid pace to fuel the hypoxic cells.⁶ The nearby aerobic cancer cells take up this lactic acid for energy generation through mitochondrial OxPhos which produces 30-36 moles of ATP.⁷ Lactic acid, as an energy substitute for survival, prevents the aerobic cells from consuming large quantities of glucose.⁵ Thus, the limited glucose available to the tumor is used most efficiently via a synergistic metabolic symbiosis called Warburg effect (Figure 1b).^{7,8} Tumor hypoxia also leads to treatment failure, relapse and, patient mortality as these cells are generally resistant to standard chemo- and radiation therapy.

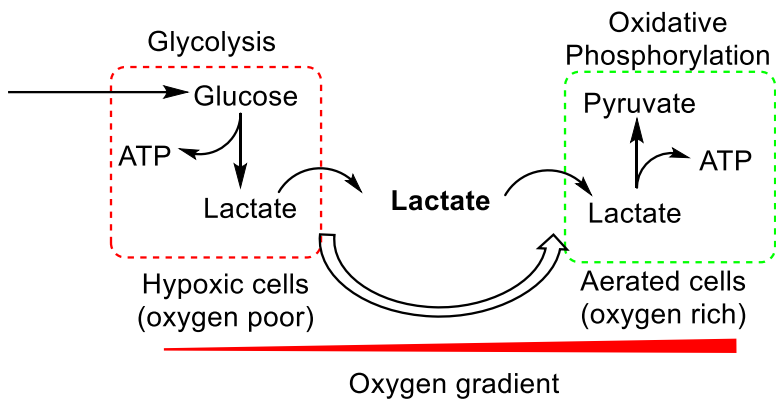


Figure 1b: Metabolic symbiosis and Warburg effect in cancer cells

1.3 Reverse Warburg effect in cancer cells

Tumor microenvironment is heterogeneous in nature and consists of epithelial cells and stromal fibroblast cells. Lactic acid as an energy substitute for cancer cell survival prevents the aerobic cells from consuming large quantities of glucose. Aerobic glycolysis takes place in cancer-associated stromal fibroblasts rather than in epithelial cancer cells. Epithelial cancer cells initiate oxidative stress in their neighboring stromal fibroblasts resulting in mitochondrial dysfunction and aerobic glycolysis (Warburg Effect). These fibroblasts undergo myofibroblastic differentiation and release lactic acid and pyruvic acid which are then taken up by the adjacent epithelial cells via monocarboxylic acid transporters (MCTs) for mitochondrial OxPhos, ATP production and further proliferation. Thus, the limited glucose available to the tumor is used most efficiently as the tumor stromal fibroblasts and epithelial cancer cells develop a host-parasite relationship called reverse Warburg Effect (Figure 1c).^{9,10}

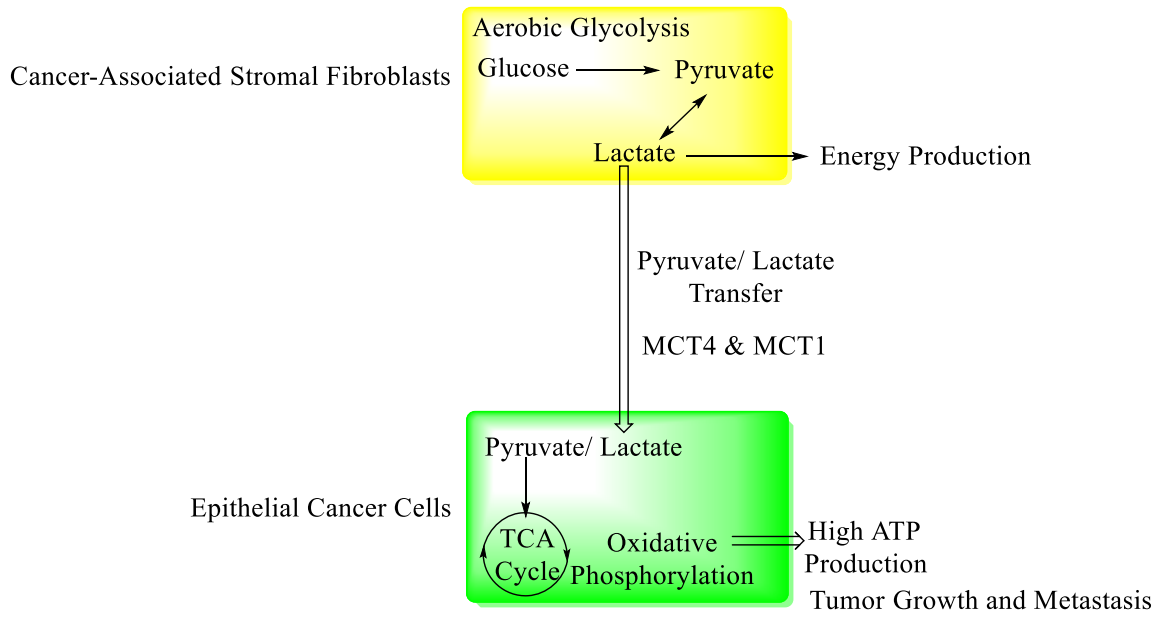


Figure 1c: Stromal-epithelial metabolic coupling and reverse Warburg effect

1.4 Monocarboxylic acid transporters and their importance in metabolism

MCTs belong to the *SLC16* gene family of proton-linked plasma membrane transporters that shuttle small molecules such as lactic acid, pyruvic acid and other ketone bodies across biological membranes of cells.^{11,12} There are 14 known isoforms of MCTs, and among these, MCT1 and MCT4 have been known to be highly involved in metabolic processes. MCT1 is encoded by *SLC16A1* gene and it is a 40 kDa protein consisting of 12 transmembrane domains which are assumed to have hydrophobic α -helical segments.^{11,13} MCT1 has intracellular N-terminal and C-terminal with loops spanning across the cellular transmembrane. Although the crystal structure of MCT1 is unknown, few homology models have been identified.^{14,15} Among MCTs 1-14, MCT1 is a predominant isoform and it is known to be expressed ubiquitously throughout the body. MCT1 has low affinity for lactic acid compared to MCT4.^{11,16} As discussed in Warburg effect, the lactic acid produced in hypoxic cancer cells is transported out of the cells via MCT1 and imported into the nearby aerobic cancer cells via MCT4 for energy generation through OxPhos, which produces 30-36 moles of ATP. Thus, cancer cells survive as glucose is taken up only by hypoxic cells whereas lactate is consumed by aerobic cells.^{8,11,12} A symbiotic relationship is maintained in the tumor microenvironment by MCT1 and MCT4 contributing to the Warburg and reverse Warburg effects. Hence, MCT1 and MCT4 can be considered as important targets for cancer treatment. Inhibition of MCT1 and/or MCT4 results in the increase of intracellular pH leading to cell acidosis, and eventually, aerobic cells do not receive lactic acid for OxPhos which results in the suppression of tumor growth (Figure 1d).

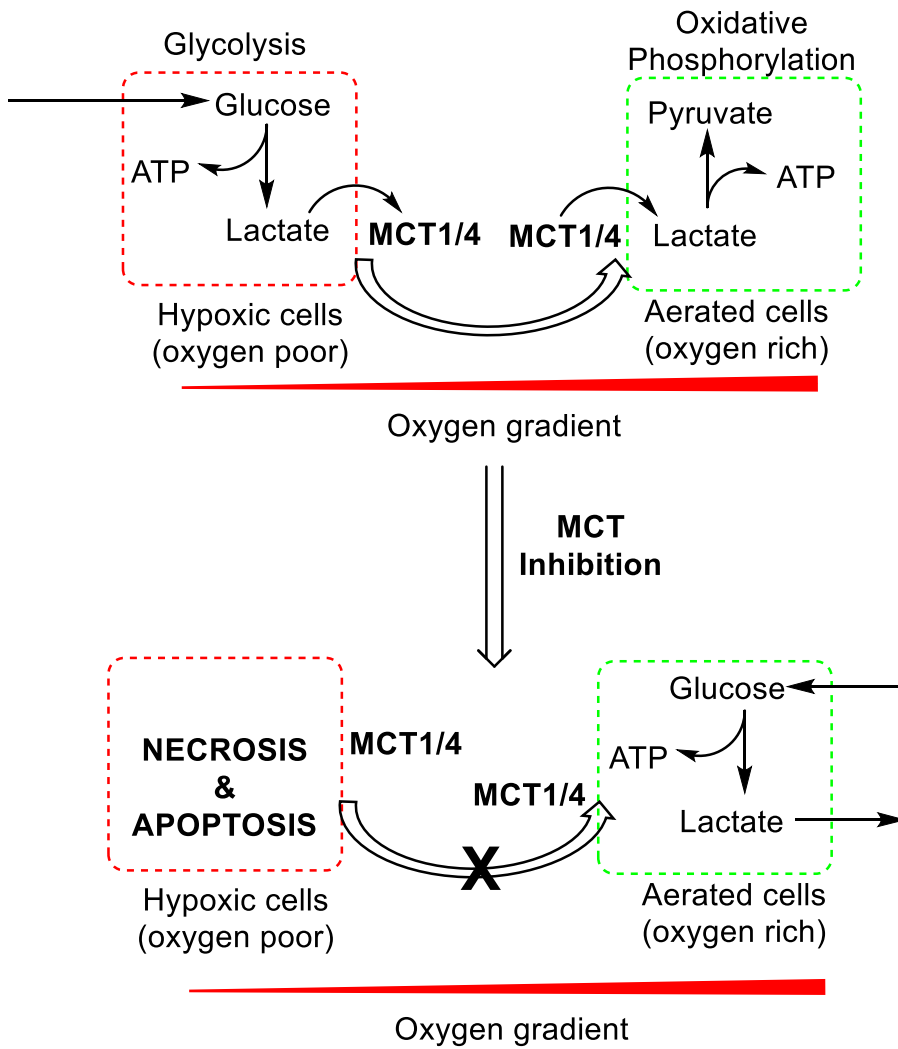


Figure 1d: Inhibition of MCT1 and/or MCT4 leads to a decrease in tumor growth

1.5 MCT1 expression in cancers

Excessive glycolysis and consequent production of lactic acid in cancer cells lead to cellular acidosis, apoptosis and necrosis. To avoid these processes, cancer cells overexpress several glycolytic enzymes and transporters including MCTs to shuttle the excess lactic acid out of the cells. As a result, extracellular pH decreases leading to the upregulation of angiogenic factors and subsequent tumor growth, invasion and metastasis.¹⁷ High MCT1 expression is also associated with poor patient prognosis in breast and lung cancer patients.^{17,18} An analysis of ~126 cases of colorectal carcinomas revealed that MCT1 is overexpressed in this cancer, and especially, plasma membrane expression of MCT1 correlates to the vascular invasion of colorectal carcinomas.¹⁹ Literature reports also suggest that MCT1 and MCT4 expression is chaperoned by CD147, an extracellular matrix metalloproteinase inducer.^{18,20-22} High MCT1 and CD147 expressions correlate with decreased survival rate in gastrointestinal stromal tumors as well as in urothelial carcinomas.^{21,22}

1.6 MCT4 expression in cancers

MCT4 is a 43 kDa protein consisting of transmembrane domains and is encoded by *SLC16A3* gene. MCT4 is expressed in various tissues that undergo vigorous glycolysis such as astrocytes, muscle cells, white blood cells, white skeletal muscle fibers, chondrocytes.²³ MCT4 is mainly involved in the efflux of glycolysis by-products lactic acid and pyruvic acid in the cell. The affinity of MCT4 for various substrates is very low when compared to that of MCT1 with K_m values for pyruvic acid being > 100 mM, whereas the affinity of MCT4 towards lactic acid is known to be 30 mM.

MCT4 is expressed in many cancers. A cohort of 223 surgically resected patient samples of pancreatic ductal carcinoma were evaluated for MCT4 expression and this study showed that the presence of MCT4 resulted in poor patient prognosis. In MCT4 expressing cell lines PL45 and MIAPaCa2, the rate of glycolysis was found to be very high. When MCT4 expression is knocked out in these cell lines, the rate of glycolysis was also substantially reduced when compared to the original cell lines.²⁴ High MCT4 expression correlates with poor patient prognosis in several other cancers including prostate cancer, triple negative breast cancer, colorectal carcinomas, and head and neck cancer.^{10,19,24–27} Owing to the importance of MCT4 expression and its association with several cancers, MCT4 could be considered as a potential biomarker and druggable target for cancer treatment.

1.7 Triple negative breast cancer and MCT4

Although there are ~60 major and ~200 subtypes of cancers, breast cancer is number one in terms of incidence and number two in terms of mortality.²⁸ Breast cancer can occur in both women and men, but it is most common in women. One out of eight women is affected by breast cancer in United States. Breast cancer can be broadly classified into three categories based on receptor status (Figure 1e).²⁹

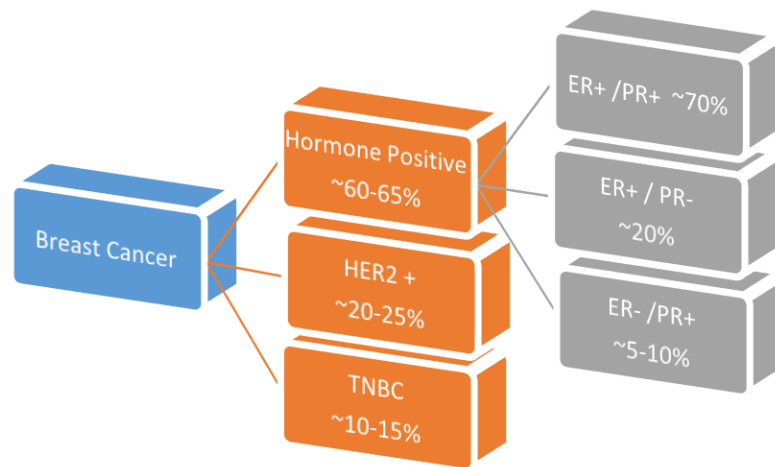


Figure 1e: Breast cancer is classification based on the receptor status. Hormone positive (HR+), human epidermal growth factor receptor-2 (HER-2), and triple negative breast cancer (TNBC). HR+ can be further classified into three types based on estrogen and progesterone receptors: ER+/PR+, ER+/PR- and ER-/PR+

Triple negative breast cancer (TNBC) constitutes 10–15% of all breast cancers and it is associated with aggressive tumor growth, recurrence, metastasis and poor patient outcome.³⁰ Despite numerous advances in tumor diagnosis, surgical procedures, and radio/chemotherapy, prognosis has not improved significantly for patients with TNBC in 25 years. Generally, breast cancers are targeted for receptor markers such as ER, PR and HER2 for treatment. Tamoxifen, raloxifen, are the drugs used for ER⁺ breast cancers. The absence of well-defined molecular targets such as estrogen/progesterone receptors or HER2 receptors makes TNBC treatment very challenging.³¹ The present treatment options include surgical resection, radiation therapy and chemotherapy with cytotoxic drugs. Paclitaxel (taxanes), carboplatin, cisplatin and anthraquinones such as doxorubicin are used for TNBC treatment.³² Anticancer agents used for TNBC treatment are hindered as they are non-specific in nature and cause serious side-effects that include permanent damage to the immune system. Most patients initially respond to the standard chemotherapy and radiation therapy but majority of them relapse and become drug resistant.³² Other pathways which involve in tumor proliferation needs to be explored and these pathways should be targeted for personalized treatment of TNBC.

Recently, it was reported that MCT4 expression in tumor-associated stromal fibroblasts is a functional marker of aggressive aerobic glycolysis, and lactic acid efflux.¹⁰ High stromal MCT4 levels are associated with decreased overall survivability with <18% of TNBC patients surviving 10-year post diagnosis. In complete contrast, patients with no stromal MCT4 expression had excellent prognosis with ~97% of the patients surviving 10-year post diagnosis. TNBC has increased expression of MCT4 and inhibition of MCT4

leads to cellular acidosis in hypoxic regions and their inhibition in aerobic regions cause greater glucose consumption instead of lactic acid, thus resulting in further stress and death of the hypoxic cancer cells.¹⁰ Hence, MCT4 could be targeted as a biomarker and MCT4 inhibition could lead to tumor growth suppression in TNBC.

1.8 Significance of caveolin-1 in TNBC

Caveolins (Cav) are scaffolding proteins and their functions in cellular processes involve endocytosis, signal transduction and cholesterol transport. Of the known three isoforms, Cav-1 and Cav-2 are ubiquitously expressed and Cav-3 is mainly expressed in muscle cells.³³ Cav-1 is considered to be one of the tumor suppressor genes.³⁴ Recent studies indicate that acute loss of stromal Cav-1 leads to oxidative stress, mitochondrial dysfunction and aerobic glycolysis in cancer related fibroblasts.³⁵ It has also been proven that dysfunctional mitochondria are removed from fibroblasts via autophagy/ mitophagy resulting in even more aggressive aerobic glycolysis.³⁶ The glycolytic end products are then transferred from tumor-associated fibroblasts to adjacent cancer cells, which in turn stimulate mitochondrial biogenesis and generate ATP via oxidative phosphorylation (reverse Warburg effect). Importantly, a loss of stromal Cav-1 in TNBC is associated with aggressive tumor initiation, growth, recurrence, angiogenesis, metastasis, and poor clinical outcome.³⁷ High patient mortality is also observed in Cav-1 deficient hormone positive (ER+ and PR+) and HER2+ breast cancer patients. Similar results were observed in brain tumors, prostate cancer and melanoma highlighting the importance of stromal Cav-1 in other types of cancers.^{25,38,39}

Loss of stromal Cav-1 also leads to tamoxifen resistance, early tumor recurrence, lymph node metastasis and high patient mortality in hormone positive breast cancers.⁴⁰ TNBC patients with loss of stromal Cav-1 expression can be classified as high-risk group. Absence of tumor epithelial Cav-1 has no prognostic importance. Stunningly, the 10-year survival rate for patients with high stromal Cav-1 is ~91% vs less than 25% rate for patients

with absent stromal Cav-1 expression. This data clearly show the significance of tumor associated stromal Cav-1 in TNBC.⁴¹ Hence, reduced Cav-1 expression can be utilized as biomarker to determine the treatment for high-risk group of cancer patients.²⁶ TNBC patients with high stromal Cav-1 have a good 5-year survival rate (~75%), while those with moderate Cav-1 levels have ~40% and absent stromal Cav-1 have just ~9% survival rate. Similar results were observed in prostate cancer and melanoma highlighting the importance of stromal Cav-1 in other types of cancers.^{25,38} Loss of stromal Cav-1 and high stromal MCT4 are inversely related and are associated with aggressive tumor growth, recurrence and metastasis. Only ~2% of the patient population (out of ~160) had high stromal expression of both Cav-1 and MCT4 indicating that these two gene products are mutually exclusive events.¹⁰

TNBC patients with loss of stromal Cav-1 and high MCT4 expression can be classified as high-risk group and these markers can also be utilized for risk assessment and personalized cancer treatment.^{9,26} The targeted inhibition of MCT4 has potential to prevent the glycolytic process in tumor associated stromal fibroblasts and restrict the nutrient supply to epithelial cancer cells arresting their growth. Tumor epithelial MCT4 expression and absence of epithelial Cav-1 had no prognostic importance indicating that the reverse Warburg effect is in fact the determining factor and conventional Warburg mechanism has less clinical importance.^{9,10,26,36}

1.9 Metabolic plasticity in cancer

Tumor microenvironment is highly heterogeneous in nature, poorly vascularized at the center and exists in highly nutrient-poor conditions with limited glucose and oxygen. Interestingly, the mitochondrial electron transport chain can operate with oxygen levels as low as 0.5% albeit with low efficiency.⁴² To compensate for suboptimal OxPhos, cancer cells exhibit high levels of mitochondrial biogenesis and generate a greater mitochondrial mass.^{43,44} OxPhos pursuing cancer cells also oxidize the glycolytic end product lactic acid to pyruvic acid and establish a symbiotic metabolic plasticity with glycolytic cancer epithelial cells (Figure 1f). These above-mentioned observations indicate that glycolysis and OxPhos are coupled within the tumor and this dynamic symbiosis can be recognized as an Achilles' heel for pharmacological intervention.

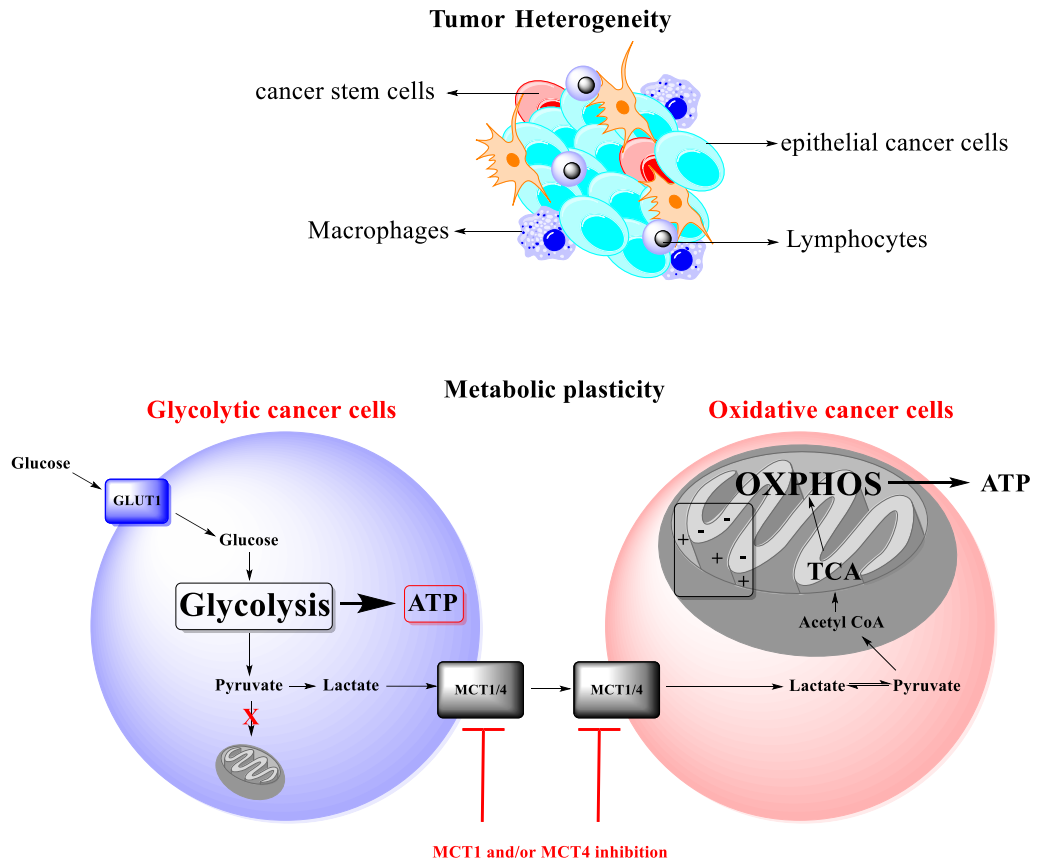


Figure 1f: Tumor heterogeneity and metabolic plasticity in cancer cells

1.10 Other processes involved in cancer cell survival

1.10.1 Oxidative stress and reactive oxygen species

Oxidative stress represents the imbalance between the production and manifestation of reactive oxygen species (ROS) and reactive nitrogen species (RNS). Oxidative stress impairs the ability of a system to efficiently eliminate these reactive intermediates before they cause any cellular damage.⁴⁵ Mitochondrial ROS includes singlet oxygen, hydroxyl radical and hydrogen peroxide. These species inhibit electron transport processes involved in ATP production. Initially, cancer cells secrete hydrogen peroxide that in turn triggers oxidative stress in adjacent fibroblasts. The mechanism of oxidative stress involves stromal autophagal destruction of Cav-1, which aggravates further oxidative stress and activation of autophagic inducers HIF-1 α and NF- κ B leading to the onset of inflammation, autophagy, mitophagy, and aerobic glycolysis.⁴⁶ Cancer cells also take up products from autophagy such as nucleotides, amino acids, and fatty acids for further energy production and also as cellular building blocks. Oxidative stress and the generation of ROS in cancer associated fibroblasts have an adverse effect on the cancer cells leading to DNA damage and genetic instability further driving tumor-stroma co-evolution.⁴⁷

In response to autophagy and mitophagy, stromal cells pursue aerobic glycolysis and at the same time, epithelial cancer cells undergo mitochondrial biogenesis to amplify their capacity for oxidative phosphorylation.^{35,36,48} These processes result in non-selective autophagy and mitochondrial selective mitophagy leading to mitochondrial dysfunction in

tumor associated stromal cells. When cancer cells are co-cultured with normal fibroblasts, mitochondrial mass is increased in cancer cells and loss of mitochondria is observed in fibroblasts.⁴⁹ Here, the aggressive cancer cells act as parasites and use oxidative stress as a weapon to derive energy rich nutrients from surrounding stromal fibroblasts.³⁶ The cancer cells utilize these nutrients for further proliferation. This evolution of cellular metabolism allows the cancer cells to seed anywhere without any angiogenesis for food supply. This evolutionary process also explains how cancer cells survive during metastasis.⁵⁰

1.10.2 Autophagy

Autophagy is a cellular homeostatic mechanism involving protein and organelle degradation and this process has an important role in human physiology and pathogenesis of several diseases.⁴⁷ Tumors constantly shape their stroma and establish an abnormal hetero-ecosystem (tumor-stroma co-evolution). Similar type of co-evolution also exists in the autophagic tumor stroma and adjacent cancer cells.⁵¹ Cancer cells induce oxidative stress in fibroblasts and establish the autophagic tumor stroma resulting in energy-rich fuel supply to adjacent epithelial cancer cells. Stromal catabolism via autophagy and mitophagy fuels the anabolic growth of tumor cell progression and metastasis. This new paradigm shifting process is called “The autophagic tumor stroma model of cancer metabolism”, or the “reverse Warburg effect”. This evolution of tumor microenvironment leads to cancer cell DNA damage, genomic instability, and evasion of cellular apoptosis. These factors are very crucial in cancer growth, advancement, and eventually metastasis.^{45,52} Autophagy is also induced via another metabolic process called glutaminolysis.^{53,54}

1.10.3 *Glutaminolysis*

Apart from vigorous glycolysis, cancer cells are often addicted to glutaminolysis for ATP generation to meet energy demands for rapid proliferation. Glutaminolysis is a process in which glutamine influxes into the tumor cells and undergoes double deamination in the presence of enzymes glutaminase and glutamate dehydrogenase to form α -ketoglutarate (α KG).^{53,54} To compensate the loss of pyruvic acid from glycolysis in normal cells, α KG enters into TCA cycle via OxPhos to degrade into pyruvic acid, lactic acid, alanine, and citrate and produce ATP to sustain energy levels in the cell. The diffusible by-product of glutaminolysis is ammonia, which is a potent inducer of autophagy.^{9,46,55} Glutamine also serves as nitrogen precursor for the synthesis of proteins and nucleotides required for tumor growth.⁹ This glutamine addiction by cancer cells is another way of inducing autophagy in the stromal microenvironment and introducing aerobic glycolysis. This vicious cycle of Cav-1 deficiency, oxidative stress, autophagy/mitophagy, aerobic glycolysis, and oxidative metabolism of energy rich nutrients explains the heterogeneity of tumor microenvironment.⁵⁶

1.11 MCT1 inhibitors reported in the literature

As discussed above, glycolysis and mitochondrial OxPhos are the main sources of energy pathways pursued by cancer cells and, MCT1 and MCT4 play an important role in these two critical processes in cancer cells. Inhibition of MCT1 and/or MCT4 could lead to anticancer efficacy and targeting these transporters has become an emerging hallmark of cancer as many tumors overexpress MCT1 and/or MCT4. Owing to the importance of targeting MCTs for cancer therapy, many MCT inhibitors have been developed in the past decade. Some of the literature reported MCT1 and MCT4 inhibitors have been summarized below.

1.11.1 α -Cyano-4-hydroxy cinnamic acid (CHC)

CHC is a known inhibitor of MCT1 and has been studied as a plant growth regulator, mitochondrial pyruvate carrier inhibitor, and for other biochemical functions (Figure 1g). Several *in vitro* transport studies and *in vivo* anticancer efficacy studies have been conducted using CHC by targeting MCT1 in various cancers.^{6,57}

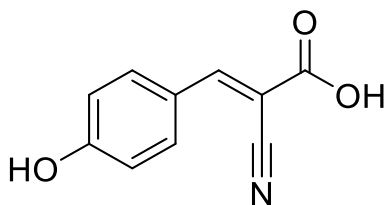


Figure 1g: Structure of CHC

Sonveaux et al. reported that the treatment of human cervix squamous cell carcinoma SiHa and human colorectal adenocarcinoma WiDr cells with 5 mmol CHC resulted in a switch from lactate-fueled respiration to glycolysis.⁶ These cells also showed an increase in extracellular lactic acid concentration. MCT1 inhibition with CHC also caused cell death in SiHa and WiDr cell lines.⁶ Intraperitoneal administration of 25 μ mol CHC (in 200 μ L saline) in Lewis lung carcinoma (LLc) bearing syngeneic C57BL6/J mice and WiDr tumor bearing athymic BALB/c mice significantly slowed the tumor growth. MCT1 inhibition via treatment with CHC also radiosensitized LLc tumor in mice.⁶ A study using mouse hepatocarcinoma transplantable liver tumor (TLT) bearing syngeneic Rj:NMRI mice revealed that CHC did not exhibit anticancer efficacy as TLT do not express MCT1.

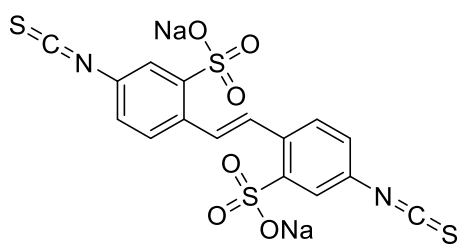
In another study, MCT1 expressing U87-MG human glioblastoma cells were intracranially implanted in Crl:NIH-rnu rats and after 14 days, an osmotic pump was implanted in the brain to deliver 40 mM CHC directly to the tumor site. After 120 days of tumor implantation, 50% survival rate was observed in the mice treated with CHC.⁵⁷ Histological analysis of the resected tumors revealed complete necrosis of the tumor, whereas no necrosis was observed in areas surrounding the tumor site. This study clearly indicated that MCT1 inhibition with CHC leads to an increased survival rate in gliomas.⁵⁷

In 2013, CHC was tested for its effect on cell viability using sulforhodamine-B (SRB) assay in 8 high-grade glioma cell lines: SW1088, SW1783, U87-MG, A172, SNB-19, GAMG, U251 and U373.⁵⁸ This study indicated that CHC exhibited IC₅₀ values in the range of 2.5-10.8 mM. Glucose consumption study also revealed that the cells treated with

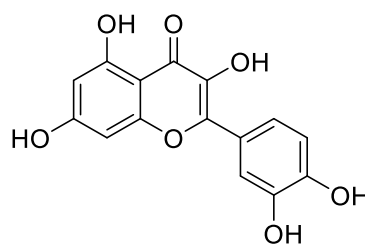
5 and 10 mM CHC lead to a significant decrease in glucose consumption in U251 cell line compared to less CHC sensitive SW1088 cell line.⁵⁸ CHC also reduced migration and invasion in U251 cell line as assessed by wound-healing and invasion assays. Another study was conducted using chicken chorioallantoic membrane (CAM) assay in chicken embryos. U251 cell line was implantated in chicken embryos, and a treatment with 5 mM CHC for 3 days resulted in a significant decrease in the perimeter of tumors as well as the vascularization of tumors compared to the control group.⁵⁸ CHC also exhibited significant anticancer efficacy in U2OS/MTX and ZOS osteosarcoma tumor xenograft models using BALB/c nude mice.⁵⁹

1.11.2 Disodium 4,4'-diisothiocyanatostilbene-2,2'-disulfonate

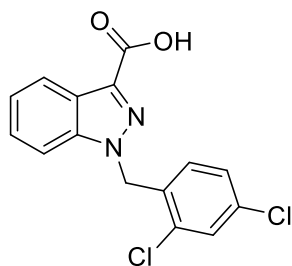
Disodium 4,4'-diisothiocyanatostilbene-2,2'-disulfonate (DIDS, Figure 1h) is a known anion exchange blocker and anti-apoptotic agent. DIDS inhibits voltage-dependent anion channel (VDAC) and results in mitochondrial dysfunction.⁶⁰ DIDS also leads to an irreversible inhibition of MCT1 with an IC_{50} value of 100 μ M and a K_i value of 40 μ M in rat erythrocytes due to the presence of reactive isothiocyanate groups.⁶¹



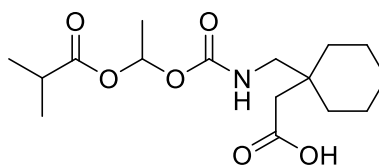
DIDS



Quercetin



Lonidamine



Gabapentin enacarbil

Figure 1h: Structures of MCT1 inhibitors DIDS, quercetin, lonidamine and gabapentin enacarbil

1.11.3 Quercetin and lonidamine

2-(3,4-dihydroxyphenyl)-3,5,7-trihydroxy-4H-chromen-4-one (quercetin, Figure 1h) is a natural flavonoid which has been identified as a potent MCT1 inhibitor.⁶² Lonidamine is an indazole carboxylic acid with 2,4-dichlorobenzyl substitution on N, and this compound is also known to inhibit MCT1 in *Xenopus laevis* oocytes (Figure 1h). This compound is also found to inhibit glycolysis and mitochondrial OxPhos, and also mitochondrial pyruvate carrier.⁶³ In another study, the efficacy of CHC, quercetin and lonidamine were tested in several human breast cancer cell lines such as MDA-MB-468, MDAMB-231, Hs578T, BT-20, MCF-7/AZ and SkBr3. Most of these cell lines express either MCT1 or MCT4 or both, whereas CD147 was expressed in all these cell lines. Glucose consumption study revealed that of all these cell lines, only MDA-MB-468, SkBr3 and Hs578T exhibited an increased lactate production.⁶⁴ After treatment with CHC, quercetin and lonidamine, MDA-MB-468 and SkBr3 cell lines showed a significant reduction in glucose consumption as well as lactate production. Cell migration assay also revealed that these MCT inhibitors significantly decreased cell invasion in a TNBC MDA-MB-468 cell line.⁶⁴

1.11.4 *Gabapentin enacarbil*

Gabapentin enacarbil, a prodrug of gabapentin, is used as an anticonvulsant and analgesic agent (Figure 1h). It has increased oral availability compared to gabapentin and approved by FDA in 2011 for the treatment of restless leg syndrome. Gabapentin enacarbil is also a substrate for MCT1 and sodium-dependent multivitamin transporter. This compound is also known to inhibit MCT1 in a ^{14}C lactic acid transport assay in human embryonic kidney cells that express MCT1.^{65,66}

1.11.5 3-Bromopyruvic acid (3-BPA) and its analog NEO218

3-BPA is a brominated derivative of pyruvic acid and a known inhibitor of MCT1 that induces cell death in various cancer cells that overexpress *MYC* oncogene. 3-BPA was tested for its anticancer efficacy in MCT1 expressing Kelly tumor xenograft model at dosage of 2.5 mg/Kg. Mice treated with 3-BPA significantly reduced tumor burden compared to the control group.⁶⁷ Recently, a perillyl alcohol conjugated 3-BPA was developed as an MCT1 inhibitor (Figure 1i). This molecule was designated as NEO218, and this compound exhibited excellent IC_{50} in various cell lines with high MCT1 expression and this activity is dependent on the level of MCT1 expression.⁶⁸ For example, NEO218 showed high micromolar activity in low MCT1 expressing cell line MCF7. Furthermore, this compound exhibited potent activity in 3-BPA resistant cell lines.⁶⁸

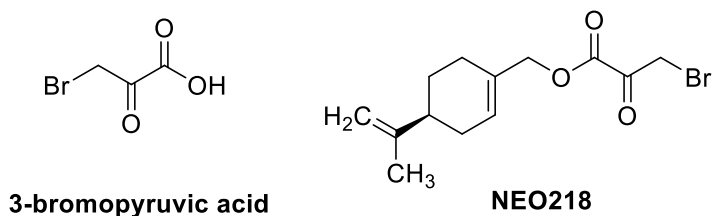


Figure 1i: Structures of 3-bromopyruvic acid and NEO218

1.11.6 AstraZeneca's AZD3965 and ARC155858

AstraZeneca developed potent MCT1 inhibitors and the lead candidate compounds AZD3965 and ARC155858 were shown in the Figure 1j.^{67,69-73} These compounds have specificity towards MCT1 inhibition and are also known to have excellent immunosuppression properties and good oral bioavailability. Currently, AZD3965 is in phase-I clinical trials for the treatment of diffuse large B-cell lymphoma, Burkitt lymphoma and other solid tumors.

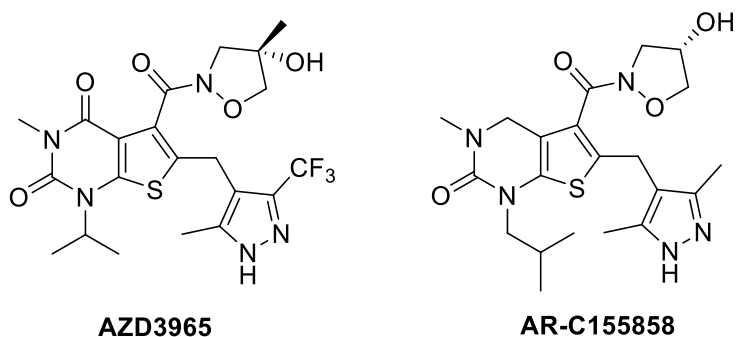


Figure 1j: Structures of AZD3965 and AR-C158858

L-lactate transport study in rat erythrocytes and *Xenopus oocytes* revealed that ARC155858 showed K_i value of 2.3 nM and 100 nM, respectively.⁶⁹ In a study of human lung small cell carcinoma COR-L103 xenografts in male nonobese diabetic scid- γ mice, treatment with AZD3965 at a dosage of 100 mg/Kg lead to significant anticancer efficacy and increased intracellular lactate concentrations *in vivo*.⁷³ In another study, luciferase-expressing CA46 Burkitt lymphoma tumor cells have been injected in NOD/LtSz-scid IL-2R γ null (NSG) mice via tail vein, and treatment with AZD3965 at a dosage of 100 mg/Kg resulted in a significant reduction of tumor burden.⁷⁴

1.11.7 Substituted pteridine diones and triones

Wang et al. reported substituted pteridine diones and triones as MCT1 inhibitors (Figure 1k). These derivatives were evaluated for their MCT1 inhibition using ^{14}C lactic uptake assay in MCF7 cell line engineered to overexpress MCT1. These studies indicated that pteridine trione derivative had MCT1 IC_{50} of 548 nM, whereas pteridine diones a-c exhibited IC_{50} values of 669 nM, 192 nM, 116 nM, respectively. These compounds were also tested for their cytotoxicity in MCT1 expressing human Raji lymphoma cell line and these results also indicated that these compounds inhibited 50% cell proliferation at 37-150 nM concentrations.⁷⁵

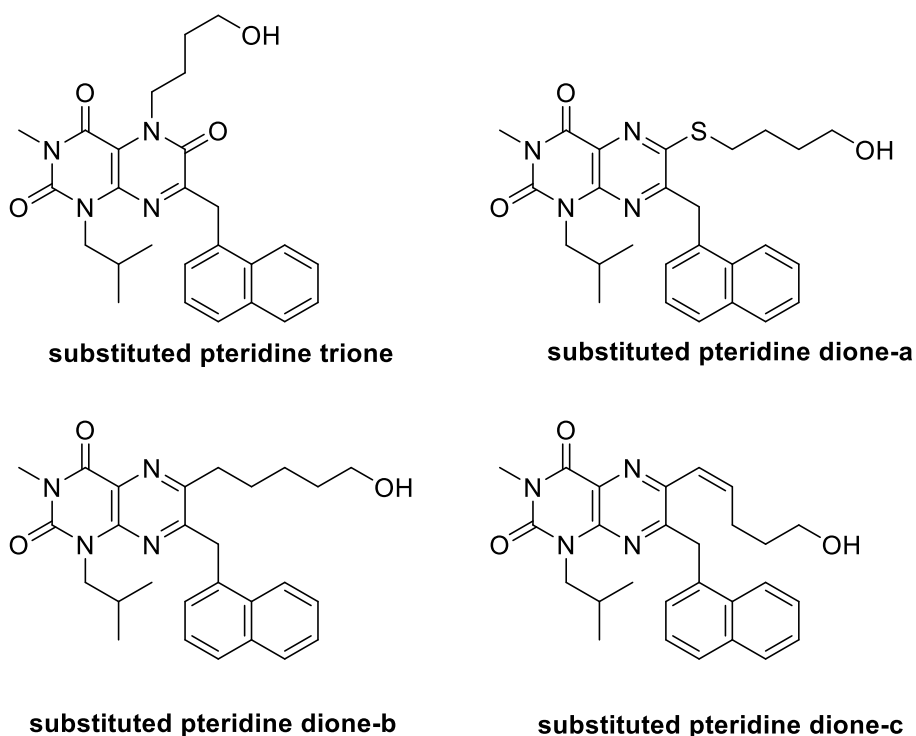


Figure 1k: Structures of substituted pteridine trione and diones

1.11.8 Coumarin derivatives 7AAC1 and 7AAC2

Draoui et al. reported few coumarin analogs as potent MCT1 inhibitors.^{76,77} Amino carboxy coumarins with *N,N*-diethyl and *N*-benzyl-*N*-methyl substitutions have been identified as lead compounds (Figure 11). These compounds 7ACC1 and 7ACC2 exhibited excellent cytotoxicity in SiHa cancer cell line with IC₅₀ values of 1.8 and 0.22 μM, respectively. Lactate uptake inhibition study show that these compounds inhibit MCT1 with IC₅₀ values 0.86 and 0.059 μM, respectively.⁷⁶

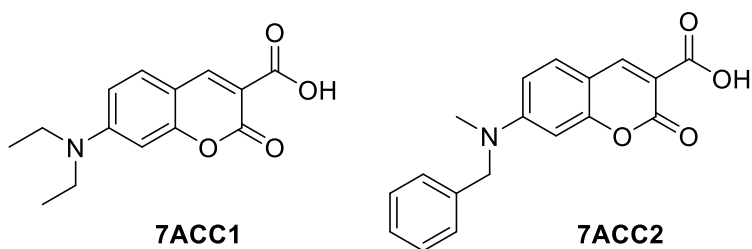
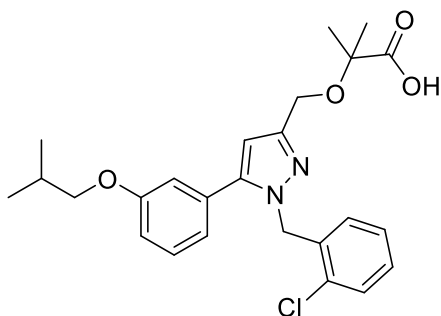


Figure 11: Structures of aminocarboxy coumarins 7ACC1 and 7ACC2

These potent compounds have also been tested for their anticancer efficacy in MCT1 expressing SiHa and HCT-116 and low MCT1 expressing UM-UC-3 tumor xenograft models using NMRI female nude mice. Treatment of these tumors with compound 7AAC1 and 7ACC2 at a dosage of 3 mg/Kg indicated that these compounds exhibit significant anticancer efficacy in MCT1 expressing SiHa and HCT-116 tumors, but did not affect UM-UC-3 tumors.⁷⁷ Another anticancer efficacy study has been conducted using MCT1 expressing MCF7 tumor orthotopic model using more potent 7ACC2, and this study also indicate that 7ACC2 exhibits excellent tumor growth inhibition.

1.11.9 Pyrazole methylpropanoic acid derivatives

Recently, a library of 2-((1-(2-chlorobenzyl)-5-(3-substituted phenyl)-1H-pyrazol-3-yl)methoxy)-2-methylpropanoic acids have been reported as specific MCT4 inhibitors. All these compounds were evaluated for MCT4 inhibition activity in MCT4 expressing MDA-MB-231 cell line and most of the pyrazole derivatives exhibited potent MCT4 inhibition in nM range. Specifically, isobutyl substituted pyrazole methylpropanoic acid depicted in Figure 1m showed 1 nM IC_{50} for MCT4 inhibition, whereas the same compound showed an IC_{50} of 5600 nM for MCT1 inhibition in MCT1 expressing BT20 cell line.⁷⁸



isobutyl substituted pyrazole methyl propanoic acid

Figure 1m: Representative example of 2-((1-(2-chlorobenzyl)-5-(3-substituted phenyl)-1H-pyrazol-3-yl)methoxy)-2-methylpropanoic acid

1.12 Conclusions

Cancer cells utilize aggressive glycolysis to produce energy required for proliferation, cancer progression and metastasis. MCT1 and MCT4 play an important role in shuttling the glycolysis end products pyruvic acid and lactic acid involved in Warburg and reverse Warburg effects. Cancer cells also shift their metabolism from glycolysis to OxPhos and vice versa depending on the microenvironment and their metabolic needs. As MCT1 and MCT4 are overexpressed in many types of cancers, they could be considered as metabolic biomarkers and their inhibition could lead to the disruption of energy, cellular acidosis and eventual cell death. Owing to the importance of MCT1 and MCT4 and its inhibition in cancer therapy, we proposed to design, synthesize and evaluate novel CHC based monocarboxylic acids for their *in vitro* and *in vivo* activity in various cancers, including colorectal cancer, breast cancer and gliomas.

1.13 Thesis objective and hypothesis

As discussed in the introduction, glycolysis and OxPhos are critical energy producing processes for cancer cell proliferation and progression. Many cancers pursue vigorous glycolysis and the end products lactic acid and pyruvic acid are effluxed via MCT4. These end products are then shuttled into adjacent cancer cells via MCT1 for further energy production by mitochondrial OxPhos. Thus, cancer cells maintain a symbiotic relationship called Warburg effect to continue cancer progression. Literature reports also indicate that cancer associated stromal fibroblasts undergo glycolysis and these glycolytic by-products are then taken up by adjacent epithelial cancer cells via MCTs for mitochondrial OxPhos to continue further proliferation. The fibroblastic tumor stroma and epithelial cancer cells develop a host-parasite relationship which is called as reverse Warburg effect. Recent studies indicate that conventional Warburg effect has less clinical importance and in fact, reverse Warburg effect is the defining factor for cancer prognosis depending on the MCT4 expression. Because of the highly heterogeneous nature of tumors, cancer cells not only depend on glycolysis, but also pursue OxPhos or intermediate phenotype as important energy sources. This malleability between one metabolic process to other is called metabolic plasticity and this process depends on the availability of nutrients and oxygen and dictate glycolytic or oxidative phenotypes.

We envision that energetic pathways such as conventional Warburg effect, reverse Warburg effect and metabolic plasticity are significant contributors for cell survival under dynamic and nutritionally challenged tumor microenvironment. MCT1 and MCT4 play a critical role in facilitating these metabolic processes via shuttling of lactic acid and other

ketone bodies in cancer cells. We hypothesize that targeted inhibition of MCT1 and/or MCT4 prevents glycolytic process, mitochondrial OxPhos, and/or metabolic plasticity, thereby affecting the symbiotic relationship in the tumor ecosystem. Although there are few MCT1 inhibitors currently under development, when we started this project, there was only one known selective MCT1 inhibitor reported by AstraZeneca. Owing to the importance of MCTs in tumor metabolism and their role in cancer cell progression, we undertook the project of developing new MCT inhibitors as potential anticancer agents. The main objective of this thesis is to design and synthesize a library of CHC and coumarin based derivatives and evaluate the *in vitro* and *in vivo* efficacy of these novel derivatives.

CHAPTER 2: Structure-activity relationship studies of α -cyano-4-hydroxycinnamic acid: Discovery of novel drug candidates with improved MCT1 inhibition properties

2.1 Structural modification of CHC

As mentioned in chapter-1, α -cyano-4-hydroxycinnamic acid (CHC) is a known MCT1 inhibitor with an IC_{50} values in high μ M range ($>100 \mu$ M). Our preliminary studies also demonstrated that CHC inhibited MCT1 function in rat brain endothelial 4 (RBE4) cell line at $\sim 150 \mu$ M. CHC also exhibited *in vivo* efficacy in various tumor models in mice but due to its low potency, most of the studies were done at high concentrations which cannot be translated into clinic for human usage. For this reason, we envisioned to carry out a detailed structure-activity relationship study to develop novel CHC derivatives that can inhibit MCT function at low μ M to nM range. CHC has five possible sites (Figure 2a) for structural modifications to create novel chemical entities and study their effects on MCT1 inhibition.

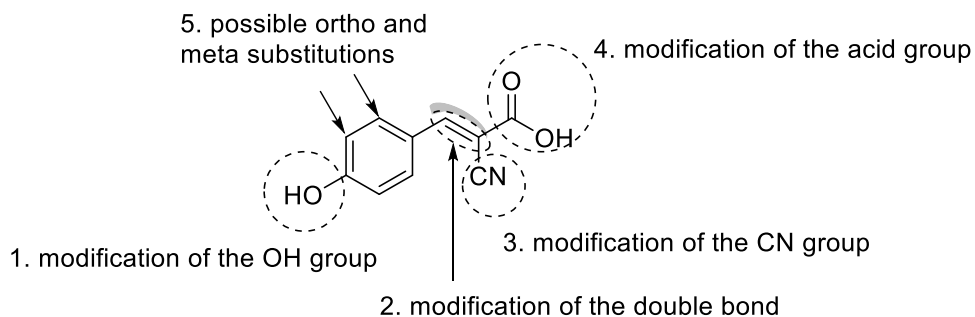


Figure 2a: Possible positions on CHC for structure-activity relationship studies

2.1.1 Structural modification of CHC via Knoevenagel condensation

Knoevenagel reaction is an important C-C bond forming reaction in which a carbonyl group and an activated methylene group are condensed in the presence of a base to create α,β -unsaturated systems efficiently (Figure 2b).⁷⁹ We envisaged that utilizing this condensation reaction will provide novel CHC derivatives and we could swiftly generate a library of structurally modified CHC derivatives.

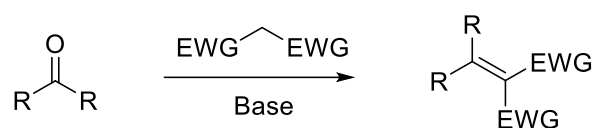
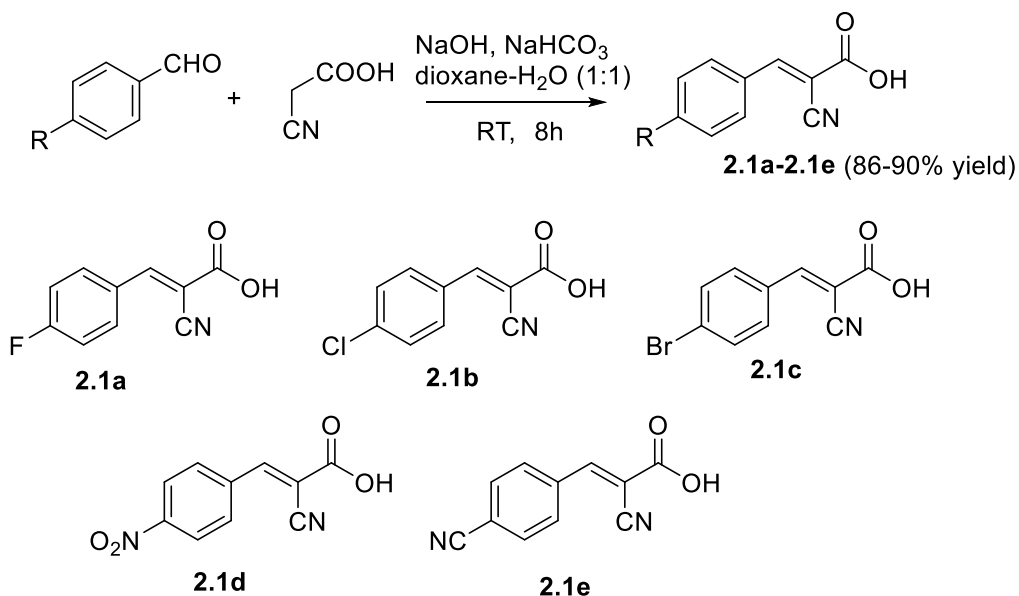


Figure 2b: Knoevenagel condensation reaction

2.1.2 Synthesis of electron withdrawing group containing CHC derivatives **2.1a-2.1e**

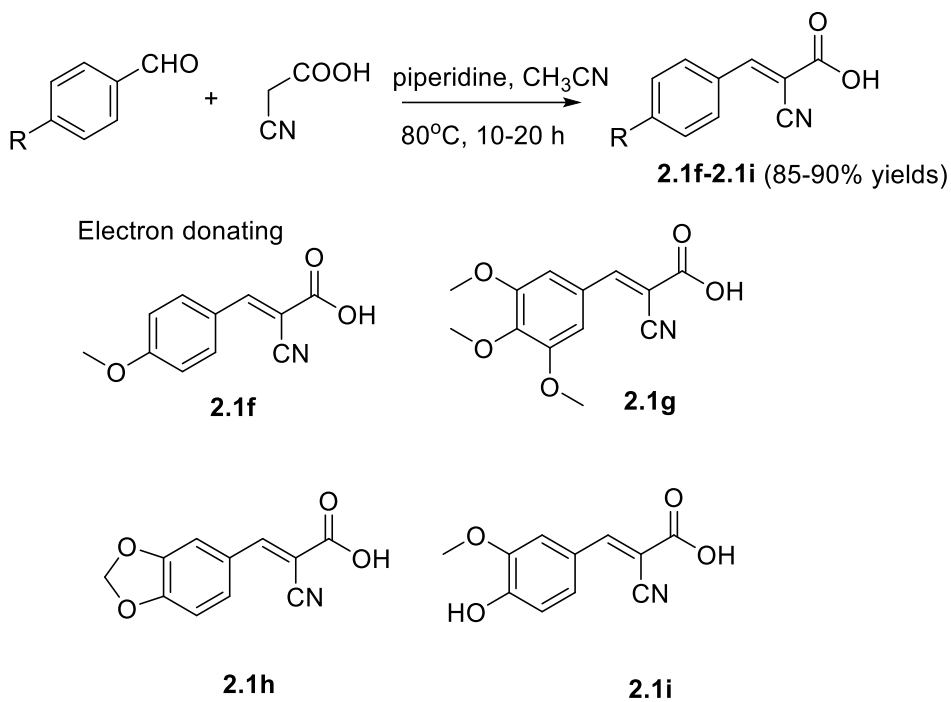
In this regard, we first focused our attention on the phenolic hydroxy group in CHC for structural modification with various substituents. This approach will cause minimal structural disturbance to CHC template by retaining other four structural components of CHC. First, we generated a small library of compounds by replacing hydroxy group at *para* position of CHC with several electron withdrawing groups such as F, Cl, Br, CN and NO₂. These compounds **2.1a-2.1e** were synthesized starting from their respective aldehydes using Knoevenagel condensation with cyanoacetic acid, in the presence of stoichiometric sodium bicarbonate and a catalytic amount of sodium hydroxide in dioxane-water mixture (Scheme 2a).



Scheme 2a: Synthesis of CHC derivatives **2.1a-2.1e** with electron withdrawing groups at *para* position

2.1.3 Synthesis of electron donating group containing CHC derivatives 2f-2i

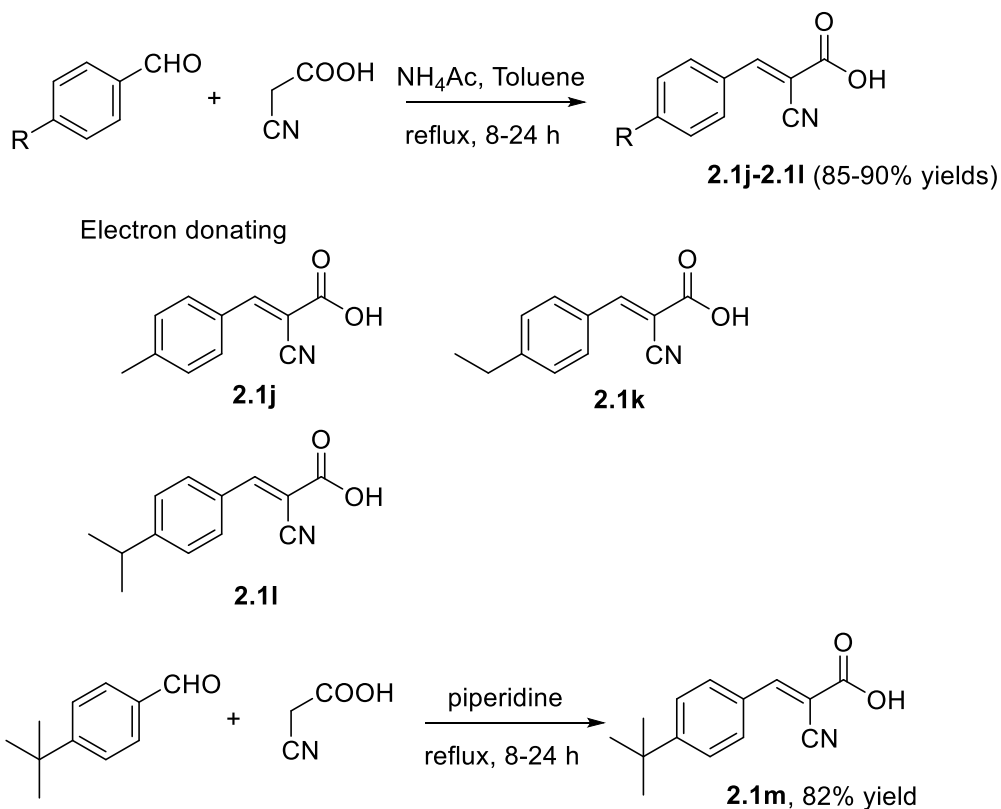
Similarly, we also synthesized CHC derivatives by replacing hydroxy group at *para* position with electron donating groups containing oxygen-based substitutions. For this purpose, we utilized various aldehydes such as 4-anisaldehyde, 3,4,5-trimethoxy benzaldehyde, vanillin, and piperonal, which were subjected to Knoevenagel condensation with cyanoacetic acid in the presence of piperidine as a base in acetonitrile to obtain corresponding cyanoacrylic acids **2.1f-2.1i**, respectively (Scheme 2b).



Scheme 2b: Synthesis of CHC derivatives **2.1f-2.1i** with electron donating groups at *para* position

2.1.4 Synthesis of 4-alkyl substituted CHC derivatives 2.1j-2.1m

We then synthesized 4-alkyl substituted CHC derivatives using tolualdehyde, 4-ethylbenzaldehyde, 4-isopropylbenzaldehyde, and 4-tertbutylbenzaldehyde. These aldehydes were reacted with cyanoacetic acid in the presence of ammonium acetate in toluene to obtain corresponding cyanoacetic acids **2.1j-2.1l**, respectively (Scheme 2c). In the case of 4-tertbutylbenzaldehyde, piperidine was used as a base to obtain the corresponding cyanoacetic acid **2.1m** in good yield.



Scheme 2c: Synthesis of CHC derivatives **2.1j-2.1m** with alkyl group substitutions at *para* position

2.1.5 Evaluation of compounds **2.1a-2.1m** for MCT1 inhibition using ^{14}C -lactate uptake assay

The synthesized compounds **2.1a-2.1m** were evaluated for MCT1 inhibition in RBE4 cell line using ^{14}C -lactate uptake assay. RBE4 cell line was chosen because of its high MCT1 expression, as confirmed by Western Blot analysis (Figure 2c-A). When a test compound is added to these cells in the presence of ^{14}C -lactate, the inhibition of the amount of lactate entering the cells can be measured by lysing the cells and measuring the amount of radioactivity in disintegrations per minute (dpm).

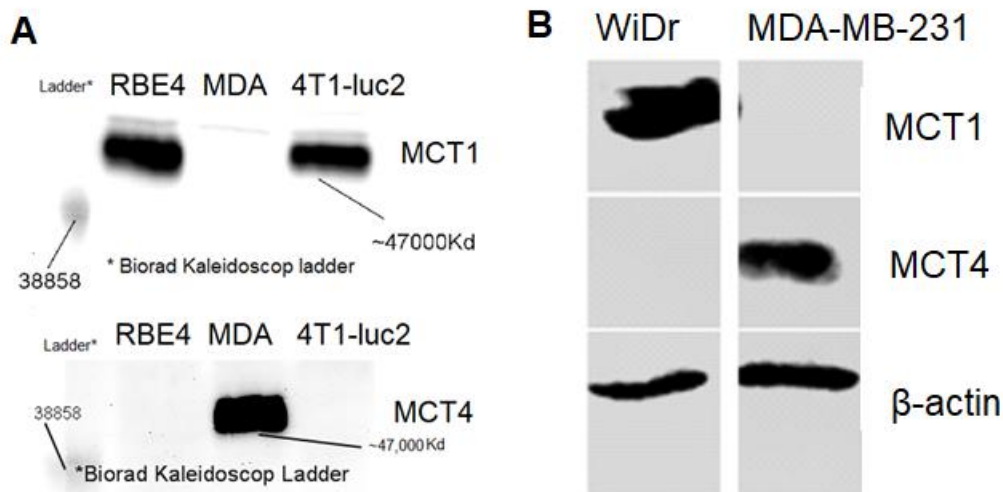


Figure 2c: Western blot analysis of MCT1 and MCT4 expressions in RBE4, MDA-MB-231, 4T1-luc2, and WiDr cell lines

Evaluation of MCT1 inhibition in electron withdrawing groups containing CHC derivatives revealed that fluoro, chloro and bromo derivatives **2.1a-2.1c** exhibited IC_{50} values of $\sim 1 \mu M$, and cyano derivative **2.1d** showed an IC_{50} value of $\sim 5 \mu M$, whereas nitro derivative **2.1e** showed the IC_{50} value at $\sim 50 \mu M$ (Figure 2d).

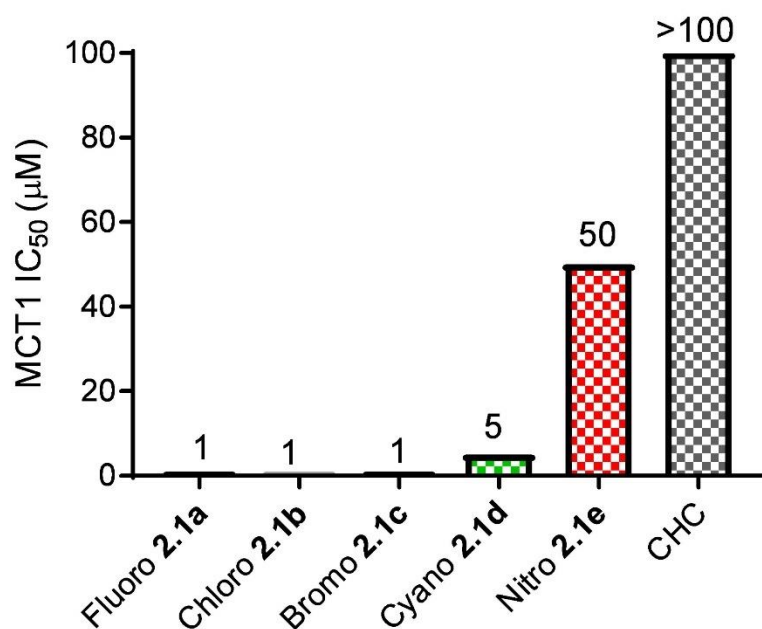


Figure 2d: MCT1 IC_{50} of CHC derivatives **2.1a-2.1e**

We next evaluated electron donating group containing CHC derivatives **2.1f-2.1i** for MCT1 inhibition. Methoxy, trimethoxy, piperonal and vanillin derivatives **2.1f-2.1i** showed IC_{50} values of ~1, 10, 7 and 50 μ M, respectively (Figure 2e).

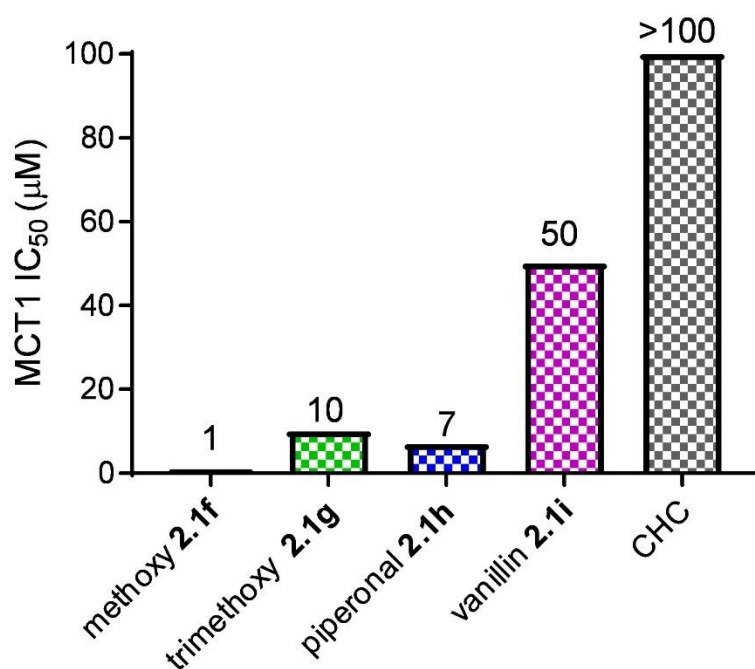


Figure 2e: MCT1 IC_{50} of CHC derivatives **2.1f-2.1i**

We also evaluated MCT1 inhibition for alkyl group containing CHC derivatives **2.1j-2.1m**. These studies showed that methyl derivative **2.1j** exhibited an IC_{50} value of 0.77 μ M, whereas ethyl and isopropyl derivatives **2.1k** and **2.1l** showed IC_{50} values of 0.38 and 0.48 μ M, respectively. The tert-butyl derivative **2.1m** exhibited an IC_{50} value of ~ 1 μ M (Figure 2f). These studies indicated that alkyl group containing derivatives of CHC are superior to electron donating group containing **2.1a-2.1e** or electron donating group containing **2.1f-2.1i** derivatives.

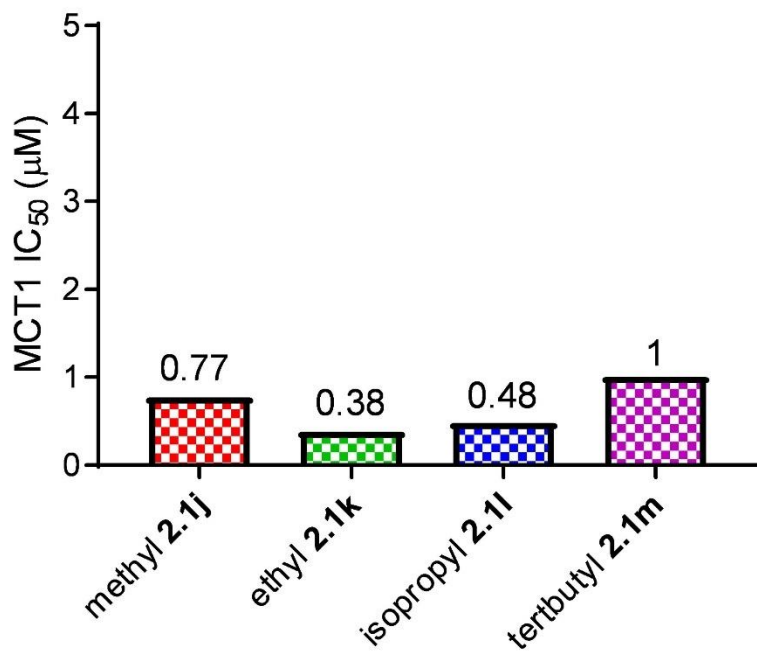


Figure 2f: MCT1 IC_{50} of CHC derivatives **2.1j-2.1m**

2.2 Synthesis of *N,N*-dialkyl CHC derivatives

Since increasing lipophilicity through alkyl group substitutions provided enhanced MCT1 inhibition compared to CHC, we further synthesized several derivatives with *N,N*-dialkyl groups at *para* position of CHC (Figure 2g). This would provide greater lipophilicity with an electron donating group in the *para* position. We hypothesized these characteristics will further improve MCT inhibition.⁸⁰ Moreover, most of the drugs used for various diseases contain at least one N atom, and nitrogen containing compounds are usually considered pharmacologically and pharmaceutically privileged structures for clinical application.

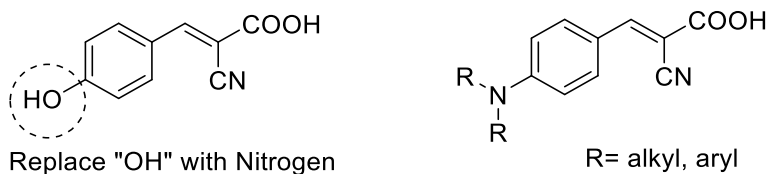
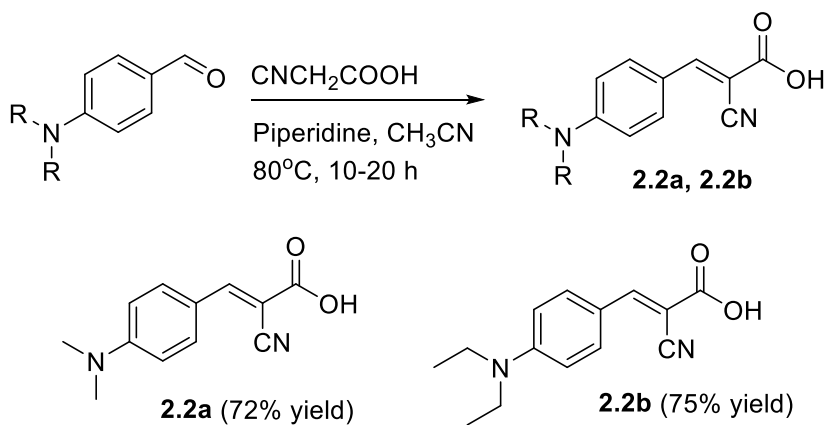


Figure 2g: Replacement of OH group with *N,N*-dialkyl groups in CHC

2.2.1 Synthesis of *N,N*-dialkyl CHC derivatives **2.2a** and **2.2b**

To explore this working hypothesis, we first synthesized *N,N*-dimethyl CHC **2.2a** starting from 4-(dimethylamino)benzaldehyde. This aldehyde was subjected to Knoevenagel condensation to obtain (*E*)-2-cyano-3-(4-(dimethylamino)phenyl)acrylic acid **2.2a** (Scheme 2d). We also synthesized *N,N*-diethyl CHC derivative (*E*)-2-cyano-3-(4-(diethylamino)phenyl)acrylic acid **2.2b** using similar procedure starting from 4-(diethylamino)benzaldehyde.



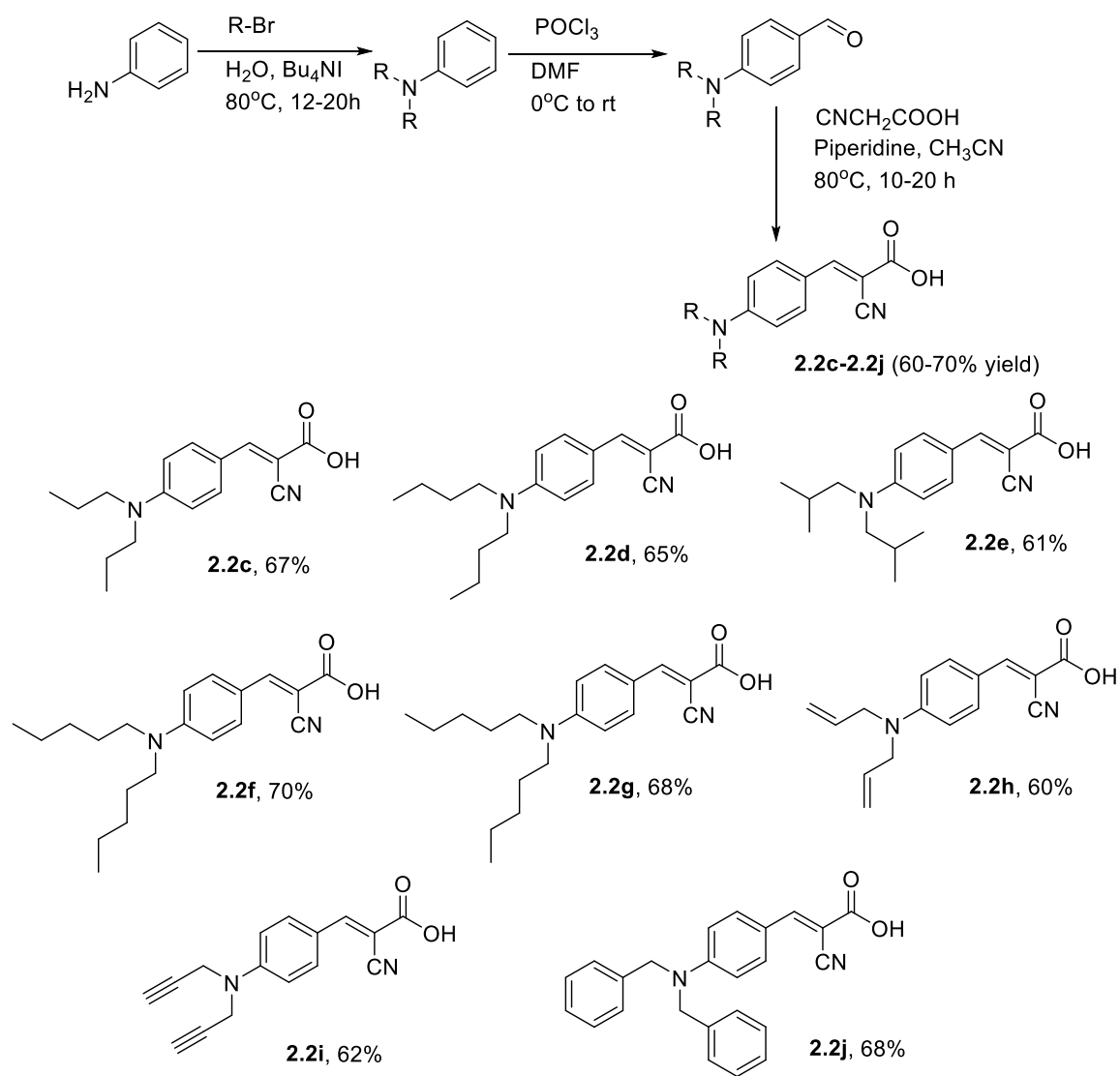
Scheme 2d: Synthesis of (*E*)-2-cyano-3-(4-(dimethylamino)phenyl)acrylic acid **2.2a** and (*E*)-2-cyano-3-(4-(diethylamino)phenyl)acrylic acid **2.2b**

2.2.2 Evaluation of *N,N*-dialkyl CHC derivatives **2.2a** and **2.2b** for MCT1 inhibition

After synthesizing *N,N*-dimethyl **2.2a** and *N,N*-diethyl **2.2b** CHC derivatives, we evaluated their MCT1 inhibition properties using ¹⁴C-lactate uptake assay in RBE4 cell line. As we anticipated, introduction of nitrogen atom with the alkyl group at the *para* position greatly enhanced MCT1 inhibition with the observed IC₅₀ values of ~138 nM for **2.2a** and ~66 nM for **2.2b**. The increase in the alkyl chain also increased the MCT1 inhibition of **2.2b** compared to **2.1a**. Excited by these results, we carried out detailed structure-activity relationship studies of *N,N*-dialkyl/diaryl derivatives.

2.2.3 Synthesis of *N,N*-dialkyl CHC derivatives 2.2c-2.2j

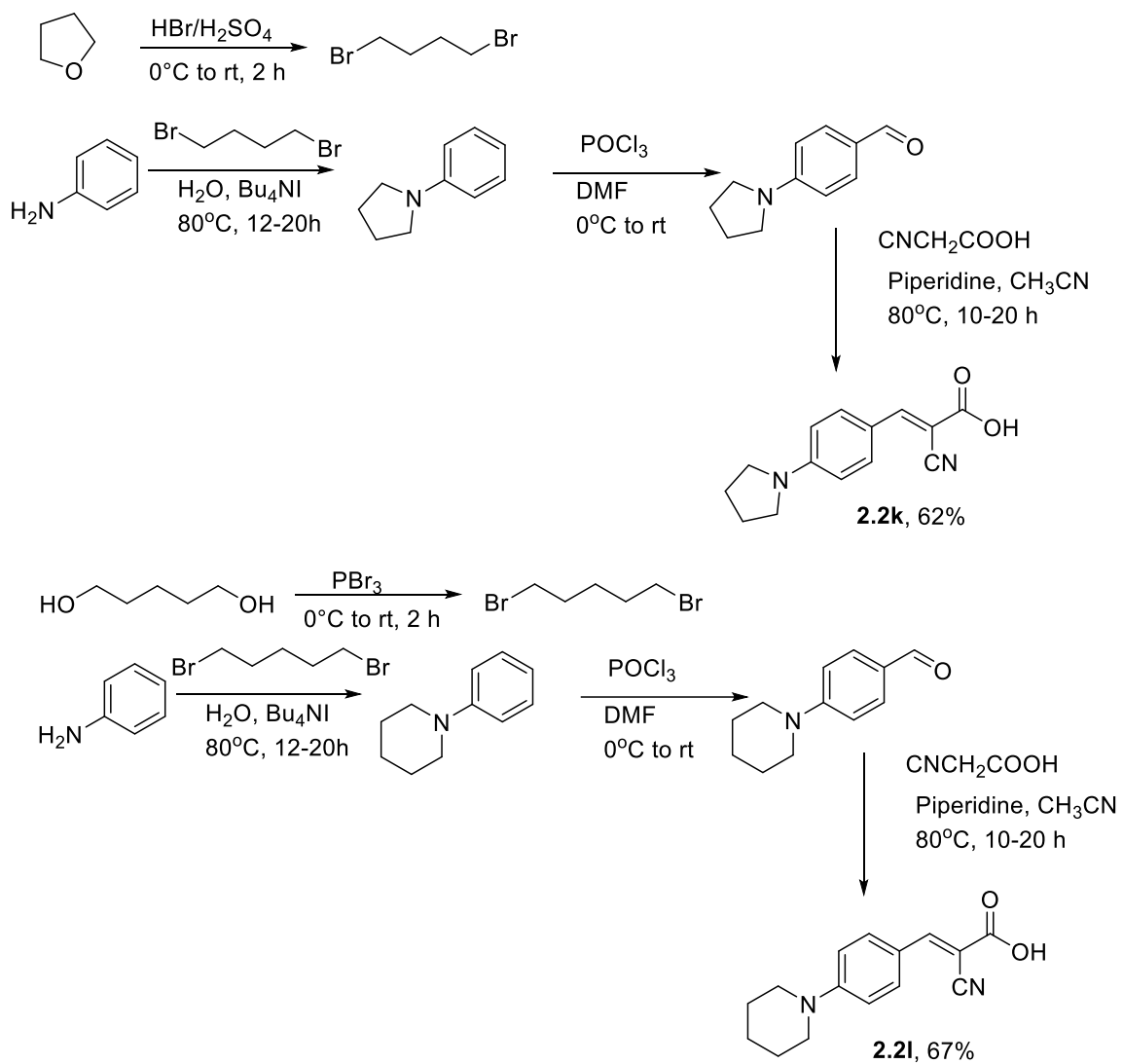
We synthesized other *N,N*-dialkyl substituted CHC derivatives starting from aniline, which was dialkylated using various alkyl bromides in the presence of catalytic amount of tetrabutylammonium iodide in water. We utilized propyl, butyl, isobutyl, pentyl, hexyl, allyl, propargyl and benzyl bromides and obtained corresponding *N,N*-dialkylated anilines. These *N,N*-dialkylated anilines were then subjected to Vilsmeier-Hack formylation using POCl₃ in DMF. The resulting aldehydes were treated with cyanoacetic acid for Knoevenagel condensation in the presence of piperidine in acetonitrile to obtain corresponding (*E*)-2-cyano-3-(4-(dialkylamino)phenyl)acrylic acids **2.2c-2.2j** (Scheme 2e).



Scheme 2e: Synthesis of (*E*)-2-cyano-3-(4-(dialkylamino)phenyl)acrylic acids **2.2c-2.2j**

2.2.4 Synthesis of *N,N*-dialkyl CHC derivatives **2.2k and **2.2l****

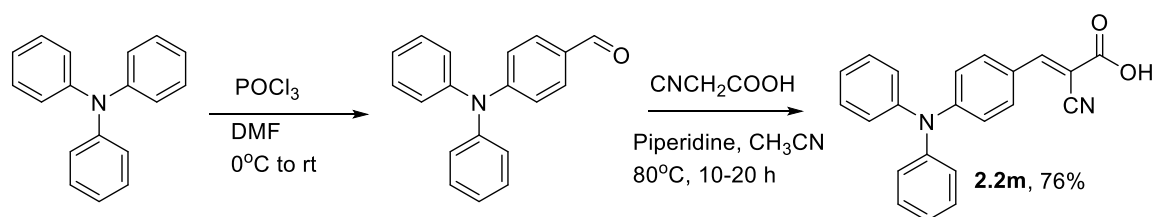
We also synthesized cyclic derivatives 4-pyrrolidinyl and 4-piperidinyl CHCs **2.2k** and **2.2l**. 1,4-dibromobutane was synthesized via bromination of THF with HBr and H₂SO₄, whereas 1,5-dibromopentane was synthesized via dibromination of 1,5-pentanol with PBr₃. Dialkylation of aniline with 1,4-dibromobutane and 1,5-dibromopentanes resulted in corresponding *N,N*-dialkylated anilines. These anilines were then reacted with POCl₃ under Vilsmeier-Haack conditions to yield corresponding aldehydes, which were then treated with cyanoacetic acid for Knoevenagel condensation to get corresponding cyanoacetic acids (*E*)-2-cyano-3-(4-(pyrrolidin-1-yl)phenyl)acrylic acid **2.2k** and (*E*)-2-cyano-3-(4-(piperidin-1-yl)phenyl)acrylic acid **2.2l**, respectively (Scheme 2f).



Scheme 2f: Synthesis of (*E*)-2-cyano-3-(4-(pyrrolidin-1-yl)phenyl)acrylic acid **2.2k** and (*E*)-2-cyano-3-(4-(piperidin-1-yl)phenyl)acrylic acid **2.2l**

2.2.5 Synthesis of *N,N*-diphenyl CHC derivative **2.2m**

Apart from *N,N*-dialkyl CHC derivatives **2.2a-2.2l**, we also synthesized an *N,N*-diphenyl CHC derivative **2.2m** starting from triphenylamine. This amine was monoformylated under Vilsmeier-Haack conditions to obtain 4-(diphenylamino)benzaldehyde, which was then reacted with cyanoacetic acid to form (*E*)-2-cyano-3-(4-(diphenylamino)phenyl) acrylic acid **2.2m** (Scheme 2g).



Scheme 2g: Synthesis of (*E*)-2-cyano-3-(4-(diphenylamino)phenyl)acrylic acid **2.2m**

2.2.6 Evaluation of *N,N*-dialkyl CHC derivatives **2.2c-2.2m** for MCT1 inhibition

The MCT1 inhibition of all these derivatives **2.2c-2.2m** were evaluated using ^{14}C -lactate uptake assay in RBE4 cell line. To our excitement, *N,N*-dialkyl derivatives **2.2c-2.2m** exhibited low to high nanomolar IC_{50} values in the range of 13-876 nM (Figure 2h and Table 2a). With an increase in the carbon content of alkyl groups in methyl to butyl derivatives **2.2a-2.2d**, the IC_{50} values improved from 138 nM to 28 nM, but with further increase in carbons in pentyl **2.2e** and hexyl **2.2f** derivatives, the IC_{50} values increased to 137 and 876 nM, respectively. The optimal alkyl chains that provided efficient MCT1 inhibition were propyl **2.2c** or butyl **2.2d** with IC_{50} values of 13 and 28 nM respectively. When the butyl group is branched such as in isobutyl derivative **2.2e**, MCT1 inhibition was decreased with an IC_{50} value of 102 nM. In the case of diallyl **2.2h** and dipropargyl **2.2i** derivatives, MCT1 inhibition did not improve as evidenced by the IC_{50} values of 114 and 396 nM, respectively. For the compound **2.2j** with dibenzyl substitution, the IC_{50} value was found to be ~29 nM. Cyclic derivatives **2.2k** and **2.2l** also showed good IC_{50} values of 70 and 142 nM, respectively. The *N,N*-diphenyl derivative **2.2m** exhibited excellent MCT1 inhibition with an IC_{50} value of 26 nM (Figure 2h and Table 2a). The candidate compounds propyl **2.2c**, butyl **2.2d** and phenyl **2.2m** showed ~5700-11,000 times potency for MCT1 inhibition than parent CHC.

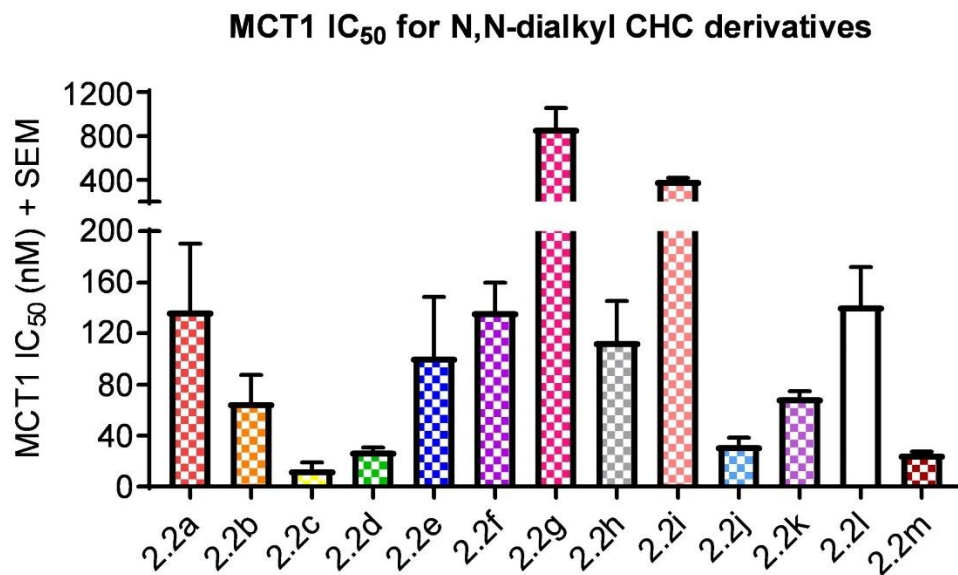
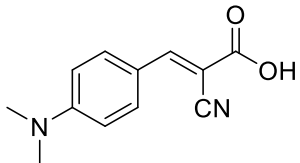
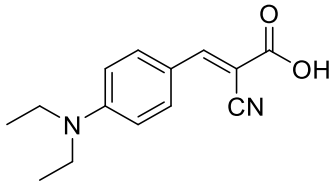
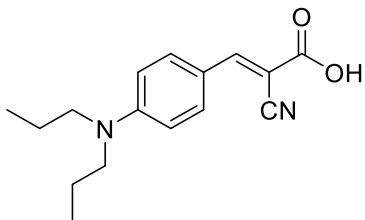
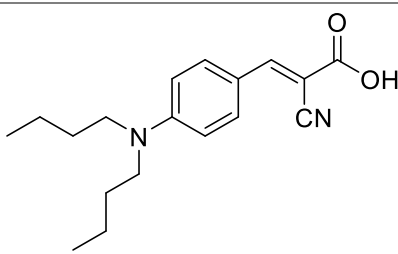
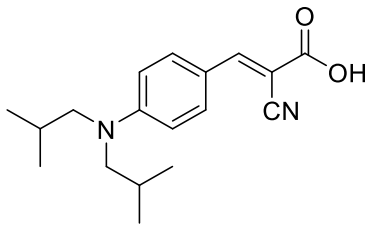


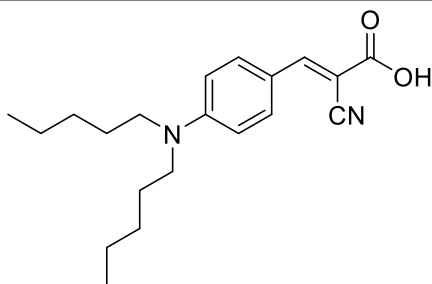
Figure 2h: MCT1 IC₅₀ (nM) of *N,N*-dialkyl CHC derivatives **2.2a-2.2m** in RBE4 cell line.

The average+sem of at least three independent experiments were presented in the bar graph.

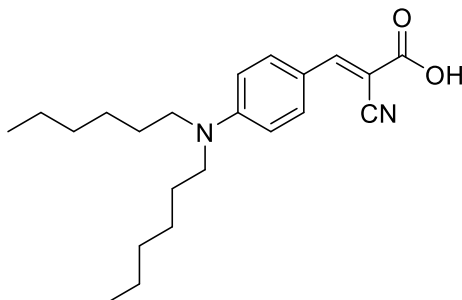
Table 2a: MCT1 IC₅₀ (nM)* of *N,N*-dialkyl CHC derivatives **2.2a-2.2m** in RBE4 cell line

Sl. No.	Compound	MCT1 IC ₅₀
2.2a		138±52
2.2b		66±21
2.2c		13±6
2.2d		28±2
2.2e		102±47

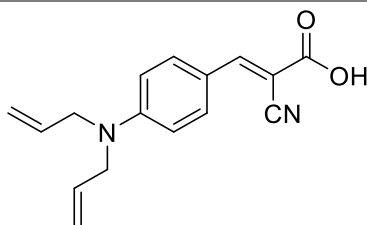
2.2f 137±23



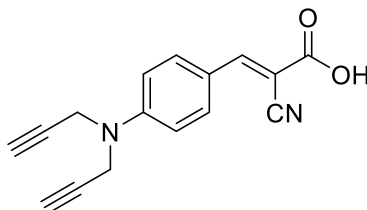
2.2g 876±182



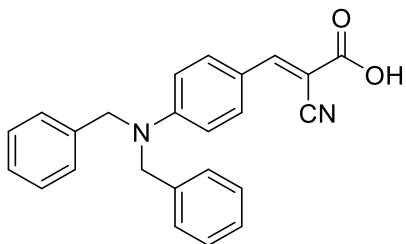
2.2h 114±32

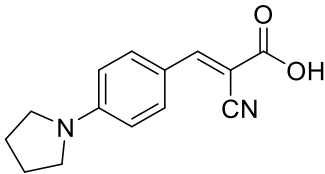
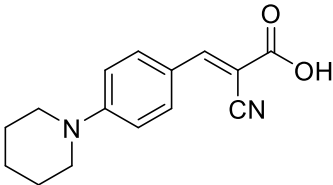
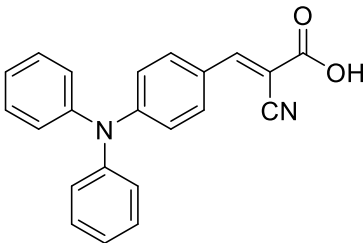


2.2i 395±22



2.2j 29±5



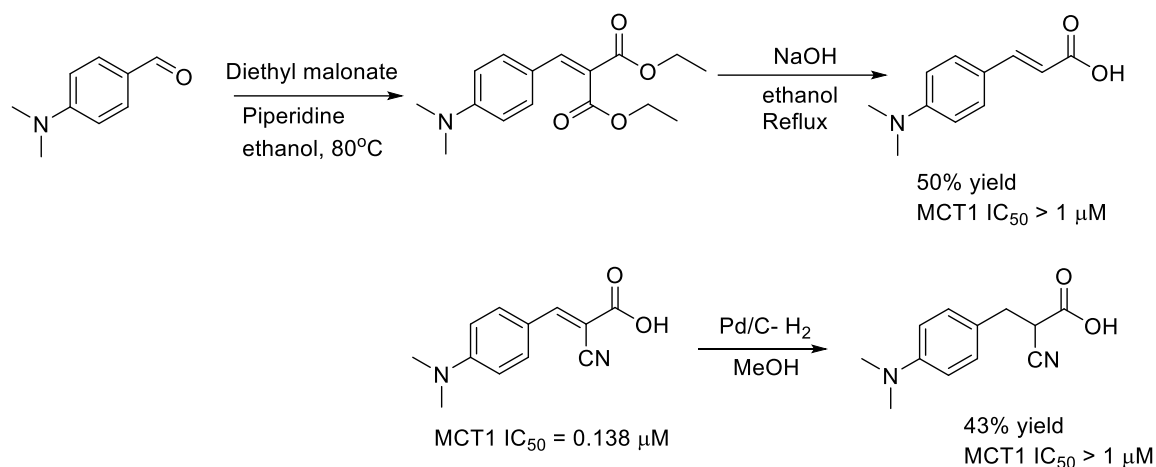
2.2k		70 ± 5
2.2l		142 ± 30
2.2m		26 ± 2

*Average \pm SEM of three independent experiments

2.3 Discussion

CHC is a known MCT1 inhibitor with IC_{50} value of $>150 \mu\text{M}$. This compound is highly non-toxic and exhibits anticancer efficacy in *in vivo* tumor models. Typically, CHC requires millimolar to high micromolar concentration to provide significant *in vivo* efficacy. However, in a clinical setting involving human subjects, achieving this level of high concentration is impractical and non-translatable. Hence, we wanted to improve the potency of CHC by carrying out a structure-activity relationship study for potential use as an anticancer agent. In this regard, we initially replaced the *para*-hydroxy group in CHC with various electron withdrawing, electron donating, and alkyl groups. We synthesized various *para*-substituted CHC derivatives **2.1a-2.1m** and evaluated their MCT1 inhibition properties using ^{14}C -lactate uptake assay in RBE4 cell line.

This structure-activity relationship study revealed that replacing the hydroxy group with an alkyl group resulted in ~ 190 - 390 times potency for MCT1 inhibition when compared to its parent CHC molecule. We also replaced the cyano group with hydrogen and carboxylic acid groups, reduced the double bond in acrylic acid in CHC and tested these derivatives for MCT1 inhibition. These modifications resulted in a total loss or significant decrease of MCT1 inhibition to high micromolar concentration (Figure 2h).



Scheme 2h: Structure-activity relationship studies on cyanoacrylic acid unit

Based on these studies, we inferred that cyanoacrylic acid is a key pharmacophore which is responsible for providing MCT1 inhibition properties. Hence, we further modified the *para*-position on CHC with *N,N*-dialkyl groups that have more hydrophobic properties than simple methyl or ethyl groups. In this regard, we synthesized a small library of cyanocinnamic acids **2.2a-2.2m** with various alkyl/aryl groups such as propyl, butyl, benzyl, phenyl, branched alkyl groups such as isobutyl, and cyclic groups such as pyrrolidine and piperidine.

All these compounds were evaluated for MCT1 inhibition and these studies indicated that the increase in homologation from ethyl to propyl and butyl chain resulted in increased MCT1 inhibition. Further increase in the carbon chain to pentyl and hexyl resulted in decreased MCT1 inhibition. Substitution with allyl and propargyl groups, and also the presence of cyclic *N,N*-dialkyl groups also resulted in decreased activity for MCT1 inhibition. Diphenyl substitution resulted in greatly improved MCT1 inhibition with low

nM IC₅₀ value. Propyl, butyl and phenyl derivatives **2.2c**, **2.2d** and **2.2m** were considered as lead molecules in this study as they exhibited ~5700-11,000 times potency for MCT1 inhibition compared to CHC. Importantly, for potent MCT1 inhibition, cyanoacrylic acid unit is required and the *para*-position should constitute *N,N*-dipropyl/dibutyl/diphenyl groups (Figure 2i). Cyanoacrylic acid is a doubly activated system with two electron withdrawing groups on the double bond and acts as a powerful 1,4-acceptor, which could react with various nucleophilic residues of MCT1 transporter. The presence of alkyl/aryl groups on the *para*-Nitrogen could potentially interact with the hydrophobic pockets of the protein. The critical role of hydrophobicity has been validated with various non-hydroxy CHC derivatives **2.1a-2.1m** and **2.2a-2.2m**.

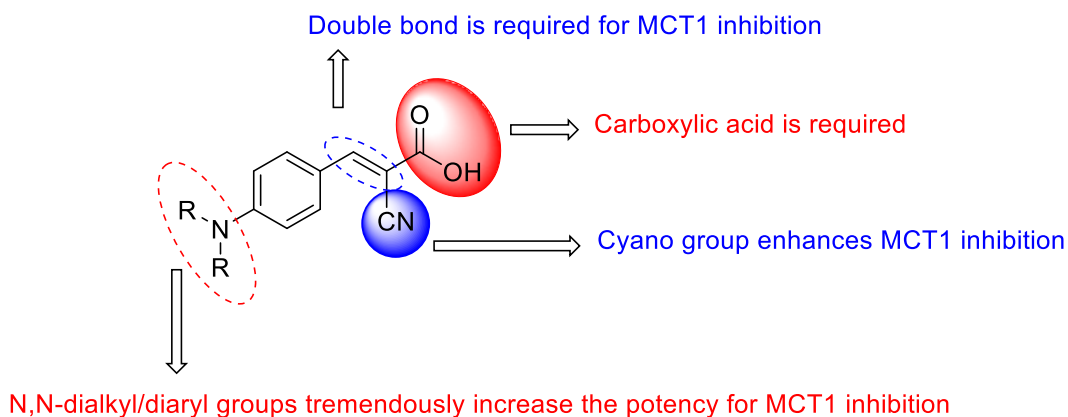


Figure 2i: Structure-activity relationship and MCT1 inhibition of *N,N*-dialkyl CHC derivatives

2.4 Conclusions

We synthesized and evaluated MCT1 inhibition of several CHC derivatives by replacing *para* hydroxy with various substituents. Compounds **2.1a-2.1e** with *para*-position substituted with electron withdrawing groups resulted in increased potency compared to parent CHC, but compounds **2.1f-2.1m** substituted with electron donating groups provided even higher efficacy of MCT1 inhibition. Especially, substitution with alkyl groups resulted in an increased efficacy compared to methoxy type substitutions. Also, compounds **2.2a-2.2m** with *N,N*-dialkyl substitution at *para* position afforded nanomolar potency for MCT1 inhibition when compared to parent compound CHC. These results suggest that cyanoacrylic acid unit in combination with *para-N,N*-dialkyl groups are necessary for potent MCT1 inhibition properties.

Chapter 3: Structure-activity relationship studies of *N,N*-dialkyl/diaryl *o*-substituted CHC derivatives as MCT1 inhibitors: *In vitro* and *in vivo* studies as potential anticancer agents

3.1 Synthesis of *N,N*-dialkyl *o*-methoxy CHC derivatives **3a-3g**

The structure-activity relationship study with various substitutions on the *para* position in CHC resulted in the discovery of *N,N*-dialkyl/diaryl groups that increased the MCT1 inhibition significantly compared to the parent CHC (Figure 2h, Table 2a). Since cyanoacrylic acid group was found to be a critical structural unit for MCT1 inhibition, we did not make any further changes to this unit. Hence, we focused our attention on the *ortho* substitution for further structure-activity relationship studies. In this regard, we chose methoxy group as a representative example (Figure 3a).⁸⁰

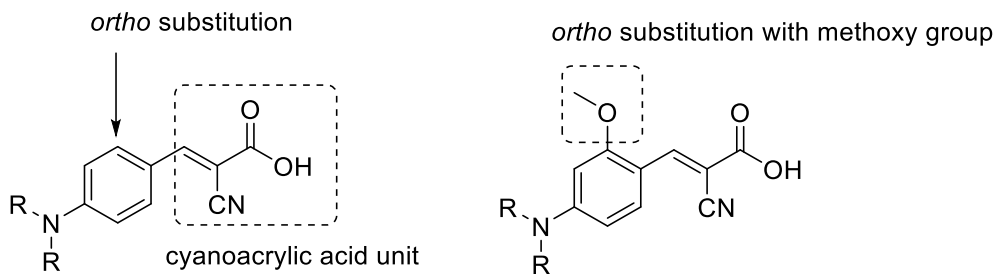
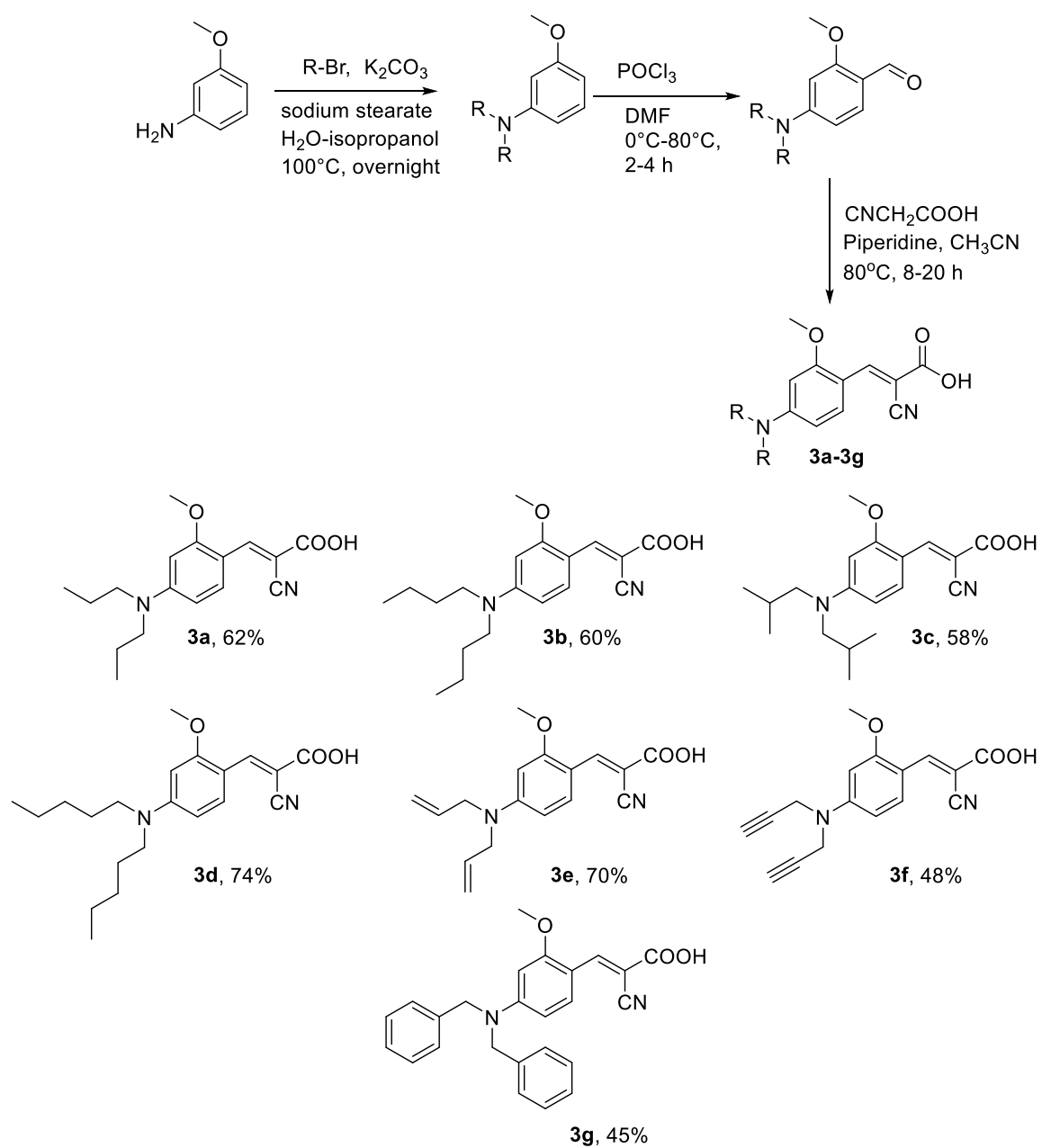


Figure 3a: Proposed modification of *ortho* position of *N,N*-dialkyl CHC derivative with a methoxy group

We synthesized *N,N*-dialkyl *o*-methoxy CHC derivatives starting with the commercially available *m*-anisidine. Dialkylation of *m*-anisidine with alkyl bromides in the presence of sodium stearate in water-isopropanol yielded the corresponding *N,N*-dialkyl *o*-methoxy anilines (Scheme 3a). Propyl, butyl, isobutyl, pentyl, allyl, propargyl and benzyl bromides were used for alkylations. These dialkylated anilines were subjected to Vilsmeier-Haack formylation in the presence of POCl₃ and DMF to obtain corresponding aldehydes, which were subsequently treated with cyanoacetic acid under Knoevenagel conditions to obtain the (*E*)-2-cyano-3-(4-(dialkylamino)-2-methoxyphenyl)acrylic acids **3a-3g** (Scheme 3a).

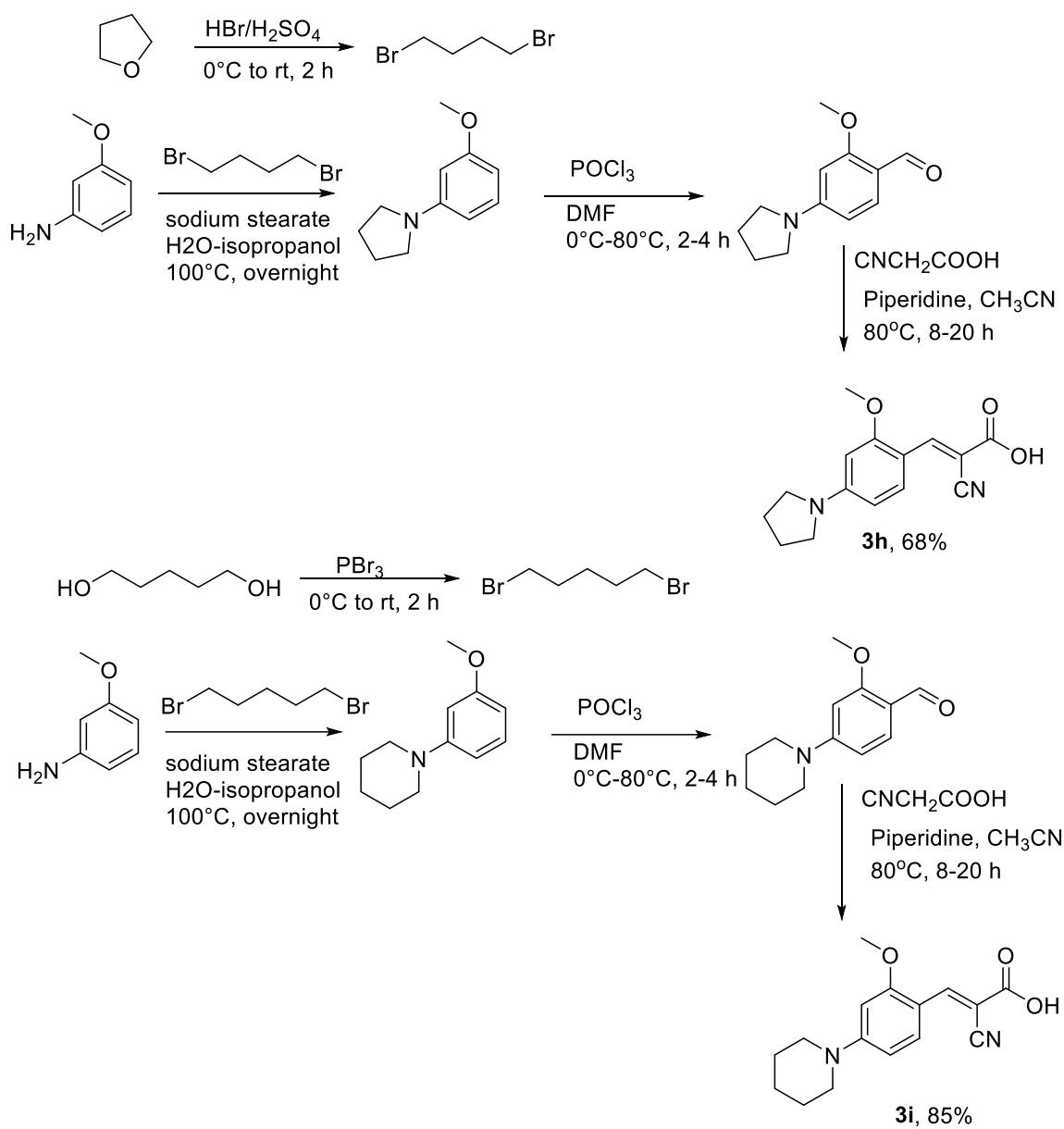


Scheme 3a: Synthesis of (*E*)-2-cyano-3-(4-(dialkylamino)-2-methoxyphenyl)acrylic acids

3a-3g

3.1.1 Synthesis of *N,N*-dialkyl *o*-methoxy CHC derivatives **3h** and **3i**

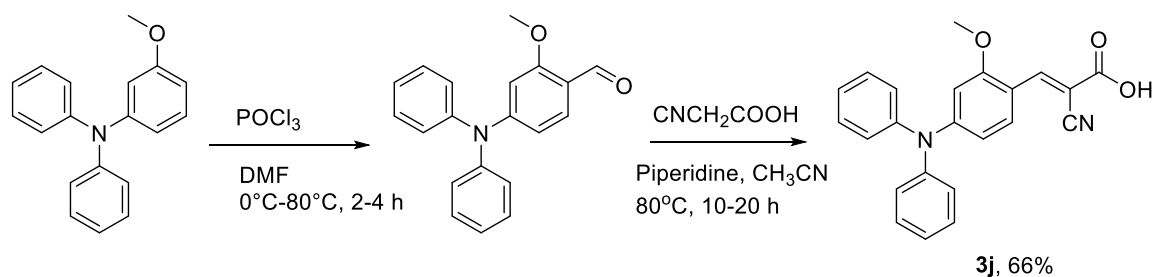
Apart from the above-mentioned compounds **3a-3g**, we also synthesized cyclic CHC derivatives 4-pyrrolidinyl and 4-piperidinyl *o*-methoxy CHCs. As described in the previous chapter, 1,4-dibromobutane was synthesized via bromination of THF in the presence of HBr and H₂SO₄, whereas 1,5-dibromopentane was synthesized via dibromination of 1,5-pentanol in the presence of PBr₃. Dialkylation of *m*-anisidine with 1,4-dibromobutane and 1,5-dibromopentanes resulted in the corresponding *N,N*-dialkylated *o*-methoxy anilines. These anilines were then reacted with POCl₃ in DMF under Vilsmeier-Haack conditions to yield corresponding aldehydes, which were then treated with cyanoacetic acid for Knoevenagel condensation to obtain (*E*)-2-cyano-3-(2-methoxy-4-(pyrrolidin-1-yl)phenyl)acrylic acid **3h** and (*E*)-2-cyano-3-(2-methoxy-4-(piperidin-1-yl)phenyl)acrylic acid **3i**, respectively (Scheme 3b).



Scheme 3b: Synthesis of (*E*)-2-cyano-3-(2-methoxy-4-(pyrrolidin-1-yl)phenyl)acrylic acid **3h** and (*E*)-2-cyano-3-(2-methoxy-4-(piperidin-1-yl)phenyl)acrylic acid **3i**

3.1.2 Synthesis of *N,N*-diphenyl *o*-methoxy CHC derivative **3j**

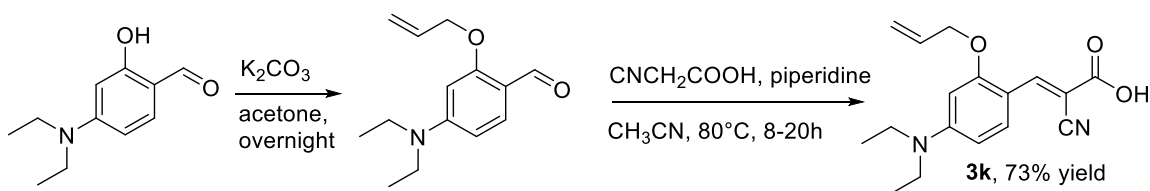
Similarly, we also synthesized an *N,N*-diphenyl *o*-methoxy CHC derivative starting from commercially available 3-methoxy-*N,N*-diphenylaniline which was monoformylated under Vilsmeier-Haack conditions to obtain 4-(diphenylamino)-2-methoxybenzaldehyde. The aldehyde was then reacted with cyanoacetic acid in the presence of piperidine to form (*E*)-2-cyano-3-(4-(diphenylamino)-2-methoxyphenyl)acrylic acid **3j** (Scheme 3c).



Scheme 3c: Synthesis of (*E*)-2-cyano-3-(4-(diphenylamino)-2-methoxyphenyl)acrylic acid **3j**

3.1.3 Synthesis of *N,N*-dialkyl *o*-allyloxy CHC derivative **3k**

To further study the effect of *ortho* position on the biological activity, we replaced the methoxy group with an allyloxy group. As a representative example, we started with a commercially available starting material 4-(diethylamino)-2-hydroxybenzaldehyde. This salicylaldehyde was treated with allyl bromide in the presence of K_2CO_3 in acetone to obtain 2-(allyloxy)-4-(diethylamino)benzaldehyde. This *o*-allyloxy product was then subjected to Knoevenagel condensation with cyanoacetic acid to get (*E*)-3-(2-(allyloxy)-4-(diethylamino)phenyl)-2-cyanoacrylic acid **3k** in 73% yield (Scheme 3d).



Scheme 3d: Synthesis of (*E*)-3-(2-(allyloxy)-4-(diethylamino)phenyl)-2-cyanoacrylic acid **3k**

3.2 Evaluation of *N,N*-dialkyl/diaryl *o*-substituted CHC derivatives 3a-3k for MCT1 inhibition properties: Results and discussion

The MCT1 inhibition of *N,N*-dialkyl/diaryl *o*-methoxy CHC derivatives **3a-3k** were then tested using ¹⁴C-lactate uptake assay in RBE4 cell line. Excitingly, the *N,N*-dialkyl/diaryl derivatives **3a-3k** exhibited further increase in MCT1 inhibition activity at low nanomolar IC₅₀ values in the range of 8-130 nM (Figure 3b, Table 3a). In this case also, with an increase in the carbon content of alkyl groups from propyl **3a** to pentyl **3d**, the IC₅₀ values decreased from 8 nM to 23 nM. With a branched diisobutyl derivative **3c**, the IC₅₀ value was found to be 11 nM, which is same as straight chained butyl derivative **3b** (8 nM). With diallyl **3e**, the IC₅₀ value was slightly decreased to 27 nM, whereas for dipropargyl **3f**, the IC₅₀ value (130 nM) was decreased compared to other derivatives **3a-3e**. With dibenzyl substitution in **3g**, the IC₅₀ value was found to be slightly decreased to ~29 nM. Cyclic derivatives **3h** and **3i** also showed moderate IC₅₀ values of 44 and 61 nM, respectively. The diphenyl derivative **3j** exhibited excellent MCT1 inhibition with an IC₅₀ value of 8 nM, whereas *o*-allyloxy derivative **3k** exhibited an IC₅₀ value of 9 nM. Overall, *N,N*-dialkyl/diaryl *o*-substituted derivatives **3a-3j** exhibited even higher MCT1 inhibition compared to their non *o*-substituted derivatives **2.2c-2.2m** (Figure 2h, Table 2a).

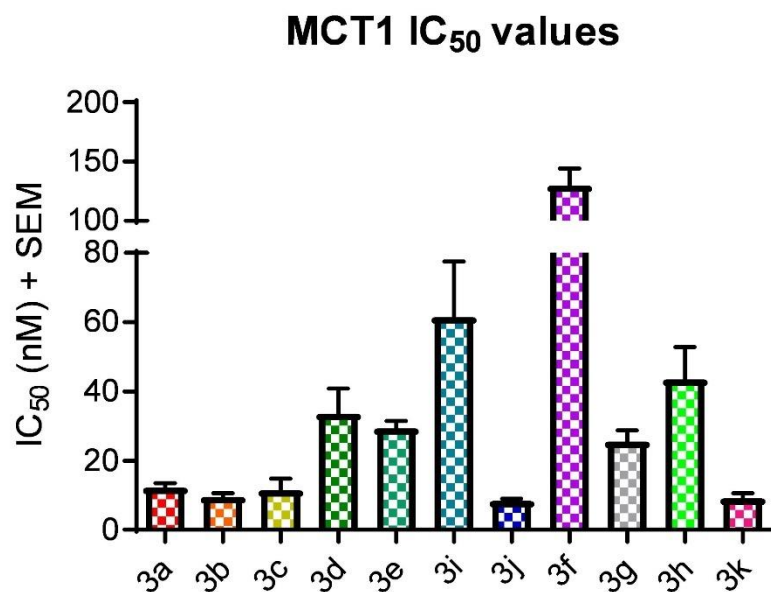
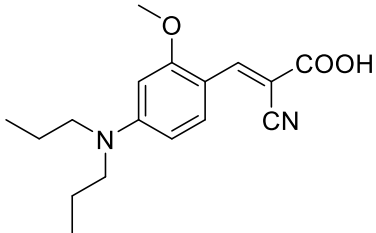
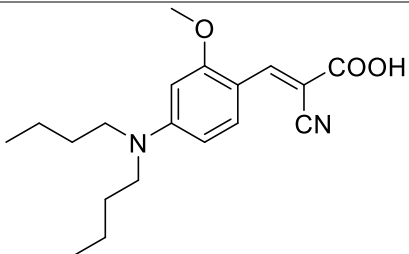
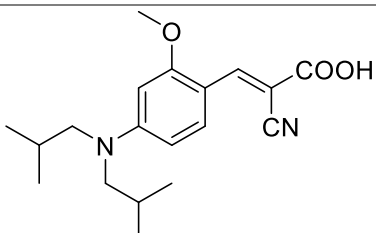
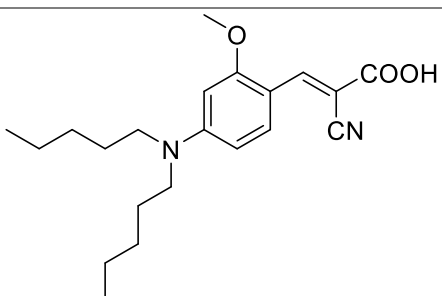
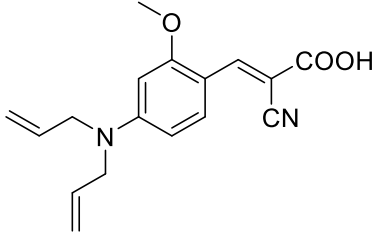
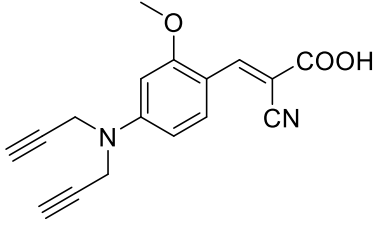
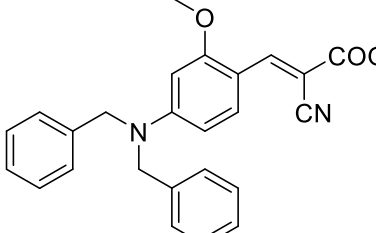
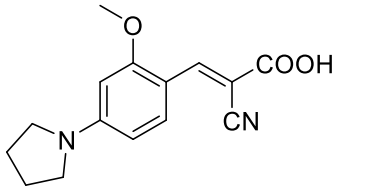
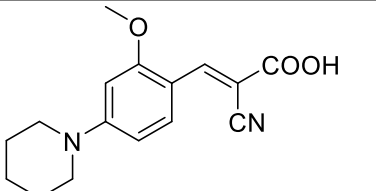
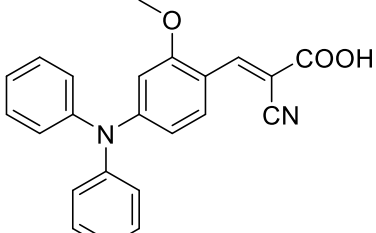
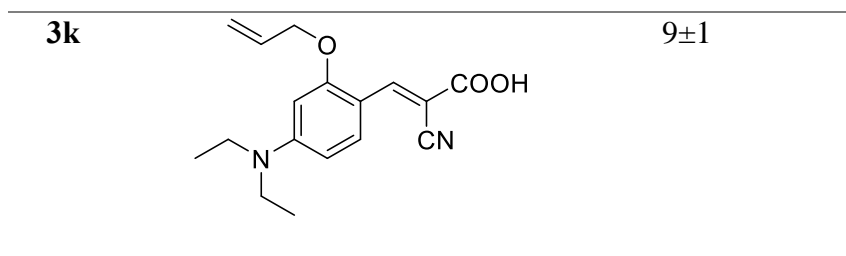


Figure 3b: MCT1 inhibition of *N,N*-dialkyl/diaryl *o*-substituted cyanoacetic acids **3a-3k** in RBE4 cell line. The average+sem of at least three independent experiments were presented in the bar graph.

Table 3a: MCT1 IC₅₀ (nM)* of *N,N*-dialkyl/diaryl *o*-substituted CHC derivatives **3a-3k** in RBE4 cell line

Sl. No.	Compound	MCT1 IC ₅₀
3a		10±1
3b		8±1
3c		11±1
3d		23±4

3e		27±3
3f		130±14
3g		19±5
3h		44±9
3i		61±16
3j		8±1



* average±sem of minimum three independent experiments

As discussed in the previous chapter, substituting hydroxy group in CHC with *N,N*-dialkyl/diaryl groups in the *para*-position increased MCT1 inhibitory activity exponentially when compared to the parent CHC molecule. The presence of double bond, cyano and carboxylic acid groups is also critical for potent MCT1 inhibition. Additionally, replacing hydrogen with a methoxy group in the *ortho*-position further enhanced MCT1 inhibition as seen in the derivatives **3a-3j**, when compared to their non methoxy derivatives **2c-2m**. We presume that methoxy group increases hydrogen bonding interactions with the MCT1 protein due to which more potent inhibition is observed. All the optimized structural features required for potent MCT1 inhibition are depicted in the Figure 3c.

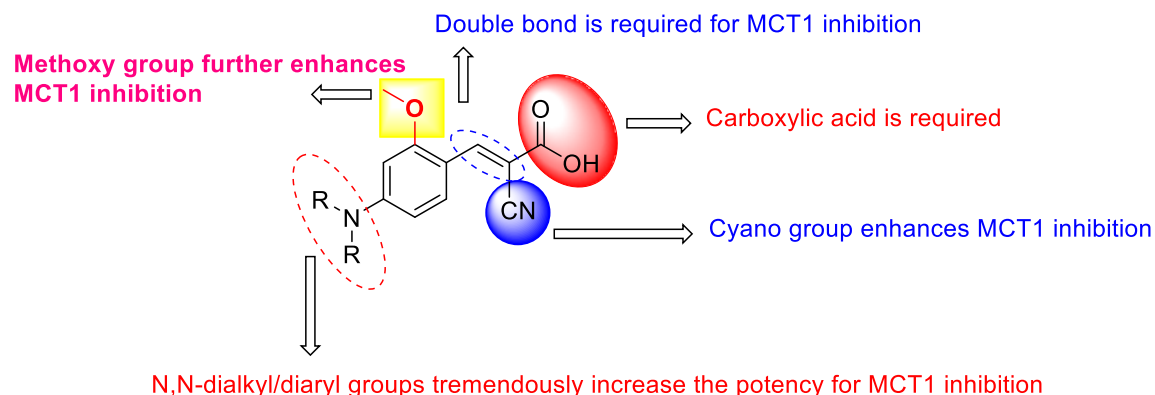


Figure 3c: Optimized structural features required for potent MCT1 inhibition

3.3 Cell proliferation/cytotoxicity study of compounds 3a-3k: Results and discussion

3.3.1 Cell proliferation inhibition of compounds 3a-3k using MTT assay

As these derivatives exhibited potent MCT1 inhibition, we then evaluated these compounds for cell proliferation/cytotoxicity inhibition to explore their potential as anticancer agents. Initial cell proliferation studies of the synthesized compounds **3a-3k** were carried out using *in vitro* cell proliferation using 3-(4,5-dimethylthiazol-2-yl)-2,5-diphenyltetrazolium bromide (MTT) assay. This colorimetric assay measures the reduction of MTT to formazan by cellular mitochondrial reductase as a measure of cell viability. For this assay, we utilized four cell lines which include MCT1 expressing human colorectal adenocarcinoma cell line WiDr, murine metastatic breast cancer cell line 4T1-luc2, and murine glioma cell line GL261-luc2 and MCT4 expressing human triple negative breast cancer cell line MDA-MB-231. Compared to their parent compound CHC, some of the test compounds exhibited several fold increased cell proliferation inhibitions (Table 3b).

In 4T1-luc2 cell line, propyl derivative **3a** showed an IC_{50} value of 0.12 mM, whereas butyl and isobutyl derivatives **3b** and **3c** exhibited IC_{50} values of 0.05 and 0.06 mM, respectively. The benzyl derivative **3g** showed an IC_{50} value of 0.09 mM, whereas the phenyl derivative **3j** exhibited excellent cytotoxicity with an IC_{50} value of 0.05 mM. CHC exhibited an IC_{50} value of 5.35 mM whereas candidate compounds **3a**, **3e**, **3f**, **3h**, **3i** and **3k** did not show cytotoxicity up to 0.25 mM concentration.

In GL261-luc2 cell line, propyl, butyl and isobutyl derivatives **3a-3c** exhibited high IC_{50} values of 0.16-0.18 mM, whereas benzyl derivative **3g** showed an IC_{50} value of 0.10 mM. The phenyl derivative **3j** exhibited moderate cytotoxicity with an IC_{50} value of 0.09

mM. CHC exhibited an IC₅₀ value of 5.27 mM whereas candidate compounds **3e**, **3f**, **3h**, **3i** and **3k** did not show cytotoxicity up to 0.25 mM concentration.

In WiDr cell line, the compounds were tested to a maximum concentration of 0.025 mM as these compounds have significantly more cell proliferation inhibition values. CHC did not exhibit cytotoxicity up to 0.5 mM. All the other compounds **3a-3j** were very potent with IC₅₀ values in the range of 0.0024-0.0125 mM. Benzyl **3g** and phenyl **3j** showed low IC₅₀ values compared to other compounds in this study.

In MDA-MB-231 cell line propyl, butyl and isobutyl derivatives **3a**, **3b** and **3c** exhibited similar IC₅₀ values ~0.12-0.13 mM, whereas benzyl derivative **3g** showed slightly higher IC₅₀ value of 0.11 mM. The phenyl derivative **3j** exhibited good cytotoxicity with an IC₅₀ value of 0.08 mM. CHC exhibited an IC₅₀ value of 5.71 mM whereas candidate compounds **3e**, **3f**, **3h**, **3i** and **3k** did not show cytotoxicity up to 0.25 mM concentration.

Table 3b: MTT assay IC₅₀* values of *N,N*-dialkyl *o*-methoxy CHC derivatives in 4T1-luc2 and GL261-luc2, WiDr and MDA-MB-231 cell lines

Sl. No	4T1-luc2	GL261-luc2	WiDr	MDA-MB-231
CHC	5.35±1.35	5.27±0.33	>0.5	5.71±0.44
3a	0.12±0.00	0.16±0.01	0.0027±0.000	0.12±0.01
3b	0.05±0.01	0.16±0.01	0.0056±0.001	0.13±0.01
3c	0.06±0.01	0.18±0.00	0.0024±0.000	0.13±0.01
3e	>0.25	>0.25	0.0044±0.000	>0.25
3f	>0.25	>0.25	ND	>0.25
3g	0.09±0.01	0.10±0.01	0.0125±0.004	0.11±0.01
3h	>0.25	>0.25	0.0027±0.000	>0.25
3i	>0.25	>0.25	0.0036±0.000	>0.25
3j	0.05±0.01	0.09±0.00	0.0077±0.000	0.08±0.01
3k	>0.25	>0.25	ND	>0.25

* IC₅₀ values reported in mM, average ± SEM of minimum three separate experimental values

3.3.2 Cytotoxicity evaluation of compounds **3a-3k** using SRB assay

The effects on cell survival of the synthesized compounds **3a-3k** were carried out using a standard sulforhodamine-B (SRB) assay. This assay is based on the ability of SRB to bind to cellular protein. We utilized same cell lines as in MTT assay and found that the SRB assay results were similar to that of the MTT assay (Figure 3c).

In 4T1-luc2 cell line, butyl and isobutyl derivatives **3b** and **3c** exhibited IC_{50} values of 0.11 and 0.08 mM, respectively whereas benzyl derivative **3g** showed an IC_{50} value of 0.06 mM. The phenyl derivative **3j** exhibited good cytotoxicity with an IC_{50} value of 0.08 mM. CHC exhibited an IC_{50} value of 4.66 mM whereas candidate compounds **3a**, **3e**, **3f**, **3h**, **3i** and **3k** did not show cytotoxicity up to 0.25 mM concentration.

In GL261-luc2 cell line, propyl, butyl and isobutyl derivatives **3a-3c** exhibited IC_{50} values of 0.08-0.12 mM, whereas benzyl derivative **3g** showed an IC_{50} value of 0.12 mM, which is two times the IC_{50} compared to MDA-MB-231 and 4T1-luc2 cell lines. The phenyl derivative **3j** exhibited moderate cytotoxicity with an IC_{50} value of 0.11 mM. CHC exhibited a high IC_{50} value of 6.49 mM whereas candidate compounds **3e**, **3f**, **3h**, **3i** and **3k** did not show cytotoxicity up to 0.25 mM concentration.

In WiDr cell line, the compounds were tested to a maximum concentration of 0.025 mM. This concentration was chosen because of selective cell proliferation inhibition values of these derivatives based on MTT. CHC showed an IC_{50} value of 2.16 mM and phenyl derivative **3j** gave an IC_{50} value of 0.0042 mM. However, all the other compounds **3a-3i** and **3k** did not exhibit cytotoxicity up to 0.025 mM concentration.

In MDA-MB-231 cell line, propyl, butyl and isobutyl derivatives **3a-3c** exhibited similar IC₅₀ values ~0.12-0.14 mM, whereas benzyl derivative **3g** showed excellent IC₅₀ value of 0.06 mM. The phenyl derivative **3j** exhibited good cytotoxicity with an IC₅₀ value of 0.08 mM. CHC exhibited an IC₅₀ value of 5.57 mM whereas candidate compounds **3e**, **3f**, **3h**, **3i** and **3k** did not show cytotoxicity up to 0.25 mM concentration.

Table 3c: SRB assay IC₅₀* values of *N,N*-dialkyl *o*-methoxy CHC derivatives in 4T1-luc2 and GL261-luc2, WiDr and MDA-MB-231 cell lines

Sl. No.	4T1-luc2	GL261-luc2	WiDr	MDA-MB-231
CHC	4.66±0.43	6.49±1.41	2.16±0.52	5.57±0.99
3a	>0.25	0.10±0.02	>0.025	0.14±0.02
3b	0.11±0.02	0.08±0.04	>0.025	0.12±0.02
3c	0.08±0.01	0.12±0.01	>0.025	0.13±0.02
3e	>0.25	0.13±0.01	>0.025	>0.25
3f	>0.25	>0.25	>0.025	>0.25
3g	0.06±0.01	0.12±0.01	>0.025	0.06±0.00
3h	>0.25	>0.25	>0.025	>0.25
3i	>0.25	>0.25	>0.025	>0.25
3j	0.08±0.01	0.11±0.00	0.0042±0.000	0.08±0.01
3k	>0.25	>0.25	>0.025	>0.25

* IC₅₀ values reported in mM, average ± SEM of minimum three separate experimental values

While the compounds have good cell proliferation inhibition towards MCT1 expressing cell line WiDr, they exhibited moderate activity towards other MCT1 expressing cell lines 4T1-luc2 and GL261-luc2 and in MCT4 expressing MDA-MB-231 cell line. Although we observed low nanomolar range MCT1 inhibition, this did not translate into potent cell proliferation inhibition and cytotoxicity. There may be several reasons for the observed differences in IC_{50} values between MTT and SRB studies in WiDr cell line. SRB shows a weaker effect of test compounds on cytotoxicity because SRB assay estimates total cellular protein whereas MTT estimates cell proliferation based on enzyme activity. Treatment with test compounds could also have a stronger effect on one cell line (WiDr) than others (MDA-MB-231 and GL261-luc2) due to their possible differences in drug efflux activity, breakdown of compound in cells, differences in pathways regulating cell cycle and apoptosis, differences in the growth media with low or high glucose (MEM, DMEM), etc.

We also attribute the low IC_{50} values of compounds in MTT assay due to less free compound that is available in comparison to their MCT1 inhibition. It is also known that potent inhibition of MCT1 (low nanomolar) may not lead to corresponding levels of cell proliferation inhibition as cells may survive on other metabolic pathways.⁸¹ However, chronic administration of the inhibitors in *in vivo* system will lead to disruption of glycolysis and OxPhos which in turn results in energy crisis and tumor growth inhibition. The 1000-fold difference between IC_{50} values for MCT1 inhibition and MTT assay could be explained due to the differences in the assay medium used for these experiments. For

MCT1 inhibition studies, the growth medium was replaced with HEPES buffer before the addition of compounds. For MTT and SRB assays, the compounds were added directly to the growth media, which contains FBS. These compounds are highly protein bound (>99%). The protein binding assay results are discussed in chapter 4. Hence, the observed differences between MCT1 inhibition and cell proliferation inhibition values could be attributed to the high protein binding properties of the candidate compounds as less free drug is available to interact with MCT and other cellular components.

Potent inhibition of MCT1 by candidate compounds generally don't cause high cytotoxicity or inhibit cell proliferation that is usually observed in chemotherapeutic drugs with traditional mechanisms involving DNA, microtubules and other cellular components. The MCT1 inhibitors cause cell proliferation inhibition by targeting glycolysis and/or OxPhos pathways. If MCT1 expressing cancer cells predominantly undergo OxPhos, two scenarios arise: in one case, cells require more glucose and in second case, they utilize less glucose. If these cells use less glucose, inhibition of MCT1 could cause extracellular acidification as lactic acid and pyruvic acid cannot enter the cell. In this case, glucose will be consumed rapidly and the transport of precursors (lactic acid and pyruvic acid) for OxPhos is already inhibited, thereby reducing mitochondrial activity. This was observed in WiDr cell line as indicated by the results for MTT assay and MCT1 inhibition. To reconfirm these results, glycolysis and mitochondrial stress tests were performed in MCT1 expressing WiDr cell line and the details were included and discussed in chapter 5. In the second scenario, if there is a greater need for glycolysis in MCT1 expressing cancer cells,

inhibition of MCT1 could result in redirecting the glycolytic metabolites (lactic acid and pyruvic acid) towards TCA cycle. In this case, cancer cells could potentially evolve and carry out other energy producing pathways including aggressive glycolysis even if MCT1 expressing cells typically utilize OxPhos.

3.4 Cell proliferation inhibition of test compounds in various cancer cell lines under hypoxic conditions using MTT assay: Results and discussion

Tumors are highly heterogenous in nature with hypoxic and aerobic regions and tumor hypoxia leads to drug resistance and aggressive cell proliferation. In this regard, we carried out cell proliferation inhibition of candidate compounds in oxygen limiting conditions (10% CO₂, 1% O₂ and 89% N₂).⁴³ Four selected compounds **3g**, **3j**, **3h** and **3k** were chosen for this experiment. Compound **3g** with benzyl group was advanced for further studies due to its potent MCT1 and MCT4 inhibition and relatively high cytotoxic properties. Pyrrolidinyll derivative **3h** was selected due to its high water-solubility and nontoxic nature at high concentrations. Compound **3j** with phenyl groups was chosen based on its potent MCT1 inhibition and higher cell proliferation inhibition. Finally, compound **3k** with an *o*-allyloxy group instead of *o*-methoxy was chosen due to its structural diversity, high solubility and excellent MCT1 inhibition properties. Cell proliferation inhibition of these candidate compounds under hypoxic conditions indicated no significant differences in the IC₅₀ values (Table 3d).

Table 3d: MTT assay IC₅₀* values of *N,N*-dialkyl *o*-methoxy CHCs in 4T1-luc2, GL261-luc2 and MDA-MB-231 cell lines in hypoxic conditions

Compound	4T1-luc2	GL261-luc2	MDA-MB-231
CHC	3.21±0.34	4.57±0.35	4.93±0.55
3g	0.04±0.01	0.08±0.01	0.09±0.00
3h	>0.25	>0.25	>0.25
3j	0.05±0.01	0.08±0.01	0.09±0.00
3k	>0.25	>0.25	>0.25

*IC₅₀ values reported in mM, average ± SEM of minimum three separate experimental values

These results suggest that under *in vitro* conditions, the tumor cell lines can adapt their metabolism to other pathways and maintain cell viability. Also, *in vitro* hypoxia, most of the metabolic processes are slowed down to a greater extent due to the lack of oxygen as the cells are under stress. In contrast, in *in vivo* systems, cancer cells are critically dependent on ATP generation via vigorous glycolysis for survival and proliferation. Hence, chronic administration of a potent MCT1 inhibitor *in vivo* will hamper the glycolytic process leading to severe energy crisis and cell death.

3.5 Cell cycle analysis of compound 3j in WiDr and MDA-MB-231 cell lines: Results and discussion

We investigated the ability of the compound **3j** to disrupt the cell cycle *in vitro*. **3j** was chosen as a lead candidate compound for its higher cell proliferation inhibition and cytotoxicity. In this regard, we carried out propidium iodide (PI) based flow cytometry (FCM) analysis. PI is a fluorescent DNA intercalating agent widely used to evaluate cell cycle phase distributions in proliferating cells and the differences due to compound treatment with respect to cell-cycle phase distributions in control cultures can be evaluated. To test whether the cell cycles of WiDr cells were affected by lead compound **3j**, these cells were treated for 24 hours with concentrations corresponding to 1X and 2X of IC₅₀ values and analyzed for DNA content and cell cycle distributions. As CHC did not exhibit cytotoxicity up to 0.5 mM, CHC was not tested for cell cycle analysis in WiDr cell line. Remarkably, WiDr cells treated at 2X the cell proliferation inhibition IC₅₀ of compound **3j** resulted in an abrupt block in S-phase (Figure 3d), indicating that treated cells did not enter the G₂/M phase. This may suggest that disruption of metabolic processes with compound **3j** may ultimately cause cell cycle arrest and defective DNA processing. Moreover, WiDr cells are less glycolytic in nature and pursue more OxPhos, and as the compound **3j** inhibits OxPhos parameters (as discussed in chapter 5). This could be the reason why the cell cycle is halted at the S phase, as G₀/G₁ phase mostly corresponds to glycolysis.

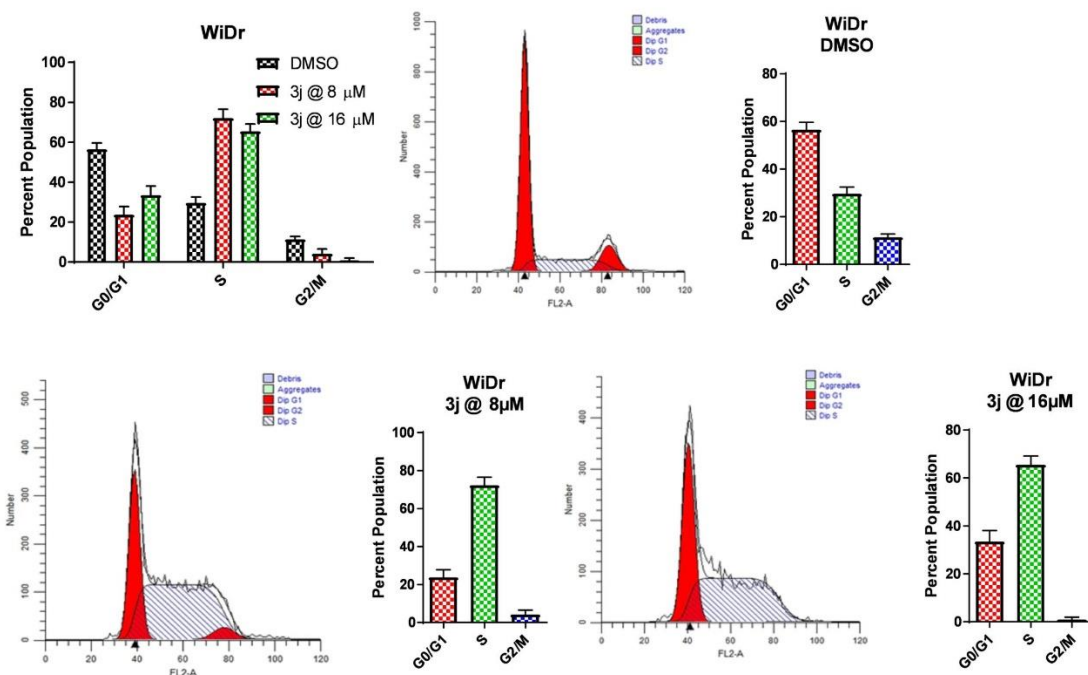


Figure 3d: Cell cycle analysis of compound **3j** at 1X and 2X of the IC₅₀ concentration in WiDr cell line.

Interestingly, MCT4 expressing MDA-MB-231 cells treated with compound **3j** at 2X the proliferation IC₅₀ resulted in a statistically significant cell cycle arrest in the G₂/M phase at the expense of G₁ (Figure 3e). In the case of CHC, even at 2X, there was no significant effect on cell cycle at any phase. This FCM data indicates that compound **3j** allows cells to replicate and enter the G₂ phase, but these cells are not able to leave G₂/M phase to form proliferating daughter cells. A lack of cells in the G₁ phase with accumulating G₂/M phase may suggest a disruption of the mitotic machinery. As MDA-MB-231 cells are more glycolytic in nature and the lead candidate compound **3j** inhibits glycolytic parameters (as discussed in chapter 5), the cell cycle is halted at G₀/G₁ phase as this phase

corresponds to glycolysis. This data also suggests that the phase of cell cycle arrest in the presence of MCT1 inhibitor **3j** may depend on the cell type and MCT status, as differential cell-cycle perturbations have been observed in MCT1 and MCT4 expressing cell lines, respectively. The differential phase of cell cycle arrest observed in compound **3j** treated WiDr and MDA-MB-231 may be a DNA-damage response of different cell types.

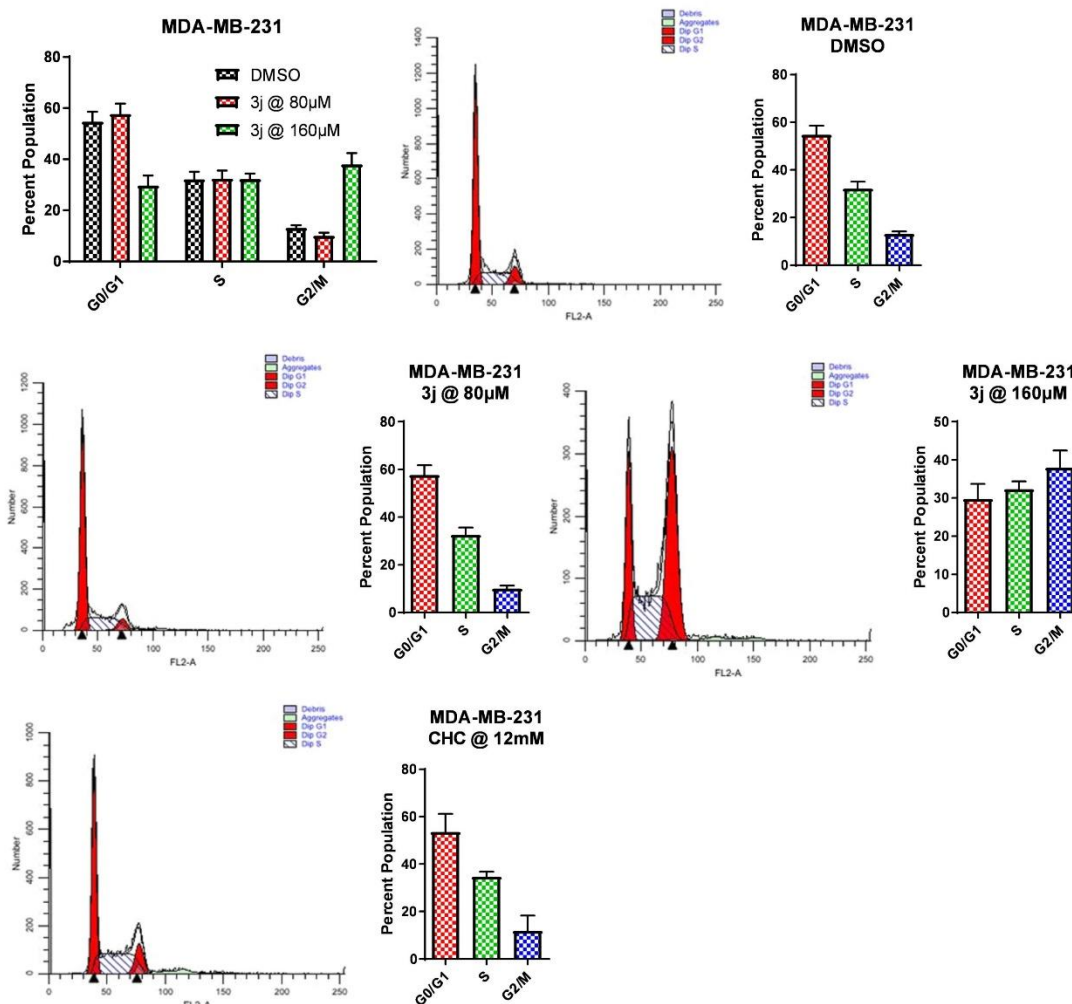


Figure 3e: Cell cycle analysis of MDA-MB-231 cell line treated with lead compound **3j**

The intricate connection between cellular metabolism (ATP generating) and proliferation (ATP consuming) is highly complex and involves crosstalk between both metabolic and cell-cycle machineries. Hence, inhibition of metabolic processes can be reasoned to disrupt cell proliferation. Rapid cell proliferation observed in cancer cells is dependent on both bio-energetic and bio-synthetic thresholds, and control of the cell cycle is highly regulated through energy sensing and biosynthetic mechanisms. It can be reasoned that potent inhibition of glycolysis and lactate transport compound **3j** may lead to a cellular metabolic crisis that prompts cell cycle machinery to stop proliferating during phases of the cell cycle that are dependent on the genetic make-up of the cell. Furthermore, it can be envisioned that the activation of cell death pathways may be dependent on the integrity of several molecular players such as p53. WiDr and MDA-MB-231 are p53 mutant cell lines, and responses to cellular and metabolic stress may result in unpredictable cell-cycle arrest and cell death responses as p53 is an important mediator between metabolic and proliferative states. Specifically, p53 has been shown to modulate MCT1 status through direct interaction with the *MCT1* gene promoter along with alterations in the stability of MCT1 mRNA. Hence, the differential phase of cell-cycle arrest in WiDr and MDA-MB-231 may be a result of a combination of cell type, MCT expression, metabolic preference, and p53 mutation status.

Specific molecular mechanisms by which the above-mentioned metabolic cell-cycle regulators function may also play a role in the phase at which the cell cycle is disrupted. The availability of acetyl CoA plays important roles in the cells ability to induce transcription and cell-cycle machineries, and metabolic dysfunction caused by compound

3j can lead to the alteration of the availability of acetyl CoA. These mechanisms also may result in arrest in other cell cycle phases such as S-phase observed in WiDr (Figure 3d) as a result of aberrant p53 activity. However, starvation of bio-synthetic building blocks through MCT1 inhibition may limit the cells ability to synthesize nucleotides necessary for completing replication and advancing from S to the G₂/M phase. Hence, limiting replication units after treatment with compound **3j** may result in the S-phase arrest observed in WiDr cells. Also, several metabolically related enzymes have been shown to play crucial roles in regulating G₂/M transitions, as evidenced by cell cycle data in MDA-MB-231 (Figure 3e). In this regard, metabolic dysfunction initiated by treatment with compound **3j** has numerous implications in the cells ability to progress through the cell cycle. As mentioned, it is quite possible that compound **3j** may exhibit off target effects due to its ability to cross the lipid bilayer and interact with intracellular components. Hence, compound **3j** may directly interact with DNA processes that could result in the cell-cycle effects observed in both WiDr and MDA-MB-231.

3.6 Systemic toxicity evaluation of *N,N*-dialkyl/diaryl *o*-methoxy CHC derivatives **3h-3k** in CD-1 mice: Results and discussion

As the compounds **3a-3k** showed excellent nanomolar potency of MCT1 inhibition, we then evaluated the systemic toxicity of some of the lead compounds in healthy CD-1 mice. We chose inhibitors **3h-3k** as lead derivatives (Figure 3f) for the further preclinical development based on their excellent dual MCT1 inhibition properties and their structural variations.

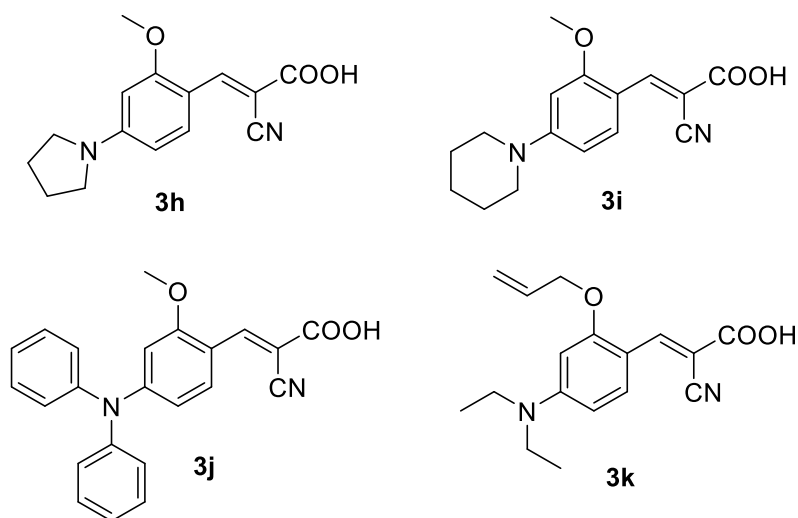


Figure 3f: Lead candidate compounds **3h-3k** for further *in vivo* studies

To improve the solubility, these lead candidate compounds **3h-3k** were converted into their corresponding sodium salts. Compound **3j** has an optimal solubility (1 mg/mL in water) and excellent MCT1 potency and higher cytotoxicity. Compound **3k** was chosen because of its with high solubility (> 40 mg/mL) and excellent MCT1 inhibition. Although **3h** and **3i** have less MCT1 inhibition than **3j** and **3k**, they have good water solubility (>14 mg/mL) and have structurally diverse pyrrolidinyl and piperidinyl groups. The compounds readily dissolved in 10% DMSO in saline with **3k** soluble up to ~2 mg/mL, **3h** and **3i** soluble up to ~7 mg/mL.

Mice were randomly assigned into groups (n = 6 mice per group) with similar average body weights and were treated with compound **3h** at 70 mg/Kg, ip, bid, and compound **3i** at 70 mg/Kg, ip, bid, compound **3j** at 50 mg/Kg, ip, qd, compound **3k** was administered at 20 mg/Kg, ip, qd,. The control groups received vehicle (10% DMSO in saline). At the end of the study, the treatment groups did not show any visible toxic effects such as abnormal grooming, hunchback, morbidity. The treatment groups had no significant differences in body weights compared to control groups (Figures 3g-A-D).

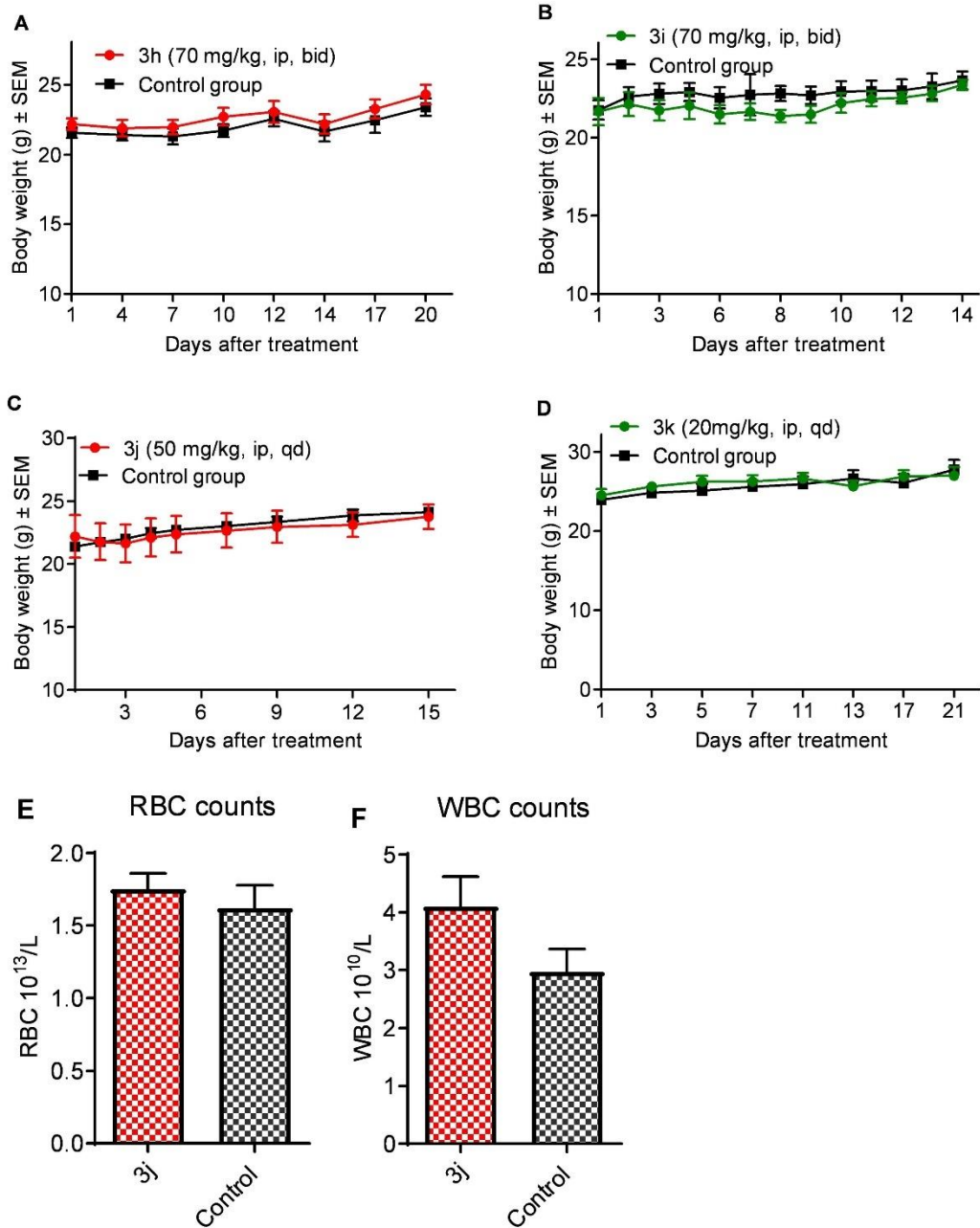


Figure 3g: Systemic toxicity study of compounds in CD-1 mice treated with: (A) **3h** at 70 mg/Kg, ip, bid, (B) **3i** at 70 mg/Kg, ip, bid, (C) **3j** at 50 mg/Kg, ip, qd and (D) **3k** at 20 mg/Kg, ip, qd. (E & F) RBC and WBC counts after treatment with **3j**

These results may appear surprising because of the presence of a doubly activated α,β -unsaturated system with two electron withdrawing groups -CN and -COOH on candidate compounds **3h-3k**. Having an olefin attached to electron withdrawing groups cyano and carboxylic acid will these inhibitors powerful 1,4-acceptors and electrophiles. However, upon addition of a nucleophile, the α -hydrogen next to carboxylic acid and cyano is highly acidic which is rapidly abstracted with concomitant release of the nucleophile making it a reversible inhibitor (Figure 3h).⁸² This aspect makes these cyanocinnamic acid based MCT1 inhibitors generally well tolerated in mice when administered systemically.

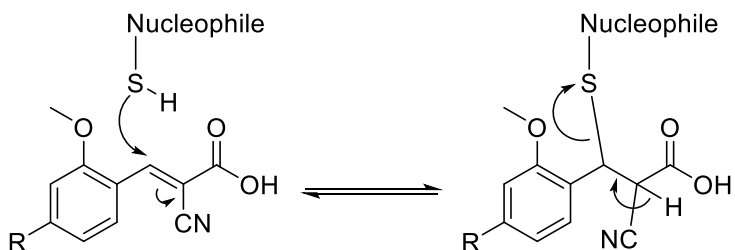


Figure 3h: 1,4-addition and reversibility of cyanocinnamic acid based MCT1 inhibitors

We also carried out the red blood cell (RBC) and white blood cell (WBC) counts after the treatment with lead candidate compound **3j** and control (vehicle). There was no significant difference in red blood cell and white blood cell blood counts in treatment group and control group (Figures 3g-E and 3g-F).

3.7 In vivo anticancer efficacy studies using lead candidate compounds: Results and discussion

3.7.1 Anticancer efficacy of compounds 3b and 3j in MCT1 expressing WiDr flank model

We then evaluated the lead candidate compounds **3b** and **3j** for *in vivo* efficacy in colorectal adenocarcinoma WiDr tumor flank model. We selected WiDr cell line because it has high expression of MCT1 and readily forms tumors in nude mice. Compound **3j** was selected for *in vivo* anticancer efficacy study because of its higher cytotoxicity and potent MCT1 inhibition. Compound **3b** was selected for this study as it has two butyl groups and one phenyl group instead of three phenyl groups as in **3j**, and this compound has similar MCT1 inhibition compared to **3j**. We also included the parent compound CHC for comparison with candidate compounds.

5 x 10⁶ WiDr cells in a 1:1 mixture of Matrigel:PBS were inoculated onto the flank of female BALB/c nude mice. After the average tumor volume reached ~120 mm³, mice were randomly assigned into 4 groups (n = 8 mice per group). Group 1 was treated with **3j** 10 mg/Kg, ip, bid, group 2 was given **3b** 8 mg/Kg, ip, bid and group 3 was administered with CHC 238 mg/Kg, ip, bid. High concentration of CHC was used based on the literature reports.⁶ Group 4 was assigned as a control group and was treated with 10% DMSO in saline. Body weights and tumor volume were measured every 2-3 days and after 21 days of treatment, mice were euthanized, and tumors were resected and weighed.

From this study, **3j**, **3b** and CHC showed 33, 35 and 44% tumor growth inhibition, respectively, based on the tumor volumes (Figure 3i-A-C). These compounds **3j**, **3b** and CHC showed 29, 34 and 46% tumor growth inhibition, respectively, based on the isolated tumor weights (Figure 3i-D). Although tumor growth inhibition was found to be moderate due to the low dosage used for this study, the lead compounds **3b** and **3j** exhibited efficacy similar to that of CHC, which was used at ~50 times higher concentration. During this study, average body weights of mice in the treatment groups were not significantly different compared to the control group (Figure 3i-E).

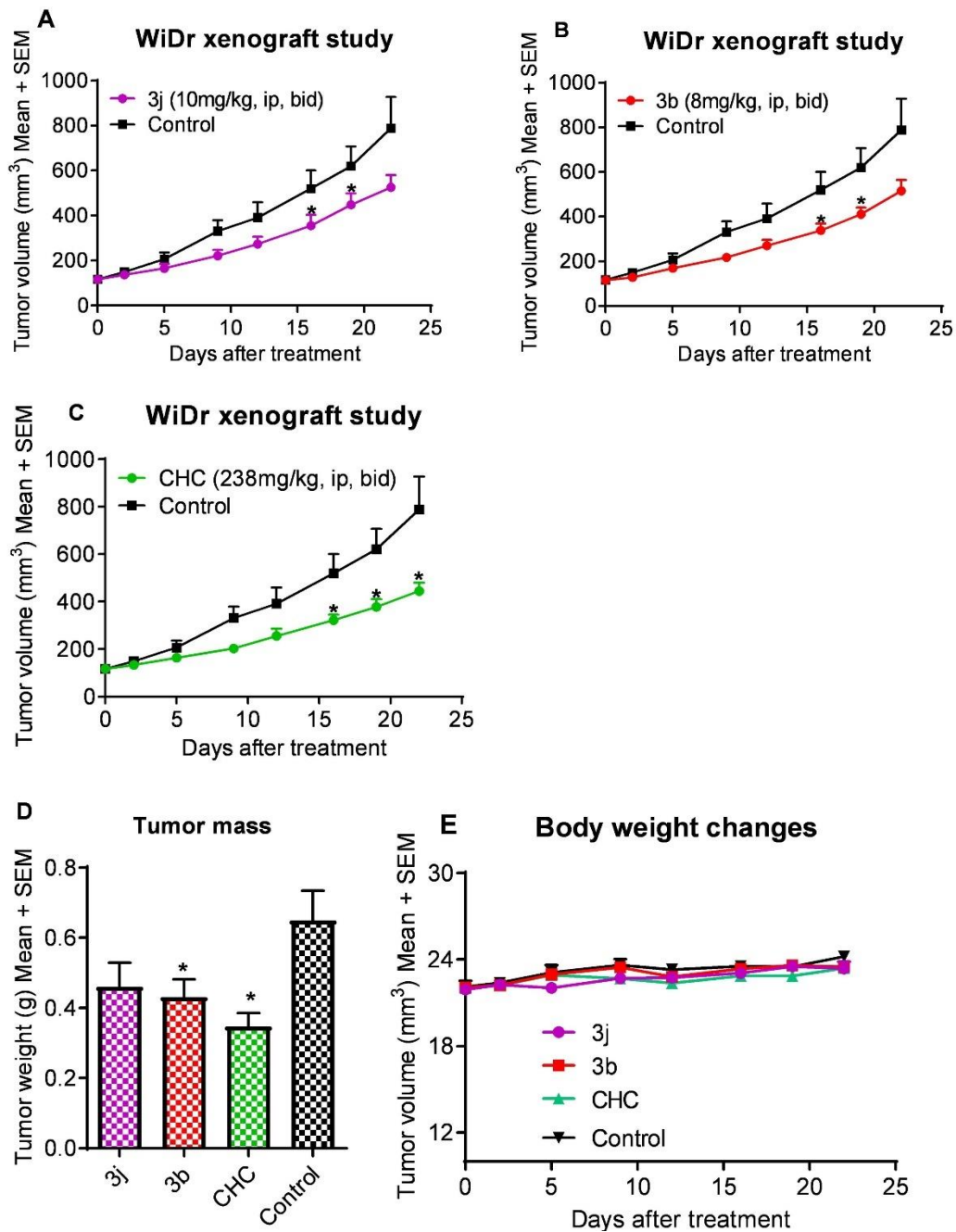


Figure 3i: Anticancer efficacy of lead compounds in a WiDr flank model based on tumor volumes (A) **3b**, (B) **3j** and (C) CHC (D) Tumor growth inhibition based on tumor mass (E) Body weight changes during the treatment period.

3.7.2 Chemoprevention study of compound 3j in MCT1 expressing WiDr flank model

As the lead candidate compound **3j** exhibited significant anticancer efficacy, we conducted another study in a WiDr flank model. In this study, the treatment was initiated on day-6 after tumor cell inoculation. In groups 1 and 2, the lead compound was administered in at a high dosage of 50 mg/Kg, ip, and 100 mg/Kg, oral gavage, respectively. The third group was assigned as the control group, which was treated with 10% DMSO in saline. At day-21, mice were euthanized and from this study, mice in group 1 and group 2 treatment groups exhibited 45 and 56% tumor growth inhibition, respectively (Figure 3j-A). In this study also, the average body weight changes in the treatment groups were not significantly different compared to the control group (Figure 3j-B).

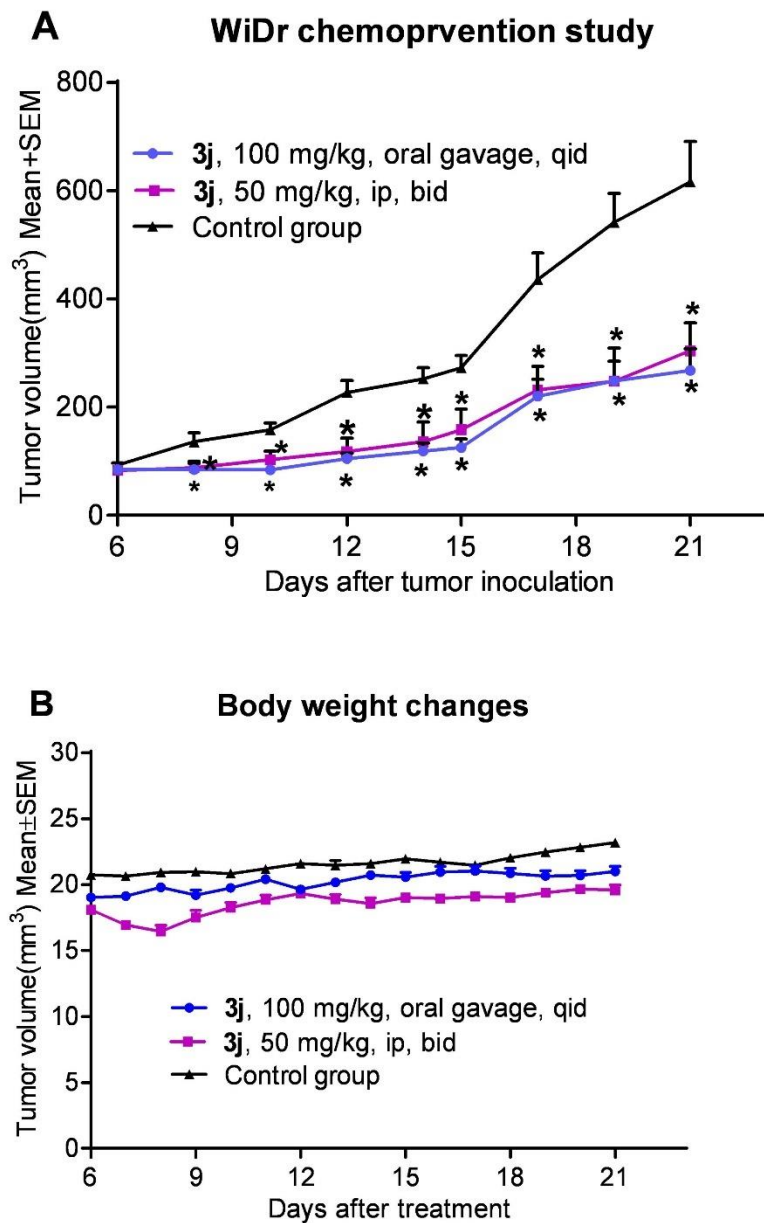


Figure 3j: Chemoprevention of lead compound **3j** in a WiDr flank model. (A) Tumor growth inhibition based on tumor volume (B) Body weight changes during the treatment period.

3.7.3 Anticancer efficacy of lead candidate compound **3j** in syngeneic 4T1-luc2 flank model

Cancer metastasis poses a critical challenge in the long term and overall survival of cancer patients. Hence, we studied the therapeutic application of our potent MCT1 inhibitor in an aggressive 4T1-luc2 murine tumor model system. Spontaneous metastasis occurs in liver, lungs, bone and brain while the primary tumor is growing *in situ*.²³ This cell line predominantly expresses MCT1 but not MCT4 (Figure 2c).

The flank of female BALB/c mice (4 weeks old) were injected with 1×10^5 cells 4T1-luc2 cells. Mice were randomized into 3 groups (n = 6 mice per group) after 48 hours of tumor inoculation. Mice in group 1 were administered with lead molecule **3j** at a dosage of 25 mg/Kg, ip, and doxorubicin was administered at 0.5 mg/Kg, i.p. five days a week as a positive control in group 2. Mice in group 3 were used as a control group and were administered with vehicle (10% DMSO in saline). Tumors were measured every 3-4 days. At the end of the study (day-21), mice were euthanized, and tumor samples were retrieved and weighed. From this study, **3j** and doxorubicin exhibited 38 and 36% tumor growth inhibition, respectively, based on tumor volume (Figure 3k-A), and 20 and 39% tumor growth inhibition based on weights from the resected tumors (Figure 3k-B).

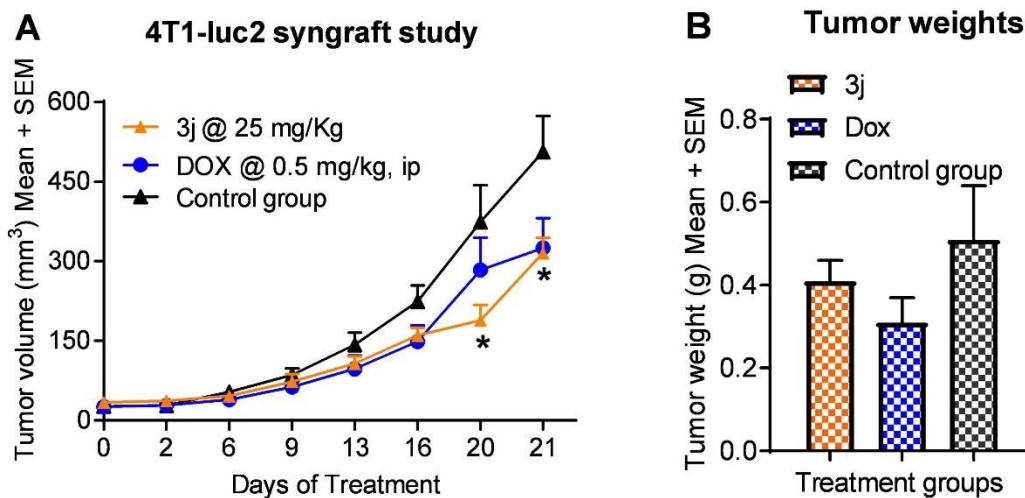


Figure 3k: Anticancer efficacy of **3j** compared with doxorubicin in a 4T1-luc2 flank model (A) Tumor growth inhibition using **3j** based on tumor volume; (B) Tumor growth inhibition using **3j** based on isolated tumor weights.

The initial anticancer efficacy study at 8-10 mg/Kg in MCT1 expressing WiDr tumor xenograft model with two candidate compounds butyl **3b** and phenyl **3j** showed ~35% tumor growth inhibition based on the recorded tumor volumes. Our second study at high concentration of 50-100 mg/Kg in the same tumor model provided ~45-55% tumor growth inhibition. This dose-dependent anticancer efficacy could be attributed to many factors such as low bioavailability, low metabolic stability, rapid elimination, high drug efflux ratio, etc. It is quite possible that inhibition of MCT1 may lead to tumors pursuing other pathways for energy generation.

Anticancer efficacy study in extremely aggressive and highly metastatic 4T1-luc2 at 25 mg/Kg dosage provided 38% tumor growth inhibition based on measured tumor

volumes. In this case, this tumor being highly aggressive with short survival period may be pursuing various metabolic pathways simultaneously and inhibition of one pathway may only lead to partial suppression of the tumor growth.

3.8 Evaluation of compound 3j for pharmacokinetic parameters: Results and discussion

To understand the metabolic stability of the lead candidate compounds, we further evaluated the **3j** for its pharmacokinetic parameters in CD-1 mice. The concentration-time profile was plotted for ip (Figure 3l-A) and oral administration of **3j** (Figure 3l-B). From the graph, the $t_{1/2}$ of **3j** was found to be 15 minutes for ip and 30 minutes for oral gavage routes of administration. These low $t_{1/2}$ values can be attributed to metabolically vulnerable phenyl groups which could have been oxidized by CYP enzymes.

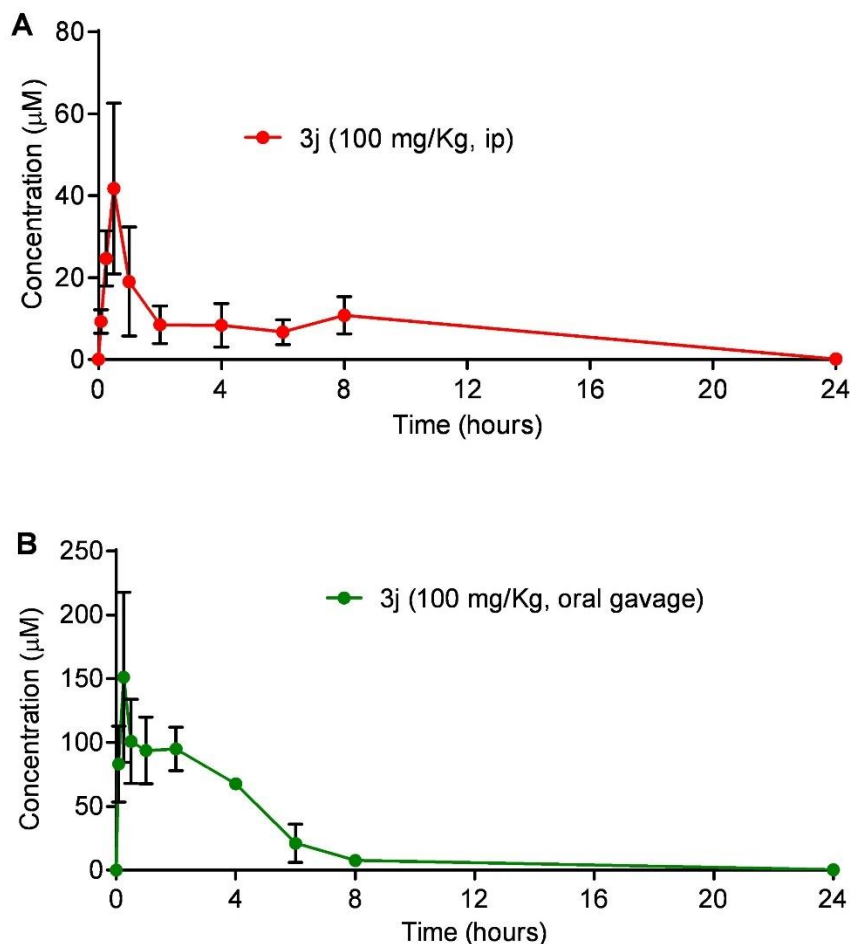


Figure 3l: Pharmacokinetic time-concentration profile in CD-1 mice for (A) intraperitoneal administration of **3j** and (B) intragastrical administration of **3j**.

The compound **3j** reached peak plasma concentration within 15-30 minutes time and most of the drug is eliminated in 1-2 hours from the system. In retrospect, this result may not be surprising as unsubstituted phenyl rings are highly susceptible for cytochrome P450 (CYP) enzymatic hydroxylation, subsequent glucuronidation, and elimination. We also attribute this rapid elimination of compound **3j** to be one of the major reasons for the moderate *in vivo* efficacy at low concentrations and dose-dependent efficacy at high concentrations.

3.9 Conclusions

In conclusion, we synthesized several *N,N*-dialkyl/diaryl *o*-substituted CHC derivatives **3a-3k** and evaluated them for MCT1 inhibition. These studies indicated that the compounds **3a-3k** exhibited potent MCT1 inhibition in RBE4 cell line. *In vitro* cytotoxicity evaluation in cancer cells expressing MCT1 and MCT4 under normoxic and hypoxic conditions revealed that compound **3j** exhibited good cytotoxicity in 4T1-luc2, GL261-luc2, WiDr, and MDA-MB-231 cell lines. Systemic toxicity study demonstrated that the candidate compounds **3h-3k** were well tolerated in mice with no significant body weight changes. Anticancer efficacy studies in MCT1 expressing WiDr and 4T1-luc2 flank models showed that the lead candidate compound **3j** provide anticancer efficacy in a dose dependent manner. Pharmacokinetic analysis showed that the lead compound **3j** has low biological half-life in mice. These novel *N,N*-dialkyl/diaryl *o*-substituted CHC derivatives could be used for the treatment of various MCT1 expressing cancers, as a single agent as well as in combination with other chemotherapeutic agents.

CHAPTER 4: Structure-activity relationship studies of 7-*N,N*-dialkyl 3-carboxy coumarins as MCT1 inhibitors: *In vitro* and *in vivo* studies as potential anticancer agents

4.1 Synthesis of 7-*N,N*-dialkyl 3-carboxy coumarin derivatives **4a** and **4b**

The lead compound CHC based diphenyl derivative **3j** exhibited potent MCT1 inhibition and significant tumor growth inhibition in MCT1 expressing WiDr and 4T1-luc2 models in mice. However, **3j** required high concentrations (50-100 mg/Kg) to achieve significant tumor growth inhibition due to its low metabolic stability. Hence, we further modified the *N,N*-dialkyl CHC template and designed 7-*N,N*-dialkyl 3-carboxy coumarins (Figure 4a) to improve metabolic stability and therapeutic efficacy at low concentrations.⁸³

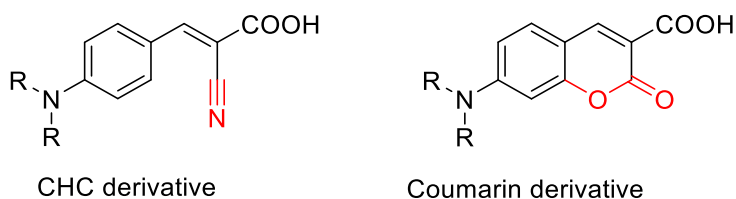


Figure 4a: CHC and coumarin derivatives.

Coumarins are heterobicyclic compounds with a proven track record of successfully making it into clinic and are considered as pharmacologically privileged structures. Some of the coumarin based biologically active drugs are depicted in the Figure 4b.

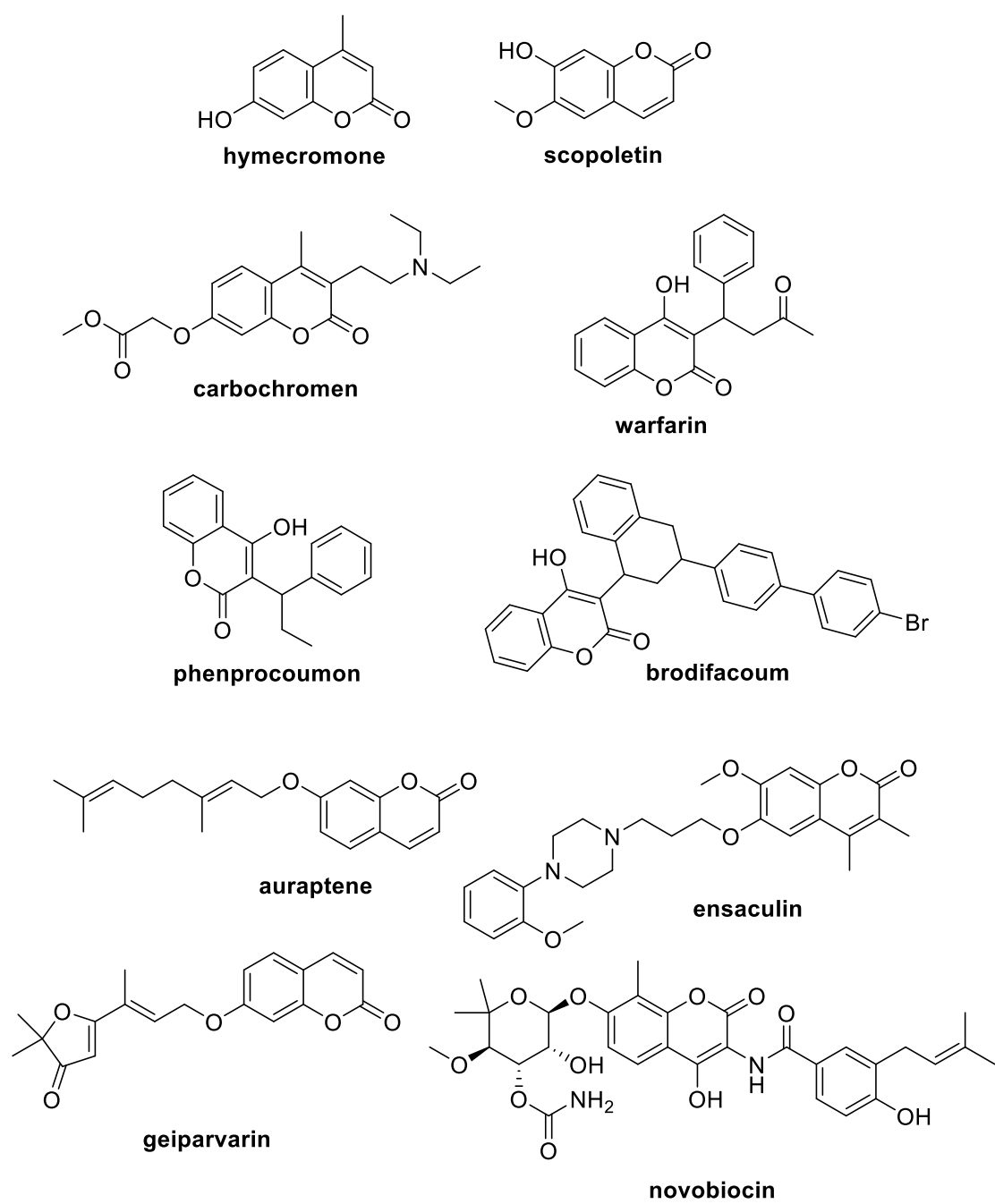
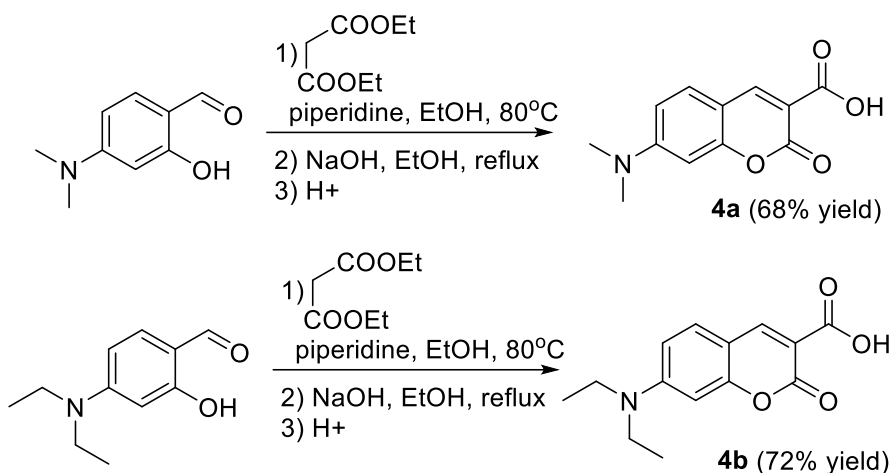


Figure 4b: Structures of the biologically active coumarin derivatives

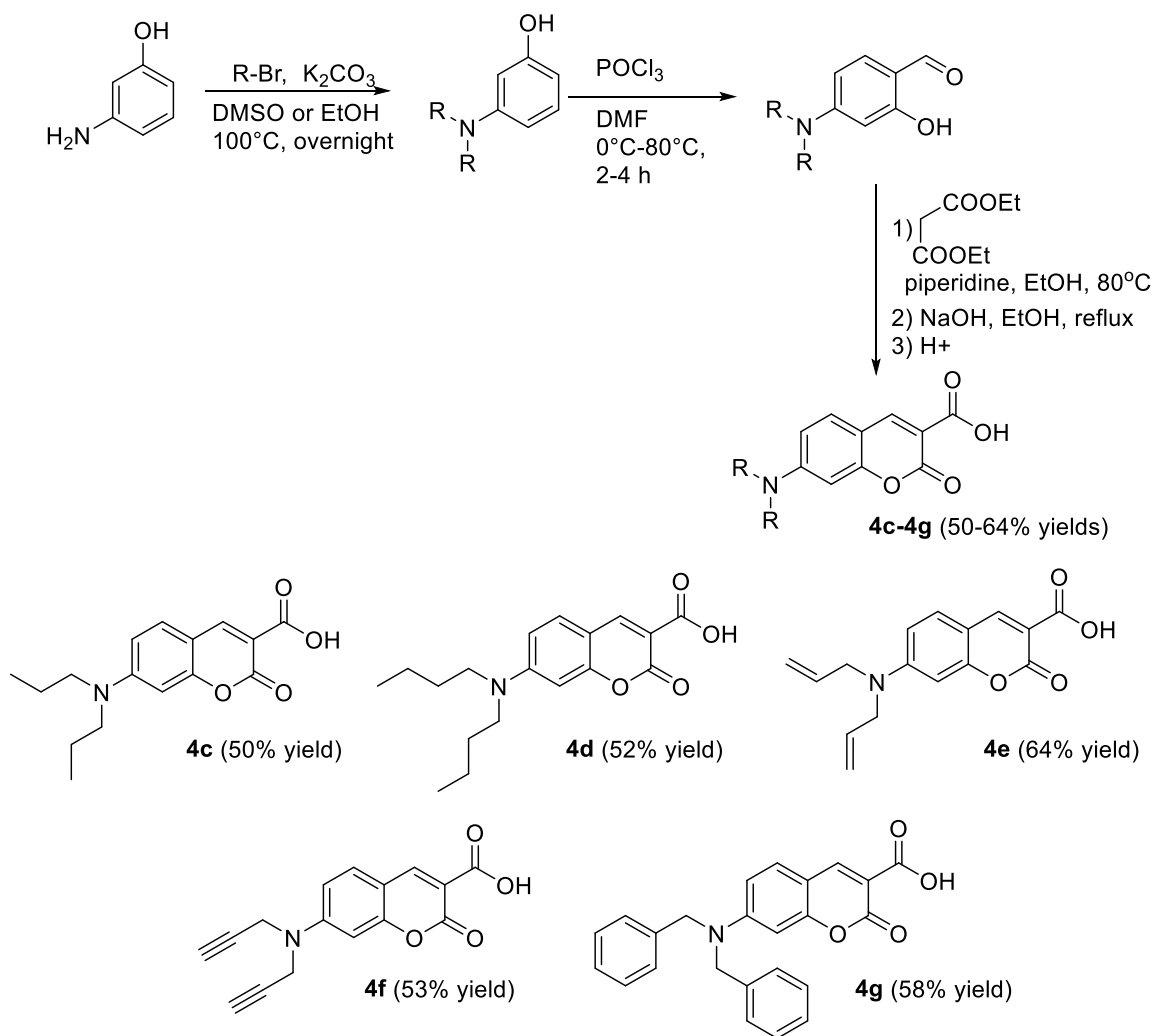
Our SAR studies on CHC indicated that cyanocinnamate unit was essential for MCT1 inhibition. In this regard, we envisioned that carboxycoumarin can stereo electronically mimic cyanocinnamate unit in its interaction with MCT1 protein. Since introduction of *N,N*-dialkyl/*N,N*-diaryl units on to the CHC provided low nM potency for inhibition for MCT1 inhibition, we also envisioned that these groups should translate similar type of activity onto the carboxycoumarin template. Based on this working hypothesis, we first synthesized *N,N*-dimethyl and *N,N*-diethyl carboxy coumarins **4a** and **4b** starting from commercially available aldehydes 4-(dimethylamino)-2-hydroxybenzaldehyde and 4-(diethylamino)-2-hydroxybenzaldehyde. These salicylaldehydes were condensed with diethyl malonate, and the resulting diesters were hydrolyzed and with NaOH and subsequently cyclized under acidic conditions to obtain the corresponding products **4a** and **4b** (Scheme 4a).



Scheme 4a: Synthesis of 7-(dimethylamino)-2-oxo-2H-chromene-3-carboxylic acid **4a** and 7-(diethylamino)-2-oxo-2H-chromene-3-carboxylic acid **4b**

4.1.1 Synthesis of 7-*N,N*-dialkyl 3-carboxy coumarin derivatives **4c-4g**

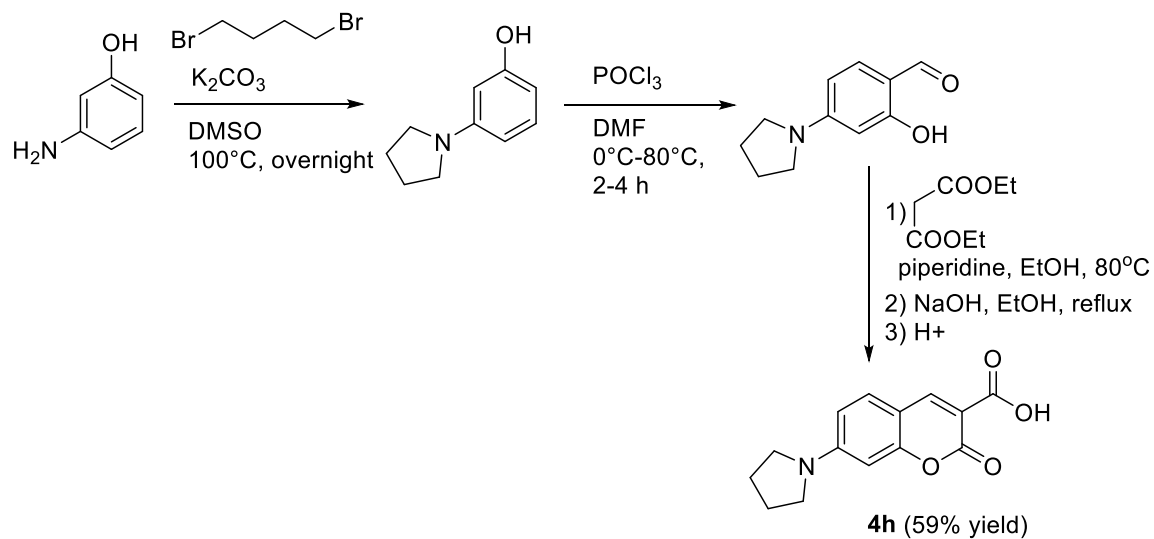
We then synthesized various *N,N*-dialkyl substituted carboxycoumarins **4c-4g** starting from *o*-aminophenol. Amine group was selectively alkylated with various bromides in the presence of K₂CO₃ in DMSO or ethanol as solvents. For alkylation, we used propyl, butyl, allyl, propargyl and benzyl bromides. The dialkylated aminophenols were then formylated using POCl₃ in DMF to obtain corresponding aldehydes. These aldehydes were condensed with diethyl malonate and hydrolyzed as mentioned in the scheme 4a to obtain corresponding 7-(dialkylamino)-2-oxo-2H-chromene-3-carboxylic acids **4c-4g** (Scheme 4b).



Scheme 4b: Synthesis of 7-(dialkylamino)-2-oxo-2H-chromene-3-carboxylic acids **4c-4g**

4.1.2 Synthesis of 7-*N,N*-dialkyl 3-carboxy coumarin derivative **4h**

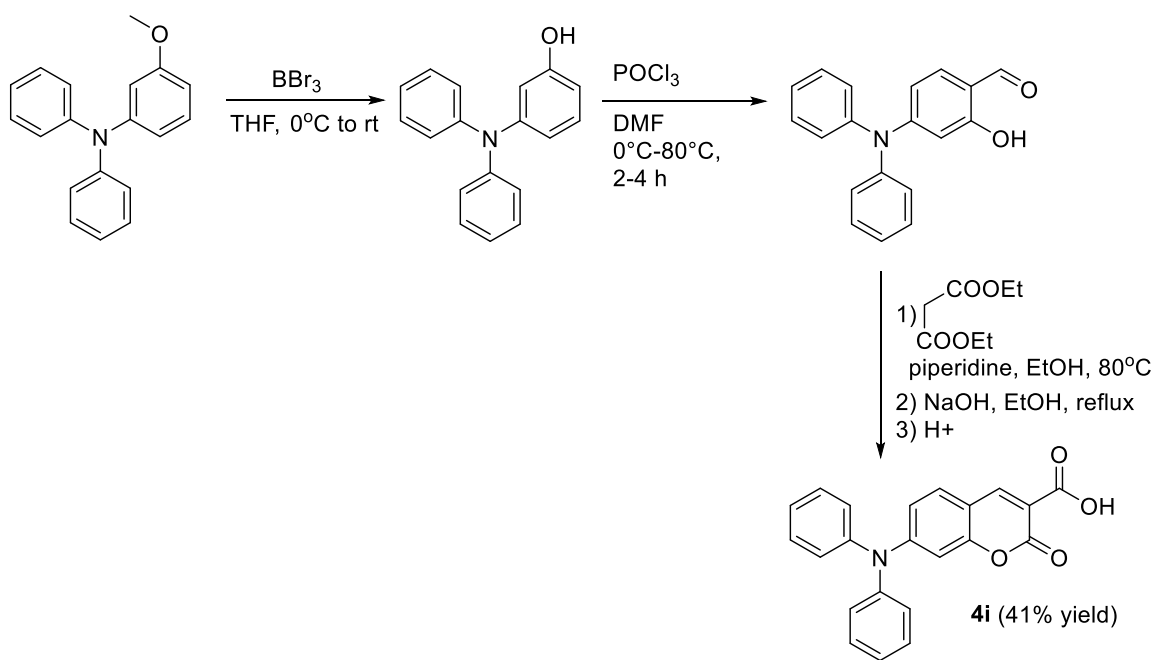
We also synthesized cyclic pyrrolidinyl carboxy coumarin **4h** via dialkylation of *o*-aminophenol with 1,4-dibromobutane (Scheme 4c).



Scheme 4c: Synthesis of 2-oxo-7-(pyrrolidin-1-yl)-2H-chromene-3-carboxylic acid **4h**

4.1.3 Synthesis of 7-*N,N*-diphenyl 3-carboxy coumarin derivative **4i**

Diphenyl carboxy coumarin **4i** was also synthesized starting from aminophenol. In this case, commercially available 3-methoxy-*N,N*-diphenylaniline was selectively demethylated using BBr_3 , followed by formylation via Vilsmeier-Haack conditions and subsequent treatment with diethyl malonate and hydrolysis to obtain **4i** (Scheme 4d).



Scheme 4d: Synthesis of 7-(diphenylamino)-2-oxo-2H-chromene-3-carboxylic acid **4i**

4.2 Evaluation of 7-*N,N*-dialkyl/diaryl carboxy coumarins 4a-4i for MCT1 inhibition:

Results and discussion

The synthesized 7-*N,N*-dialkyl/diaryl carboxy coumarins **4a-4i** were then evaluated for MCT1 inhibitory properties using ¹⁴C-lactate uptake assay in RBE4 cell line. We found that with an increase in the length of carbon chain methyl to butyl, there was a decrease in MCT1 inhibitory activity from 72 to 333 nM. Methyl derivative **4a** showed an IC₅₀ value of 72 nM, whereas ethyl, propyl and butyl carboxy coumarins **4b**, **4c** and **4d** exhibited IC₅₀ values of 97, 299 and 333 nM, respectively (Figure 4c, Table 4a). This result was a contrast to their counterparts in CHC based *N,N*-dialkyl/diaryl derivatives, where MCT1 inhibition was increased with an increase in alkyl chain. With diallyl **4e**, the IC₅₀ value was 254 nM, whereas for dipropargyl **4f**, the IC₅₀ value was found to be 151 nM. However, with dibenzyl substitution in **4g**, the IC₅₀ value was improved to 57 nM. Cyclic derivatives **4h** gave an IC₅₀ value 229 nM, which was comparable to propyl derivative **4b**, whereas the diphenyl carboxy coumarin **4i** exhibited an IC₅₀ value of 131 nM. Overall, the dibenzyl carboxy coumarin **4g** showed highest MCT1 inhibition and was chosen as the lead candidate compound for further studies.

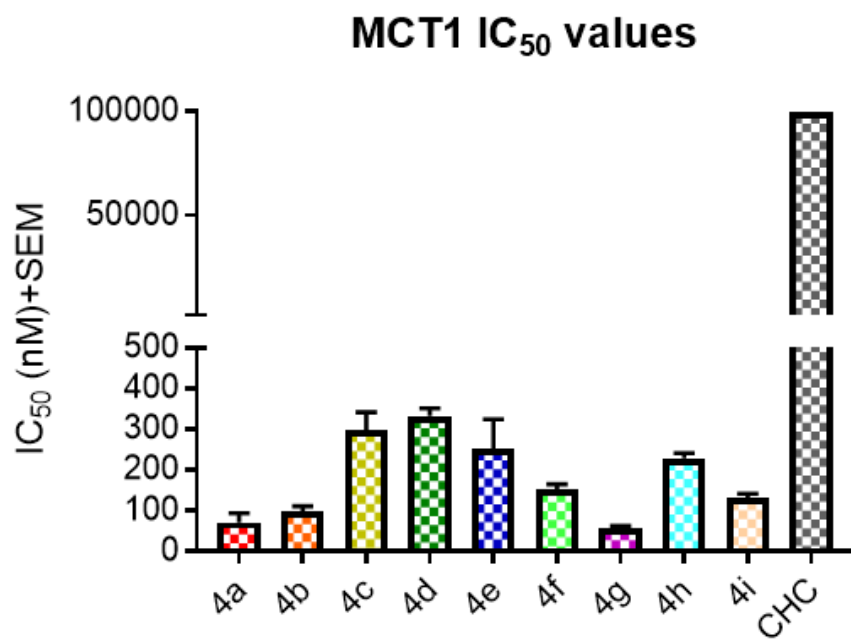
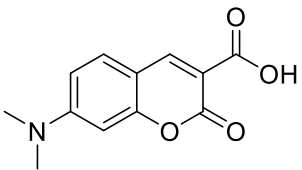
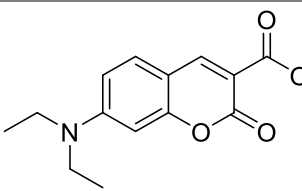
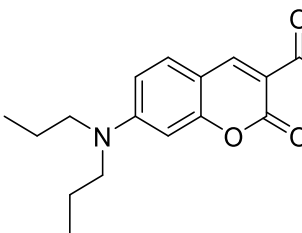
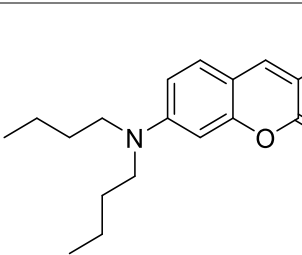
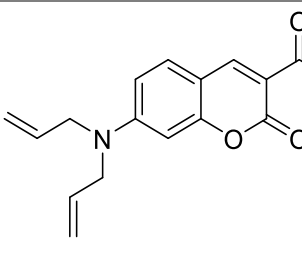
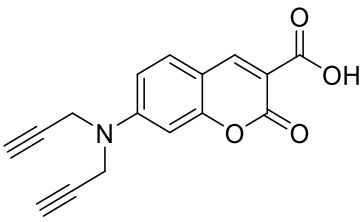
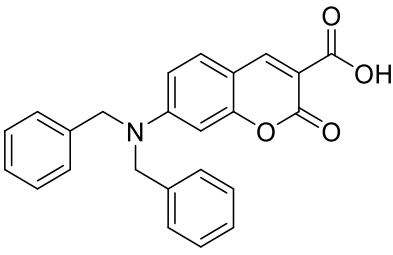
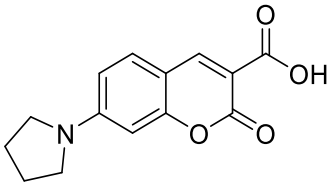
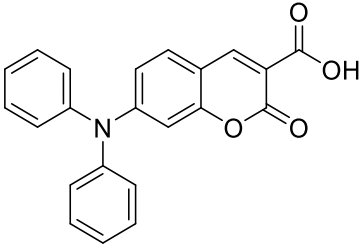


Figure 4c: MCT1 inhibition of *N,N*-dialkyl/diaryl 3-carboxy coumarins **4a-4i** in RBE4 cell line. The average+sem of at least three independent experiments were presented in the bar graph.

Table 4a: MCT1 IC₅₀ (mM)* of 7-*N,N*-dialkyl/aryl carboxy coumarins **4a-4i** in RBE4 cell

line

Sl. No.	Compound	MCT1 IC ₅₀
4a		72±22
4b		97±14
4c		299±43
4d		333±19
4e		254±71

4f		151±14
4g		57±6
4h		229±13
4i		131±11

* average±sem of three independent experiments

From the MCT1 inhibition studies in RBE4 cell line, all the candidate *N,N*-dialkyl/diaryl substituted carboxy coumarins **4a-4i** were found to be less potent than the corresponding *N,N*-dialkyl/diaryl substituted CHC derivatives **2.2a-2.2m** and **3a-3j**. Compounds **4a-4i** have doubly activated system with carboxylic acid and cyclic ester groups whereas CHC derivatives **2.2a-2.2m** and **3a-3j** have carboxylic acid and cyano

groups. In terms of electron withdrawing capability, nitrile and ester have similar capacity as measured by the acidity of α -Hydrogens with pKa values ~25. We attribute higher potency of CHC derivatives for lesser sterics of CHC system which provides optimal interactions with MCT1 compared to bicyclic coumarin system. However, carboxy coumarins **4a-4i** still exhibit nanomolar to low micromolar range IC₅₀ values for MCT1 inhibition and were highly potent compared to parent CHC molecule.

4.3 Cell proliferation inhibition of compounds 4a-4i in GL261-luc2 and MDA-MB-231 cell lines using MTT assay: Results and discussion

We then evaluated cell proliferation inhibition of 7-*N,N*-dialkyl carboxy coumarins **4a-4i** in MCT1 expressing GL261-luc2 and MCT4 expressing MDA-MB-231 cell line. The compounds were tested up to a maximum concentration of 0.25 mM, and all these compounds did not show any cell proliferation, except for dibenzyl carboxy coumarin **4g**, which showed an IC₅₀ of 0.24 mM in MDA-MB-231 cell line (Table 4b).

Table 4b: MTT assay IC₅₀* values of 7-*N,N*-dialkyl/diaryl carboxy coumarins **4a-4i** in GL261-luc2 and MDA-MB-231 cell lines

Compound	GL261-luc2	MDA-MB-231
4a	>0.25	>0.25
4b	>0.25	>0.25
4c	>0.25	>0.25
4d	>0.25	>0.25
4e	>0.25	>0.25
4f	>0.25	>0.25
4g	>0.25	0.24±0.01
4h	>0.25	>0.25
4i	>0.25	>0.25

*IC₅₀ values reported in mM, average±SEM of minimum three separate experimental values

From the cell proliferation inhibition studies using MTT assay, the candidate carboxy coumarins **4a-4i** were found to be generally non-toxic up to 0.25 mM concentration in MCT1 expressing GL261-luc2 and MCT4 expressing MDA-MB-231. The dibenzyl carboxy coumarin **4g** with an MCT1 IC₅₀ value of 57 nM was found to inhibit cell proliferation in MDA-MB-231 with an IC₅₀ value of 0.24 mM. Compound **4g** was also evaluated for cell proliferation inhibition in MCT1 expressing WiDr cell line and the IC₅₀ value was found to be 0.023 mM. It should be noted that the CHC derivatives dibutyl **3b**, dibenzyl **3g** and diphenyl **3j** showed much higher cell proliferation inhibition with IC₅₀ values of 0.0056, 0.0125, and 0.0077 mM, respectively. This higher potency may be due to higher nucleophilic accepting capacity of CHC derivatives due to lower sterics compared to carboxy coumarins. As mentioned in chapter 3, potent MCT1 inhibition may not translate to higher cell proliferation inhibition as cells may adapt to other metabolic processes for survival under *in vitro* conditions.

4.4 Cell cycle analysis of compound 4g in MDA-MB-231 cell line: Results and discussion

As the lead compound **4g** did not exhibit cell proliferation inhibition in GL261-luc2 cell line, we tested whether the cell cycle of MDA-MB-231 was affected by this compound. For this purpose, the cells were treated with compound **4g** for a period of 24 hours with concentrations corresponding to the of IC₅₀ value and analyzed for DNA content and cell cycle distributions (Figure 4d). Interestingly, MCT4 expressing MDA-MB-231 cells treated with compound **4g** inhibited S phase where DNA replication occurs in the cell cycle at 250 μ M concentration and G2/M phase is considerably increased compared to the control. As discussed in chapter 3.5, these results suggest that disruption of metabolic processes with compound **4g** may ultimately cause cell cycle arrest and defective DNA processing.

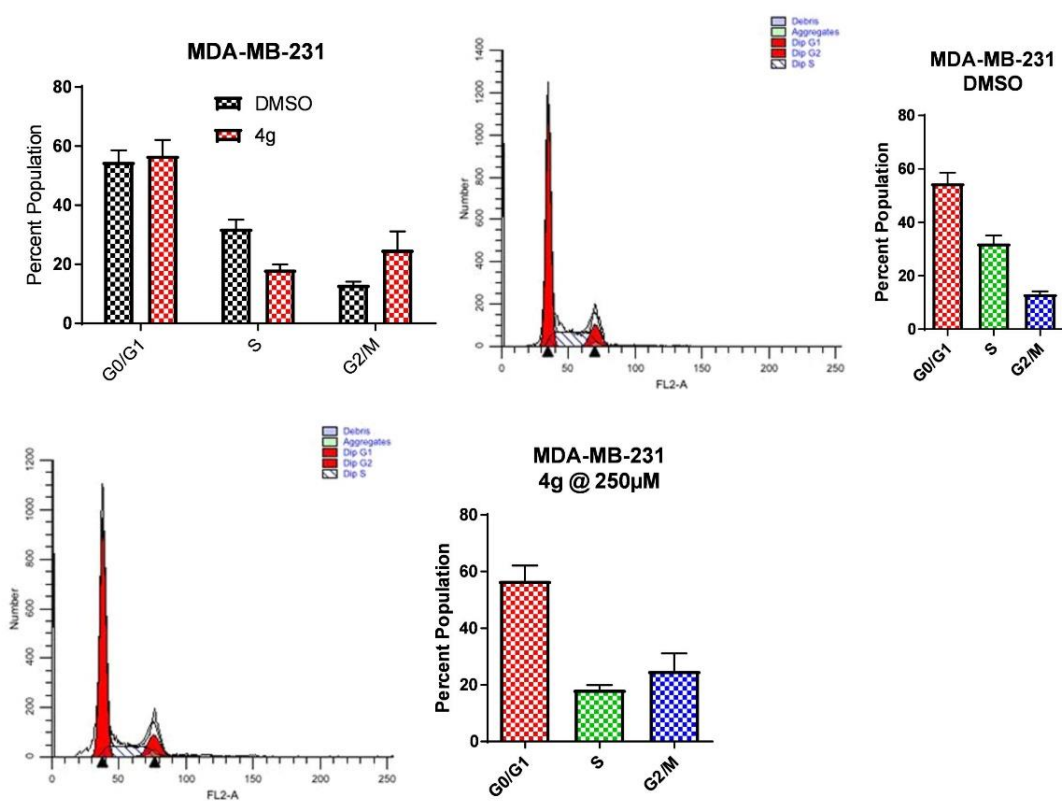


Figure 4d: Cell cycle analysis of compound **4g** at IC₅₀ concentration in MDA-MB-231 cell line

4.5 *In vitro* protein binding, Caco-2 permeability and metabolic stability studies: Results and discussion

To evaluate their pharmaceutical properties, *N,N*-dialkyl/diaryl CHC derivatives **3g**, **3h**, **3j**, **3k** and *N,N*-dibenzyl carboxy coumarin **4g** were tested for *in vitro* human plasma protein binding, bidirectional Caco-2 cell monolayer permeability, and metabolic stability in human and mouse liver microsomes using standard reported protocols.^{84,85} Due to its potent MCT1 inhibition and moderate cell proliferation inhibition, we assigned **4g** as the lead candidate compound which consists of *N,N*-dibenzyl on the 7-position of the aromatic system. We compared this lead compound **4g** with *N,N*-dibenzyl *o*-methoxy CHC derivative **3g** as its counterpart. We also chose the lead molecule **3j** described in chapter 3, and compounds **3h** and **3k** due to their high solubility to carry out further *in vitro* metabolic stability studies (Figure 4e).

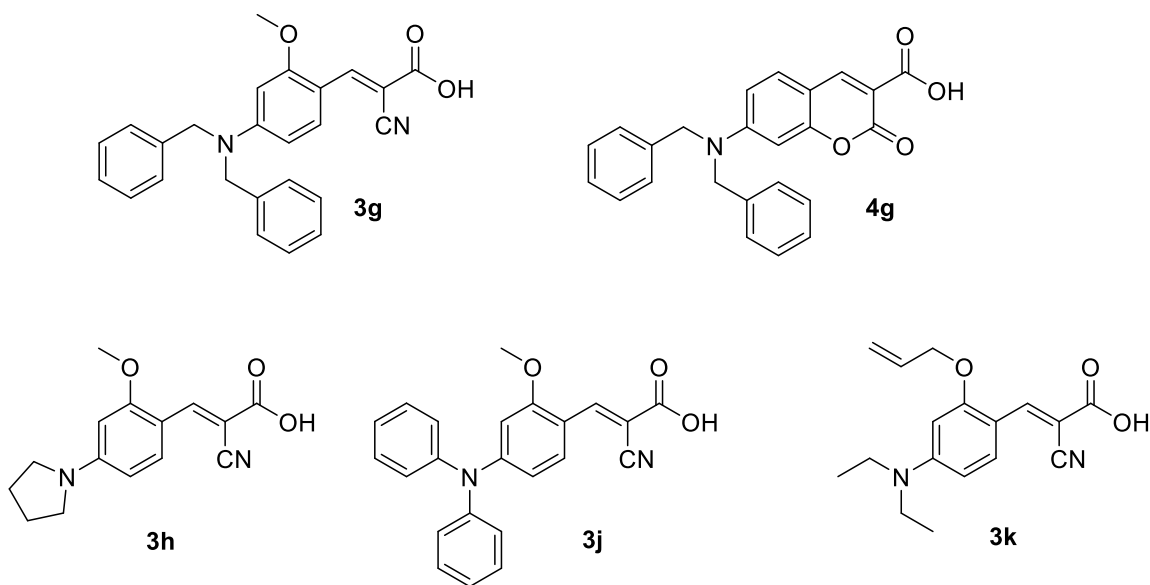


Figure 4e: Lead molecules chosen for *in vitro* metabolic stability studies

4.5.1 Protein binding studies of compounds **3g**, **3h**, **3j**, **3k** and **4g** in human plasma

The compounds **3g**, **3h**, **3j**, **3k** and **4g** were tested for their protein binding capacity in human plasma. From this study, all of these compounds were found to be highly protein bound (>99%) with excellent recovery values (Table 4c). Acebutolol, quinidine, and warfarin with low, medium and high protein binding values, respectively, were used as controls.

Table 4c: *In vitro* protein binding studies (protein binding: plasma, human)

Compound	Test Concentration	% Protein Bound			% Recovery		
		1st	2nd	Mean	1st	2nd	Mean
3g	1.0E-05 M	>99.9	100	>99	91	95	93
3h	1.0E-05 M	99.5	100	>99	97	99	98
3j	1.0E-05 M	99.5	100	>99	89	94	91
3k	1.0E-05 M	99.8	100	>99	97	92	94
4g	1.0E-05 M	99.7	100	>99	93	91	92
Acebutolol	1.0E-05 M	21	18	19	118	118	118
Quinidine	1.0E-05 M	71	71	71	105	110	108
Warfarin	1.0E-05 M	99	99	99	83	86	84

4.5.2 Caco-2 permeability studies of compounds **3g, **3h**, **3j**, **3k** and **4g****

Caco-2 permeability assays for compounds **3g**, **3h**, **3j**, **3k** and **4g** in both apical to basolateral (A-B) and basolateral to apical (B-A) directions were carried out to predict their oral bioavailability. Caco-2 is a heterogeneous human epithelial colorectal adenocarcinoma cell line that mimics the human enterocytic intestinal layer. This assay estimates human intestinal permeability and drug efflux of the compounds, predicts oral bioavailability. Compounds **3g** and **3j** exhibited relatively low A-B and B-A permeability values whereas compounds **3h** and **3k** showed relatively low A-B and moderate B-A permeability, respectively (Tables 4d and 4e). Compound **4g** exhibited high A-B and low B-A permeability. Propranolol (highly permeable), labetalol (moderately permeable), ranitidine (poorly permeable), and colchicine (P-glycoprotein substrate) were used as controls.

Table 4d: A-B Caco-2 permeability studies of compounds **3g**, **3h**, **3j**, **3k** and **4g**:

A-B permeability (Caco-2, pH 6.5/7.4)							
Compound	Test	Permeability (10^{-6} cm/s)			Percent Recovery (%)		
	Concentration	1st	2nd	Mean	1st	2nd	Mean
3g	1.0E-05 M	5.9	5.15	5.5	28	30	29
3h	1.0E-05 M	3.08	2.43	2.8	76	67	71
3j	1.0E-05 M	5.96	6.15	6.1	28	28	28
3k	1.0E-05 M	3.65	2.78	3.2	67	64	66
4g	1.0E-05 M	30.32	33.73	32	33	35	34
colchicine	1.0E-05 M	0.36	0.32	0.3	75	75	75
labetalol	1.0E-05 M	8.68	8.31	8.5	61	71	66
propranolol	1.0E-05 M	41.45	40.34	40.9	67	66	67

Table 4e: B-A Caco-2 permeability studies of compounds **3g**, **3h**, **3j**, **3k** and **4g**:

B-A permeability (Caco-2, pH 6.5/7.4)							
Compound	Test	Permeability (10^{-6} cm/s)			Percent Recovery (%)		
	Concentration	1st	2nd	Mean	1st	2nd	Mean
3g	1.0E-05 M	4.39	5.41	4.9	26	39	33
3h	1.0E-05 M	41.12	43.92	42.5	80	73	77
3j	1.0E-05 M	5.28	5.78	5.5	31	29	30
3k	1.0E-05 M	48.26	47.19	47.7	75	75	75
4g	1.0E-05 M	6.32	6.54	6.4	53	58	55
colchicine	1.0E-05 M	15.25	15.39	15.3	81	82	81
labetalol	1.0E-05 M	34.59	38.49	36.5	72	73	72
propranolol	1.0E-05 M	38.02	44.94	41.5	80	80	80
ranitidine	1.0E-05 M	3.59	3.85	3.7	88	82	85

4.5.3 Metabolic stability assay in mouse and human liver microsomes using compounds **3g, **3h**, **3j**, **3k** and **4g****

The half-life of compounds **3g**, **3h**, **3j**, **3k** and **4g** in human and mouse liver microsomes were determined in order to assess their hepatic clearance rates because liver microsomes contain many enzymes that are responsible for metabolism of drugs. Compounds **3g**, **3h**, **3k** and **4g** exhibited good metabolic stability ($T_{1/2} \geq 50$ minutes) in both human and mouse liver microsomes with high intrinsic clearance rates (Tables 4f and 4g). Surprisingly, the diphenyl derivative **3j** exhibited low stability ($T_{1/2} = 12$ min) in human liver microsomes. Propranolol, imipramine, verapamil and terfenadine were used as controls with high, medium and low metabolic stabilities, respectively.

Table 4f: Metabolic stability in human liver microsomes for compounds **3g**, **3h**, **3j**, **3k** and**4g:**

Intrinsic clearance (liver microsomes, human)					
Compound	Test Concentration	Half-Life (minute)			Clint
		1st	2nd	Mean	
3g	1.0E-07 M	103.4	75.5	>60	<115.5
3h	1.0E-07 M	>60	>60	>60	<115.5
3j	1.0E-07 M	12.9	11.5	12	571.1
3k	1.0E-07 M	210.7	153.3	>60	<115.5
4g	1.0E-07 M	922.2	>60	>60	<115.5
imipramine	1.0E-07 M	213.9	194.4	>60	<115.5
propranolol	1.0E-07 M	334.4	373	>60	<115.5
terfenadine	1.0E-07 M	9.8	9.1	9	736.8
verapamil	1.0E-07 M	21.1	21.5	21	324.8

Table 4g: Metabolic stability in mouse liver microsomes for compounds **3g**, **3h**, **3j**, **3k** and **4g**:

Intrinsic clearance (liver microsomes, mouse, CD-1)					
Compound	Test Concentration	Half-Life (minute)			Clint
		1st	2nd	Mean	
3g	1.0E-07 M	46.8	53.6	50	138.6
3h	1.0E-07 M	1077.4	>60	>60	<115.5
3j	1.0E-07 M	52.6	71.2	>60	<115.5
3k	1.0E-07 M	455.9	299.3	>60	<115.5
4g	1.0E-07 M	90.6	73.5	>60	<115.5
imipramine	1.0E-07 M	15.7	15.4	16	446.2
propranolol	1.0E-07 M	9.1	9.5	9	744.5
terfenadine	1.0E-07 M	7.5	6.1	7	1027.4
verapamil	1.0E-07 M	17.6	17.5	18	394.6

From these *in vitro* studies, coumarin based lead compound **4g** showed good metabolic stability in mouse and human liver microsomes. This compound also exhibited low efflux ratio of 0.2, whereas CHC based derivatives **3g**, **3h**, **3j** and **3k** exhibited efflux ratio values of 0.9, 15.2, 0.9, and 14.9, respectively. A drug efflux ratio of <2 indicated that CHC derivatives **3g**, **3j** and carboxy coumarin derivative **4g** were not good substrates for drug efflux pumps, thereby have the capability to be inside the cell for a longer time period to elicit anticancer efficacy. Caco-2 permeability studies also indicated that carboxy

coumarin **4g** exhibited good oral bioavailability with 33% absorption whereas CHC derivatives **3g**, **3h**, **3j** and **3k** had lower absorption values in the range of 2.8-6.1%. Due to its high metabolic stability, oral bioavailability, low drug efflux ratio, the lead candidate **4g** was chosen for further *in vivo* systemic toxicity in healthy CD-1 mice and anticancer efficacy evaluation in mouse models.

4.6 Systemic toxicity evaluation of the lead candidate compound **4g** in CD-1 mice:

Results and discussion

We next tested the lead candidate compound **4g** for systemic toxicity in CD-1 mice. Mice were procured and acclimatized for one week and randomly assigned into three groups (n = 6 mice per group) based on average body weights. Mice in group-1 was administered with **4g** once daily at a high dosage of 100 mg/Kg via oral gavage. Mice in group-2 was given **4g** at a low dosage of 20 mg/Kg, ip, once daily. The control group was treated with vehicle (10% DMSO in saline). The treatment continued for 14 days and at the end of the study, mice in groups 1 and 2 did not show any toxicity compared to control group based on their average body weight (Figure 4f).

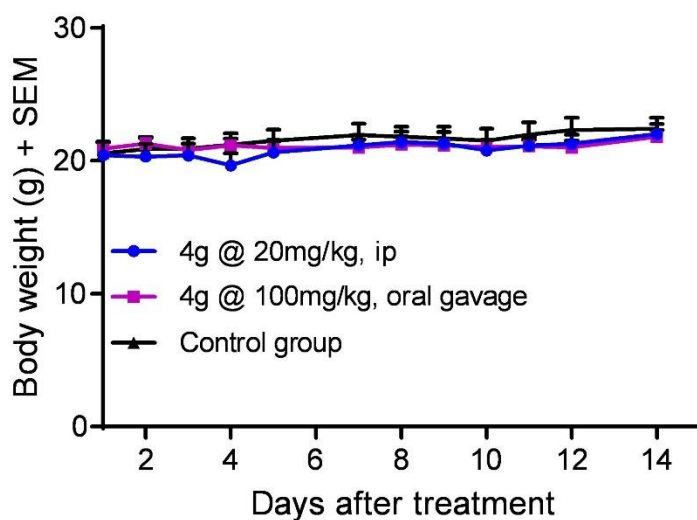


Figure 4f: Body weight changes in systemic toxicity study of compound **4g** in CD-1 mice.

Carboxy coumarin **4g** has a doubly activated α,β -unsaturated system with two electron withdrawing cyclic ester and carboxylic acid groups. This doubly activated α,β -unsaturated system is a powerful 1,4-acceptor but upon addition of a nucleophilic residue, the highly acidic α -hydrogen is rapidly abstracted with concomitant release of the nucleophile making it a reversible inhibitor similar to that of CHC derivatives (Figure 4g). This aspect makes these carboxy coumarin based MCT1 inhibitors generally well tolerated in mice when administered systemically.

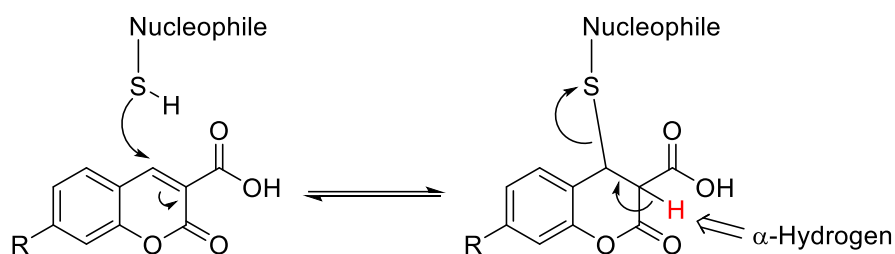


Figure 4g: 1,4-addition and reversibility of carboxy coumarin based MCT1 inhibitors

4.7 Anticancer efficacy of lead compound 4g in a glioblastoma tumor model: Results and discussion

Glioblastoma multiforme is a highly aggressive brain malignancy associated with rapid tumor growth, recurrence, metastasis and poor patient outcome even after surgery followed by chemo/radiation therapy. Currently, temozolomide is the only chemotherapeutic used for the treatment of glioblastoma. The absence of well-defined molecular targets and the inability of most drugs to cross the blood-brain barrier make glioblastoma treatment very challenging. Hence, we planned to evaluate the efficacy of carboxy coumarins for the treatment of glioblastoma.

In this regard, we chose GL261 cell line for tumor inoculation. GL261 is an established murine model system for the study of human gliomas and predominantly expresses MCT1 as confirmed by western blot (Figure 2c). GL261 gliomas have reduced growth following anti-angiogenic effects induced by therapeutic down regulation of HIF-1 α , are sensitive to radiation following chemotherapy, respond to vascular disrupting agents, and display properties of invasiveness along micro vessels.^{86,87} All these features of human glioblastoma are therefore modeled with GL261 model system, and hence are highly suitable for analysis of the effect of MCT1 inhibition on tumor vasculature and the hypoxic environment of solid brain tumors. GL261 syngeneic gliomas introduced into the C57BL/6 mouse is an established model of human glioblastoma. Hence, we utilized C57BL/6J mice for this study.

Briefly, mice were injected with a mixture of 5×10^6 cells in 1:1 matrigel and 1X PBS. After tumor volume reached $\sim 200 \text{ mm}^3$, mice were randomly assigned into three

groups. Group-1 was administered once daily with **4g** at a dosage of 20 mg/Kg, ip, and group-2 was treated with clinical glioblastoma drug temozolomide at a dosage of 20 mg/Kg, ip, and group-3 was injected with vehicle (10% DMSO in saline). After 14 days, based on tumor volume, mice treated with lead compound **4g** exhibited 70% tumor growth inhibition whereas mice in temozolomide treatment group showed 76% tumor growth inhibition compared to the control group (Figure 4h-A). These results correlate with isolated tumor mass, where **4g** treatment group exhibited 77% tumor growth inhibition, whereas temozolomide treatment group showed 81% tumor growth inhibition (Figure 4h-B).

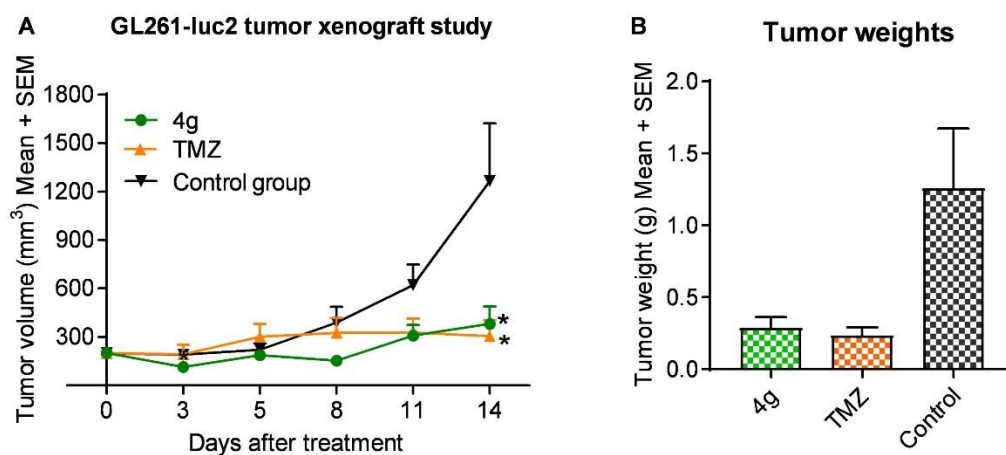


Figure 4h: Anticancer efficacy of lead compound **4g** in a GL261-luc2 flank model (A) Tumor growth inhibition based on tumor volume; (B) Tumor growth inhibition based on tumor weights.

When the carboxy coumarin **4g** was tested in MCT1 expressing GL261-luc2 glioma syngraft tumor model, this compound exhibited significant tumor suppression which was

comparable to clinical glioblastoma drug temozolomide. Also, as discussed in chapter 1, Draoui et. al. also synthesized similar coumarin derivatives 7ACC1 and 7ACC2 and these compounds were tested in MCT1 expressing breast cancer MCF7, cervical cancer SiHa, colorectal cancer HCT-116 tumor models. These carboxy coumarins exhibited significant tumor growth inhibition in all these tumor models and also exhibited excellent synergy when treated with chemotherapeutic agent cisplatin.⁷⁷

4.8 Conclusions

In conclusion, we synthesized several *N,N*-dialkyl/diaryl 3-carboxy coumarins **4a-4i** and evaluated them for MCT1 inhibition. These studies indicated that these compounds **4a-4i** exhibited good MCT1 inhibition with nanomolar to low micromolar range IC₅₀ values in RBE4 cell line. *In vitro* cytotoxicity evaluation in MCT1 expressing GL261-luc2 and MCT4 expressing MDA-MB-231 cell lines showed that carboxy coumarins did not exhibit good cell proliferation inhibition up to 0.25 mM concentration. Lead carboxy coumarin **4g** with high potency was further studied for its *in vitro* human plasma protein binding, bidirectional Caco-2 cell permeability, and metabolic stability in human and mouse liver microsomes. In these studies, **4g** was also compared with CHC based MCT1 inhibitors **3g**, **3h**, **3j** and **3k**. All the tested derivatives were found to be highly protein bound with excellent percent recovery. Compound **4g** was found to exhibit good metabolic stability and oral bioavailability. Systemic toxicity study in healthy CD-1 mice showed that the lead compound **4g** was well-tolerated in mice with no significant body weight changes. Anticancer efficacy studies in MCT1 expressing GL261-luc2 flank model demonstrated that the lead candidate compound **4g** provides significant anticancer efficacy comparable to clinical drug temozolomide. Based on our *in vivo* anticancer efficacy results, and also based on excellent anticancer efficacy results from other groups, the lead candidate compound **4g** has an excellent potential to be developed as a single agent anticancer therapy. Candidate compound **4g** could also be used in combination with other chemotherapeutic agents for the treatment of wide variety of MCT1 expressing cancers.

CHAPTER 5: Evaluation of *N,N*-dialkyl/diaryl *o*-substituted CHC derivatives and 7-*N,N*-dialkyl/diaryl 3-carboxy coumarins as MCT4 inhibitors: *In vitro* and *in vivo* studies as potential anticancer agents

MCTs are transmembrane proteins which transport small monocarboxylate compounds such as lactic acid, pyruvic acid and other ketone bodies. MCT4 is overexpressed in many tumors and high MCT4 expression is correlated with poor patient prognosis and therefore, MCT4 is a good therapeutic target for the treatment of cancer. As discussed in the previous chapters, CHC derivatives **3a-3k** and carboxy coumarins **4a-4i** exhibited potent MCT1 inhibition, were well tolerated in mice, and showed anticancer efficacy in various MCT1 expressing tumor models. MCT1 is involved in influx of lactic acid and MCT4 for efflux of lactic acid in cancer cells, and these processes are pH dependent. We envisioned that our synthesized compounds with the doubly activated α,β -unsaturated system could act as MCT4 inhibitor also.

5.1 Evaluation of compounds 3a-3k and 4a-4i for MCT4 inhibition in MDA-MB-231 cell line: Results and discussion

We evaluated CHC based *N,N*-dialkyl/diaryl derivatives **3a-3k** and carboxy coumarins **4a-4i** for MCT4 inhibition. For this purpose, we utilized a TNBC cell line MDA-MB-231, which predominantly expresses MCT4 (Figure 2c). Although MCT1 is associated with lactate influx and MCT4 is associated with lactate efflux in cells, in *in vitro* systems, transport of lactate is a reversible process and is highly dependent on the pH of the assay

media and anion gradients. Therefore, high pH (basic) assay media favors lactate influx and low pH (acidic) favors lactate efflux. For this reason, in MCT4 inhibition assay, a low pH assay media (HEPES buffer, pH 7.0) was used to facilitate lactate influx to measure lactate uptake.

All the candidate compounds were evaluated for their MCT4 inhibition properties using this modified ^{14}C lactate uptake assay in MCT4 expressing MDA-MB-231 cell line. CHC derivatives **3a-3k** exhibited excellent inhibitory activity against MCT4 with IC_{50} values in the range of 11-85 nM (Table 5a, Figure 5a).⁸⁸ Similar to MCT1 inhibition, with an increase in the carbon content of alkyl groups from propyl **3a** to pentyl **3d**, the MCT4 IC_{50} values increased from 11 nM to 85 nM. With a branched diisobutyl derivative **3c**, the IC_{50} value was found to be 17 nM, which showed slightly lower potency than its straight chain butyl derivative **3b** which exhibited IC_{50} of 14 nM. With diallyl **3e**, the IC_{50} value was slightly decreased to 28 nM, whereas for dipropargyl **3f**, the IC_{50} value was found to be 50 nM which was less potent compared to other derivatives **3a-3e**. With dibenzyl substitution in **3g**, the IC_{50} value was found to be slightly increased to 32 nM. Cyclic derivatives **3h** and **3i** also showed decreased potency with IC_{50} values of 53 and 58 nM, respectively. The diphenyl derivative **3j** exhibited potent MCT4 inhibition with an IC_{50} value of 23 nM, whereas *o*-allyloxy derivative **3k** exhibited an IC_{50} value of 12 nM. Overall, *N,N*-dialkyl/diaryl *o*-substituted derivatives **3a-3k** exhibited excellent MCT4 inhibition. Compared to the MCT1 and MCT4 IC_{50} values of their parent compound CHC ($\text{IC}_{50} > 150 \mu\text{M}$), **3a-3k** exhibited several thousand-fold greater potencies for MCT4 inhibition. Specificity towards MCT1 or MCT4 inhibition was not observed for these

candidate compounds, and they showed equal potency for both MCT1 and MCT4 inhibitory activity. In most cases, MCT1 inhibition is same as or slightly greater (lower IC_{50}) than MCT4 inhibition.

7-*N,N*-dialkyl carboxy coumarins **4a-4i** did not show exhibit any significant MCT4 inhibition up to a concentration of 1000 nM, except for the lead candidate compound **4g**, which showed MCT4 inhibition with an IC_{50} of ~200 nM. These results suggest that 7-*N,N*-dibenzyl carboxy coumarin **4g** selectively inhibits MCT1 over MCT4.

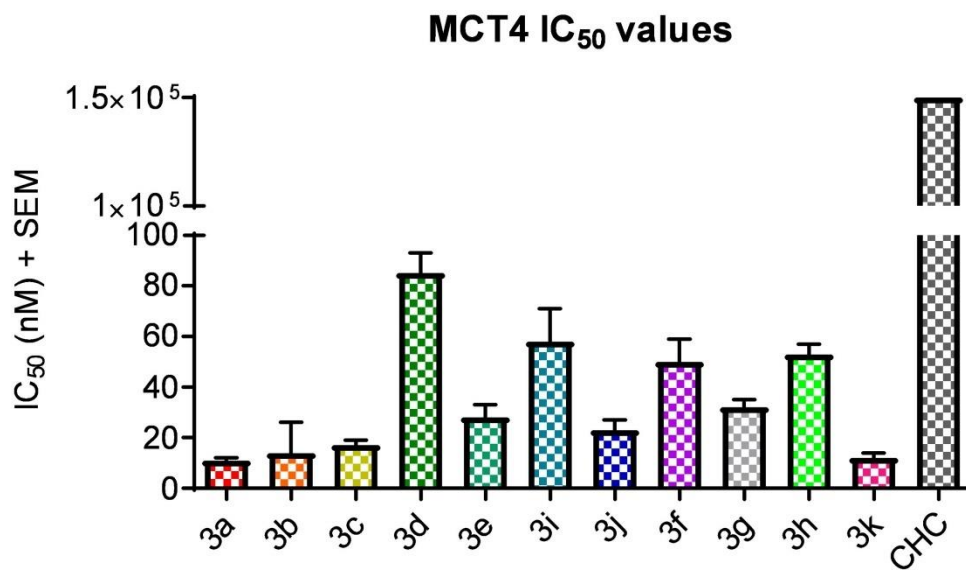
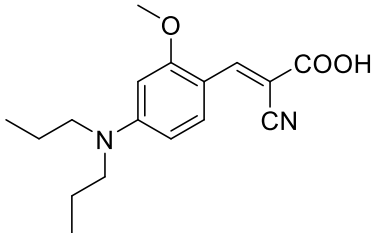
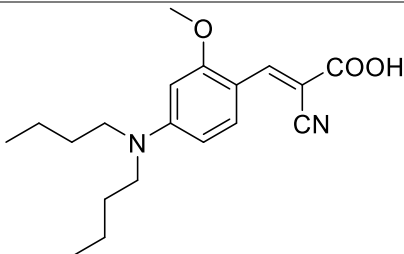
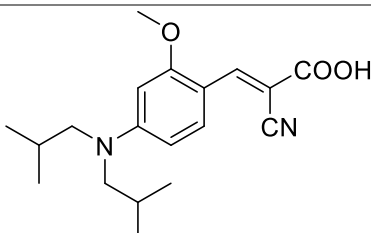
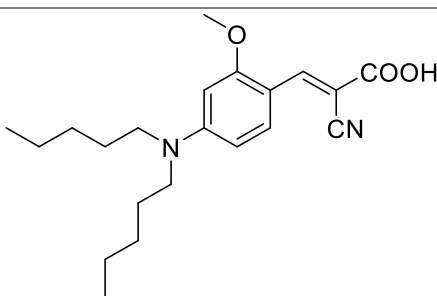
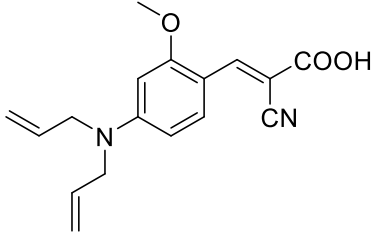
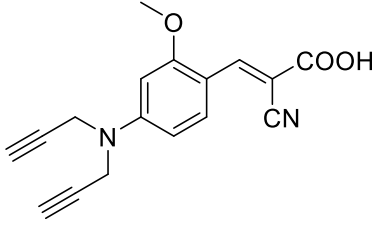
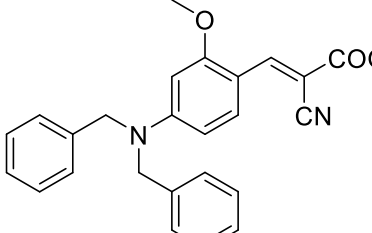
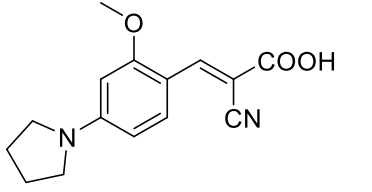
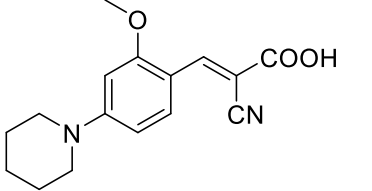
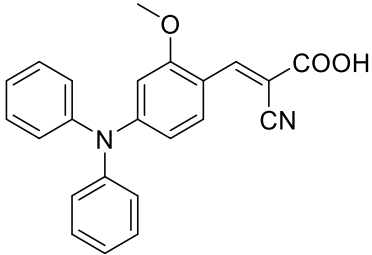


Figure 5a: MCT4 IC₅₀ (nM)* of *N,N*-dialkyl/diaryl *o*-methoxy CHC derivatives **3a-3k** in MDA-MB-231 cell line

Table 5a: MCT4 IC₅₀ (nM)* of *N,N*-dialkyl/diaryl *o*-methoxy CHC derivatives **3a-3k** in MDA-MB-231 cell line

Sl. No.	Compound	MCT4 IC ₅₀
3a		11±1
3b		14±2
3c		17±2
3d		85±8

3e		28±5
3f		50±9
3g		32±3
3h		53±4
3i		58±13
3j		23±4

3k		12±2
4g		202±47

* average±sem of minimum three independent experiments

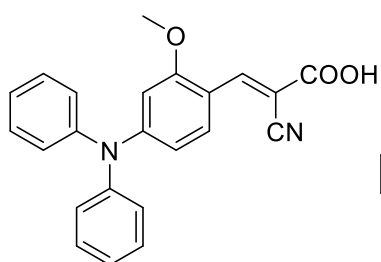
MCT4 inhibition studies revealed that *N,N*-dialkyl/diaryl compounds **3a-3k** exhibited low nanomolar potency in MCT4 expressing MDA-MB-231 cell line. These compounds did not show any selectivity towards MCT4 inhibition when compared to their MCT1 IC₅₀ values. In most of the cases, candidate compounds were equipotent towards MCT1 and MCT4 inhibition, and in few cases, these compounds were slightly more potent towards MCT1 inhibition. Although MCT4 is primarily involved in the efflux of lactic acid, depending on the intracellular and extracellular pH, MCT4 could also lead to the influx of lactic acid. Hence, *N,N*-dialkyl/diaryl CHC compounds acted as bidirectional-transporter inhibitors based on the results of MCT1 and MCT4 IC₅₀ values. The presence of doubly activated α,β -unsaturated system in cyanoacrylic acid unit with lower steric factors facilitate optimal interactions with both MCT1 and MCT4 transporter proteins and inhibit the activity of these transporters. Homology modeling and computational docking

studies on MCT1 and MCT4 using compound **3j** also revealed that there was no difference in the docking position of lead compound **3j** on MCT1 and MCT4. This study also showed that the phenyl rings of compound **3j** interact with hydrophobic residues of MCT1 and MCT4 and the polar groups on **3j** potentially interact with polar amino acid residues via hydrogen bond formation. These studies explain the dual selectivity of the lead compound **3j** for MCT1 and MCT4 inhibition.

In contrast, most of the 7-*N,N*-dialkyl/diaryl 3-carboxy coumarins did not show MCT4 inhibition up to 1000 nM concentration, except for the dibenzyl derivative **4g**, which exhibited an IC_{50} value of ~200 nM. Thus, coumarin derivatives **4a-4i** could be considered as selective inhibitors of MCT1. It is quite possible that the combination of lower electrophilic capacity of doubly activated α,β -unsaturated system and higher sterics of bicyclic coumarin moiety could interfere with the interactions of these compounds with transporter proteins.

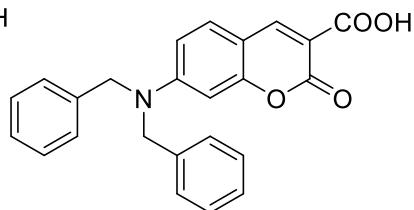
5.2 Effect of lead compounds 3j and 4g on glycolysis and mitochondrial OxPhos

Since, influx and efflux of lactic acid and other ketone bodies via MCTs could have direct or indirect impact on rate of glycolysis and mitochondrial OxPhos, we evaluated the ability of CHC based *N,N*-dialkyl/diaryl compounds for their effect on these parameters. For this purpose, we compared dual MCT1 and MCT4 inhibitor **3j** with predominantly MCT1 inhibitor **4g**, as well as with parent CHC compound, and a known specific MCT1 inhibitor, AZD3965 (Figure 5b). We evaluated glycolysis stress test (GST) and mitochondrial stress test (MST) parameters to understand the effects on these compounds on glycolysis and mitochondrial OxPhos. Seahorse XFe96 extracellular flux analyzer was used to carry out GST and MST. This instrument records the changes in extracellular acidification rate (ECAR) and mitochondrial oxygen consumption rate (OCR) in real time, which are key indicators of glycolysis and mitochondrial respiration, respectively. The flux plate has 96-wells and the cartridge plate consists of four drug delivery ports and optical sensors that record ECAR in mpH/minute and OCR in pmol/minute.



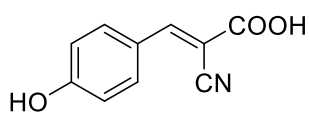
3j

MCT1 IC_{50} = 6 nM
MCT4 IC_{50} = 23 nM



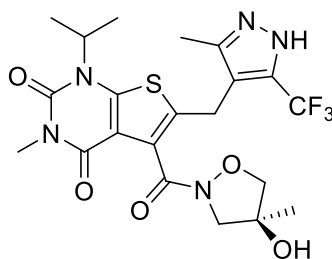
4g

MCT1 IC_{50} = 57 nM
MCT4 IC_{50} = ~200 nM



CHC

MCT1 IC_{50} = >100 μ M
MCT4 IC_{50} = >100 μ M



AZD3965 (AZD)

MCT1 IC_{50} = 5-10 nM
MCT4 IC_{50} = no activity

Figure 5b: Lead compounds evaluated for extracellular flux analysis using Seahorse XFe96 based GST and MST

5.2.1 Glycolysis stress test in MDA-MB-231 and WiDr cell lines using 3j and 4g

GST parameters that we studied included glycolysis, glycolytic capacity and glycolytic reserve. In this assay, glycolysis is defined as an increase in the ECAR due to the addition of saturated concentration of glucose in the second drug delivery port after the addition of test compound in the first drug delivery port. If the compound inhibits glycolysis, the ECAR recorded in real time should be less when compared to the control. The third drug delivery port is injected with ATP synthase inhibitor oligomycin A, and this addition leads to a decreased mitochondrial ATP production and consequently, the cells are under stress and redirect the energy generation towards glycolytic pathway. As a result, ECAR drastically increases in the control wells. The maximum increase in the ECAR when compared to glycolysis is defined as glycolytic capacity. When OxPhos is inhibited by oligomycin A, all the energy needs are driven towards glycolysis. In hypoxic conditions, when OxPhos is minimum, this stage could be considered as vigorous glycolysis. The final drug delivery port is injected with glycolysis inhibitor 2-deoxy-glucose. With this addition, ECAR is reduced to basal levels and the difference between glycolysis and glycolytic capacity can be defined as glycolytic reserve, which indicates the flexibility of cells to overcome stressful conditions.

At 10 μM concentration, compounds **3j**, **4g**, CHC and AZD slightly decreased or had no effect on glycolysis in MCT4 expressing MDA-MB-231 cell line (Figures 5c-A and 5e-A). In the case of MCT1 expressing WiDr cell line all the candidate compounds had practically no effect on glycolysis at 10 μM concentration (Figures 5d-A and 5e-C). At 30 μM concentration, only compounds **3j** and **4g** exhibited a decrease in glycolysis as evidenced by low ECAR compared to the control in MDA-MB-231 cells (Figures 5c-B and 5e-B). In the case of WiDr cells, compound **3j** showed a slight decrease in glycolysis compared to control, but compared to CHC and AZD, **3j** exhibited a significant decrease in glycolysis (Figures 5d-B and 5e-D). Similarly, coumarin **4g** also showed a significant inhibition of glycolysis compared to CHC and AZD compounds. As CHC is a weak MCT1 and MCT4 inhibitor, this compound did not inhibit glycolysis even at a high concentration of 30 μM . MCT1 specific inhibitor AZD did not affect glycolysis in MCT4 expressing MDA-MB-231 cell line and showed an increased glycolysis in WiDr cell line.

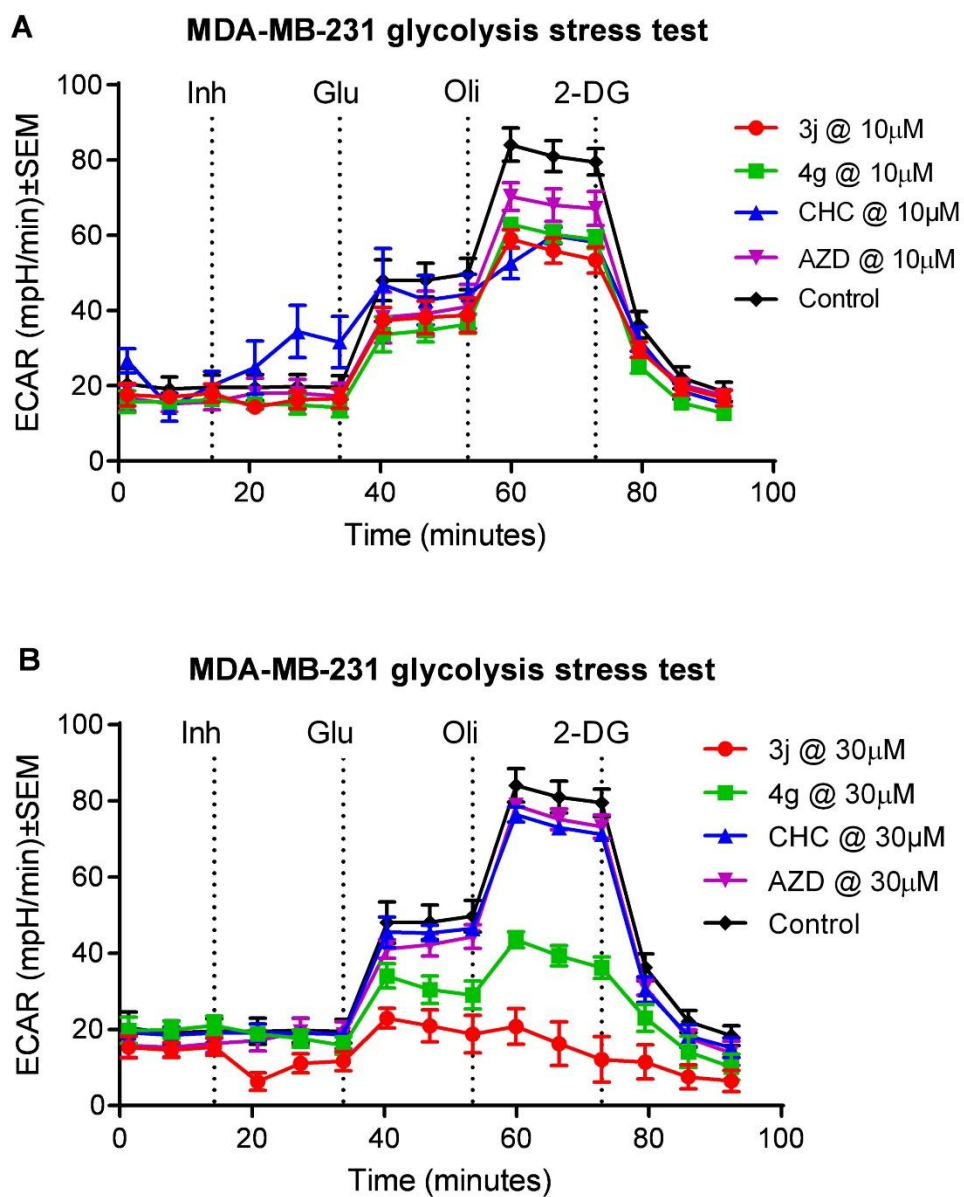


Figure 5c: Glycolysis stress test profiles in MDA-MB-231 cell line using compound 3j, 4g, CHC and AZD3965 at (A) 10 and (B) 30 μ M concentrations

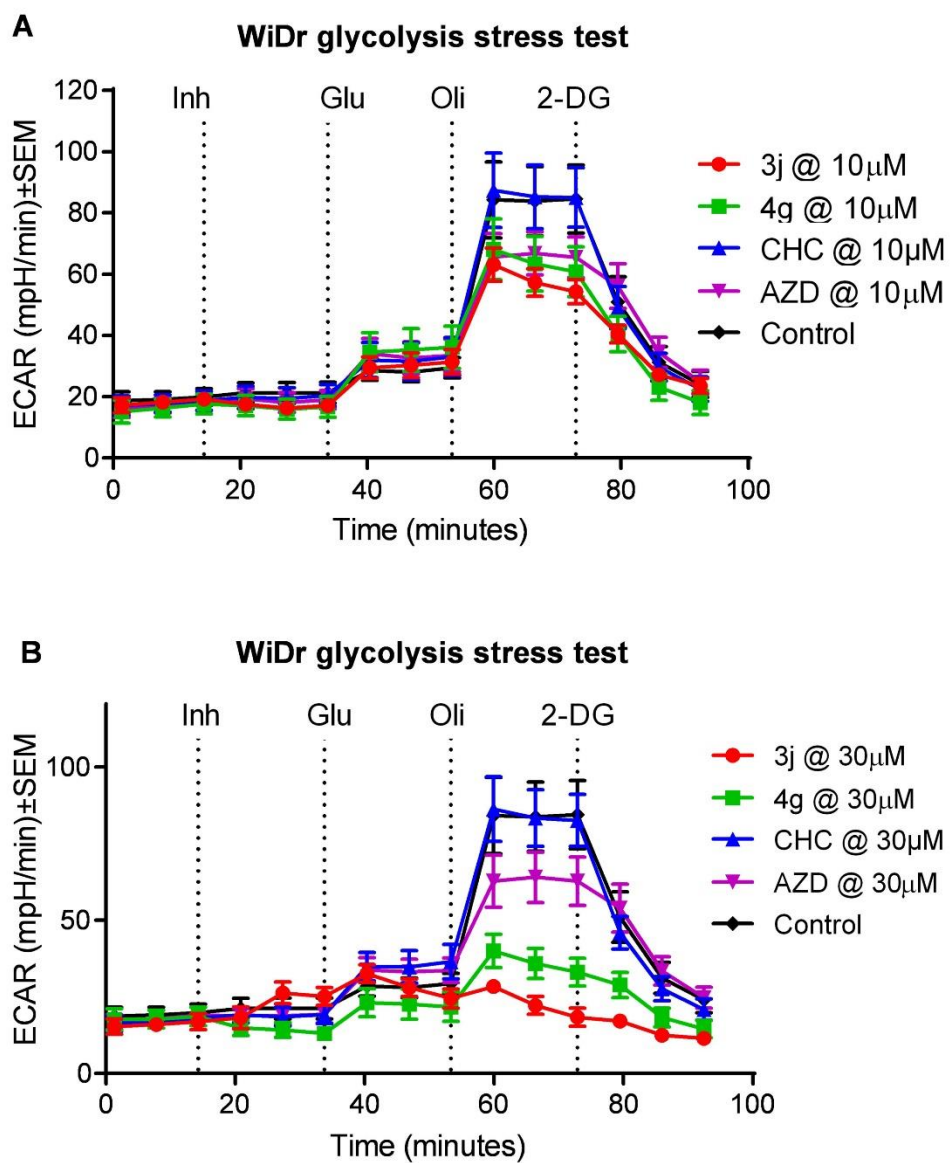


Figure 5d: Glycolysis stress test profiles in WiDr cell line using compound 3j, 4g, CHC and AZD3965 at (A) 10 and (B) 30 μ M concentrations

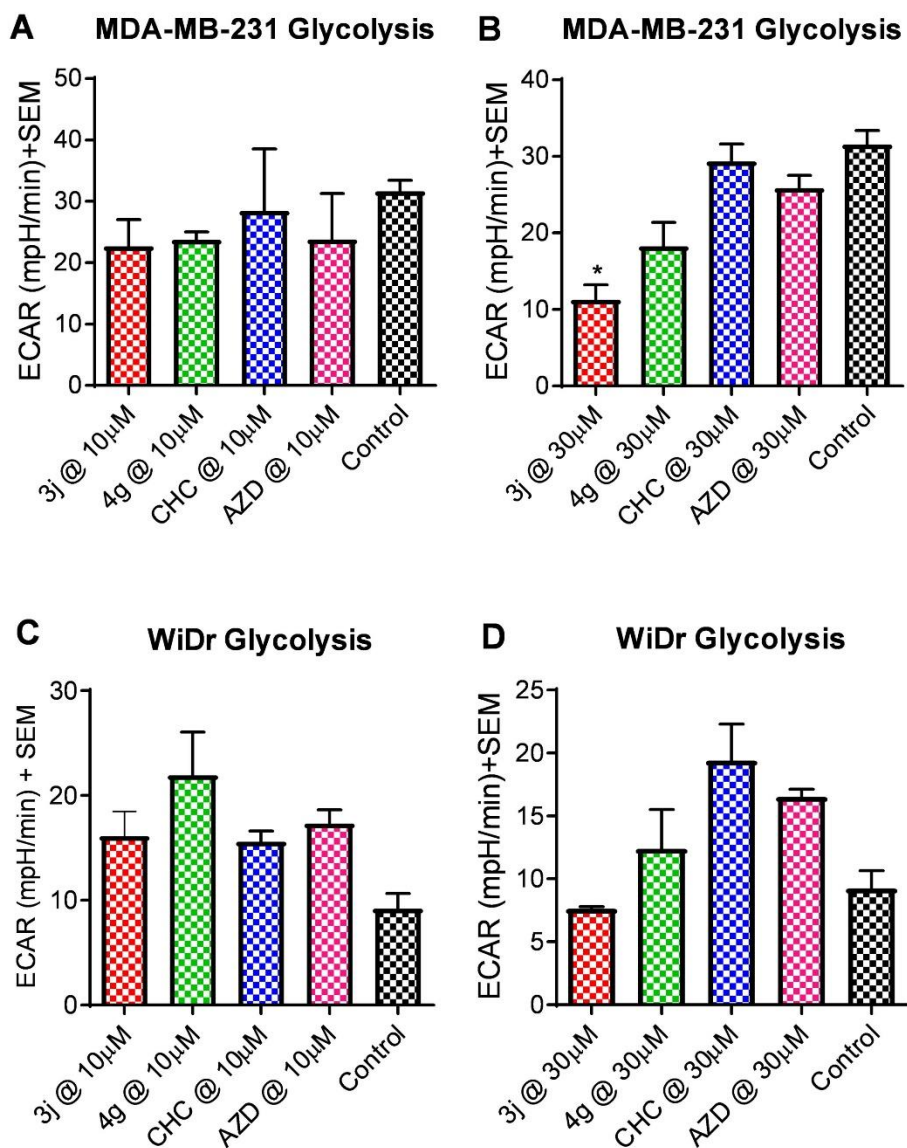


Figure 5e: Effect of compounds **3j**, **4g**, CHC and AZD on glycolysis in (A) MDA-MB-231 cell line at 10 μ M concentration; (B) MDA-MB-231 cell line at 30 μ M concentration; In (C) WiDr cell line at 10 μ M concentration and (D) WiDr cell line at 30 μ M concentration. The values are generated using wave software, and an average \pm SEM of minimum three independent experiments were calculated.

In the case of glycolytic capacity, at 10 μ M concentration, candidate compounds **3j** and **4g** exhibited significant inhibition compared to that of control, whereas CHC and AZD showed a slight decrease in the glycolytic capacity in MDA-MB-231 cell line (Figure 5f-A). At 30 μ M concentration, compounds **3j** and **4g** showed significant decrease in glycolytic capacity (Figure 5f-B). In the case of CHC and AZD, the effect on glycolytic capacity at 10 and 30 μ M concentration was similar. In WiDr cell line, at 10 μ M concentration, compounds **3j**, **4g** and AZD exhibited significant reduction of glycolytic capacity, whereas CHC did not have any effect on glycolytic capacity (Figure 5f-C). At 30 μ M concentration, compounds **3j** and **4g** exhibited significant decrease in glycolytic capacity (Figure 5f-D). Although AZD exhibited significant inhibition, compounds **3j** and **4g** were found to be superior to AZD in reducing glycolytic capacity. As expected, AZD, being a specific inhibitor of MCT1, showed efficacy in glycolysis inhibition in MCT1 expressing WiDr cell line, compared to MCT4 expressing MDA-MB-231 cell line.

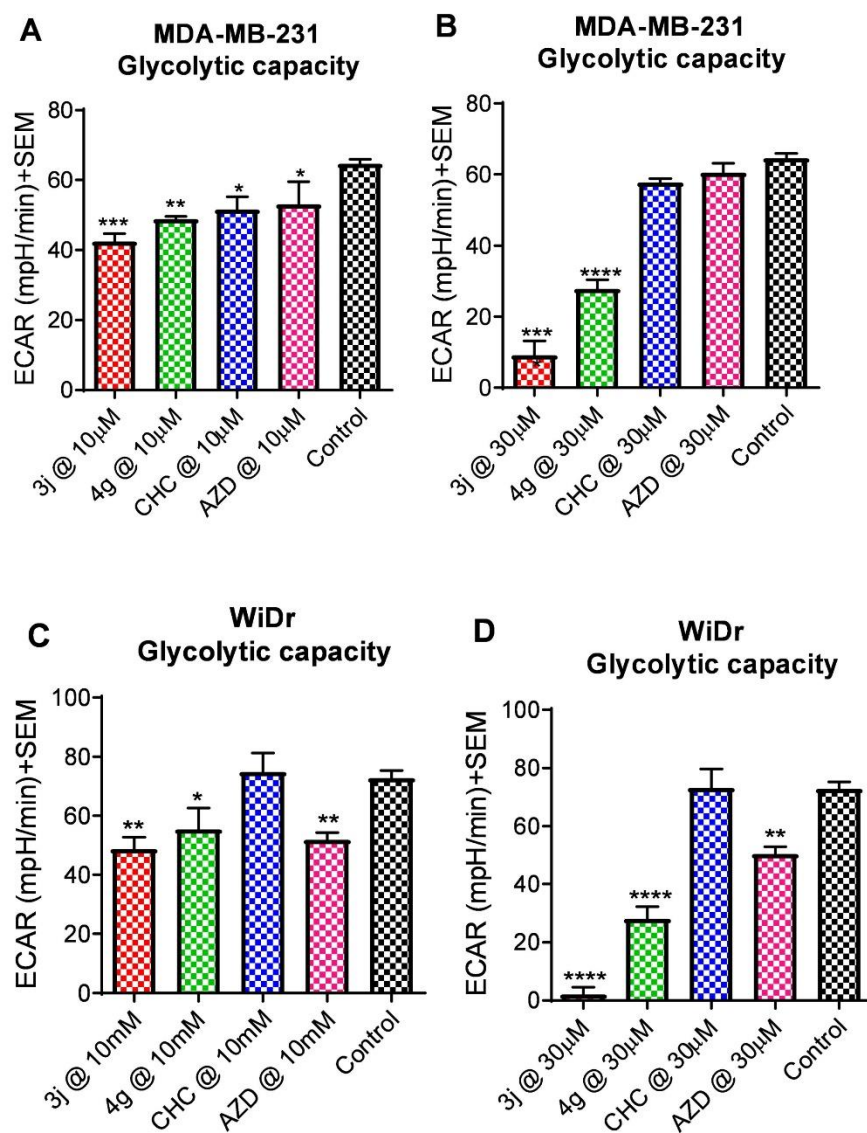


Figure 5f: Effect of compounds **3j**, **4g**, CHC and AZD on glycolytic capacity in (A) MDA-MB-231 cell line at 10 μ M concentration; (B) MDA-MB-231 cell line at 30 μ M concentration; In (C) WiDr cell line at 10 μ M concentration and (D) WiDr cell line at 30 μ M concentration. The values are generated using wave software, and an average \pm SEM of minimum three independent experiments were calculated.

Although compounds **3j**, **4g**, CHC and AZD did not affect glycolytic reserve at 10 μM concentration in MDA-MB-231 cell line, compounds **3j** and **4g** exhibited significant decrease in glycolytic reserve at 30 μM concentration (Figures 5g-A and 5g-B). As expected, MCT1 specific inhibitor AZD did not show any effect on glycolytic reserve in this cell line. In MCT1 expressing WiDr cell line, compounds **3j**, **4g** and AZD showed significant reduction in glycolytic reserve at both 10 and 30 μM concentrations. In contrast, CHC exhibited activity only at 30 μM concentration (Figure 5g-C and 5g-D).

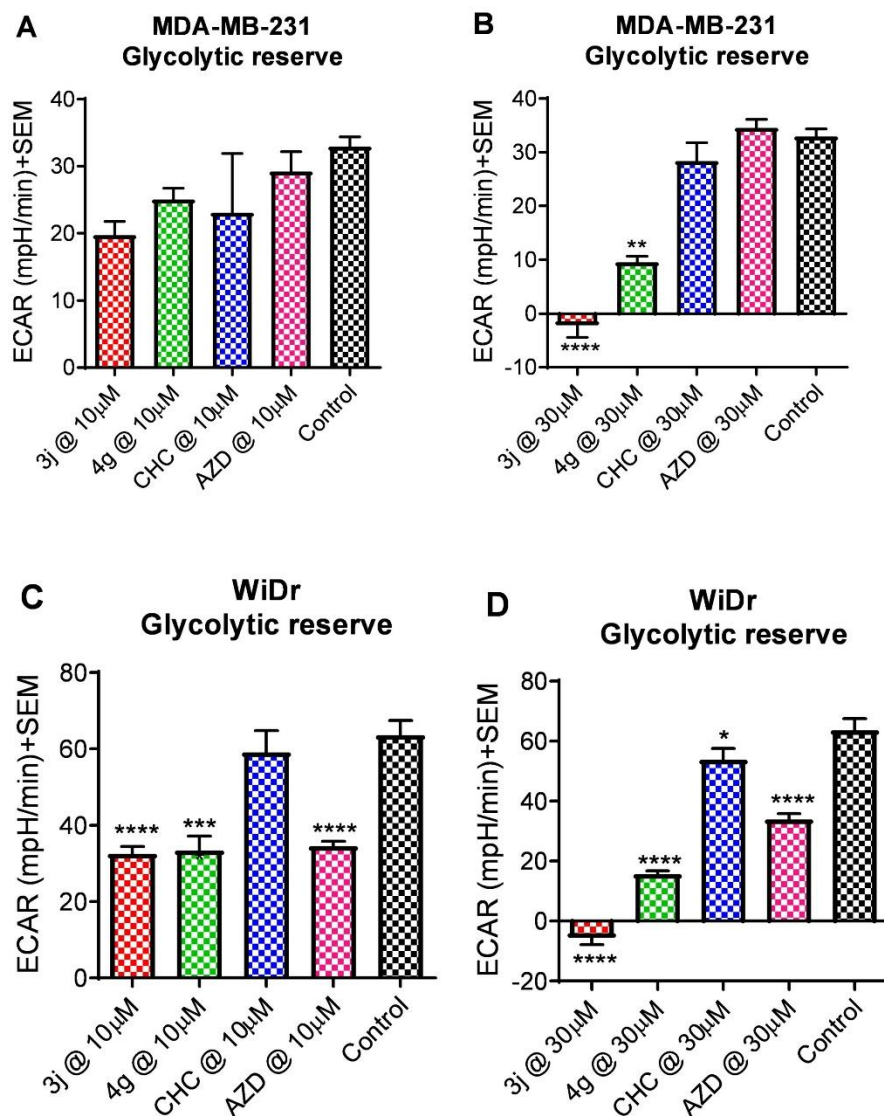


Figure 5g: Effect of compounds **3j**, **4g**, CHC and AZD on glycolytic reserve in (A) MDA-MB-231 cell line at 10 μ M concentration; (B) MDA-MB-231 cell line at 30 μ M concentration; In (C) WiDr cell line at 10 μ M concentration and (D) WiDr cell line at 30 μ M concentration. The values are generated using wave software, and an average \pm SEM of minimum three independent experiments were calculated.

5.2.2 Glycolysis stress test in 4T1 cell line using 3j and 4g

We also evaluated GST parameters of CHC based lead derivative **3j** and coumarin based lead candidate **4g** in MCT1 expressing 4T1 cell line. These compounds were tested at 30 μ M concentration because at this concentration, significant inhibition of GST parameters was observed in WiDr cell line. This study revealed that glycolysis, glycolytic capacity and glycolytic reserve were significantly decreased in the presence of 30 μ M of **3j** and **4g** (Figures 5h-A-D). These results are not surprising as both these candidate compounds exhibit potent MCT1 inhibition, thereby reducing the ECAR in this cell line.

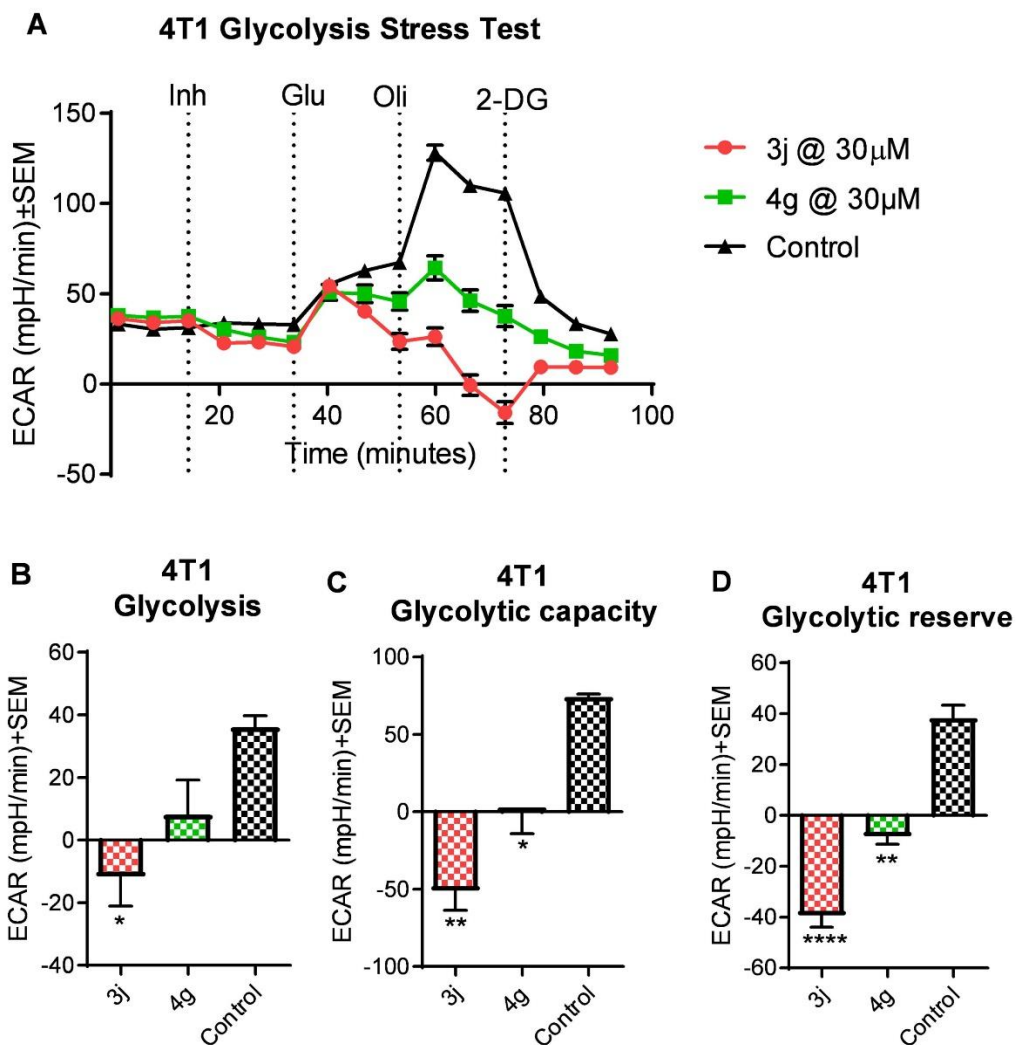


Figure 5h: Glycolysis stress test of compounds **3j** and **4g** in 4T1 cell line (A) Glycolysis stress test profile; (B) Effect of compounds **3j** and **4g** on glycolysis; (C) Effect of compounds **3j** and **4g** on glycolytic capacity; (D) Effect of compounds **3j** and **4g** on glycolytic reserve. The values are generated using wave software, and an average+SEM of minimum three independent experiments were calculated.

5.2.3 Mitochondrial stress test in MDA-MB-231 and WiDr cell lines using 3j and 4g

Because of the presence of lipophilic groups, the candidate compounds may cross the cell membrane, enter the cytoplasm, interact directly or indirectly and alter the mitochondrial function. To evaluate the effects of these candidate compounds, we studied the MST parameters such as maximal respiration, ATP production, proton leak and spare respiratory capacity. MST targets various electron transport chain components such as ATP synthase, ETC complexes I, III and V. After the addition of test compound via first drug delivery port, ATP synthase inhibitor oligomycin A was added through second drug delivery port. This decrease in the OCR after the addition of oligomycin constitutes ATP-linked respiration and considered to be ATP production. The basal OCR after the inhibition of ATP production is considered to be proton leak. Here, ATP production and proton leak are complementary to each other. An increase in the ATP production leads to a decrease in proton leak, and vice-versa.

The addition of a proton uncoupler 2-[[4-(trifluoromethoxy)phenyl]hydrazinylidene]propanedinitril (FCCP) in the third drug delivery port leads to the stress of the cells as FCCP disrupts the ATP synthesis by hindering the entry of protons into mitochondrial membrane and redirecting them out of the membrane. As a result, the cells have an urgent need to overcome energy demands and operates at a high capacity by oxidizing other substrates such as fatty acids, amino acids, etc. to produce ATP. This process, in fact, increases OCR significantly and the cell achieves maximum possible respiration. This increase in the OCR is considered as maximum respiration. The flexibility

of the cells to adapt to these stressful conditions to produce maximum energy is called spare respiratory capacity, which can be calculated by the difference between the value of OCR at first injection and the value of maximum OCR. The fourth drug delivery port is injected with a cocktail of rotenone and antimycin-A, which inhibit ETC complexes I and III, respectively. This results in a complete shutdown of respiration and leads to a minimal OCR, which can be considered as non-mitochondrial respiration.

From these studies, CHC derivative **3j** and coumarin compound **4g** decreased OCR at 10 and 30 μM concentrations in both MCT4 expressing MDA-MB-231 and MCT1 expressing WiDr cell lines (Figures 5i-A-B and 5j-A-B). In MDA-MB-231 cell line, all of the test compounds did not exhibit any effect on maximal respiration at 10 μM concentration, whereas compounds **3j** and **4g** showed a significant reduction in maximal respiration at 30 μM concentration (Figures 5k-A and 5k-B). In WiDr cell line, compounds **3j** and **4g** significantly decreased maximal respiration at both 10 and 30 μM concentrations (Figures 5k-C and 5k-D). Again, in this case also, CHC did not show any effect on maximal respiration as it is a weak MCT1 and MCT4 inhibitor. AZD being a specific MCT1 inhibitor, did not affect maximal respiration in both the cell lines even at 30 μM concentration.

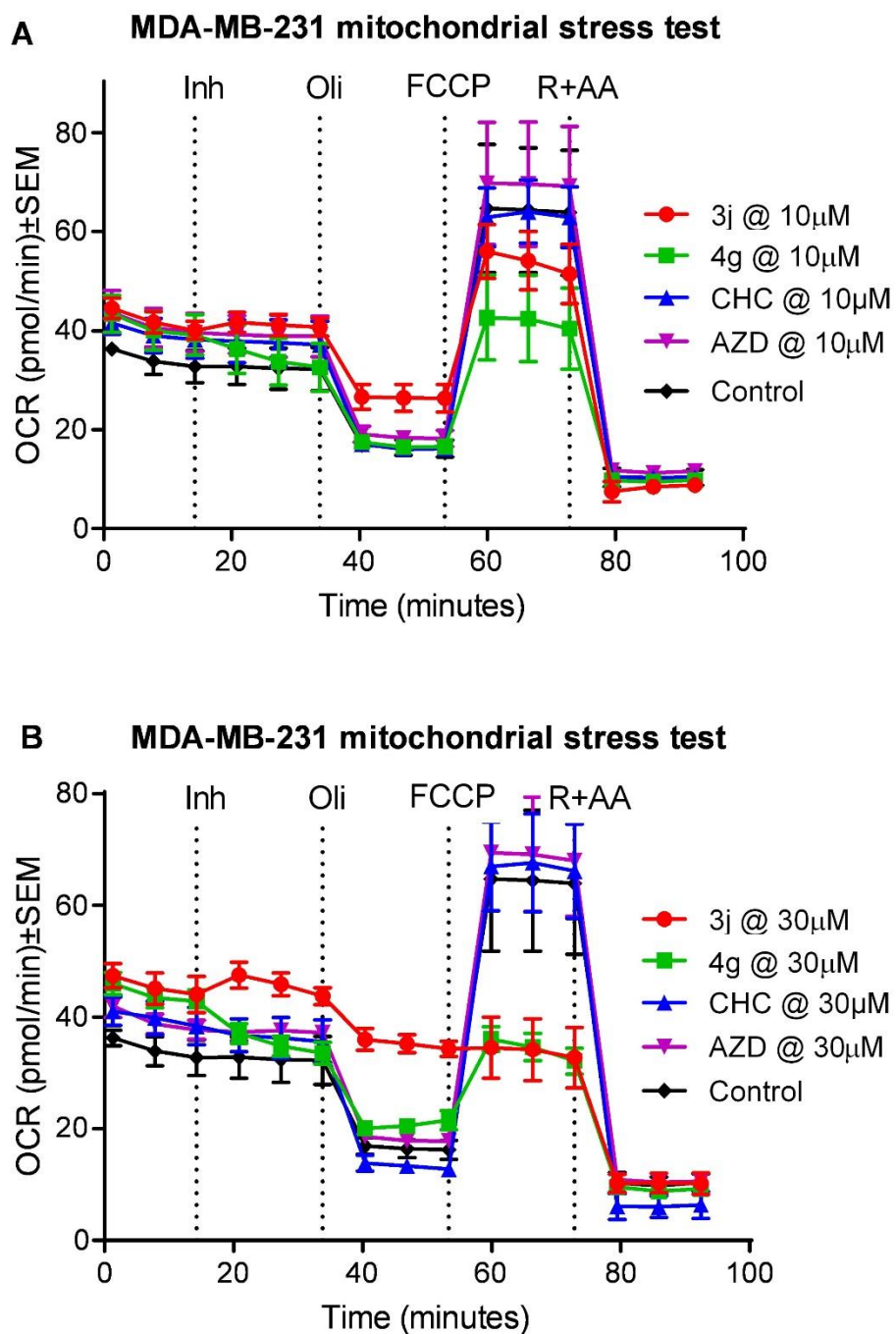


Figure 5i: Mitochondrial stress test profiles in MDA-MB-231 cell line using compound 3j, 4g, CHC and AZD3965 at (A) 10 and (B) 30 μ M concentrations

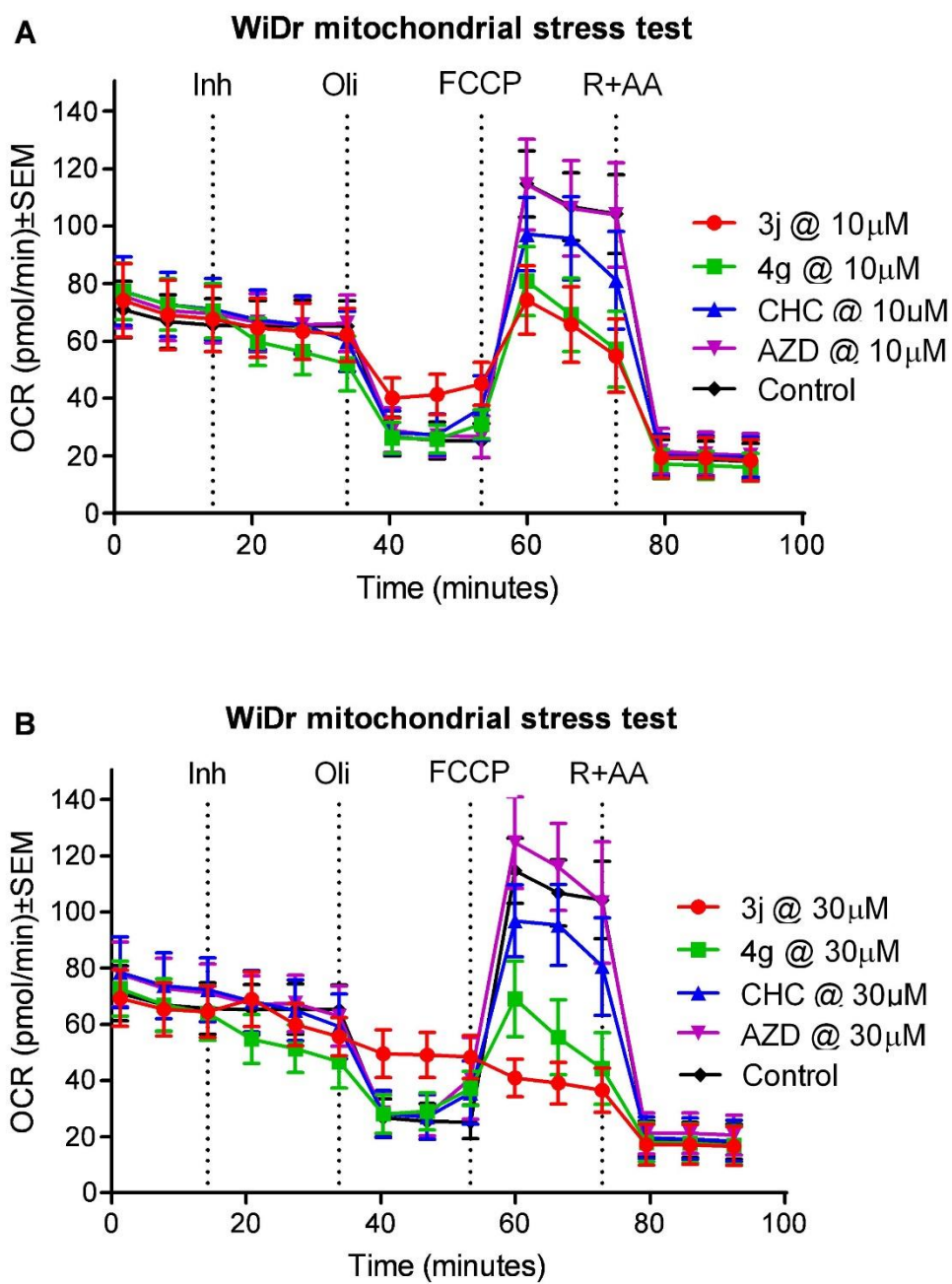


Figure 5j: Mitochondrial stress test profiles in WiDr cell line using compound 3j, 4g, CHC and AZD3965 at (A) 10 and (B) 30 μ M concentrations

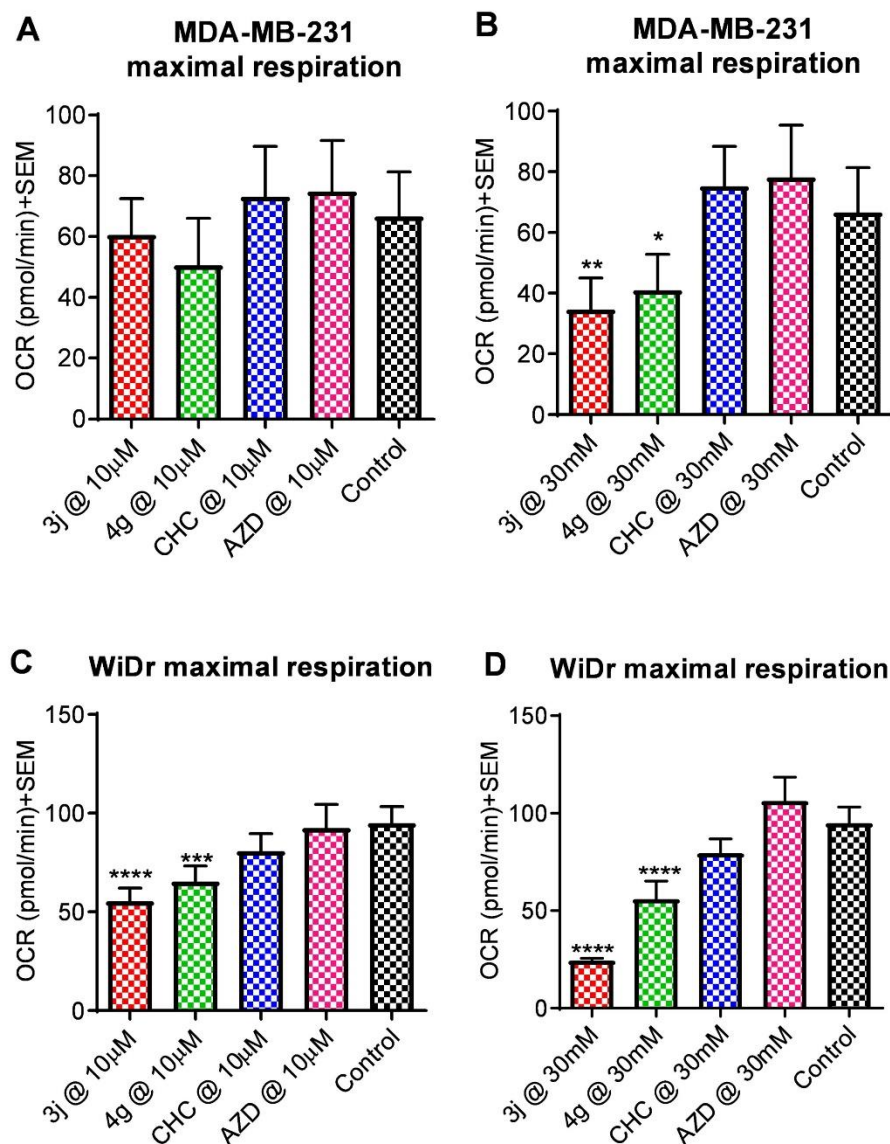


Figure 5k: Effect of compounds **3j**, **4g**, CHC and AZD on maximal respiration in (A) MDA-MB-231 cell line at 10 μ M concentration; (B) MDA-MB-231 cell line at 30 μ M concentration; In (C) WiDr cell line at 10 μ M concentration and (D) WiDr cell line at 30 μ M concentration. The values are generated using wave software, and an average \pm SEM of minimum three independent experiments were calculated.

In MDA-MB-231 cell line, the test compounds **3j**, **4g**, CHC and AZD did not decrease ATP production at 10 μ M concentration, whereas compound **3j** significantly decreased ATP production at 30 μ M concentration (Figures 51-A and 51-B). Similarly, in WiDr cell line, only compound **3j** exhibited a significant decrease in ATP production at 10 and 30 μ M concentrations, whereas coumarin **4g** decreased ATP production only at 30 μ M concentration (Figures 51-C and 51-D). CHC and AZD did not affect ATP production at both concentrations in MDA-MB-231 and WiDr cell lines.

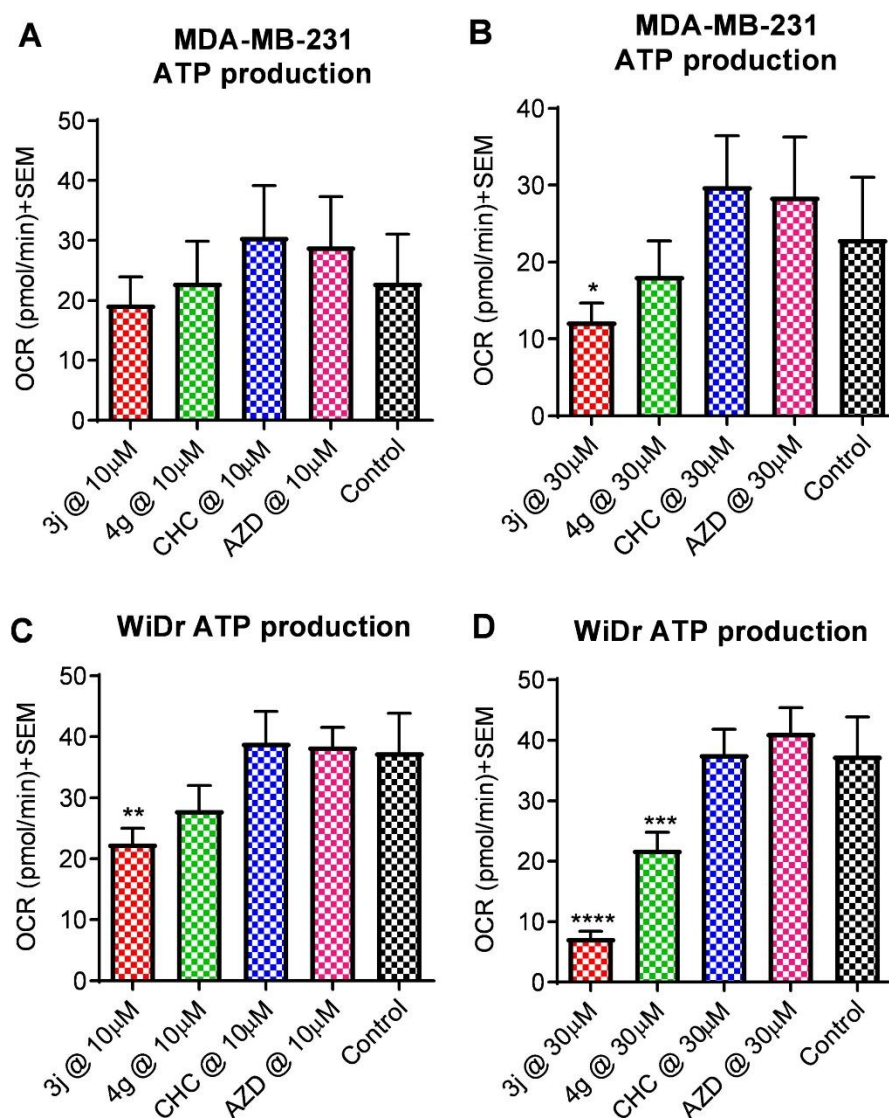


Figure 5I: Effect of compounds **3j**, **4g**, CHC and AZD on ATP production in (A) MDA-MB-231 cell line at 10 μ M concentration; (B) MDA-MB-231 cell line at 30 μ M concentration; In (C) WiDr cell line at 10 μ M concentration and (D) WiDr cell line at 30 μ M concentration. The values are generated using wave software, and an average \pm SEM of minimum three independent experiments were calculated.

While proton leak is significantly increased in both the cell lines at 10 and 30 μM concentrations using compound **3j**, the other compounds **4g**, CHC and AZD did not show any effect on proton leak (Figures 5m-A-D). These results indicate that while decreasing ATP production, proton leak is not affected, hence, the compound **3j** could be considered as proton uncoupler.

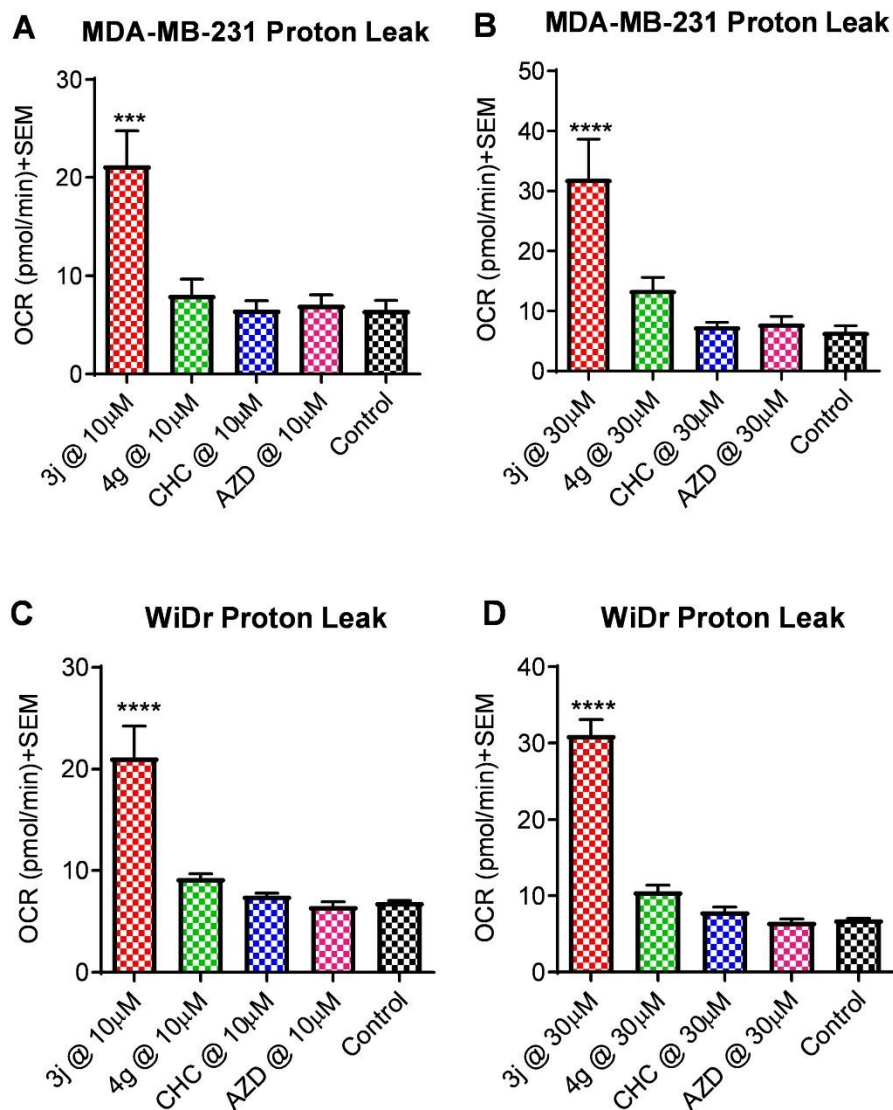


Figure 5m: Effect of compounds **3j**, **4g**, CHC and AZD on proton leak in (A) MDA-MB-231 cell line at 10 μ M concentration; (B) MDA-MB-231 cell line at 30 μ M concentration; In (C) WiDr cell line at 10 μ M concentration and (D) WiDr cell line at 30 μ M concentration. The values are generated using wave software, and an average \pm SEM of minimum three independent experiments were calculated.

In MDA-MB-231 cell line, compounds **3j** and **4g** reduced spare respiratory capacity at 10 and 30 μ M concentrations, whereas compounds CHC and AZD did not affect this parameter (Figures 5n-A-D). In the case of MCT1 expressing WiDr cell line, compounds **3j**, **4g** and CHC significantly decreased spare respiratory capacity.

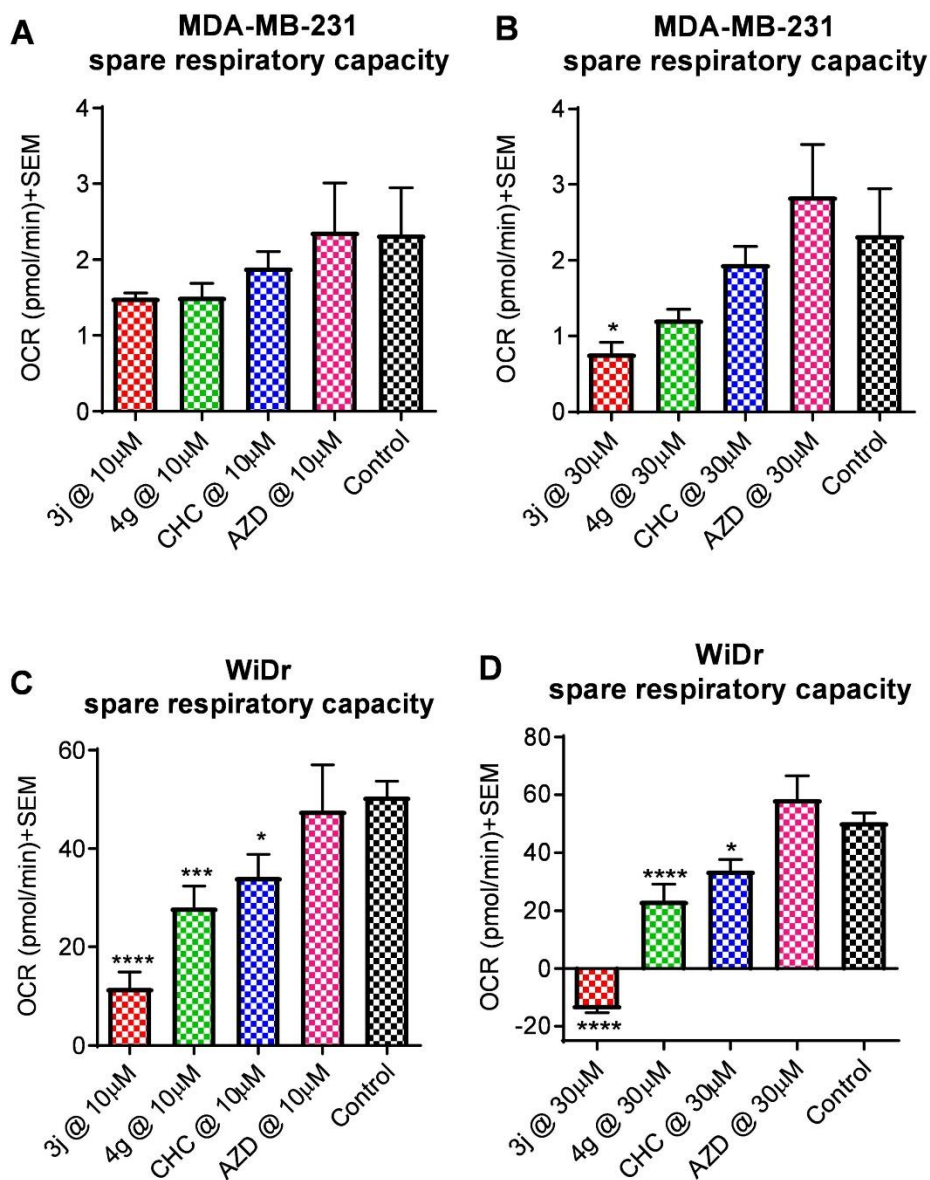


Figure 5n: Effect of compounds **3j**, **4g**, CHC and AZD on spare respiratory capacity in (A) MDA-MB-231 cell line at 10 μ M concentration; (B) MDA-MB-231 cell line at 30 μ M concentration; In (C) WiDr cell line at 10 μ M concentration and (D) WiDr cell line at 30 μ M concentration. The values are generated using wave software, and an average \pm SEM of minimum three independent experiments were calculated.

5.2.4 Mitochondrial stress test in 4T1 cell line using 3j

We also evaluated MST parameters of CHC based lead derivative **3j** in MCT1 expressing 4T1 cell line. This study revealed that maximal respiration, ATP production and spare respiratory capacity were significantly decreased in the presence of 30 μ M of **3j** compared to the control wells (Figures 5o-A-C and 5o-E). In this cell line, proton leak was found to be significantly increased, reiterating that the compound **3j** acts as a proton uncoupler (Figure 5o-D).

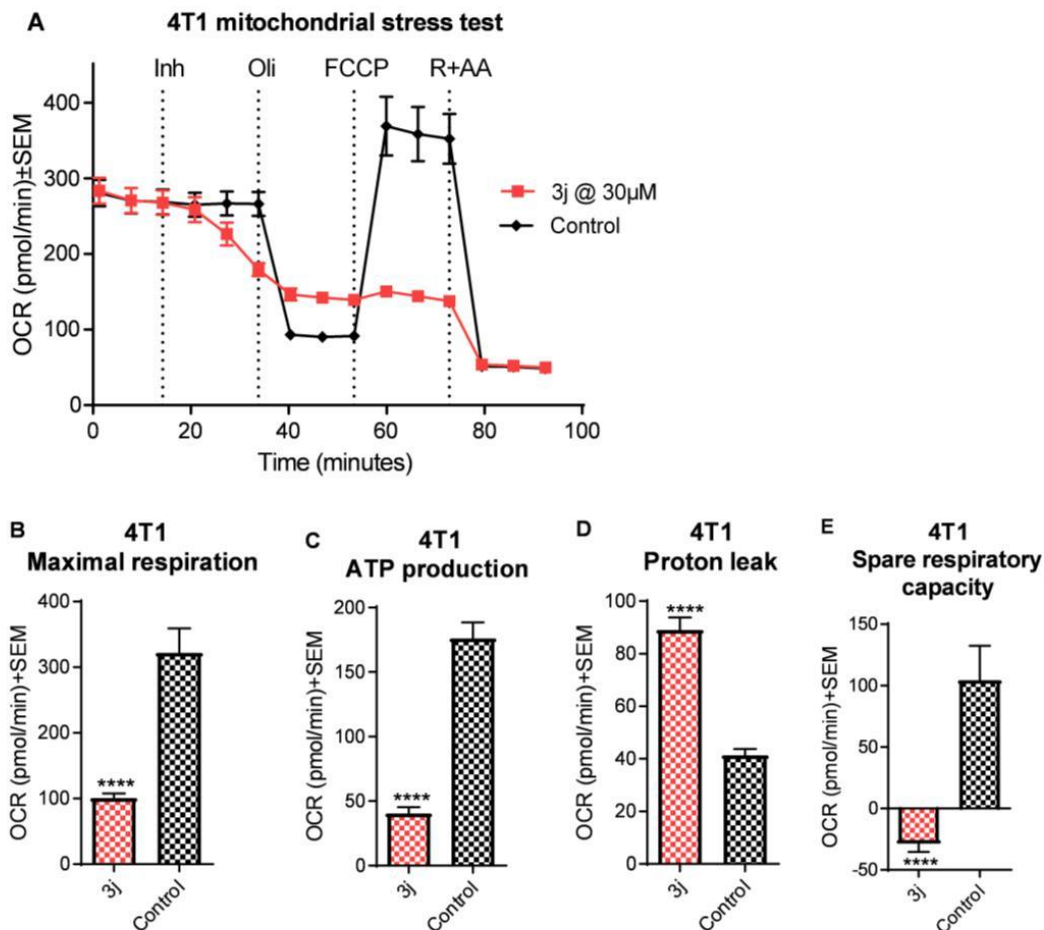


Figure 5o: Mitochondrial stress test of compound **3j** in 4T1 cell line (A) Mitochondrial stress test profile; (B) Effect of compound **3j** on maximal respiration; (C) Effect of compound **3j** on ATP production; (D) Effect of compound **3j** on proton leak; (E). Effect of compound **3j** on spare respiratory capacity. The values are generated using wave software, and an average+SEM of minimum three independent experiments were calculated.

5.2.5 Glycolysis stress test in MDA-MB-231 and WiDr cell lines using **3b** and **3j**

We also compared the GST parameters of *N,N*-diphenyl substituted derivative **3j** with an *N,N*-dibutyl substituted derivative **3b** in MCT4 expressing MDA-MB-231 and MCT1 expressing WiDr cell lines. These compounds were tested at both 10 and 30 μ M concentrations. At 10 μ M concentration, both **3b** and **3j** did not decrease glycolysis in both the cell lines (Figures 5p-A, 5p-B, 5q-A and 5q-B). At 30 μ M concentration, only compound **3j** exhibited a decrease in glycolysis in MDA-MB-231 cells (Figure 5p-B). In the case of WiDr cells, compound **3j** showed a significant decrease in glycolysis compared to control wells (Figure 5q-B). In the case of glycolytic capacity, compound **3j** showed significant inhibition at 10 and 30 μ M concentrations whereas compound **3b** inhibited only at 30 μ M concentration in MDA-MB-231 cell line (Figure 5p-C). Also, both compounds exhibited significant reduction in glycolytic reserve in MDA-MB-231 cell line (Figure 5p-D). In WiDr cell line, glycolytic capacity and glycolytic reserve were significantly reduced by both the compounds at both the concentrations (Figures 5q-D).

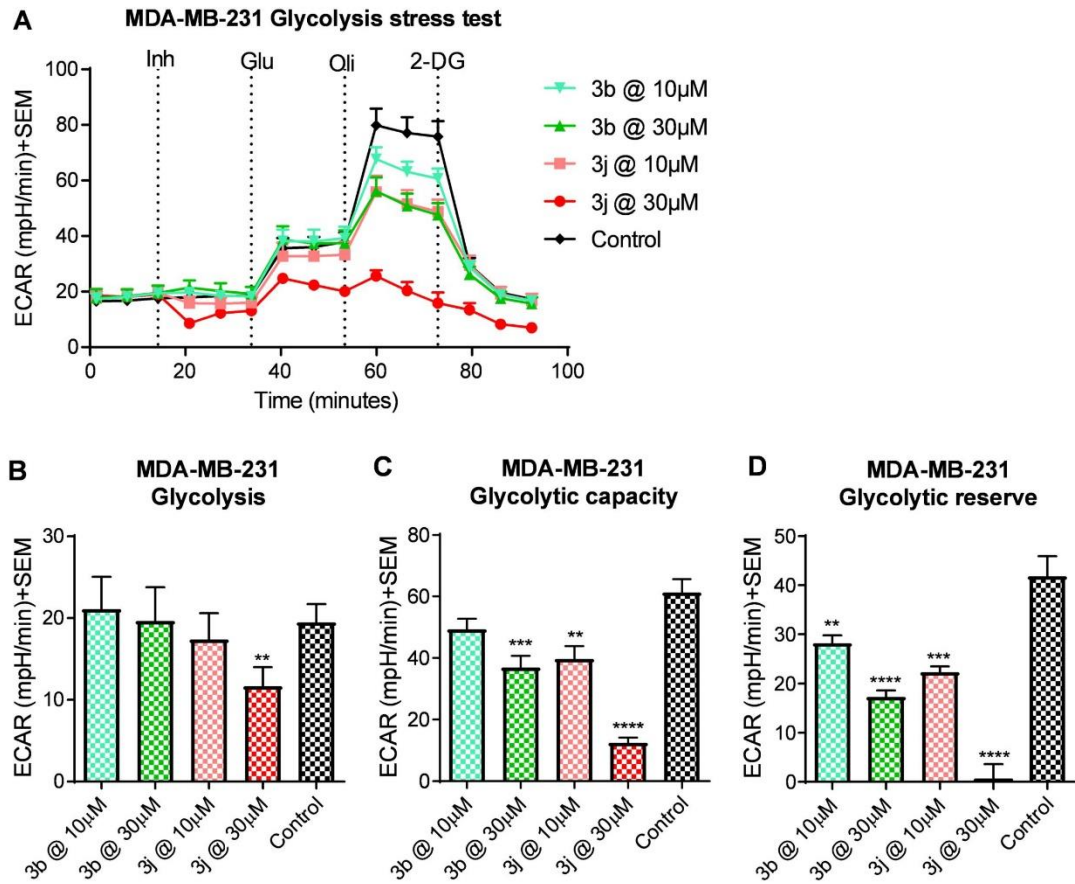


Figure 5p: Glycolysis stress test of compounds **3b** and **3j** in MDA-MB-231 cell line (A) Glycolysis stress test profile; (B) Effect of compounds **3b** and **3j** on glycolysis; (C) Effect of compounds **3b** and **3j** on glycolytic capacity; (D) Effect of compounds **3b** and **3j** on glycolytic reserve. The values are generated using wave software, and an average+SEM of minimum three independent experiments were calculated.

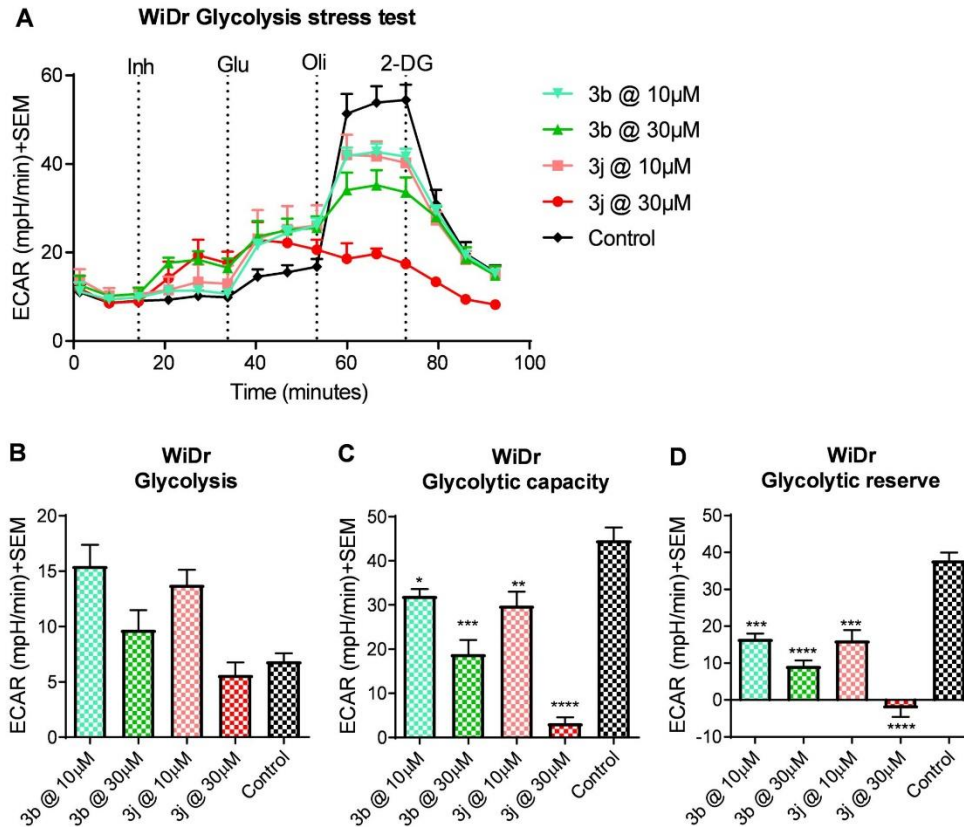


Figure 5q: Glycolysis stress test of compounds **3b** and **3j** in WiDr cell line (A) Glycolysis stress test profile; (B) Effect of compounds **3b** and **3j** on glycolysis; (C) Effect of compounds **3b** and **3j** on glycolytic capacity; (D) Effect of compounds **3b** and **3j** on glycolytic reserve. The values are generated using wave software, and an average+SEM of minimum three independent experiments were calculated.

5.2.6 Mitochondrial stress test in MDA-MB-231 and WiDr cell lines using **3b** and **3j**

We also compared the MST parameters of *N,N*-diphenyl substituted derivative **3j** with an *N,N*-dibutyl substituted derivative **3b** in MCT4 expressing MDA-MB-231 and MCT1 expressing WiDr cell lines. Like GST, these compounds were also tested at both 10 and 30 μ M concentrations. At 10 μ M concentration, both **3b** and **3j** did not decrease maximal respiration in MDA-MB-231 cell line but showed significant reduction only at 30 μ M concentration (Figures 5r-A, 5r-B). In WiDr cell line both compounds **3b** and **3j** exhibited a significant decrease in maximal respiration at both concentrations (Figures 5s-A and 5s-B). In both cell lines, ATP production was reduced in the presence of compounds **3b** and **3j** (Figures 5r-C and 5s-C). Proton leak was significantly increased at 30 μ M concentration in MDA-MB-231 and WiDr cells with compounds **3b** and **3j** whereas proton leak was increased only with compound **3j** in both cells at 10 μ M concentration (Figures 5r-D and 5s-D). Also, both compounds exhibited significant reduction in spare respiratory capacity in MDA-MB-231 cell line only at 30 μ M concentration, whereas only both compounds **3b** and **3j** decreased spare respiratory capacity at 10 μ M concentration in WiDr cell line (Figures 5r-E and 5s-E).

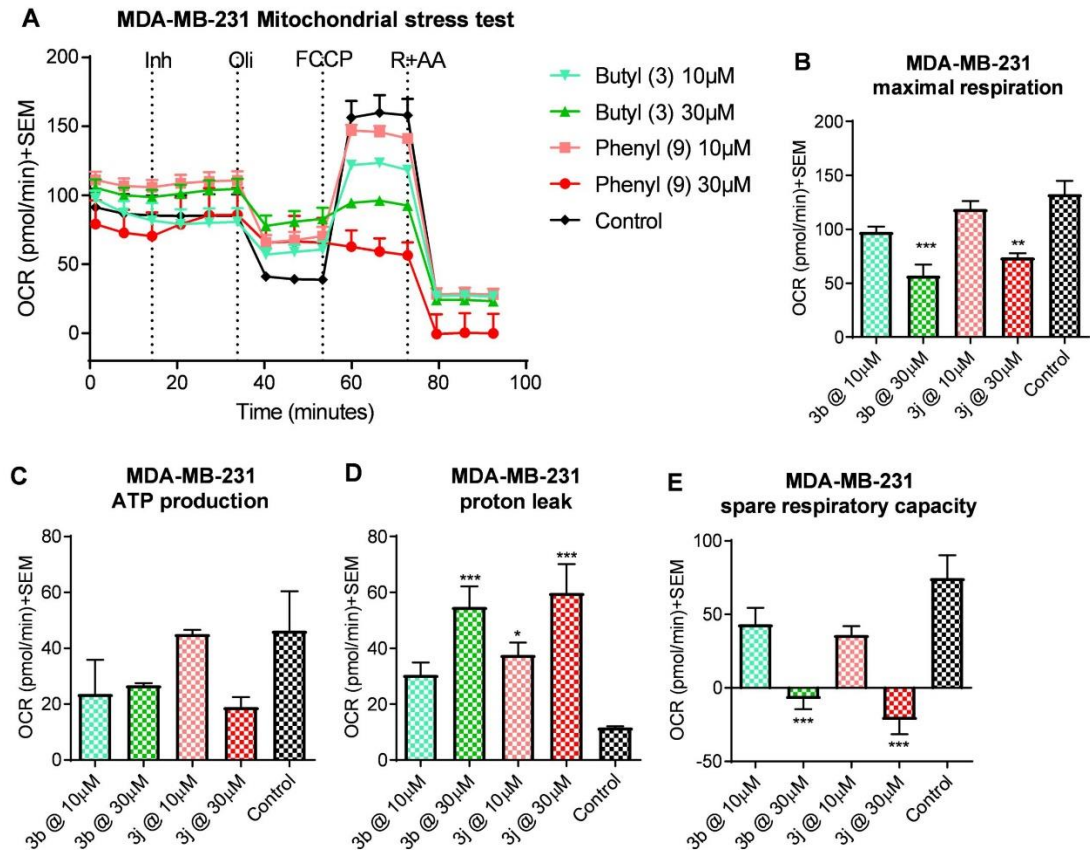


Figure 5r: Mitochondrial stress test of compounds **3b** and **3j** in MDA-MB-231 cell line (A) Mitochondrial stress test profile; (B) Effect of compounds **3b** and **3j** on maximal respiration; (C) Effect of compounds **3b** and **3j** on ATP production; (D) Effect of compounds **3b** and **3j** on proton leak; (E). Effect of compounds **3b** and **3j** on spare respiratory capacity. The values are generated using wave software, and an average+SEM of minimum three independent experiments were calculated.

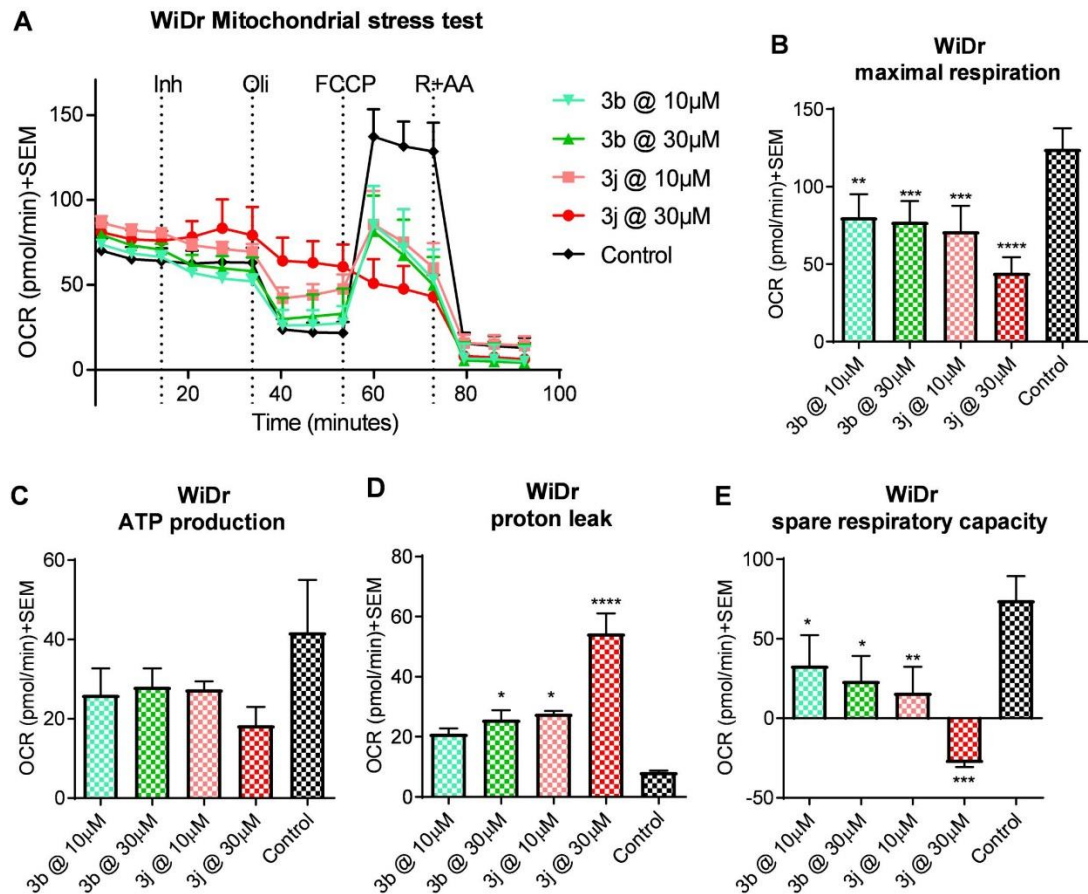


Figure 5s: Mitochondrial stress test of compounds **3b** and **3j** in WiDr cell line (A) Mitochondrial stress test profile; (B) Effect of compounds **3b** and **3j** on maximal respiration; (C) Effect of compounds **3b** and **3j** on ATP production; (D) Effect of compounds **3b** and **3j** on proton leak; (E). Effect of compounds **3b** and **3j** on spare respiratory capacity. The values are generated using wave software, and an average+SEM of minimum three independent experiments were calculated.

As previously hypothesized, dual MCT1 and/or MCT4 inhibition could interrupt the transport of glycolytic metabolites lactic acid and pyruvic acid in cancer cells, and hence, energy flow in cells will be disrupted which causes lactic acid acidosis. This could be clearly observed by the increase in the intracellular pH of cells as evidenced by GST in MCT4 expressing TNBC MDA-MB-231 cell line. The lead MCT1 and/or MCT4 inhibitors **3b**, **3j** and **4g** also significantly inhibited glycolysis and mitochondrial parameters using Seahorse XFe96 analyzer, indicating that these compounds have the potential to target metabolic plasticity in cancer cells.

All these results from GST and MST suggest that these compounds effect these processes in negative way. Basal ECAR and Basal OCR reading from GST and MST, respectively suggest that MDA-MB-231 is more glycolytic and less oxidative in nature, whereas WiDr is less glycolytic and more oxidative in nature. This can be seen even after the addition of glucose in GST where high rate of glycolysis was observed in MDA-MB-231 cell line compared to WiDr cell line. After the addition of oligomycin-A in GST, all the OxPhos related processes were completely inhibited, and to meet the energy demands, higher rates of glycolysis was observed. At high concentrations, compounds **3b**, **3j** and **4g** did not allow these processes to occur suggesting the vigorous glycolysis was inhibited to a greater extent in these cell lines. Although there is an equal need for glycolysis ubiquitously observed in several cell lines, the process of aggressive glycolysis is observed in various fast-growing cells including cancer cells. Metabolic plasticity is dependent on altering mainly glycolysis and OxPhos. These GST and MST studies point towards

disruption of both these processes simultaneously using our dual MCT1 and MCT4 inhibitors. Although *N,N*-dibutyl derivative **3b** exhibited significant inhibition of GST and MST parameters, *N,N*-diphenyl derivative **3j** exhibited superior efficacy in inhibiting the above mentioned parameters compared to **3b**. Hence, compound **3j** was selected as a lead candidate compound for further *in vitro* and *in vivo* studies.

5.3 Florescence microscopy study of compound 3j in MDA-MB-231 and WiDr cell lines

The lead compound **3j** exhibited significant effect on mitochondrial parameters, and this activity could be observed only if the compound **3j** crosses the cell membrane and interact directly or indirectly with mitochondria. The phenyl rings attached to the nitrogen atom in conjugation with cyanoacrylic acid makes **3j** a fluorescent compound and it fluoresces at 470/40 excitation and 525/50 emission. To test the ability of the compound **3j** to cross the cell membrane, we utilized MDA-MB-231 and WiDr cell lines and studied fluorescence by labeling mitochondria with MitoTracker Red. The images were obtained using Nikon epifluorescence microscope. These studies indicated that in MDA-MB-231 cells, compound **3j** is localized in areas surrounding mitochondria, but not co-localized with mitochondria (Figure 5t). The same results were observed in WiDr cells also (Figure 5u).

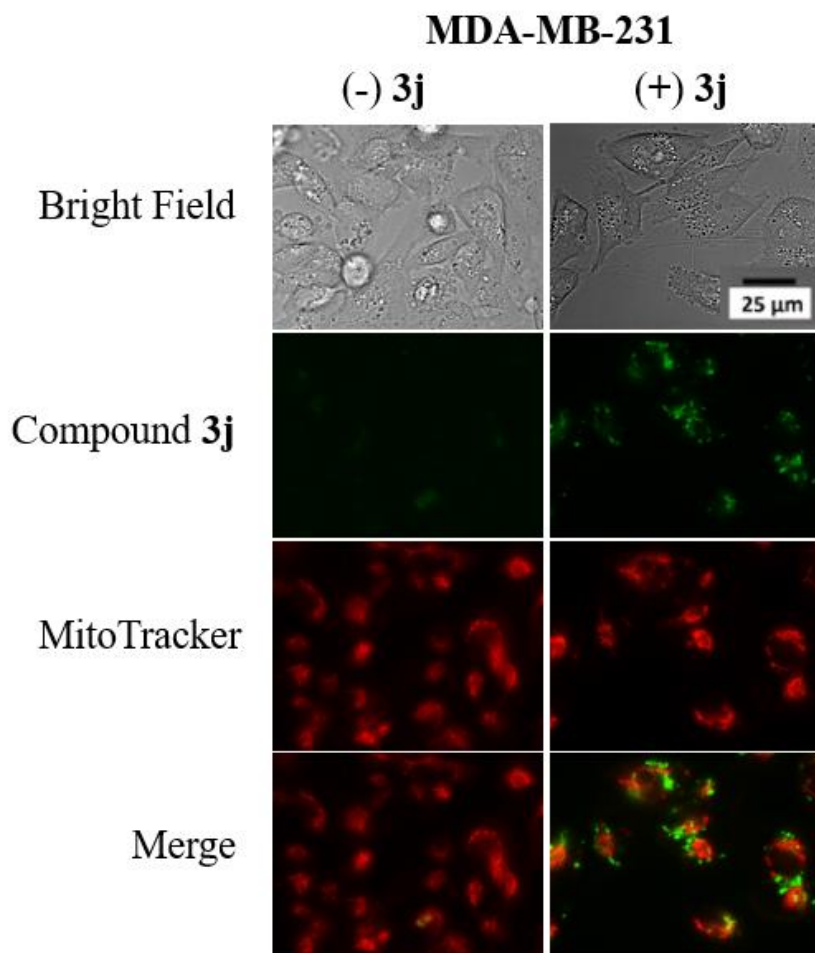


Figure 5t: Representative fluorescence microscopy images of MDA-MB-231 cells treated with compound **3j** and labeled with mitotracker red. Scale bar is 25 μ m.

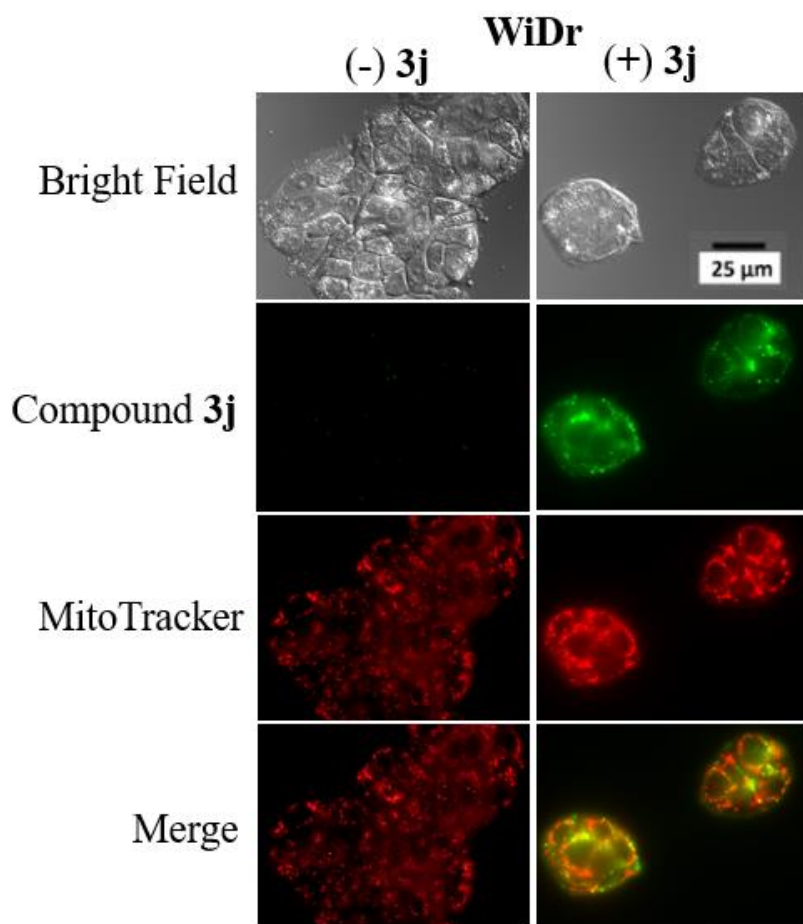


Figure 5u: Representative fluorescence microscopy images of WiDr cells treated with compound **3j** and labeled with mitotracker red. Scale bar is 25 μm .

5.4 Anticancer efficacy of lead candidate compounds in MDA-MB-231-luc tumor xenograft models

Compound **3j** showed significant tumor growth inhibition in MCT1 expressing WiDr colorectal and 4T1-luc2 tumor models and exhibited potent MCT4 inhibition. This compound also exhibited significant inhibition of glycolysis and mitochondrial parameters as evidenced by GST and MST discussed above. Hence, compound **3j** was chosen for carrying out *in vivo* studies in the predominantly MCT4 expressing TNBC MDA-MB-231-luc flank xenograft model. MDA-MB-231 is a mesenchymal like grade 3 ductal carcinoma. This cell line forms poorly differentiated cancer in nude mice and serves an excellent model to evaluate the therapeutic efficacy of the lead inhibitor.

5.4.1 *Anticancer efficacy of compound 3j in MDA-MB-231-luc tumor xenograft model*

Female NOD SCID mice were injected with 10^7 MDA-MB-231-luc cancer cells in 1:1 PBS-matrigel combination in their flanks. The tumors were allowed to reach $\sim 150 \text{ mm}^3$ volume before starting the treatment. The mice were randomly chosen by chance and assigned into 2 groups (n = 6 mice per group). Group 1 was designated as the control group (10% DMSO in saline) and group 2 mice were administered with compound **3j** once daily by ip at a dose of 25 mg/kg. However, after 1 week of treatment, moderate levels of tumor growth inhibition was observed as measured by external tumor volume with calipers. Consequently, the dosage was increased to 50 mg/kg and the tumor growth reduction was higher with this elevated dosage. At the end of the study (22 days), the mice were euthanized, and tumor masses were isolated and weighed. The tumor growth inhibition was found to be 29% compared to the control group based on tumor volume (Figure 5v-A) and 20% based on tumor weight (Figure 5v-B). At this dosage, compound **3j** did not exhibit any toxicity and was well tolerated in tumor bearing mice as evidenced in Figure 5v-C.

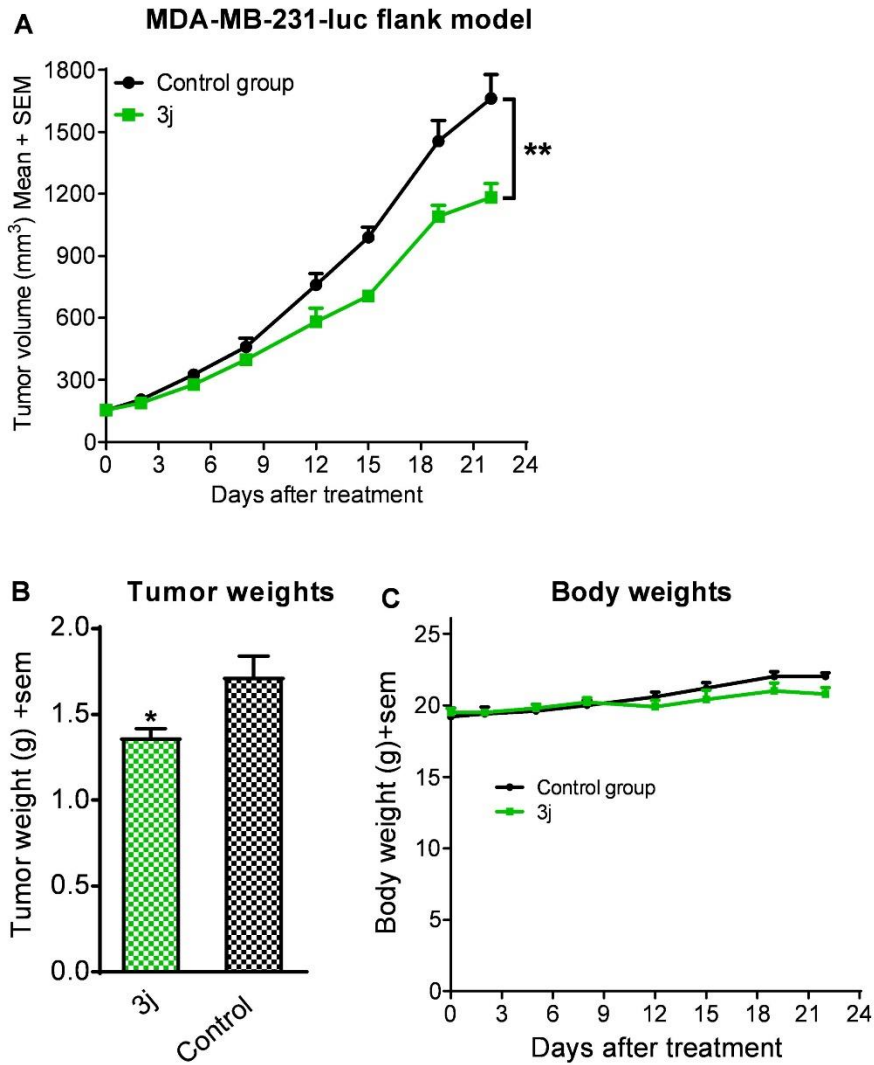


Figure 5v: Tumor growth inhibition study with compound **3j** in MDA-MB-231-luc tumor xenograft model. (A) Based on tumor volume; (B) Based on tumor weights; (C) Body weight changes during the treatment regimen.

5.4.2 *Anticancer efficacy of compound 3j compared to doxorubicin in MDA-MB-231-luc tumor xenograft model*

Because we observed tumor growth inhibition at higher dosage, another study was conducted using the MDA-MB-231 tumor xenograft model to compare compound **3j** with the clinically relevant compound doxorubicin. Female NOD SCID mice were inoculated with cancer cells (1×10^7) and allowed to grow to a volume of $\sim 240 \text{ mm}^3$. This time, group-1 mice were administered with **3j** at 50mg/kg, ip, qd and group-2 mice were given doxorubicin at 0.5mg/kg, ip, five days per week. Group-3 was treated with a combination of **3j** and doxorubicin. At the end of the study (17 days), mice were euthanized, and tumors were isolated and weighed. Gratifyingly, excellent synergy was observed between MCT inhibitor **3j** and DNA topoisomerase poison doxorubicin. Tumor growth inhibition of group-1 was found to be same as group-2, whereas tumor growth inhibition in the combination therapy (group-3) was 47% compared to group-2 based on tumor volume (Figure 5w-A) and 44% compared to group-2 based on isolated tumor mass (Figure 5w-B). In this study, significant body weight changes were not observed compared to doxorubicin or combination groups (Figure 5w-C). From this study, the combination therapy was found to be highly effective than single agent action either by **3j** or doxorubicin.

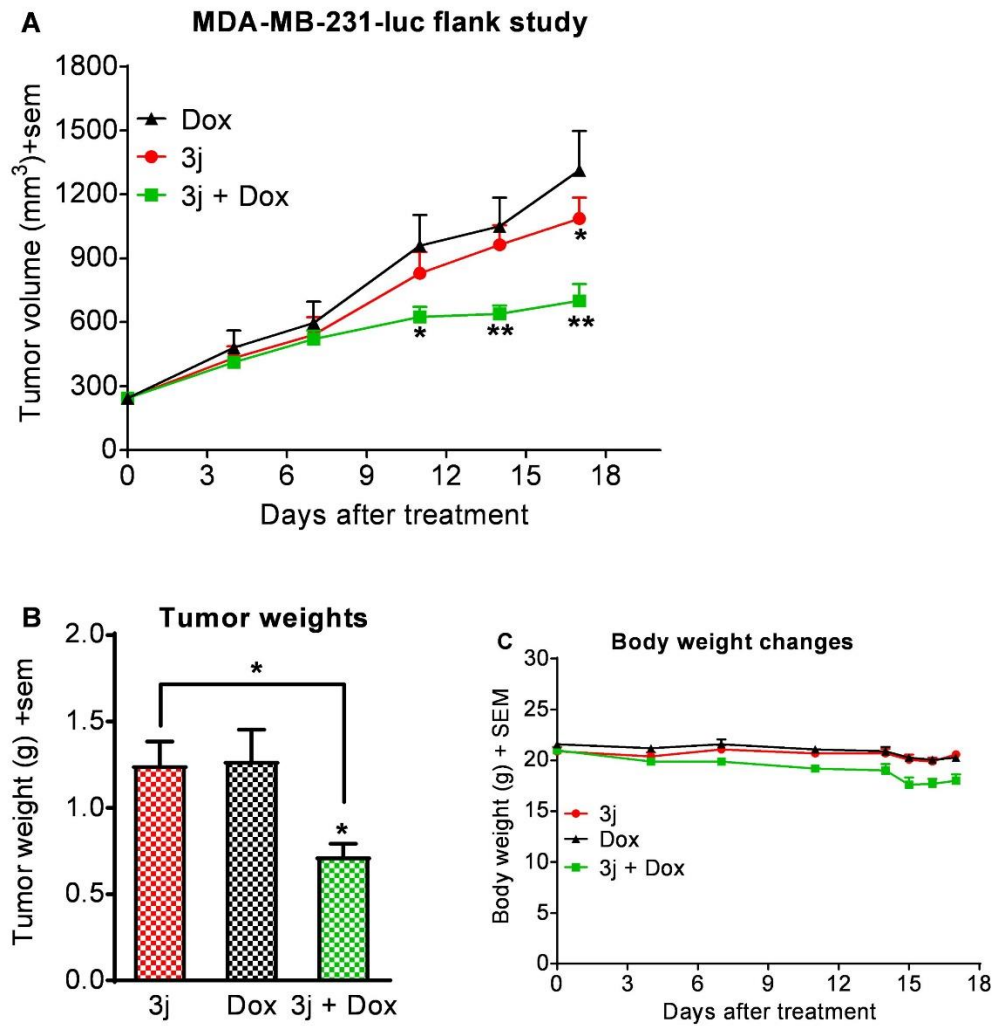


Figure 5w: Anticancer efficacy with compound **3j** and doxorubicin in MDA-MB-231-luc tumor xenograft model. (A) Based on tumor volume; (B) Based on tumor weights; (C) Body weight changes during the treatment regimen.

5.4.3 *Anticancer efficacy of compound 3j at a higher dosage in MDA-MB-231-luc flank model*

Because we observed significant tumor growth inhibition at higher doses, we also carried out another study by further increasing in dosage of compound **3j** and doxorubicin in the MDA-MB-231 tumor model. The treatment was started when the tumor volume reached 195 mm³. Group-1 was administered with **3j** at 70 mg/kg, ip, bid, group-2 was treated with a combination of **3j** and doxorubicin at 1mg/kg, ip, 5 times a week, group-3 was given doxorubicin and group-4 was the control group which was administered with vehicle (10% DMSO in saline). After four days, ~12% body weight loss was observed in group-1 mice and hence the dosage was readjusted to once daily dosage (70 mg/kg, ip, qd). Tumor volume was measured every three days and body weights were measured every day. The treatment was stopped at day 18 in both groups and at the end of the study on day 20, the mice were euthanized, and tumor masses were isolated. Based on the tumor volume, tumor growth inhibitions were found to be ~61%, 58% and 71% in groups 1, 2, and 3, respectively (Figure 5x-A). Based on the tumor weights, tumor growth inhibitions were found to be ~56%, 52% and 67% in groups 1, 2, and 3, respectively (Figure 5x-B). These studies clearly exhibit the potential of MCT1 and MCT4 inhibitors in a dose-dependent manner in TNBC treatment.

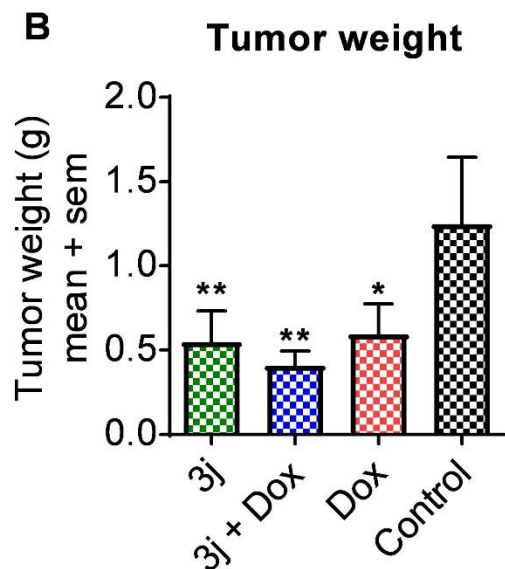
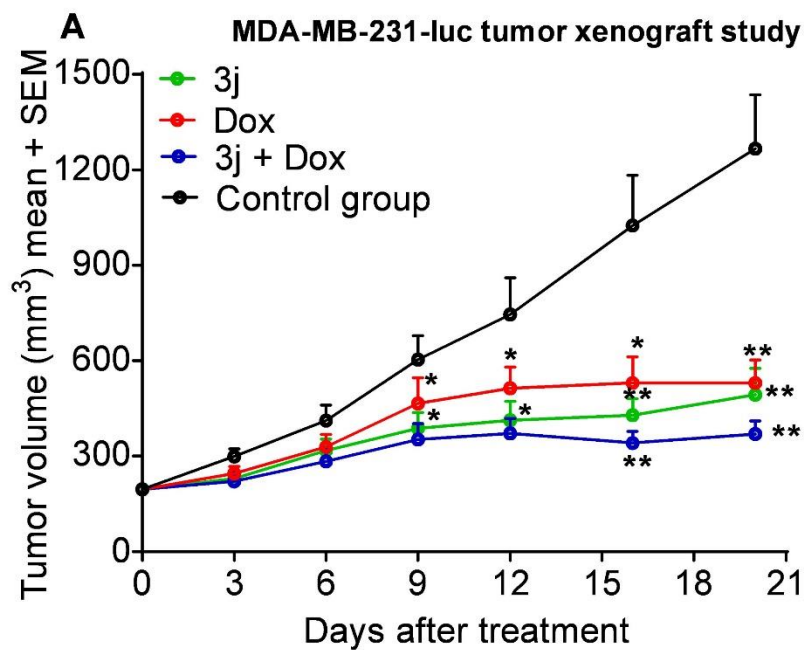


Figure 5x: *In vivo* anticancer efficacy study using compound **3j** in MDA-MB-231 xenograft model. (A) Tumor volume during the treatment. (B) Tumor growth inhibition based on isolated tumor mass.

5.4.4 Anticancer efficacy of the lead candidate compound **4g** in MDA-MB-231-luc tumor model

The coumarin based candidate compounds did not exhibit potent MCT4 inhibition compared to CHC based derivatives, except for compound **4g** which showed ~200 nM IC₅₀ for MCT4 inhibition. Since this compound had significant effect on mitochondrial parameters in MST, **4g** was tested for its anticancer efficacy in an MCT4 expressing MDA-MB-231-luc tumor model. After tumor inoculation, the treatment was initiated when the tumors reached a volume of ~100 mm³. Groups 1 and 2 were treated with **4g** at 20 mg/Kg, ip, and 100 mg/Kg via oral gavage, respectively. Group-3 was administered with clinical breast cancer drug doxorubicin at a dosage of 0.5 mg/Kg, ip, five times a week, and group-4 was designated as a control group and injected with vehicle (10% DMSO in saline). In this study, although the treatment was continued for 28 days, treatment groups 1 and 2 did not exhibit any tumor growth inhibition, whereas mice treated with doxorubicin showed 50% tumor growth inhibition based on tumor volume (Figure 5y-A). When resected tumor weights were compared, similar result was obtained with compound **4g**, whereas doxorubicin exhibited 43% tumor growth inhibition (Figure 5y-B). These results prove our hypothesis that 7-*N,N*-dialkyl carboxy coumarins show selective MCT1 inhibition and may not have off-target effects. Also, as discussed in chapter 1, Draoui et al. also synthesized similar coumarin derivatives 7ACC1 and 7ACC2 and when these compounds were tested in low MCT1 expressing UM-UC-3 tumor model, these compounds did not show anticancer efficacy, further confirming that our coumarin derivatives do not exhibit off target effects.

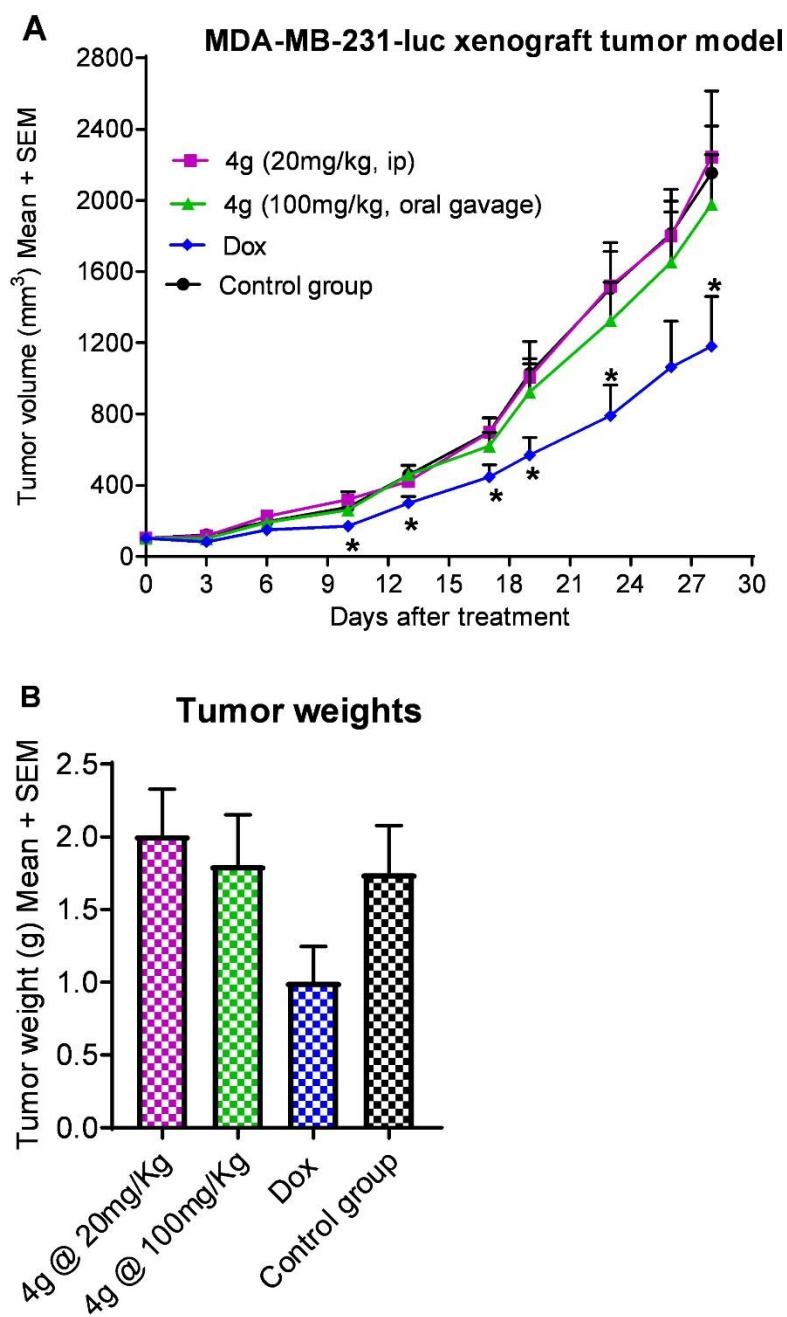


Figure 5y: Anticancer efficacy of lead compound **4g** in MDA-MB-231-luc flank model.

Tumor growth inhibition (A) based on tumor volumes; (B) based on tumor weights

5.5 In vitro and in vivo evaluation of reverse Warburg effect in TNBC MDA-MB-231

As discussed in the introduction chapter-1, acute loss of stromal caveolin-1 leads to oxidative stress, mitochondrial dysfunction and aerobic glycolysis in cancer related fibroblasts.⁶ It has also been proven that dysfunctional mitochondria are removed from fibroblasts via autophagy/ mitophagy resulting in even more aggressive aerobic glycolysis.¹⁸ The energy rich glycolytic end products such as lactate and ketone bodies are then transferred from fibroblasts to adjacent cancer cells via monocarboxylate transporters (MCT1 and MCT4), which in turn stimulate mitochondrial biogenesis and generate ATP via oxidative phosphorylation (Reverse Warburg Effect).⁷ To test the reverse Warburg hypothesis *in vitro*, we co-cultured TNBC MDA-MB-231 cells with caveolin-1 expressing 3T3 MEF WT and caveolin-1 knock out 3T3 MEF KO fibroblasts and evaluated the lead MCT1 and MCT4 inhibitors for their cytotoxicity.

5.5.1 Optimization of seeding concentration of cells for co-culture of 3T3 MEFs WT and 3T3 MEFs KO fibroblasts with MDA-MB-231 cell line

We utilized a SRB assay to evaluate the growth curves for 3T3 MEF WT and 3T3 MEF KO cells. Cells (3T3 MEF WT and 3T3 MEF KO) were cultured at four different concentrations in duplicates in 48-well plates. Growth medium in each row was removed each day for six days and the wells were washed with PBS and dried at the end of day-6. SRB (0.5% in 1% acetic acid) was added to the wells and incubated for 30-45 minutes. The wells were washed 3 times with 1% acetic acid and dried. The cellular protein was

dissolved in trizma base (10mM, pH 10.2) and absorbance was recorded at 540 nm. Percent survival was calculated using the formula

$$\% \text{ Survival} = \frac{\text{Abs}_{\text{test compound}}}{\text{Abs}_{\text{control}}} \times 100.$$

A graph was generated using GraphPad by plotting number of days on x-axis and % survival on y-axis (Figure 5z). This study determined optimal seeding concentration as 1×10^4 cells/mL and 0.5×10^4 cells/mL for 3T3 MEF WT and 3T3 MEF KO cells respectively.

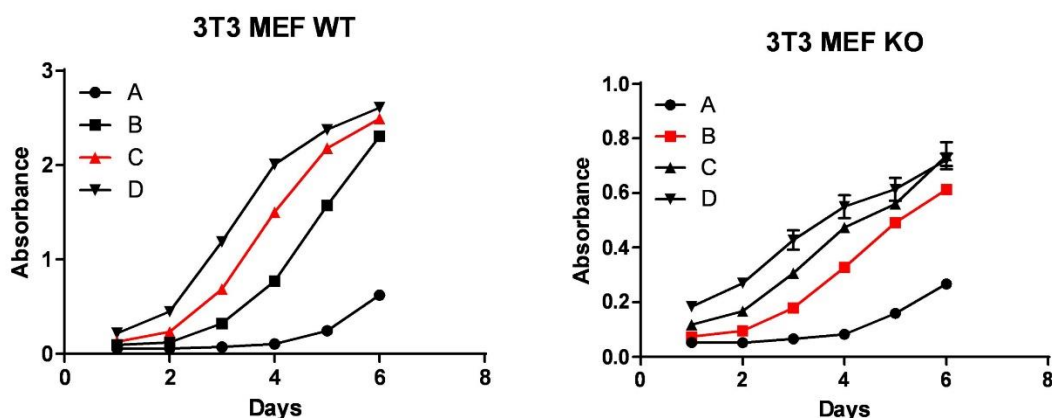


Figure 5z: Determination of optimal seeding concentration of 3T3 MEFs cells. (i) Growth curve of 3T3 MEF WT cells: A) 5×10^4 cells/mL, B) 2×10^4 cells/mL, C) 1×10^4 cells/mL and D) 0.5×10^4 cells/mL (cells in $400 \mu\text{L}$ of growth media); (ii) Growth curve of 3T3 MEF KO cells: A) 1×10^4 cells/mL, B) 0.5×10^4 cells/mL, C) 0.25×10^4 cells/mL and D) 0.1×10^4 cells/mL (cells in $400 \mu\text{L}$ of growth media).

Similarly, we utilized SRB assay to determine the optimal concentration of MDA-MB-231 for co-culturing them with fibroblast cells 3T3 MEF WT and 3T3 MEF KO. We co-cultured MDA-MB-231 cells at four different concentrations with 3T3 MEF WT and 3T3 MEF KO by keeping their concentration at 1×10^4 and 0.5×10^4 cells/mL respectively. SRB assay was performed and the optimal concentration of MDA-MB-231 was determined as 5×10^4 cells/mL (Figure 5aa).

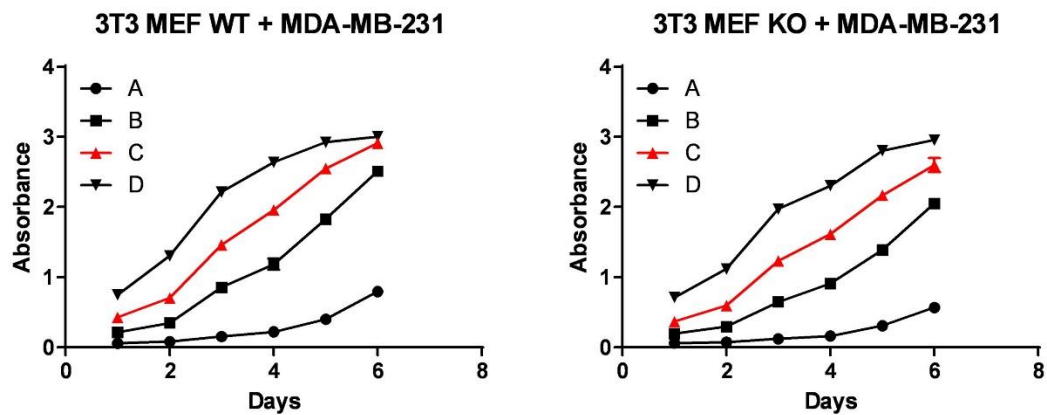


Figure 5aa: Determination of optimal seeding concentration of MDA-MB-231 cells with 3T3 MEFs cells. (i) Growth curve for co-culture of MDA-MB-231 and 3T3 MEF WT cells (1×10^4 cells/mL): A) 20×10^4 cells/mL, B) 10×10^4 cells/mL, C) 5×10^4 cells/mL and D) 2.5×10^4 cells/mL (cells in $400 \mu\text{L}$ of growth media); (ii) Growth curve for co-culture of MDA-MB-231 and 3T3 MEF KO cells (0.5×10^4 cells/mL): A) 20×10^4 cells/mL, B) 10×10^4 cells/mL, C) 5×10^4 cells/mL and D) 2.5×10^4 cells/mL (cells in $400 \mu\text{L}$ of growth media)

5.5.2 Cell proliferation inhibition of compounds 3h-3k in MDA-MB-231, and co-cultures with 3T3 MEF WT and 3T3 MEF KO under normal conditions

We evaluated cell proliferation of lead compounds **3h-3k** using MTT assay in normal conditions (5% CO₂ atmosphere at 37° C). These results indicate that compound **3j** did not show significant difference of IC₅₀ values among MDA-MB-231 cells and their co-culture with 3T3 MEF WT and KO. Compounds **3h**, **3i**, and **3k** did not show any cytotoxicity in single cell as well as in cocultures (Table 5b).

Table 5b: MTT assay IC₅₀* values of compounds **3h-3k** in MDA-MB-231, and co-cultures with 3T3 MEF WT and 3T3 MEF KO under normal conditions

Compound	MDA-MB-231	MDA-MB-231	MDA-MB-231
		+ 3T3 MEF WT	+ 3T3 MEF KO
3h	>0.25	>0.25	>0.25
3i	>0.25	>0.25	>0.25
3j	0.08±0.01	0.08±0.01	0.06±0.01
3k	>0.25	>0.25	>0.25

* IC₅₀ values reported in mM, average ± SEM of minimum three separate experimental values

5.5.3 Cell proliferation inhibition of compounds 3h-3k in MDA-MB-231, and co-cultures with 3T3 MEF WT and 3T3 MEF KO under hypoxic conditions

Cells were cultured in 96-well plates and incubated for 24 hours. After the addition of test compounds, the plates were placed in a hypoxic chamber (flushed with 10% CO₂, 1% O₂ and 89% N₂ for 5 minutes) and incubated for 72 hours. The plates were processed and IC₅₀ was calculated similar to the MTT assay. These results indicate that compound **3j** showed decreased IC₅₀ values in co-cultured cells. Compounds **3h**, **3i**, and **3k** did not show any cytotoxicity in single cell as well as in cocultures (Table 5c).

Table 5c: MTT assay IC₅₀* values of compounds **3h-3k** in MDA-MB-231, and co-cultures with 3T3 MEF WT and 3T3 MEF KO under hypoxic conditions

Compound	MDA-MB-231	MDA-MB-231	MDA-MB-231
		+ 3T3 MEF WT	+ 3T3 MEF KO
3h	>0.25	>0.25	>0.25
3i	>0.25	>0.25	>0.25
3j	0.09±0.00	0.13±0.00	0.14±0.00
3k	>0.25	>0.25	>0.25

*IC₅₀ values reported in mM, average ± SEM of minimum three separate experimental values

5.6 Anticancer efficacy of lead MCT inhibitor 3j in MDA-MB-231-luc based orthotopic models

All above-mentioned cytotoxicity studies were carried out in *in vitro* systems where the cells are cultured in monolayers. In *in vivo* systems, tumors have a complex network of microenvironment that is highly heterogeneous in nature, containing primary cancer cells, fibroblasts, lymphocytes, macrophages etc. Hence, translation of *in vitro* to *in vivo* based on cytotoxicity may not be similar. Also, evaluation of anticancer efficacy in flank-based xenograft models provided valuable *in vivo* data, but it is crucial to translate these results into orthotopic models. Therefore, we evaluated MCT1 and MCT4 inhibitors in MDA-MB-231 orthotopic models, which include co-injection of WT and KO fibroblasts.

5.6.1 Anticancer efficacy of lead MCT inhibitor **3j** in MDA-MB-231-luc orthotopic model

Female NOD SCID mice (Jacksons laboratory) were employed for this study. Tumors were allowed to reach ~160 mm³ (day-16) before grouping and the treatment was started in groups 1 and 2 using **3j** at 25 mg/Kg, ip, bid and 40 mg/Kg, ip, bid, respectively. Group 3 was treated with doxorubicin at 0.5 mg/Kg, ip, five days a week and group 4 was assigned as control group and injected with vehicle (10% DMSO in saline). Treatment was continued for nine days and the study was terminated, and tumors were isolated. From this study, lead compound **3j** exhibited 26, 35 and 24% tumor growth inhibition in groups 1, 2 and 3, respectively, compared to the control group (Figure 5ab).

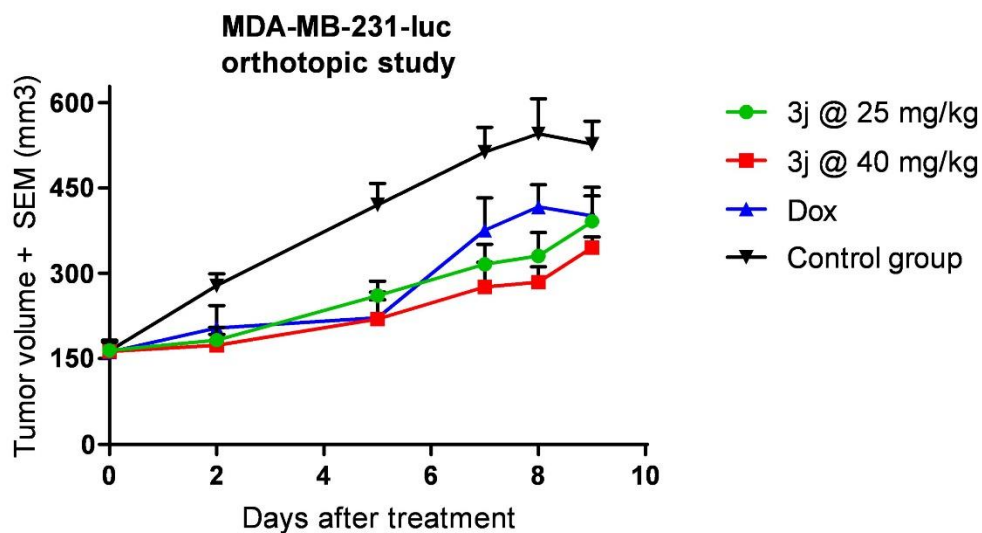


Figure 5ab: *In vivo* anticancer efficacy study in MDA-MB-231-luc orthotopic model. Treatment with compound **3j** at 25 and 40 mg/Kg, ip, bid compared to doxorubicin treatment

5.6.2 Anticancer efficacy of lead MCT inhibitor 3j in MDA-MB-231-luc orthotopic model co-injected with 3T3 MEF WT cells

We carried out another study with a co-injection of MDA-MB-231-luc (5×10^6 cells) with 3T3 MEF WT (1×10^6 cells) into mammary gland surgically, under anesthesia. In this case, tumors were allowed to reach $\sim 140 \text{mm}^3$ (day-11) tumor volume before grouping ($n = 6$ mice per group) and the treatment was started in groups 1 and 2 using **3j** at higher doses of 40 mg/Kg, ip, bid and 55 mg/Kg, ip, bid. Group 3 was treated with doxorubicin at 0.5 mg/Kg, ip, five times a week, and group 4 was assigned as control group and injected with vehicle (10% DMSO in saline). Treatment was continued for 13 days and the study was terminated, and tumors were isolated. From this study, treatment groups 1, 2 and 3 exhibited 43, 35 and 37% tumor growth inhibition, respectively, based on the tumor volume measurements (Figures 5ac-A and 5ac-B), whereas these groups showed 10, 27 and 21% tumor growth inhibition, respectively, based on isolated tumor masses (Figure 5ac-C).

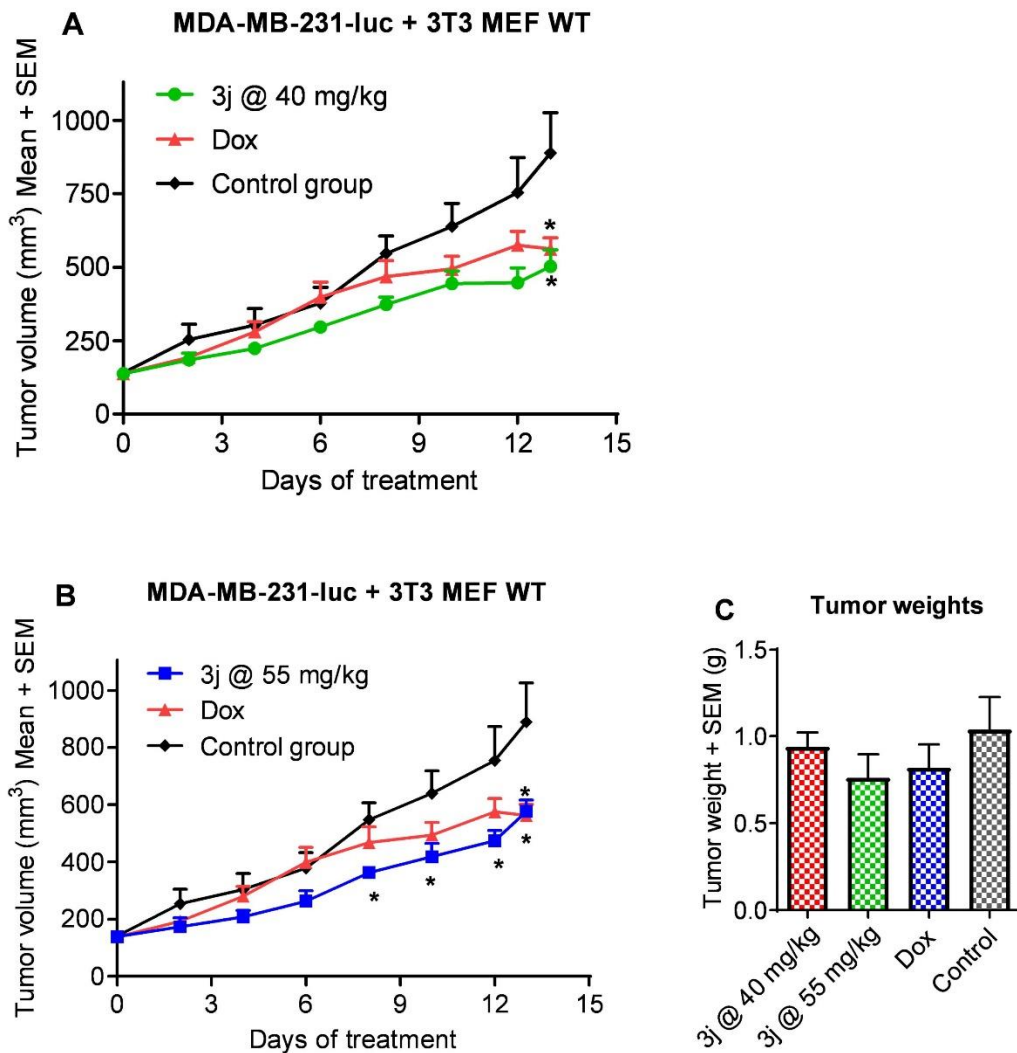
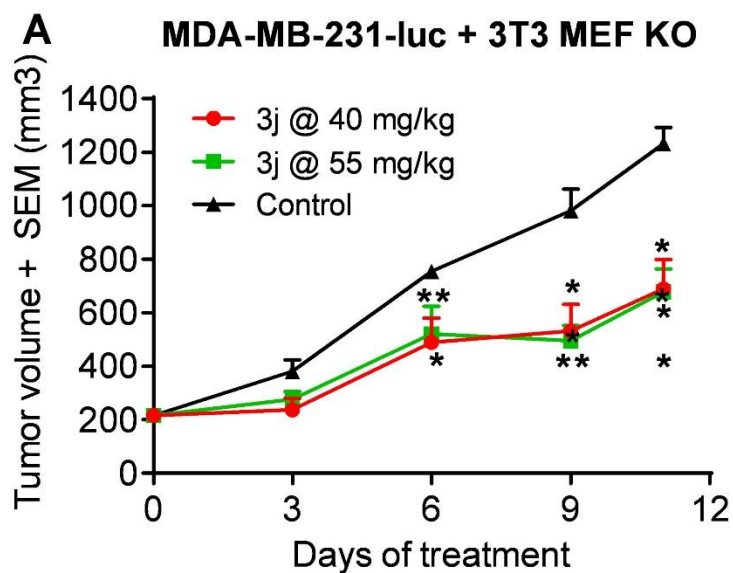


Figure 5ac: *In vivo* anticancer efficacy study in MDA-MB-231-luc + 3T3 MEF WT orthotopic model. (A) Tumor growth inhibition with treatment of **3j** at 40 mg/Kg, ip, bid, in comparison to doxorubicin (B) Tumor growth inhibition with treatment of **3j** at 55 mg/Kg, ip, bid, in comparison to doxorubicin, (C) Tumor growth inhibition based on isolated tumor mass.

5.6.3 *Anticancer efficacy of lead MCT inhibitor 3j in MDA-MB-231-luc orthotopic model co-injected with 3T3 MEF KO cells*

We then evaluated anticancer efficacy of compound **3j** using MDA-MB-231-luc (5×10^6 cells) co-injected with 3T3 MEF KO (5×10^5 cells) into mammary gland surgically, under anesthesia. In this study, tumors were allowed to reach $\sim 215 \text{ mm}^3$ (day-15) tumor volume before grouping ($n = 6$ mice per group) and the treatment was started in groups 1 and 2 using **3j** at doses of 40 mg/Kg, ip, qd and 55 mg/Kg, ip, qd. Group 3 was treated with vehicle (10% DMSO in saline). Treatment was continued for 11 days and the study was terminated, and tumors were isolated. From this study, groups 1 and 2 showed 44 and 53% tumor growth inhibition, respectively, based on the tumor volume measurements (Figure 5ad-A), whereas these groups exhibited 39 and 42% tumor growth inhibition based on isolated tumor masses (Figure 5ad-B).



B Tumor weights

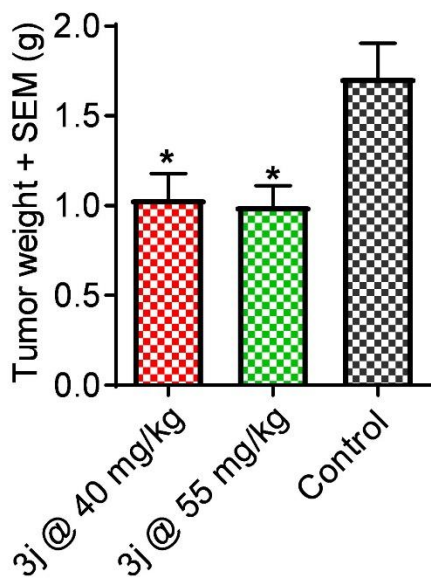


Figure 5ad: *In vivo* anticancer efficacy study in MDA-MB-231-luc + 3T3 MEF KO orthotopic model. (A) Tumor growth inhibition with treatment of **3j** at 40 mg/Kg, ip, qd, and 55 mg/Kg, ip, qd (B) Tumor growth inhibition based on isolated tumor mass.

The lead inhibitor **3j** caused dose-dependent tumor growth inhibition as a single agent in flank TNBC MDA-MB-231 based xenograft models in NOD SCID mice. In combination with clinical breast cancer chemotherapeutic agent doxorubicin, **3j** also exhibited synergistic effect of tumor growth inhibition in MDA-MB-231 model. Reverse Warburg effect also plays an important role in cancer progression and in MCT4 expressing cancers such as TNBC, the key factors include the down regulation of tumor suppressor gene Cav-1, pursuance of aerobic glycolysis, production of energy rich nutrients, mitochondrial biogenesis, OxPhos, genomic instability and evading cellular apoptosis. In all these factors, MCTs play an important role in glycolysis and OxPhos and inhibition of these transporters have therapeutic implications in TNBC treatment. Since the reverse Warburg effect is a common factor in most cancers, this strategy could be applicable to the treatment of several other cancers also.

In vivo anticancer efficacy studies in a TNBC MDA-MB-231-luc co-injected with caveolin-1 wild type and knock out fibroblasts in orthotopic models were carried out using dual MCT1 and MCT4 inhibitor **3j** as a single agent. These studies showed that the tumor growth in control groups of MDA-MB-231-luc and MDA-MB-231-luc co-injected with 3T3 MEF WT were similar, whereas in MDA-MB-231-luc co-injected with 3T3 MEF KO, control group showed significantly high tumor growth on day-9 after treatment (Figure 5ae). These results indicate that caveolin-1 KO results in high tumor growth, and caveolin-1 WT and normal MDA-MB-231-luc exhibit low tumor growth. The anticancer efficacy exhibited by the lead candidate compound **3j** was also significantly higher in MDA-MB-231-luc co-injected with 3T3 MEF KO, compared to WT tumors, indicating that caveolin-

1 KO results in high MCT4 expression and hence, our MCT4 inhibitor **3j** also exhibited high anticancer efficacy in TNBC models.

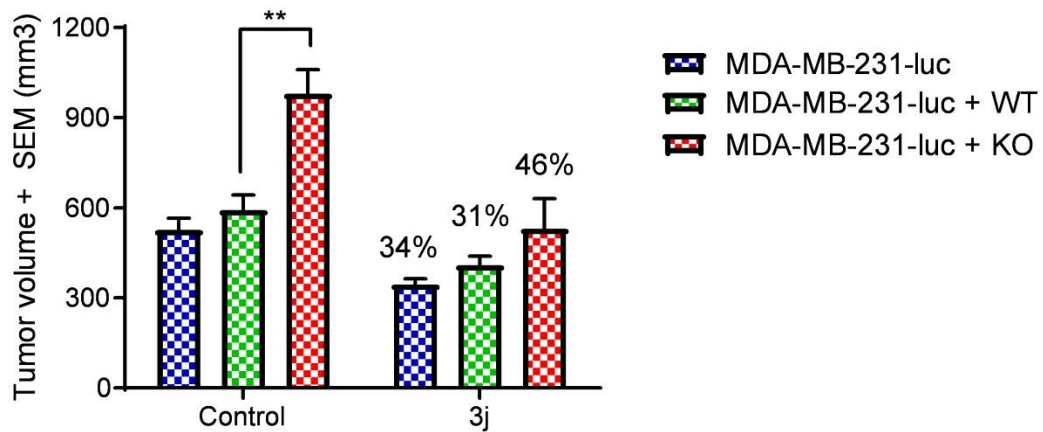


Figure 5ae: Tumor growth in control groups on day-9 after treatment in MDA-MB-231-luc, MDA-MB-231-luc co-injected with 3T3 MEF WT, and MDA-MB-231-luc co-injected with 3T3 MEF KO.

5.7 Conclusions

In conclusion, we evaluated *N,N*-dialkyl *o*-alkoxy CHC derivatives **3a-3k** for MCT4 inhibition and found that these compounds show potent and dual MCT1 and MCT4 inhibition. 7-*N,N*-dialkyl 3-carboxy coumarins were also evaluated for MCT4 inhibition, and these compounds were found to be specific MCT1 inhibitors. Especially, compounds **3a**, **3b**, **3j** and **3k** exhibited nM potency for MCT4 inhibition. CHC derivative **3j**, coumarin derivative **4g** were evaluated for their metabolic properties using Seahorse XFe96 based glycolysis and mitochondrial stress tests. These studies indicated that the compounds **3b** and **3j** exhibited significant inhibition of glycolytic capacity, glycolytic reserve, maximal respiration, ATP production, and spare respiratory capacity in MCT1 expressing WiDr and 4T1, and MCT4 expressing MDA-MB-231 cell line. Compound **4g** inhibited the above-mentioned parameters only in WiDr and 4T1 cell lines, as it is a selective MCT1 inhibitor. Fluorescence microscopy studies in MDA-MB-232 and WiDr cell lines using MitoTracker red revealed that compound **3j** was also localized in areas surrounding mitochondria.

CHC based lead compound **3j** was evaluated for *in vivo* tumor growth inhibition in predominantly MCT4 expressing MDA-MB-231 flank and orthotopic tumor models. These *in vivo* studies indicated that compound **3j** significantly inhibited tumor growth in both tumor models. Compound **3j** was effective as a single agent and had a synergistic effect with doxorubicin. Coumarin lead compound **4g** did not exhibit any anticancer efficacy in MDA-MB-231 flank mode. Evaluation of anticancer efficacy in MDA-MB-

231-luc co-injected with caveolin-1 WT and caveolin-1 KO orthotopic models revealed that candidate compound **3j** exhibited significant tumor growth reduction in KO orthotopic model compared to WT orthotopic model. These results indicated that Warburg effect and reverse Warburg effect could be targeted via MCT1 and MCT4 inhibitors to treat various MCT1 and MCT4 expressing cancers.

CHAPTER 6: Experimental procedures and spectral characterization

6.1 *Chemicals and methods of compound characterization*

Aniline and potassium carbonate were obtained from Fisher Scientific, aldehydes, *m*-anisidine, propyl bromide, butyl bromide, isobutyl bromide, pentyl bromide, hexyl bromide, allyl bromide, phosphorous (V) oxy chloride, cyanoacetic acid, and piperidine were purchased from Millipore-Sigma, tetrabutylammonium bromide was purchased from AKSci, L-[¹⁴C]-lactic acid sodium salt was purchased from Perkin Elmer. All other chemicals were of reagent grade quality and purchased from Millipore-Sigma. The ¹H- and ¹³C-NMR spectra were recorded on a Varian Oxford-500 spectrometer. High-resolution mass spectra (HRMS) were recorded using a Bruker BioTOF II ESI mass spectrometer. Elemental analysis (CHN) results were obtained from Atlantic Microlab services.

6.2 Cell lines and culture conditions

RBE4 cells were obtained as a gift from Dr. Drewes's lab. These cells were cultured in a medium consisting of 1:1 mixture of α -MEM and Ham's F-10 nutrient mix with HEPES (Gibco), heat inactivated FBS (10%, Atlanta Biologicals), basic fibroblast growth factor (1 ng/mL, US Biologicals), geneticin G418 (0.3 mg/mL, VWR International), and antibiotic-antimycotic (10,000 U/mL of penicillin, 10,000 μ g/mL of streptomycin, and 25 μ g/mL of Fungizone, Gibco).

MDA-MB-231 cells were purchased from ATCC and were cultured in DMEM supplemented with FBS (10%, Atlanta Biologicals) and penicillin-streptomycin (50 U/mL, 50 μ g/mL, Invitrogen).

4T1-luc2 cells were purchased from Caliper Life Sciences and were cultured in RPMI-1650 supplemented with heat inactivated FBS (10%) and penicillin-streptomycin (50 U/mL, 50 μ g/mL).

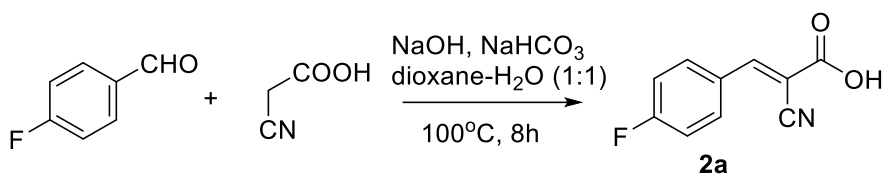
WiDr cells were purchased from ATCC and were cultured in MEM supplemented with FBS (10%) and penicillin-streptomycin (50 U/mL, 50 μ g/mL).

GL261-luc2 cells were purchased from Perkin-Elmer and cultured in DMEM supplemented with geneticin G418 (50 μ g/mL), FBS (10%) and penicillin-streptomycin (50 U/mL, 50 μ g/mL).

MDA-MB-231-luc cells were purchased from Cell Biolabs (AKR-231). The cells were cultured in DMEM supplemented with FBS (10%) and penicillin-streptomycin (50 U/mL, 50 μ g/mL).

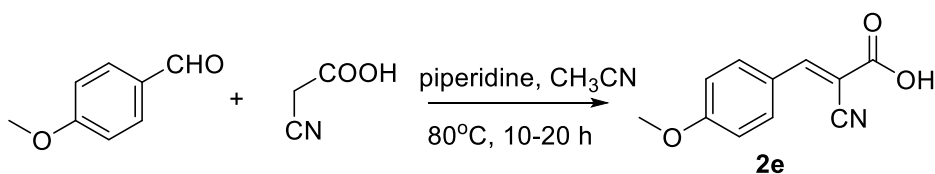
3T3 MEF WT and 3T3 MEF KO cells were purchased from ATCC. The cells were cultured in DMEM supplemented with FBS (10%) and penicillin-streptomycin (50 U/mL, 50 µg/mL).

The antibodies used for Western blot were rabbit polyclonal IgG antibody for MCT1 (Santa Cruz Inc.), rabbit polyclonal IgG antibody for MCT4 (Santa Cruz Inc.), goat anti-rabbit IgG horseradish peroxidase-conjugated antibodies (Jackson ImmunoResearch).



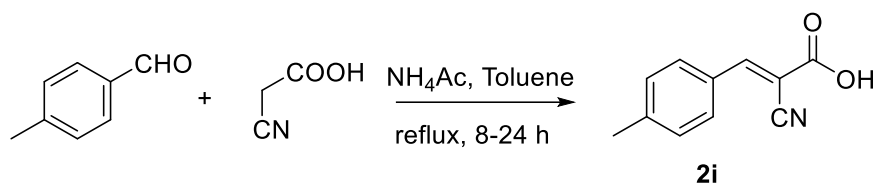
6.3 Representative synthesis of (*E*)-2-cyano-3-(4-fluorophenyl)acrylic acid **2.1a**

To a solution of 4-fluorobenzaldehyde (10 mmol) dissolved in dioxane (20 mL), another solution of cyanoacetic acid (15 mmol) dissolved in 1:1 dioxane-water (10 mL each) was added, followed by the addition of sodium hydroxide (15 mmol) and sodium bicarbonate (15 mmol), and the reaction mixture was heated at 100°C for 8 hours. Upon completion (TLC), the reaction mixture was poured into ice-cold 3M HCl and water and stirred. The resulting product was filtered using Buchner funnel, washed with water, and dried. The crude product was recrystallized in ethylacetate-hexane (10:1) to get pure (*E*)-2-cyano-3-(4-fluorophenyl)acrylic acid **2.1a** in 87% yield.



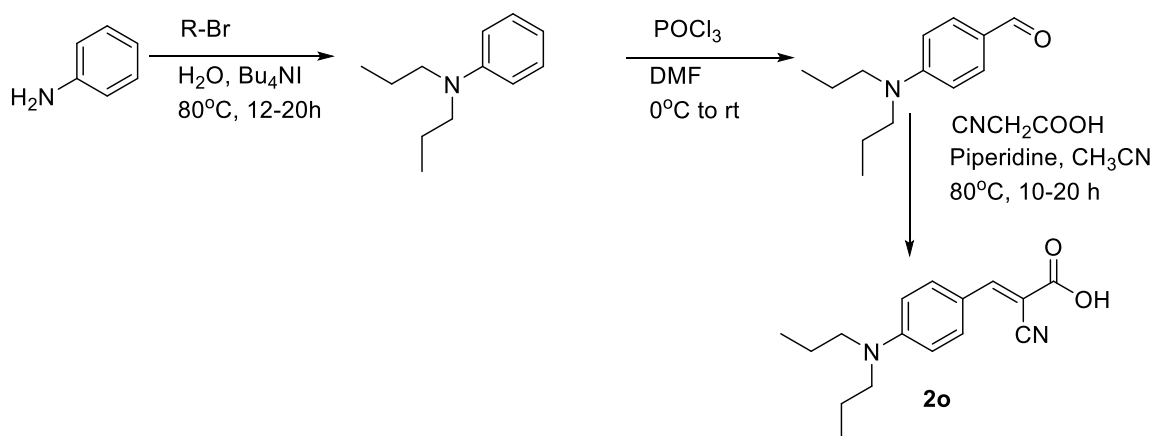
6.4 Representative synthesis of (*E*)-2-cyano-3-(4-methoxyphenyl)acrylic acid **2.1f**

To a solution of 4-methoxybenzaldehyde (10 mmol) dissolved in acetonitrile (20 mL), cyanoacetic acid (15 mmol) and piperidine (13 mol) were added and the reaction mixture was heated at 80°C for 10-20 hours. Upon completion (TLC), the reaction mixture was poured into ice-cold 3M HCl and water and stirred. The resulting product was filtered using Buchner funnel, washed with water, and dried. The crude product was recrystallized in ethylacetate-hexane (10:1) to get pure (*E*)-2-cyano-3-(4-methoxyphenyl)acrylic acid **2.1f** in 76% yield.



6.5 Representative synthesis of (*E*)-2-cyano-3-(4-methylphenyl)acrylic acid **2.1j**

To a solution of 4-methylbenzaldehyde (10 mmol) dissolved in toluene (20 mL), cyanoacetic acid (15 mmol) and ammonium hydroxide (15 mol) were added and the reaction mixture was refluxed for 8-24 hours. Upon completion (TLC), the reaction mixture was poured into ice-cold 3M HCl and water and stirred. The resulting product was filtered using Buchner funnel, washed with water, and dried. The crude product was recrystallized in ethylacetate-hexane (10:1) to get pure (*E*)-2-cyano-3-(4-methylphenyl)acrylic acid **2.1j** in 83% yield.

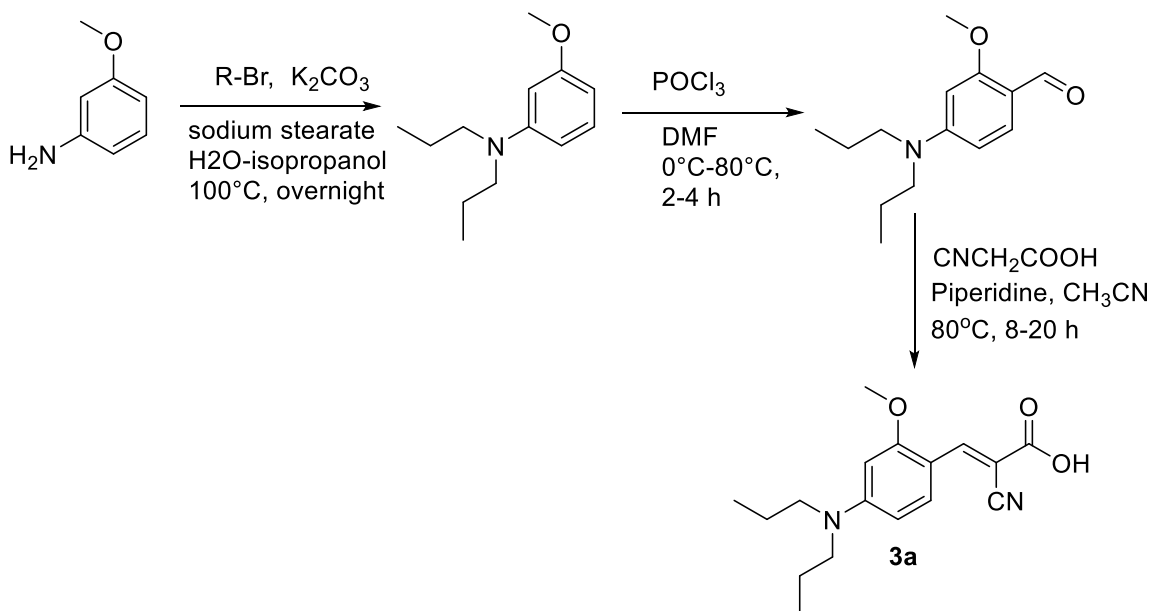


6.6 Representative synthesis of *(E)*-2-cyano-3-(4-(dipropylamino)phenyl)acrylic acid

2.2c

Aniline (10 mmol) was dissolved in a mixture of ethanol-water (10 mL each) and propyl bromide (40 mmol), K_2CO_3 (20 mmol) and tetrabutyl ammonium iodide (1 mmol) were added and the reaction mixture was refluxed at $80^\circ C$ for 20 hours. After the completion of reaction, the reaction mixture was extracted with ether and water. Without further purification, the crude dipropyl amine was formylated using dropwise addition of $POCl_3$ (12 mmol) in the solvent DMF (30 mL) at $0^\circ C$ and the reaction mixture was stirred for 4-6 hours. Once the reaction is complete (TLC 5% Ethyl acetate and hexane), the reaction mixture was added slowly into saturated solution of Na_2CO_3 . The product was extracted with ether and volatiles were evaporated. The crude aldehyde was dissolved in acetonitrile (20 mL) and 15 mmol of piperidine and cyanoacetic acid were added and refluxed for 8 hours. Upon completion, the reaction contents were added into 5 mL of 6M HCl and ice and stirred for 1 hour. The resulting yellow solid was filtered and washed with

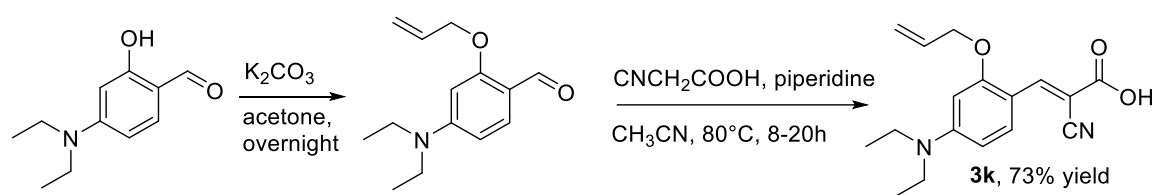
water, hexane and ether, and recrystallized in methanol and ethyl acetate. The resulting cyanocinnamate was obtained in three step yield of 52%.



6.7 Representative synthesis of (E)-2-cyano-3-(4-(dipropylamino)-2-methoxyphenyl) acrylic acid **3a**

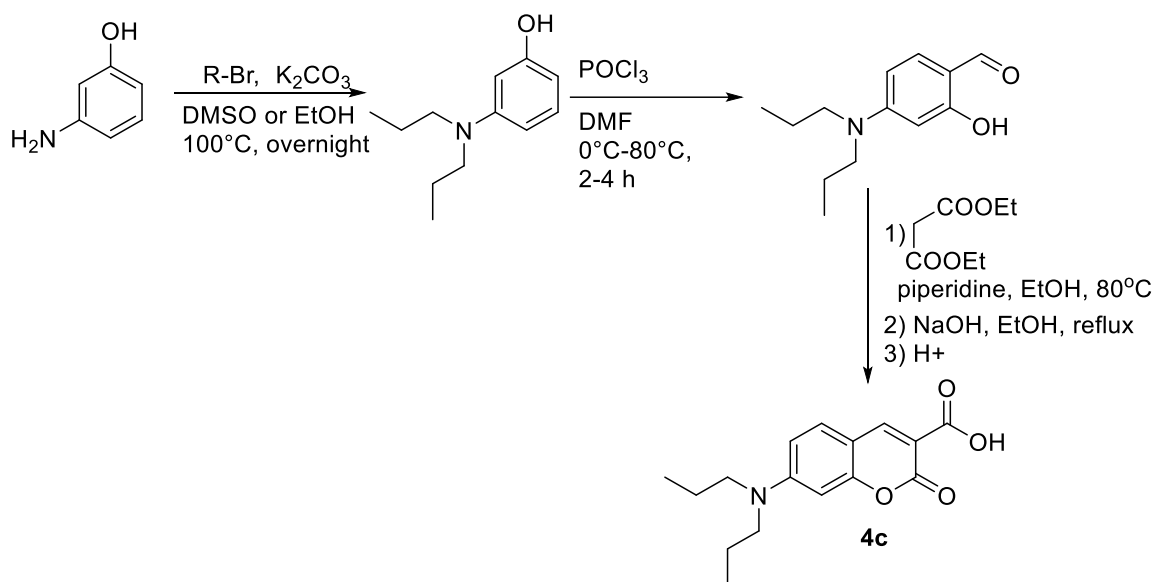
3-methoxy aniline (10 mmol) was dissolved in a mixture of isopropanol-water (10 mL each) and propyl bromide (40 mmol), K_2CO_3 (20 mmol) and sodium stearate (1 mmol) were added and the reaction mixture was refluxed at 100°C for 20 hours. After the completion of reaction, the reaction mixture was extracted with ether and water. Without further purification, the crude dipropyl amine was formylated using dropwise addition of $POCl_3$ (12 mmol) in the solvent DMF (30 mL) at 0°C and the reaction mixture was stirred for 4-6 hours. Once the reaction is complete (TLC 5% Ethyl acetate and hexane), the reaction mixture was added slowly into saturated solution of Na_2CO_3 . The product was extracted with ether and volatiles were evaporated. The crude aldehyde was dissolved in

acetonitrile (20 mL) and 15 mmol of piperidine and cyanoacetic acid were added and refluxed for 8 hours. Upon completion, the reaction contents were added into 5 mL of 6M HCl and ice and stirred for 1 hour. The resulting yellow solid was filtered and washed with water, hexane and ether, and recrystallized in methanol and ethyl acetate.



6.8 Synthesis of *(E)*-3-(2-(allyloxy)-4-(diethylamino)phenyl)-2-cyanoacrylic acid **3k**

N,N-diethyl salicylaldehyde (10 mmol) was dissolved in acetone (40 mL) and allyl bromide (20 mmol) and K_2CO_3 (20 mmol) were added and the reaction mixture was refluxed for 10 hours. The product was extracted with ether and volatiles are evaporated. The crude aldehyde was dissolved in acetonitrile (20 mL) and 15 mmol of piperidine and cyanoacetic acid are added and refluxed for 8 hours. Upon completion of the reaction was added into 5 mL of 6M HCl and ice and stirred for 1 hour and the yellow solid was filtered and washed with plenty of water and hexane and ether and recrystallized in methanol and ethyl acetate.

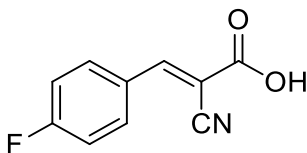


6.9 Representative procedure for the synthesis of 7-(dipropylamino)-2-oxo-2H-chromene-3-carboxylic acid **4c**

3-amino phenol (10 mmol) was dissolved in ethanol (30 mL) and propyl bromide (40 mmol) and K₂CO₃ (20 mmol) were added and the reaction mixture was refluxed at 100°C for 12 hours. After the completion of reaction, the reaction mixture is extracted with ethyl acetate and water and organic volatiles were evaporated. Without further purification the crude dipropyl amine was formylated using dropwise addition of POCl₃ (12 mmol) in the solvent DMF (30 mL) at 0°C. Once the reaction is complete (TLC 10% Ethyl acetate and hexane), the reaction mixture was added slowly into saturated solution of Na₂CO₃. The product was extracted with ether and volatiles are evaporated. The crude aldehyde was dissolved in ethanol (20 mL) and 15 mmol of piperidine and diethyl malonate were added and refluxed for 8 hours. Upon completion, the reaction was extracted with ethylacetate and the volatiles were evaporated. The crude diethyl malonate product was then refluxed in ethanol (30 mL) and 10% NaOH (40 mmol) for 2-4 hours. Upon hydrolysis (TLC), the

reaction contents were brought to pH 7.0 with 3M HCl in ice. The resulting yellow solid was filtered and washed with water and hexane and recrystallized in ethanol.

6.10 Spectral characterization of synthesized compounds



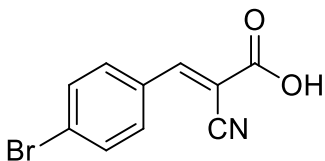
(*E*)-2-cyano-3-(4-fluorophenyl)acrylic acid, **2a**

¹H-NMR (500 MHz, acetone-*d*₆):

δ 8.30 (s, 1H), 8.09 (d, *J* = 15.0 Hz, 2H), 7.39 (t, *J* = 15.0 Hz, 2H)

¹³C-NMR (125 MHz, acetone-*d*₆):

δ 166.17, 163.87, 153.68, 134.07, 128.88, 117.25, 116.67, 104.50



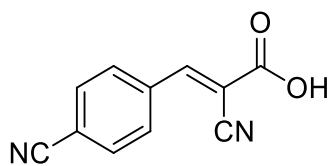
(*E*)-3-(4-bromophenyl)-2-cyanoacrylic acid, **2b**

¹H-NMR (500 MHz, DMSO-*d*₆):

δ 8.31 (s, 1H), 7.95 (d, *J* = 8.5 Hz, 2H), 7.79 (d, *J* = 8.5 Hz, 2H)

¹³C-NMR (125 MHz, DMSO-*d*₆):

δ 163.76, 153.85, 133.07, 133.02, 131.40, 127.55, 116.57, 105.21



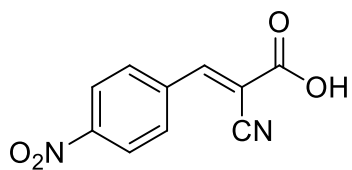
(*E*)-2-cyano-3-(4-cyanophenyl)acrylic acid, **2c**

¹H-NMR (500 MHz, DMSO-*d*₆):

δ 8.16 (s, 1H), 7.95 (d, *J* = 8.5 Hz, 2H), 6.93 (d, *J* = 8.0 Hz, 2H)

¹³C-NMR (125 MHz, DMSO-*d*₆):

δ 164.72, 163.23, 154.75, 134.36, 123.34, 117.62, 117.0, 99.10



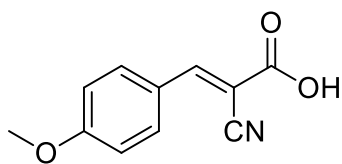
(*E*)-2-cyano-3-(4-nitrophenyl)acrylic acid, **2d**

¹H-NMR (500 MHz, acetone-*d*₆):

δ 8.45 (s, 1H), 8.405 (d, *J* = 5.0 Hz, 2H), 8.24 (d, *J* = 10.0 Hz, 2H)

¹³C-NMR (125 MHz, acetone-*d*₆):

δ 162.82, 151.94, 149.84, 137.82, 131.57, 124.04, 115.08, 108.09



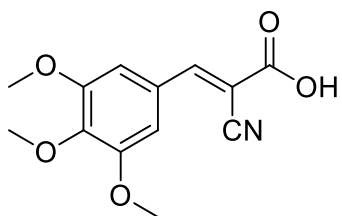
(*E*)-2-cyano-3-(4-methoxyphenyl)acrylic acid, **2e**

¹H-NMR (500 MHz, DMSO-*d*₆):

δ 8.16 (s, 1H), 7.98 (d, *J* = 10.0 Hz, 2H), 7.06 (d, *J* = 10.0 Hz, 2H), 3.82 (s, 3H)

¹³C-NMR (125 MHz, DMSO-*d*₆):

δ 164.47, 163.91, 154.46, 133.88, 124.69, 117.34, 115.46, 100.19, 56.29



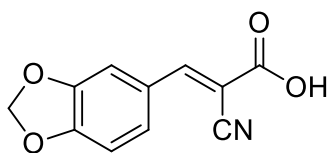
(*E*)-2-cyano-3-(3,4,5-trimethoxyphenyl)acrylic acid, **2f**

¹H-NMR (500 MHz, DMSO-*d*₆):

δ 8.25 (s, 1H), 7.46 (s, 2H), 3.79 (s, 6H), 3.68 (s, 3H)

¹³C-NMR (125 MHz, DMSO-*d*₆):

δ 164.15, 155.04, 153.55, 142.41, 127.20, 117.33, 117.20, 109.28, 102.62, 60.99, 56.67.



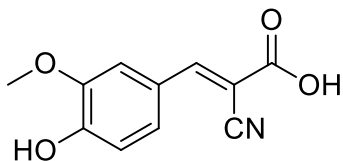
(*E*)-3-(benzo[d][1,3]dioxol-5-yl)-2-cyanoacrylic acid, **2g**

¹H-NMR (500 MHz, DMSO-*d*₆):

δ 8.19 (s, 1H), 7.71 (s, 1H), 7.51 (d, *J* = 10.0 Hz, 1H), 7.02 (d, *J* = 10.0 Hz, 1H), 6.15 (s, 2H)

¹³C-NMR (125MHz, DMSO-*d*₆):

δ 164.22, 154.23, 125.57, 148.94, 129.79, 126.26, 116.36, 108.84, 108.27, 102.84, 100.27.



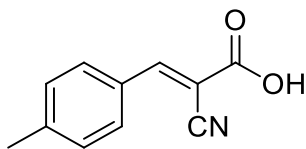
(*E*)-2-cyano-3-(4-hydroxy-3-methoxyphenyl)acrylic acid, **2h**

¹H-NMR (500 MHz, DMSO-*d*₆):

δ 8.06 (s, 1H), 7.64 (s, 1H), 7.50 (d, *J* = 7.0 Hz, 2H), 6.84 (d, *J* = 7.0 Hz, 2H), 3.72 (s, 3H)

¹³C-NMR (125 MHz, DMSO-*d*₆):

δ 164.67, 154.99, 152.91, 148.40, 127.56, 123.62, 117.70, 116.58, 114.33, 98.98, 56.15.



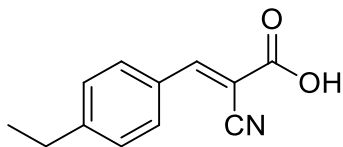
(*E*)-2-cyano-3-(*p*-tolyl)acrylic acid, **2i**

¹H-NMR (500 MHz, DMSO-*d*₆):

δ 8.21 (s, 1H), 7.88 (s, 2H), 7.33 (s, 2H), 2.35 (s, 3H)

¹³C-NMR (125 MHz, DMSO-*d*₆):

δ 164.13, 154.89, 144.61, 131.45, 130.53, 129.50, 116.50, 102.97, 21.97.



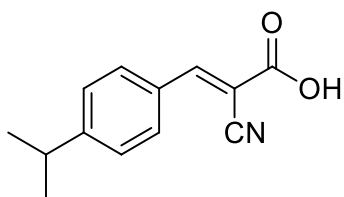
(*E*)-2-cyano-3-(4-ethylphenyl)acrylic acid, **2j**

¹H-NMR (500 MHz, DMSO-*d*₆):

δ 8.25 (s, 1H), 7.93 (d, *J* = 8.5 Hz, 2H), 7.36 (d, *J* = 8.5 Hz, 2H), 2.64 (q, *J* = 8, 15.5 Hz, 2H), 1.16 (t, *J* = 8 Hz, 3H)

¹³C-NMR (125 MHz, DMSO-*d*₆):

δ 164.14, 154.93, 150.62, 131.57, 129.76, 129.36, 116.92, 103.07, 29.0, 15.66.



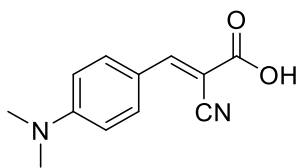
(*E*)-2-cyano-3-(4-isopropylphenyl)acrylic acid, **2k**

¹H-NMR (500 MHz, CD₃OD):

δ 8.21 (s, 1H), 7.91 (d, *J* = 7.0 Hz, 2H), 7.36 (d, *J* = 6.5 Hz, 2H), 2.95-2.93 (m, 1H), 1.24 (s, 6H)

¹³C-NMR (125 MHz, CD₃OD):

δ 164.14, 154.93, 150.62, 131.57, 129.76, 129.36, 116.92, 103.07, 29.0, 15.66.



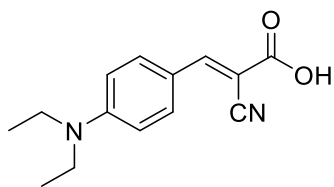
(*E*)-2-cyano-3-(4-(dimethylamino)phenyl)acrylic acid, **2m**

¹H-NMR (500 MHz, DMSO-*d*₆):

δ 13.291 (s, 1H), 8.037 (s, 1H), 7.926 (d, *J* = 9.5 Hz, 2H), 6.833 (d, *J* = 9.0 Hz, 2H), 3.06 (s, 6H)

¹³C-NMR (125 MHz, DMSO-*d*₆):

δ 165.561, 154.543, 154.217, 134.224, 119.112, 118.666, 112.378, 94.158



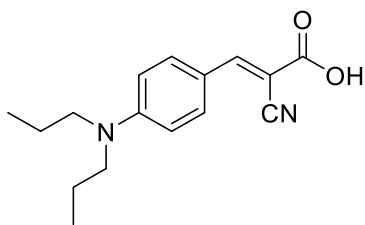
(*E*)-2-cyano-3-(4-(diethylamino)phenyl)acrylic acid, **2n**

¹H-NMR (500 MHz, DMSO-*d*₆):

δ 8.02 (s, 1H), 7.9 (d, *J* = 10.0 Hz, 2H), 6.78 (d, *J* = 10.0 Hz, 2H), 3.44 (q, *J* = 5.0 Hz, 16.0 Hz, 4H), 1.11 (t, *J* = 10.0 Hz, 3H)

¹³C-NMR (125 MHz, DMSO-*d*₆):

δ 165.64, 154.29, 152.07, 134.59, 118.73, 118.61, 111.98, 93.47, 13.08.



(*E*)-2-cyano-3-(4-(dipropylamino)phenyl)acrylic acid, **2o**

¹H-NMR (500 MHz, DMSO-*d*₆):

δ 8.11 (s, 1H), 7.97 (d, *J* = 9.0 Hz, 2H), 6.69 (d, *J* = 9.5 Hz, 2H), 3.38 (t, *J* = 7.5 Hz, 4H),

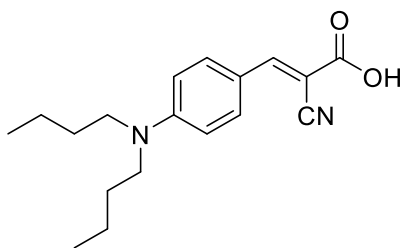
1.70 (m, 4H), 1.00 (t, *J* = 7.0 Hz, 6H)

¹³C-NMR (125 MHz, DMSO-*d*₆):

δ 190.1, 152.9, 132.4, 129.4, 124.8, 111.9, 111.0, 53.0, 20.6, 11.6

Anal. Calcd for C₁₆H₂₀N₂O₂ (272.35): C 70.56, H 7.40, N 10.29

Found: C 70.70, H 7.46, N 10.32



(*E*)-2-cyano-3-(4-(dibutylamino)phenyl)acrylic acid, **2p**

¹H-NMR (500 MHz, DMSO-*d*₆):

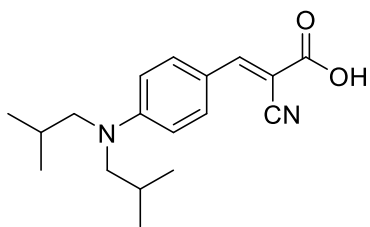
δ 8.03 (s, 1H), 7.92 (d, *J* = 9.0 Hz, 2H), 6.80 (d, *J* = 9.0 Hz, 2H), 3.40 (t, *J* = 7.5 Hz, 4H),
1.54 (m, 4H), 1.34 (m, 4H), 0.93 (t, *J* = 7.0 Hz, 6H)

¹³C-NMR (125 MHz, DMSO-*d*₆):

δ 165.6, 154.3, 152.5, 134.5, 118.7, 118.6, 112.1, 105.0, 50.6, 29.6, 20.2, 14.5

Anal. Calcd for C₁₈H₂₄N₂O₂ (300.40): C 71.97, H 8.05, N 9.33.

Found: C 71.83, H 8.38, N 9.35



(*E*)-2-cyano-3-(4-(diisobutylamino)phenyl)acrylic acid, **2q**

¹H-NMR (500 MHz, CDCl₃):

δ 8.11 (s, 1H), 7.96 (d, *J* = 9.0 Hz, 2H), 6.71 (d, *J* = 9.0 Hz, 2H), 3.31 (d, *J* = 7.0 Hz, 4H),

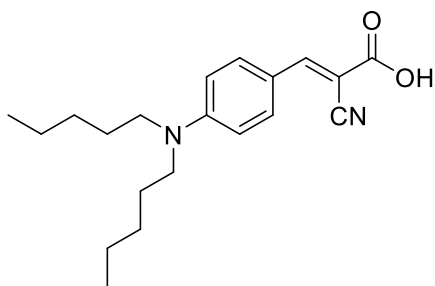
2.17-2.11 (m, 1H), 0.97 (d, 12H)

¹³C-NMR (125 MHz, CDCl₃):

δ 170.1, 155.8, 152.9, 134.9, 118.9, 117.5, 112.4, 92.1, 60.3, 27.0, 20.5

Anal. Calcd for C₁₈H₂₄N₂O₂ (300.40): C 71.97, H 8.05, N 9.33.

Found: C 71.48, H 8.49, N 9.23



(*E*)-2-cyano-3-(4-(dipentylamino)phenyl)acrylic acid, **2r**

¹H-NMR (500 MHz, CDCl₃):

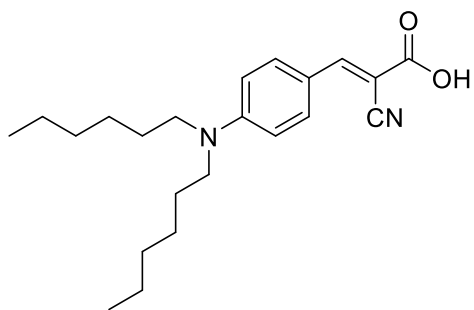
δ 8.10 (s, 1H), 7.96 (d, *J* = 9.0 Hz, 2H), 6.67 (d, *J* = 5.0 Hz, 2H), 3.39 (t, *J* = 8.0 Hz, 4H),
1.68-1.62 (m, 4H), 1.43-1.33 (m, 8H), 0.95 (t, *J* = 7.0 Hz, 6H)

¹³C-NMR (125 MHz, CDCl₃):

δ 170.0, 155.8, 152.7, 135.1, 118.8, 117.6, 111.6, 91.8, 51.4, 29.4, 27.2, 22.7, 14.2.0

Anal. Calcd for C₂₀H₂₈N₂O₂ (328.46): C 73.14, H 8.59, N 8.53.

Found: C 72.61, H 8.37, N 8.16



(*E*)-2-cyano-3-(4-(dihexylamino)phenyl)acrylic acid, **2s**

¹H-NMR (500 MHz, CDCl₃):

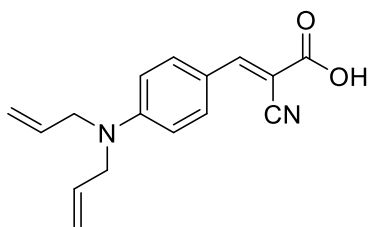
δ 8.10 (s, 1H), 7.97 (d, *J* = 9.0 Hz, 2H), 6.68 (d, *J* = 9.0 Hz, 2H), 3.39 (t, *J* = 7.5 Hz, 4H),
1.65 (br m, 4H), 1.36 (br m, 12H), 0.93 (t, *J* = 6.0 Hz, 6H)

¹³C-NMR (125 MHz, CDCl₃):

δ 170.4, 155.8, 152.7, 135.2, 118.8, 117.6, 111.7, 91.8, 51.5, 31.8, 27.4, 26.9, 22.8, 14.2

Anal. Calcd for C₂₂H₃₂N₂O₂ (356.51): C 74.12, H 9.05, N 7.86.

Found: C 74.18, H 9.99, N 7.74



(*E*)-2-cyano-3-(4-(diallylamino)phenyl)acrylic acid, **2t**

¹H-NMR (500 MHz, DMSO-*d*₆):

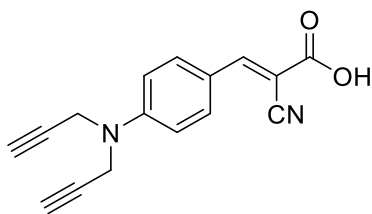
δ 8.06 (s, 1H), 7.92 (d, *J* = 8.0 Hz, 2H), 6.81 (d, *J* = 8.0 Hz, 2H), 5.90-5.84 (m, 2H), 5.19-5.14 (m, 4H), 4.08 (d, *J* = 3.0 Hz, 4H)

¹³C-NMR (125 MHz, DMSO-*d*₆):

δ 165.4, 154.4, 152.9, 134.1, 133.6, 119.5, 118.5, 117.1, 112.7, 94.6, 53.0

Anal. Calcd for C₁₆H₁₆N₂O₂ (268.32): C 71.62, H 6.01, N 10.44.

Found: C 70.98, H 6.66, N 11.36



(*E*)-2-cyano-3-(4-(di(prop-2-yn-1-yl)amino)phenyl)acrylic acid, **2u**

¹H-NMR (500 MHz, CDCl₃):

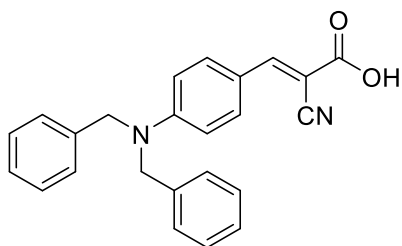
δ 8.10 (s, 1H), 7.95 (d, *J* = 9.0 Hz, 2H), 6.94 (d, *J* = 9.0 Hz, 2H), 4.21 (d, *J* = 2.0 Hz, 4H),
2.36 (s, 2H)

¹³C-NMR (125 MHz, CDCl₃:DMSO-*d*₆(1:1)):

δ 165.5, 164.9, 151.3, 133.7, 121.9, 117.4, 113.8, 97.0, 78.1, 73.4, 40.2.

Anal. Calcd for C₁₆H₁₂N₂O₂ (264.28): C 72.72, H 4.58, N 12.11.

Found: C 70.62, H 4.70, N 10.28



(*E*)-2-cyano-3-(4-(dibenzylamino)phenyl)acrylic acid, **2v**

¹H-NMR (500 MHz, DMSO-*d*₆):

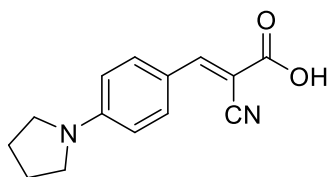
δ 8.03 (s, 1H), 7.86 (d, *J* = 8.5 Hz, 2H), 7.33-7.32 (m, 5H), 7.26 (br m, 5H), 6.84 (d, *J* = 8.5 Hz, 2H), 4.84 (s, 4H)

¹³C-NMR (125 MHz, DMSO-*d*₆):

δ 165.3, 154.3, 152.9, 138.2, 134.1, 129.4, 129.3, 127.7, 127.2, 119.9, 118.3, 113.0, 95.2, 54.6.

Anal. Calcd for C₂₄H₂₀N₂O₂ (368.44): C 78.24, H 5.47, N 7.60.

Found: C 77.30, H 5.33, N 7.88



(*E*)-2-cyano-3-(4-(pyrrolidin-1-yl)phenyl)acrylic acid, **2w**

¹H-NMR (500 MHz, DMSO-*d*₆):

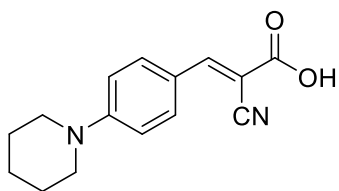
δ 8.01 (s, 1H), 7.88 (br s, 2H), 6.63 (br s, 2H), 3.34 (br s, 4H), 1.95 (br s, 4H)

¹³C-NMR (125 MHz, DMSO-*d*₆):

δ 165.5, 154.5, 151.6, 134.3, 118.8, 118.0, 93.3, 48.1, 25.5

Anal. Calcd for C₁₄H₁₄N₂O₂ (242.28): C 69.41, H 5.82, N 11.56.

Found: C 68.75, H 5.50, N 11.20



(*E*)-2-cyano-3-(4-(piperidin-1-yl)phenyl)acrylic acid, **2x**

¹H-NMR (500 MHz, DMSO-*d*₆):

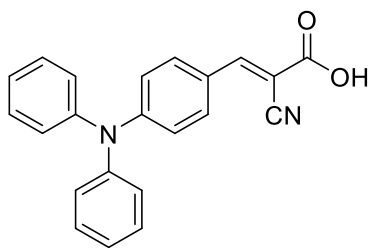
δ 8.05 (s, 1H), 7.91 (d, *J* = 9.0 Hz, 2H), 9.02 (d, *J* = 9.0 Hz, 2H), 3.47 (t, *J* = 5.0 Hz, 4H),
1.62-1.61(m, 2H), 1.57-1.56 (m, 4H)

¹³C-NMR (125 MHz, DMSO-*d*₆):

δ 165.4, 154.2, 154.2, 134.3, 119.8, 118.4, 113.8, 48.1, 25.6, 24.6

Anal. Calcd for C₁₅H₁₆N₂O₂ (256.31): C 70.29, H 6.29, N 10.93.

Found: C 70.51, H 6.45, N 11.01



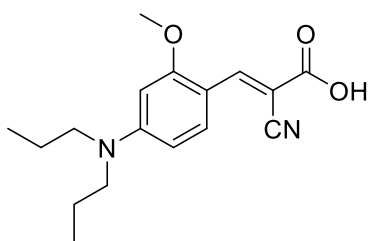
(*E*)-2-cyano-3-(4-(diphenylamino)phenyl)acrylic acid, **2y**

¹H-NMR (500 MHz, acetone-*d*₆):

δ 8.18 (s, 1H), 8.00 (d, *J* = 9 Hz, 2H), 7.46 (m, 4H), 7.28 (6H), 6.99 (d, *J* = 9 Hz, 2H)

¹³C-NMR (125 MHz, acetone-*d*₆):

δ 205.6, 153.9, 152.7, 146.1, 133.3, 130.2, 126.9, 125.9, 123.7, 118.9, 116.8, 98.0



(*E*)-2-cyano-3-(4-(dipropylamino)-2-methoxyphenyl)acrylic acid, **3a**

¹H-NMR (500 MHz, DMSO-*d*₆):

δ 8.43 (s, 1H), 8.22 (d, *J* = 9.0 Hz, 1H), 6.52 (d, *J* = 9.5 Hz, 1H), 6.19 (s, 1H), 3.90 (s, 3H), 3.41 (t, *J* = 7.0 Hz, 4H), 1.61 (m, 4H), 0.93 (t, *J* = 7.0 Hz, 6H)

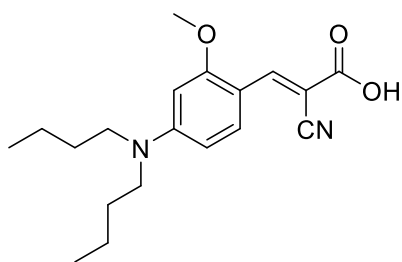
¹³C-NMR (125 MHz, DMSO-*d*₆):

δ 166.2, 162.4, 154.9, 146.9, 130.6, 119.3, 108.3, 106.2, 93.8, 91.3, 56.4, 52.6, 20.9, 11.8.

Anal. Calcd for C₁₇H₂₂N₂O₃ (302.37): C 67.53, H 7.33, N 9.26.

Found: C 67.52, H 7.51, N 9.28

HRMS (ESI) m/z: calc'd for C₁₇H₂₂N₂O₃ [M+Na]⁺: 325.15, found 325.15



(*E*)-2-cyano-3-(4-(dibutylamino)-2-methoxyphenyl)acrylic acid, **3b**

¹H-NMR (500 MHz, DMSO-*d*₆):

δ 13.0 (br, s, 1H), 8.42 (s, 1H), 8.21 (d, *J* = 9.0 Hz, 1H), 6.50 (d, *J* = 9.5 Hz, 1H), 6.17 (s, 1H), 3.89 (s, 3H), 3.44 (t, *J* = 7.5 Hz, 4H), 1.55 (m, 4H), 1.35 (m, 4H), 0.94 (t, *J* = 7.5 Hz, 6H)

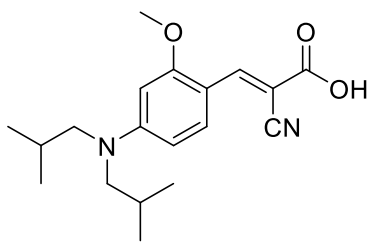
¹³C-NMR (125 MHz, DMSO-*d*₆):

δ 166.2, 162.3, 154.7, 146.8, 130.6, 119.3, 108.2, 106.2, 93.8, 91.3, 56.4, 50.7, 29.8, 20.3, 14.5.

Anal. Calcd for C₁₉H₂₆N₂O₃ (330.43): C 69.06, H 7.93, N 8.48.

Found: C 68.83, H 7.90, N 8.46

HRMS (ESI) m/z: calc'd for C₁₇H₂₂N₂O₃ [M+Na]⁺: 353.18, found 353.18



(*E*)-2-cyano-3-(4-(diisobutylamino)-2-methoxyphenyl)acrylic acid, **3c**

¹H-NMR (500 MHz, DMSO-*d*₆):

δ 13.05 (br s, 1H), 8.43 (s, 1H), 8.20 (d, *J* = 9.5 Hz, 1H), 6.56 (d, *J* = 9.5 Hz, 1H), 6.23 (s, 1H), 3.89 (s, 3H), 3.35 (d, *J* = 7.0 Hz, 4H), 2.09-2.03 (m, 2H), 0.91 (d, *J* = 6.5 Hz, 12H)

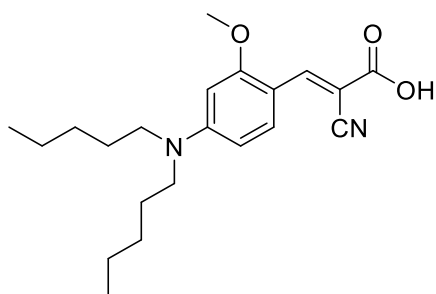
¹³C-NMR (125 MHz, DMSO-*d*₆):

δ 166.1, 162.1, 155.0, 146.9, 130.4, 119.2, 108.3, 106.9, 94.7, 91.6, 59.5, 56.4, 27.2, 20.6.

Anal. Calcd for C₁₉H₂₆N₂O₃ (330.43): C 69.06, H 7.93, N 8.48.

Found: C 68.93, H 7.81, N 8.58

HRMS (ESI) m/z: calc'd for C₁₇H₂₂N₂O₃ [M+Na]⁺: 353.18, found 353.18



(*E*)-2-cyano-3-(4-(dipentylamino)-2-methoxyphenyl)acrylic acid, **3d**

¹H-NMR (500 MHz, DMSO-*d*₆):

δ 8.43 (s, 1H), 8.22 (d, *J* = 9.5 Hz, 1H), 6.50 (d, *J* = 9.5 Hz, 1H), 6.17 (s, 1H), 3.90 (s, 3H),
3.43 (t, *J* = 7.5 Hz, 4H), 1.58 (m, 4H), 1.37-1.30 (m, 8H), 0.91 (t, *J* = 6.5 Hz, 6H)

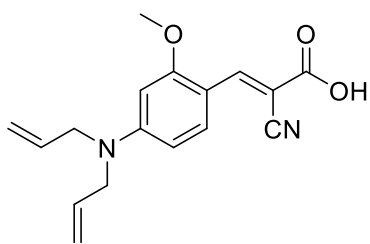
¹³C-NMR (125 MHz, DMSO-*d*₆):

δ 166.2, 162.4, 154.7, 146.9, 130.6, 119.3, 108.2, 106.2, 93.8, 91.4, 56.4, 50.9, 29.2, 27.3,
22.7, 14.7

Anal. Calc'd for C₂₁H₃₀N₂O₃ (358.48): C 70.36, H 8.44, N 7.81.

Found: C 70.36, H 8.50, N 7.81

HRMS (ESI) m/z: calc'd for C₁₇H₂₂N₂O₃ [M+Na]⁺: 381.22, found 381.21



(*E*)-2-cyano-3-(4-(diallylamino)-2-methoxyphenyl)acrylic acid, **3e**

¹H-NMR (500 MHz, CD₃OD):

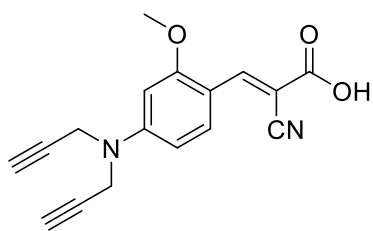
δ 8.59 (s, 1H), 8.28 (d, *J* = 9.0 Hz, 1H), 6.44 (d, *J* = 9.5 Hz, 1H), 6.25 (s, 1H), 5.96-5.89 (m, 2H), 5.25-5.19 (m, 4H), 4.11-4.10 (m, 4H), 3.88 (s, 3H)

¹³C-NMR (125 MHz, CD₃OD):

δ 166.5, 162.3, 155.4, 147.9, 132.8, 130.4, 118.2, 115.9, 109.4, 105.6, 93.9, 55.0, 52.9.

Anal. Calcd for C₁₇H₁₈N₂O₃ (298.34): C 68.44, H 6.08, N 9.39.

Found: C 68.14, H 6.16, N 9.30



(*E*)-2-cyano-3-(4-(diallylamino)-2-methoxyphenyl)acrylic acid, **3f**

¹H-NMR (500 MHz, DMSO-*d*₆):

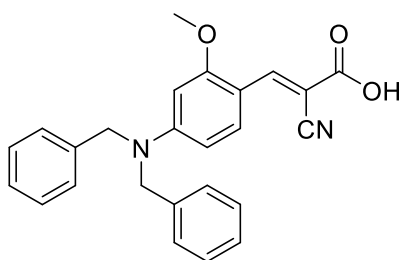
δ 8.51 (s, 1H), 8.24 (d, *J* = 9.0 Hz, 1H), 6.71 (d, *J* = 9.0 Hz, 1H), 6.55 (s, 1H), 4.41 (s, 4H),
3.94 (s, 3H), 3.30 (s, 2H)

¹³C-NMR (125 MHz, DMSO-*d*₆):

δ 165.49, 161.70, 153.81, 147.48, 130.14, 118.50, 110.52, 107.58, 96.97, 95.39, 79.90,
76.17, 56.70.

Anal. Calcd for C₁₇H₁₄N₂O₃ (294.31): C 69.38, H 4.79, N 9.52.

Found: C 69.89, H 4.99, N 9.78



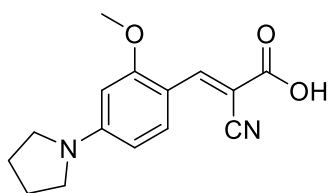
(*E*)-2-cyano-3-(4-(dibenzylamino)-2-methoxyphenyl)acrylic acid, **3g**

¹H-NMR (500 MHz, DMSO-*d*₆):

δ 8.36 (s, 1H), 8.10 (d, *J* = 7.5 Hz, 1H), 7.33-7.27 (m, 10H), 6.53 (d, *J* = 6.5 Hz, 1H), 6.30 (s, 1H), 4.86 (s, 4H), 3.66 (s, 3H)

¹³C-NMR (125 MHz, DMSO-*d*₆):

δ 165.7, 161.8, 155.2, 147.0, 138.3, 130.3, 129.3, 127.8, 127.4, 118.8, 106.2, 106.8, 95.4, 93.2, 56.2, 54.9



(*E*)-2-cyano-3-(2-methoxy-4-(pyrrolidin-1-yl)phenyl)acrylic acid, **3h**

¹H-NMR (500 MHz, DMSO-*d*₆):

δ 8.43 (s, 1H), 8.20 (d, *J* = 9.0 Hz, 1H), 6.35 (d, *J* = 7.5 Hz, 1H), 6.09 (s, 1H), 3.90 (s, 3H),
3.41 (m, 4H), 1.99 (m, 4H)

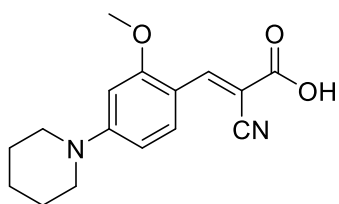
¹³C-NMR (125 MHz, DMSO-*d*₆):

δ 166.2, 162.2, 153.8, 147.1, 130.4, 119.4, 108.4, 106.6, 94.2, 90.8, 56.4, 48.3, 25.5.

Anal. Calc'd for C₁₅H₁₆N₂O₃ (272.30): C 66.16, H 5.92, N 10.29.

Found: C 65.21, H 5.95, N 9.92

HRMS (ESI) m/z: calc'd for C₁₇H₂₂N₂O₃ [M+Na]⁺: 295.11, found 295.10



(*E*)-2-cyano-3-(2-methoxy-4-(piperidin-1-yl)phenyl)acrylic acid, **3i**

¹H-NMR (500 MHz, DMSO-*d*₆):

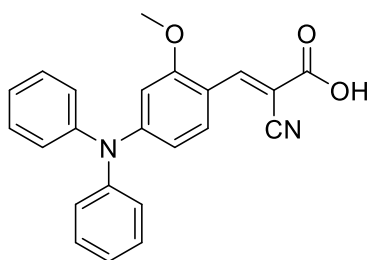
δ 8.40 (s, 1H), 8.17 (d, *J* = 9 Hz, 1H), 6.68 (d, *J* = 9.5 Hz, 1H), 6.43 (s, 1H), 3.87 (s, 3H),
3.50 (m, 4H), 1.60 (m, 6H)

¹³C-NMR (125 MHz, DMSO-*d*₆):

δ 165.7, 162.2, 156.2, 146.7, 130.3, 118.8, 109.0, 107.2, 95.5, 56.4, 48.1, 25.6, 24.4

Anal. Calcd for C₁₆H₁₈N₂O₃ (286.33): C 67.12, H 6.34, N 9.78

Found: C 66.43, H 6.22, N 9.80



(*E*)-2-cyano-3-(4-(diphenylamino)-2-methoxyphenyl)acrylic acid, **3j**

¹H-NMR (500 MHz, DMSO-*d*₆):

δ 8.44 (s, 1H), 8.11 (d, *J* = 9.0 Hz, 1H), 7.43 (m, 5H), 7.25 (m, 5H), 6.43 (d, *J* = 9.5 Hz, 1H), 6.41 (s, 1H), 3.65 (s, 3H)

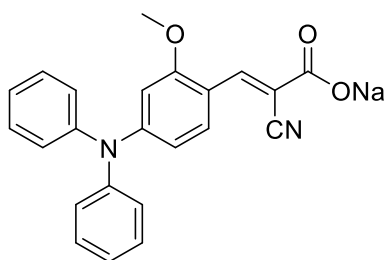
¹³C-NMR (125 MHz, DMSO-*d*₆):

δ 165.2, 161.2, 154.6, 147.1, 145.7, 130.7, 130.3, 127.4, 126.6, 118.1, 112.6, 111.7, 100.9, 97.1, 56.3.

Anal. Calc'd for C₂₃H₁₈N₂O₃ (370.41): C 67.97, H 5.46, N 6.89

Found: C 66.0, H 5.39, N 6.28

HRMS (ESI) m/z: calc'd for C₁₇H₂₂N₂O₃ [M+Na]⁺: 393.12, found 393.12



Sodium (*E*)-2-cyano-3-(4-(diphenylamino)-2-methoxyphenyl)acrylate, **sodium salt of 3j**

¹H-NMR (500 MHz, DMSO-*d*₆):

δ 8.14 (s, 1H), 7.95 (d, *J* = 14.0 Hz, 1H), 7.36 (m, 4H), 7.14 (m, 6H), 6.45 (m, 2H), 3.61 (s, 3H)

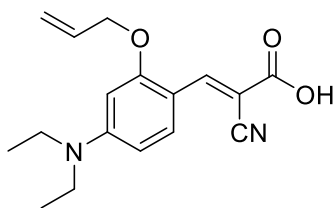
¹³C-NMR (125 MHz, CDCl₃):

δ 165.2, 159.5, 151.8, 146.7, 141.8, 130.5, 129.4, 126.3, 125.4, 120.8, 115.6, 113.2, 110.4, 103.6, 56.1.

Anal. Calcd for C₂₃H₁₇N₂NaO₃ (392.39): C 64.48, H 4.94, N 6.54

Found: C 64.08, H 5.06, N 6.46

HRMS (ESI) m/z: calc'd for C₁₇H₂₂N₂O₃ [M+Na]⁺: 415.10, found 415.10



(*E*)-3-(2-(allyloxy)-4-(diethylamino)phenyl)-2-cyanoacrylic acid, **3k**

¹H-NMR (500 MHz, D₂O):

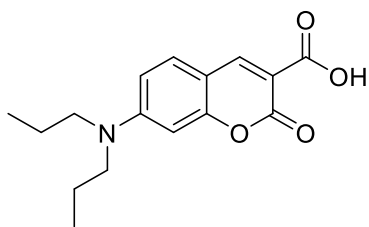
δ 8.21 (s, 1H), 7.80 (d, *J* = 10.0 Hz, 1H), 5.97-5.84 (m, 2H), 5.71 (s, 1H), 5.24 (d, *J* = 17.5 Hz, 1H), 5.15 (d, *J* = 10.5 Hz, 1H), 4.67 (s, 1H), 4.30 (d, *J* = 5.5 Hz, 2H), 3.08-3.04 (m, 4H), 0.93-0.85 (m, 6H)

¹³C-NMR (125 MHz, D₂O):

δ 170.74, 159.94, 152.55, 145.89, 133.11, 129.76, 121.35, 117.48, 108.22, 104.88, 97.02, 94.39, 69.09, 44.51, 12.07

Anal. Calcd for C₁₇H₂₀N₂O₃ (300.36): C 67.98, H 6.71, N 9.33

Found: C 67.86, H 6.75, N 9.29



7-(dipropylamino)-2-oxo-2H-chromene-3-carboxylic acid, **4c**

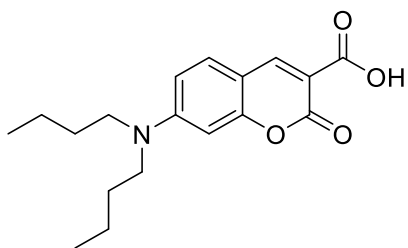
¹H-NMR (500 MHz, DMSO-*d*₆): δ 12.51 (s, 1H), 8.60 (s, 1H), 7.64 (d, *J* = 9.0 Hz, 1H), 6.70 (dd, *J* = 9.0, 2.5 Hz, 1H), 6.58 (s, 1H), 3.40 (t, *J* = 8.0 Hz, 4H), 1.62-1.55 (m, 4H), 0.92 (t, *J* = 7.5 Hz, 6H)

¹³C-NMR (125 MHz, DMSO-*d*₆):

δ 165.21, 160.24, 158.53, 154.12, 150.15, 132.44, 110.95, 108.09, 107.88, 96.80, 52.67, 20.70, 11.69

Anal. Calcd for C₁₆H₁₉NO₄ (289.33): C 66.42, H 6.62, N 4.84

Found: C 66.54, H 6.76, N 4.91



7-(dibutylamino)-2-oxo-2H-chromene-3-carboxylic acid, **4d**

¹H-NMR (500 MHz, DMSO-d₆):

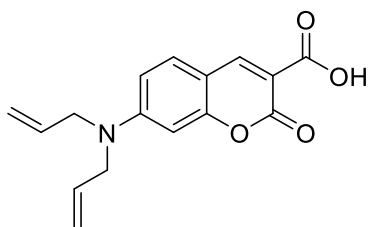
δ 8.59 (s, 1H), 7.64 (d, *J* = 9.0 Hz, 1H), 6.78 (d, *J* = 9.0 Hz, 1H), 6.54 (s, 1H), 3.42 (t, *J* = 7.5, 4H), 1.57-1.51 (m, 4H), 1.39-1.33 (m, 4H), 0.931 (t, *J* = 7.5 Hz, 6H)

¹³C-NMR (125 MHz, DMSO-d₆):

δ 165.20, 160.23, 158.51, 154.00, 150.14, 132.46, 110.89, 108.08, 107.86, 96.74, 50.88, 29.61, 20.22, 14.52

Anal. Calcd for C₁₈H₂₃NO₄ (317.39): C 68.12, H 7.30, N 4.41

Found: C 68.16, H 7.35, N 4.50



7-(diallylamino)-2-oxo-2H-chromene-3-carboxylic acid, **4e**

¹H-NMR (500 MHz, CDCl₃):

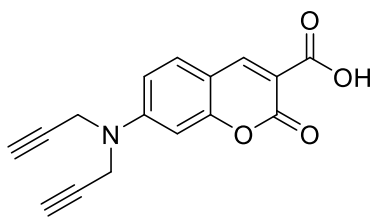
δ 12.35 (s, 1H), 8.67 (d, *J* = 5.0 Hz, 1H), 7.47 (dd, *J* = 9.0, 3.0 Hz, 1H), 6.70 (d, *J* = 7.5 Hz, 1H), 6.59 (s, 1H), 5.90-5.83 (m, 2H), 5.29 (d, *J* = 10 Hz, 2H), 5.20 (d, *J* = 17 Hz, 2H), 4.08 (d, *J* = 2.5 Hz, 4H)

¹³C-NMR (125 MHz, CDCl₃):

δ 165.65, 164.52, 157.92, 155.15, 150.73, 132.03, 131.34, 117.77, 111.82, 109.42, 106.73, 98.16, 53.53

Anal Calc'd for C₁₆H₁₅NO₄ (285.30): C 67.36, H 5.30, N 4.91

Found: C 67.38, H 5.19, N 4.98

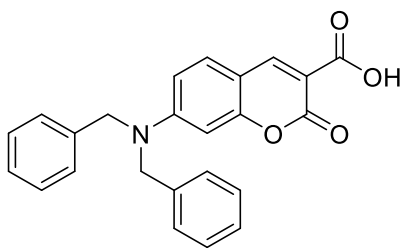


7-(di(prop-2-yn-1-yl)amino)-2-oxo-2H-chromene-3-carboxylic acid, **4f**

¹H-NMR (500 MHz, DMSO-*d*₆): δ 8.67 (s, 1H), 7.77 (d, *J* = 9.0 Hz, 1H), 6.99 (dd, *J* = 9.0, 2.5 Hz, 1H), 6.82 (s, 1H), 4.39 (d, *J* = 2.0 Hz, 4H), 3.28 (t, *J* = 2.0 Hz, 2H)

¹³C-NMR (125 MHz, DMSO-*d*₆): 165.21, 160.25, 158.54, 154.12, 150.15, 132.44, 110.95, 108.10, 107.88, 52.70, 52.67, 20.70, 11.69

Anal. Calcd for C₁₆H₁₁NO₄ (281.27): C 68.32, H 3.94, N 4.98 Found: C 68.39, H 3.97, N 4.86



7-(dibenzylamino)-2-oxo-2H-chromene-3-carboxylic acid, **4g**

¹H-NMR (500 MHz, CDCl₃):

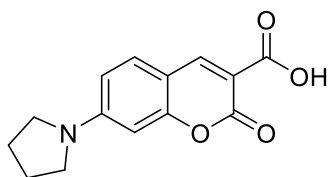
δ 12.31 (s, 1H), 8.69 (s, 1H), 7.48-7.23 (m, 11H), 6.86 (dd, *J* = 8.5, 1.5 Hz, 1H), 6.67 (s, 1H), 4.84 (s, 4H)

¹³C-NMR (125 MHz, CDCl₃):

δ 165.53, 164.24, 157.89, 155.60, 150.75, 135.84, 132.23, 129.46, 128.16, 126.52, 112.02, 109.79, 107.24, 98.63, 55.03

Anal. Calc'd for C₂₄H₁₉NO₄ (385.42): C 74.79, H 4.97, N 3.63

Found: C 74.87, H 4.56, N 3.84



2-oxo-7-(pyrrolidin-1-yl)-2H-chromene-3-carboxylic acid. **4h**

¹H-NMR (500 MHz, CDCl₃):

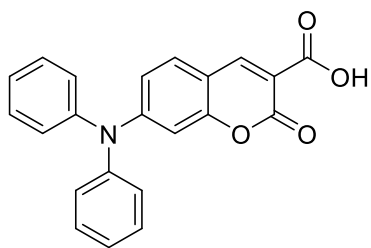
δ 12.38 (s, 1H), 8.68 (s, 1H), 7.47 (d, *J* = 8.0 Hz, 1H), 6.64 (d, *J* = 7.0 Hz, 1H), 6.44 (s, 1H), 3.49 (m, 4H), 2.15 (m, 4H)

¹³C-NMR (125 MHz, CDCl₃):

δ 165.76, 164.56, 158.00, 153.43, 150.72, 132.01, 111.95, 109.06, 105.99, 97.66, 48.48, 25.55

Anal. Calc'd for C₁₄H₁₃NO₄ (259.26): C 64.86, H 5.05, N 5.40

Found: C 64.21, H 4.87, N 5.12



7-(diphenylamino)-2-oxo-2H-chromene-3-carboxylic acid, **4i**

¹H-NMR (500 MHz, DMSO-d₆):

δ 12.83 (s, 1H), 8.62 (s, 1H), 7.66 (d, *J* = 8.00 Hz, 1H), 7.46-7.23 (m, 10H), 6.72 (d, *J* = 7.0 Hz, 1H), 6.44 (s, 1H)

¹³C-NMR (125 MHz, DMSO-d₆):

δ 164.93, 158.22, 157.26, 153.94, 149.55, 145.52, 132.12, 130.90, 127.56, 126.99, 115.56, 112.59, 111.40, 103.32

6.11 Western blot of RBE4, MDA-MB-231, WiDr and 4T1-luc2 cell lines

The cells were grown to confluence in a 75 cm² culture flask and the growth medium was removed. The cells were washed twice with 1X phosphate buffered saline (PBS) and lysed by adding 200 µL of SDS boiling buffer (5% SDS, 10% glycerol, and 60mM tris base and pH to 6.8) and scraped into a 1.6 mL Eppendorf vial. The cells were homogenized and denatured at 90°C for 10 minutes and stored at -80°C until further use. Cell lysates were equilibrated using BCA protein assay and equal protein amounts (10 µg) were loaded on to the polyacrylamide gel along with precision ladder for standard electrophoresis at 60 mA for ~1 hour. The proteins were then transferred on to a nitrocellulose membrane under 200 mA for 1.5 hours. The membranes were then blocked using 10% milk block in PBST and treated with 1^o antibody at -4°C overnight. Next day, the membranes were washed with PBST and treated with 2^o antibody for 1 hour at 37°C. The membranes were once again washed and treated with a mixture of luminol supersignal® west pico luminol enhancer and supersignal® west pico stable peroxide solution for two minutes. The membranes were then imaged and analyzed using Licor imager.

6.12 MCT1 inhibition using ¹⁴C-lactate uptake assay

Briefly, 2×10^5 cells/mL were seeded in a 24-well plate (500 μ L in each well) and incubated for 18-24 hours prior to the addition of the test compounds. The growth media in the wells was washed twice with HEPES buffer at pH 7.43 (140 mM NaCl, 5 mM KCl, 2 mM CaCl₂, 2 mM MgCl₂, and 10 mM HEPES). Test compounds were diluted in a solution containing 3 μ M ¹⁴C-lactic acid sodium salt, 2 μ M lactic acid sodium salt, and HEPES buffer. Test compounds were added to the wells and incubated for 20 minutes. This solution was then replaced with ice-cold cold buffer containing 100 μ M CHC and placed on ice. The wells were washed three times with cold buffer and a solution of 0.1 M NaOH in 5% triton X-100 was added to solubilize the cells. This solution was then transferred to a 7 mL plastic scintillation vial that contained 4 mL of ecolite (+). The vials were then placed in a Beckman scintillation counter to obtain dpm readings for ¹⁴C content. The % uptake and % inhibition of lactate were then obtained using % uptake = (Test compound/DMSO control)x100, and % inhibition = 100-(% uptake). The % inhibition values were then plotted on y-axis and logC were plotted on x-axis in GraphPad Prism and analyzed using interpolation of sigmoidal curve in four-parameter logistic logC to obtain IC₅₀ values.

6.13 MCT4 inhibition using ¹⁴C-lactate uptake assay

Briefly, 4×10^5 cells/mL were seeded in a 24-well plate (500 μ L in each well) and incubated for 18-24 hours prior to the addition of the test compounds. The growth media in the wells was washed twice with HEPES buffer (pH 7.40). Test compounds were diluted in a solution containing 3 μ M ¹⁴C-lactic acid sodium salt, 2 μ M lactic acid sodium salt, and HEPES buffer. Test compounds were added to the wells and incubated for 1 hour. This solution was then replaced with ice-cold cold buffer (pH 7.43) containing 100 μ M CHC and placed on ice. The wells were washed three times with cold buffer and a solution of 0.1 M NaOH in 5% triton X-100 was added to solubilize the cells. This solution was then transferred to a 7 mL plastic scintillation vial that contained 4 mL of ecolite (+). The vials were then placed in a Beckman scintillation counter to obtain dpm readings for ¹⁴C content. The IC₅₀ values were calculated using same procedure as MCT1 ¹⁴C-lactate uptake assay.

6.14 *Sulforhodamine-B assay*

Briefly, 5×10^4 cells/mL (400 μ L) were plated in 48-well plates and incubated in 5% CO₂ atmosphere at 37°C for 24 hours. Stock solution of compound was made up at 250 mM concentration in DMSO. The final concentration of DMSO in the wells were < 0.01%. Concentration range of compounds from 250 μ M to 0.98 μ M was tested by adding 2x concentration of test compound to the first well and then the serial dilutions by going from well to well. All the compounds were tested in duplicates. After 72 hours of treatment, growth media was aspirated, and the cells were washed with 1x PBS. The plates were left to be dried at room temperature overnight and SRB assay was performed. 100 μ L of 0.5% SRB (0.5 g of SRB dissolved in 1% acetic acid) was added in each well and incubated at 37°C for 45 minutes. SRB solution was removed and the wells were washed three times with 1% acetic acid solution and dried at room temperature overnight. The fixed cells were dissolved in 400 μ L of 10 mM Tris base (pH 10.2) and absorbance was recorded at 540 nm using BioTek Synergy 2 plate reader. The absorbance is directly proportional to the cell survival. % Survival was calculated using the formula

$$\% \text{ survival} = (\text{absorbance of test compound} / \text{absorbance of control}) \times 100\%.$$

IC₅₀ was calculated using GraphPad Prism software, by plotting a dose-response curve with log[concentration] on x-axis and % survival on y-axis and analyzing via nonlinear regression with variable slope.

6.15 MTT assay

Cells (5×10^3 cells/well) were cultured in 96-well plates and incubated for 24 hours. Stock solution of compound was made up at 250 mM concentration in DMSO. The final concentration of DMSO in the wells were $< 0.01\%$. Concentration range of compounds from 250 μM to 0.98 μM was tested by adding 2x concentration of test compound to the first well and then the serial dilutions by going from well to well. All the compounds were tested in duplicates. After 72 hours of treatment, 10 μL of MTT (5 mM in 1x PBS) was added into the wells and the cells were incubated for a period of 4 hours. At this point, the conversion of MTT to formazan was quenched by the addition of 100 μL of SDS (1 g of SDS dissolved in 0.01 N HCl) and the cells were incubated for further 4 hours. The absorbance was recorded at 570 nm using BioTek Synergy 2 plate reader. The absorbance is directly proportional to the cell viability. % Survival was calculated using the formula $\% \text{ survival} = (\text{absorbance of test compound} / \text{absorbance of control}) \times 100\%$.

IC_{50} was calculated using GraphPad Prism software, by plotting a dose-response curve with $\log[\text{concentration}]$ on x-axis and % survival on y-axis and analyzing via nonlinear regression with variable slope.

6.16 MTT assay in hypoxic conditions

Cells (5×10^3 cells/well) were cultured in 96-well plates and incubated for 24 hours. After the addition of test compounds, the plates were placed in a hypoxic chamber (flushed with 10% CO₂, 1% O₂ and 89% N₂ for 5 minutes) and incubated for 72 hours. The plates were processed and IC₅₀ was calculated same as the MTT assay as described in the previous page.

6.17 Cell cycle analysis using propidium iodide

5×10^5 MDA-MB-231 and WiDr cells were seeded in 10 cm culture dishes and incubated for 24 hours at 37°C in 5% CO₂ atmosphere. Cells were then treated with test compound at concentrations corresponding to 1X and 2X the IC₅₀ value of cell proliferation inhibition as indicated by the MTT assay for 24 hours (one cell cycle). 0.1% DMSO treated cells were used as negative control. Cells were then rinsed with cold PBS, trypsinized and fixed in 85% ethanol for at least one hour at -20°C. Cells were then resuspended in DNA-staining solution (20 µg/mL propidium iodide (Sigma, Cat. No. P4170, PI), 100µg/mL RNase A (Machery-Nagel GmbH & Co., cat. no. R1622S), in PBS containing 0.1% sodium citrate and 0.05% Tween (PBST)) and incubated for 30 min at 37°C. Cellular PI content was then analyzed through flow cytometry using a Becton Dickinson FACSCalibur flow cytometer. Doublet-discrimination was performed by gating single cell populations (PI-width:PI-area). Histograms were generated, and intracellular accumulation of PI resulted in fluorescent intensities corresponding to 2N DNA (G₀/G₁ phase) 4N DNA (G₂/M phase), and between 2N and 4N DNA (S phase) which were deconvoluted with ModFitLT 5.0 software. Data shown are representative of at least three independent experiments.

6.18 Ethical Considerations for animal studies

The experimental procedures involving animals that were conducted at the University of Minnesota Duluth were in compliance with the U.S. National Institutes of Health Guide for Care and Use of Laboratory Animals and approved by the Institutional Animal Care and Use Committee at the University of Minnesota (UMN). The remaining animal studies were conducted by GenScript Corporation (Piscataway, NJ) according to their approved IACUC protocols. The following is the list of IACUC protocols for all the animal studies conducted for this thesis.

Systemic toxicity study in CD-1 mice: IACUC1307-30773A and 1311-31063A (UMN)

WiDr flank model in BALB/c mice: IACUC075.03

WiDr chemoprevention study in BALB/c mice: GSIACUC-184115

Pharmacokinetic study in CD-1 mice: IACUC 003.04

GL261-luc2 study in C57BL/6J mice: 1312-31108A (UMN)

MDA-MB-231-luc study using **4g** in SCID Beige mice: GS-PAMD1401SN052

MDA-MB-231-luc flank study using **3j** and Dox in NOD SCID mice: GSIACUC-363793
and GS-PANM1301SN024

MDA-MB-231-luc, MDA-MB-231-luc + 3T3 MEF WT and MDA-MB-231-luc + 3T3
MEF KO orthotopic studies using **3j** and Dox in NOD SCID mice: IACUC 1411-32085A
(UMN)

6.19 General procedure for systemic toxicity evaluation

Mice were procured from Charles River, and acclimatized at room temperature for a period of 7 days. The mice were weighed and randomized into groups (n = 6 mice per group) based on same average weights. Mice were housed as two mice per cage. One of the mice was identified by marking the tail with a black sharpie. Treatment was started via i.p. or oral gavage and body weights were monitored for a period of 14-21 days. At the end of the study, mice were euthanized using CO₂, followed by decapitation.

6.20 Anticancer efficacy of compound 3j in MCT1 expressing WiDr flank model

5 x 10⁶ WiDr cells were suspended in a mixture of 1:1 matrigel-PBS and loaded on to a 0.3 mL syringe and the syringe was kept on ice until mice were ready to be injected. These cells were then injected subcutaneously onto the right flank of BALB/c nude mice and tumors were measured via calipers and the tumor volume was calculated using the formula

$$V = \frac{1}{2} \times a \times b^2$$

where 'a' is the long diameter of the tumor and 'b' is the short diameter of the tumor. Mice were assigned into groups (n = 8 mice per group) when the average tumor volume reached 117 mm³ and the treatment was initiated and continued for a period of 21 days. Tumor volume was recorded every 2-3 days and at the end of the study, mice were euthanized, and tumors were resected and weighed. The tumor growth inhibition amount was determined using the formula

$$\% \text{ inhibition} = \frac{(C-T)}{C} \times 100$$

where C is average tumor weight of the control group and T is the average tumor weight of the test group.

6.21 Chemoprevention study of compound 3j in MCT1 expressing WiDr flank model

In this study, BALB/c nude mice were injected subcutaneously with 5×10^6 WiDr cells and the mice were randomly assigned ($n = 8$ mice per group) based on average body weights and the treatment was initiated on day-6 of tumor inoculation. On day-21 of tumor inoculation, the study was terminated, and tumors were resected and weighed. During the study, tumor volume was recorded every 2-3 days via caliper measurements.

6.22 Anticancer efficacy of MCT1 inhibitor in 4T1-luc2 flank model

In this study, 1×10^5 4T1-luc2 cells in a mixture of 1:1 PBS-matrigel were implanted on the right flank of BALB/c mice. The mice were randomly assigned into groups on day-3 of tumor inoculation and the treatment was initiated on the same day and continued for a period of 21 days. During this time, tumor volumes were recorded every 2-4 days via caliper measurements.

6.23 Evaluation of pharmacokinetic parameters in CD-1 mice

For this study, 60 CD-1 mice were separated into 2 groups with $n = 30$ mice per group, for intraperitoneal (ip) and intragastrical (oral gavage) administration of compound **3j**. The mice in these two groups were further assigned into 10 groups with $n = 3$ mice per each time point for blood collection via orbital sinus method. All these mice were injected with 100 mg/Kg of compound **3j** via ip and oral gavage in groups 1 and 2, respectively. Blood collection times after the treatment of compound was 0, 0.083, 0.25, 0.5, 1, 2, 4, 6, 8, 24 hours. After extracting blood in anticoagulant tubes, the mice were euthanized immediately. Blood samples were maintained at room temperature for 30 minutes and then placed in ultracentrifuge with 10,000 rpm for 5 minutes at 4°C. After plasma was separated from the blood samples, the resulting serum was then used immediately for analysis of concentration of **3j** using LC-MS/MS or stored at -80°C. Pharmacokinetic parameters maximum plasma concentration (C_{max}), time of maximum drug concentration (T_{max}), half-life of the drug ($t_{1/2}$), area under the curve (AUC_{0-last}), apparent total drug clearance (CL/F), etc. were then obtained using standard non-compartmental model.

LC-MS/MS method was used for analysis of compound **3j** in mouse plasma. The HPLC system included ternary pumps (model LC-20AD, Shimadzu), a solvent degasser (model DGU-20A5, Shimadzu), an autosampler (model SIL-20AC, Shimadzu), a column oven (model CTO-20A) and a system controller for communication (model CBM-20A, Shimadzu). The conditions of HPLC are shown in Table 6a.

Table 6a: HPLC conditions of analyte and internal standard (diazepam)

Column	ACE phenyl column (4.6 × 50 mm, 5 μm, S/N: A63134)		
Mobile Phase	Time (min)	Phase A	Phase B
	0.01~0.50	80%	20%
	0.50~1.50	80→10%	20→90%
	1.50~2.50	10%	90%
	2.50~2.70	10→80%	90→20%
	3.70~3.50	80%	20%
	Total flow	1.0 mL/min	
Autosampler Cooler Temp.	10°C		
Oven Temp.	35°C		
Valco Valve	Total Time (min)	Position	
	1.0	B	
	3.0	A	
RT (min)	3j: 2.34 min; Diazepam: 2.23 min.		

The analyte was detected and quantified using a triple quadrupole mass spectrometer (API4000, Applied Biosystems) equipped with a Turbo IonsprayTM interface. The mass spectrometer was operated in the positive ionization mode with multiple reactions monitoring (MRM). Analyst[®] 1.5 was used to control the mass spectrometer and to analyze and process data.

6.24 Protein binding studies

The assay was performed in a 96-well format in a dialysis block constructed from Teflon. The dialysate compartment was loaded with PBS (pH 7.4) and the sample side was loaded with 1:1 mixture of test compound (10 μ M) and protein matrix (human bovine albumin). Protein matrix without test compound (without dialysis) was considered as control. The dialysis plate was sealed and incubated at 37 °C for 4 h. Samples from each compartment were diluted with PBS, followed by addition of acetonitrile and centrifuged. The supernatants were analyzed using HPLC-MS/MS analysis. The percent of test compound bound to proteins and the recovery were calculated as *Protein binding* % = $\frac{area_p - area_b}{area_p} \times 100$ and *Recovery* % = $\frac{area_{p+} + area_b}{area_c} \times 100$, where $area_p$ = peak area of analyte in the protein matrix, $area_b$ = peak area of analyte in the assay buffer and $area_c$ = peak area of analyte in control sample. The recovery determination serves as an indicator of reliability of the calculated protein binding value.

6.25 Caco-2 permeability studies

Briefly, Caco-2 cells were seeded at 1×10^5 cells/cm² in 96-well Multiscreen™ plates (Millipore). Permeability assays were performed with the cells at day 21-25 post-seeding. Test compounds (10 μ M in HEPES pH 7.4) were added to the donor side and was incubated at 37 °C with gentle shaking for 60 min for A-B and 40 min for B-A assay. Samples were aliquoted from the donor side at time zero and the end point, and from the receiver side at the end point. Samples were analyzed by HPLC-MS/MS using selected reaction monitoring. Fluorescein permeability was assessed in the A-B direction at pH 7.4

on both sides after the permeability assay with test compounds. The cell monolayer with a fluorescein permeability of less than 1.5×10^{-6} cm/s was considered intact. The apparent permeability coefficient (P_{app}) of the test compound and its recovery were calculated as

$$P_{app}(\text{cm/s}) = \frac{V_R \times C_{R,end}}{\Delta t} \times \frac{1}{A \times (C_{D,mid} - C_{R,mid})} \quad \text{and} \quad \text{Recovery}(\%) = \frac{V_D \times C_{D,end} + V_R \times C_{R,end}}{V_D \times C_{D0}} \times 100,$$

where A = surface area of the cell monolayer (0.11 cm^2), C = concentration of the test compound expressed as peak area, D = donor and R = receiver, 0, mid, and end denote time zero, mid-point, and end of the incubation, Δt = incubation time and V = volume of the donor or receiver.

6.26 Microsomal stability studies

Test compounds were pre-incubated with pooled liver microsomes in phosphate buffer (pH 7.4) for 5 min in a 37°C shaking water bath. The reaction was initiated by adding 10mM NADPH and incubated for 0, 15, 30, 45, and 60 min and the reaction was quenched by adding acetonitrile/methanol. Samples were then mixed vigorously, centrifuged and supernatants were analyzed using HPLC-MS/MS where the peak areas corresponding to the test compound were recorded. The compound remaining was calculated by comparing the peak area at each time point to time zero. The half-life was calculated from the slope of the initial linear range of the logarithmic curve of compound remaining (%) vs. time, assuming first order kinetics. The intrinsic clearance (CL_{int}) was calculated from the half-life using the following equation.

$$CL_{int} (\mu\text{L}/\text{min}/\text{mg protein}) = \frac{0.693}{T_{\frac{1}{2}} \times \text{protein conc.}}$$

6.27 Seahorse XFe96[®] assessment of glycolysis and mitochondrial respiration

20,000 cells/well were plated in 96-well Seahorse plates (Agilent, part no. 101085-004) and incubated 16-24 hours at 37°C at 5% CO₂. Flux pack sensors (Agilent, part no. 102416-100) were hydrated with XF calibrant solution (Agilent, part no. 100840-000) overnight at 37°C in a non-CO₂ incubator. Serum free assay media were prepared using Seahorse base medium (Agilent, part no. 102353-100) with the addition of glutamine (1mM) and sodium pyruvate (1mM) for glycolysis stress test, whereas for mitochondrial stress test, glucose (10mM), glutamine (1μM), and sodium pyruvate (1mM) were used. The pH of these media was adjusted to 7.4 and warmed to 37°C. An 8X stock concentration of test compounds was prepared for microplate injections in port A. Stock solutions of glucose, oligomycin, and 2-deoxyglucose (Chem Impex) were prepared such that their final working concentrations are 10mM, 1μM and 50mM, respectively, for glycolysis stress test. For mitochondrial stress test, stock solutions of oligomycin, FCCP, rotenone+antimycin A were prepared such that their final concentrations are 1 μM, 0.25-1 μM, and 0.5μM, respectively. Under glycolytic stress test, the cells were treated with test compounds, followed by the addition of glucose, oligomycin and 2-deoxyglucose at 14.29, 33.8, 53.35, 72.87 minutes, respectively. Under mitochondrial stress test, cells were treated with test compounds, followed by the addition of oligomycin, FCCP, and rotenone+antimycin A, at 14.29, 33.8, 53.35, 72.87 minutes, respectively. Extracellular acidification rates (ECAR) and oxygen consumption rates (OCR) were recorded in real-time for glycolysis and mitochondrial stress tests, respectively, using a Seahorse XFe96[®] analyzer (Agilent). The

parameters related to glycolytic and mitochondrial functions were calculated utilizing the Wave 2.4.0 software (Agilent) according to manufactures protocol.

6.28 Florescence microscopy study

The cells (2 mL) were seeded at a concentration of 5×10^4 cells/mL in a 2 cm MatTek (MatTek Corp, #P35G010C) culture dish with glass bottom and were incubated at 37°C in 5% CO₂ atmosphere for 48 hours. The growth medium was removed and 2 mL of fresh growth medium with compound 3j at IC₅₀ concentration was added to the culture dish. The cells were incubated for a period of one hour, and the medium was aspirated and washed once with 5% FBS in 1X PBS solution, and further 2 mL of 5% FBS was added to the culture dish. The cells were then imaged to observe the localization of compound in the cells. In the case of MitoTracker Red CMXRos (Invitrogen, M7512), the compound was incubated for 45 minutes, and a 20 µL solution of mitotracker red (100 nM) was added to the cells and further incubated for 15 minutes and cells were washed and replaced with 5% FBS solution for imaging.

6.29 Anticancer efficacy in MDA-MB-231-luc flank xenograft tumor model

In this study, NOD SCID mice were injected subcutaneously with 1×10^7 MDA-MB-231-luc cells and the mice were randomly assigned into groups (n = 6 mice per group) when the average tumor volumes reached 195-280 mm³ and the treatment was initiated. After a period of 20 day-treatment, the study was terminated, and tumors were resected and weighed. During the study, tumor volume was recorded every 2-3 days via caliper measurements.

6.30 Anticancer efficacy of lead MCT inhibitor 3j in MDA-MB-231-luc orthotopic model

After procuring mice, they were acclimatized for a week. Mice were anesthetized under 5% isoflurane and surgical incision site was scrubbed with a disinfective agent betadine starting from the center of the site and moving outwards and repeated with 70% ethanol and repeated until the surgical site is free of debris. Then, a 5 mm dorsoventral incision is made through the skin close to the nipple of the 4th mammary gland. The skin is reflected and 5×10^6 MDA-MB-231-luc cells (in 50 μ L of 1:1 PBS and Matrigel) were transplanted in the gland. The incision then was closed with wound clips in skin and mice were injected with 5 mg/kg ketofen (sc) at the end of surgery, and three days post-surgery. Mice were monitored for three days post-surgery for wound healing at the site of incision, food and water intake, bedding, grooming, posture, etc. Once the tumors reached ~ 150 mm³ average volume, mice were randomized into groups (n = 6 mice per group) and the treatment was initiated. Compounds **3j** and Dox were administered intraperitoneally for a period of 9 days. Tumor volumes were recorded via caliper measurements every 2-3 days.

6.31 Anticancer efficacy of lead MCT inhibitor 3j in MDA-MB-231-luc orthotopic model co-injected with 3T3 MEF WT cells

In this study, a mixture of 5×10^6 MDA-MB-231 cells and 1×10^6 cells 3T3 MEF WT cells (in 50 μ L of 1:1 PBS and Matrigel) were implanted via orthotopic surgery as described above. Mice were assigned into groups (n = 6 mice per group) and the treatment was started when average tumor volumes reached ~ 140 mm³ and the treatment was

continued for 13 days. Tumor volumes were recorded via caliper measurements every 2-3 days.

6.32 Anticancer efficacy of lead MCT inhibitor 3j in MDA-MB-231-luc orthotopic model co-injected with 3T3 MEF KO cells

In this study, a mixture of 5×10^6 MDA-MB-231 cells and 5×10^5 cells 3T3 MEF KO cells (in 50 μ L of 1:1 PBS and Matrigel) were implanted via orthotopic surgery as described above. Mice were assigned into groups ($n = 6$ mice per group) and the treatment was started when average tumor volumes reached $\sim 200 \text{ mm}^3$ and the treatment was continued for 11 days. Tumor volumes were recorded via caliper measurements every 2-3 days.

6.33 Statistical analysis

For *in vitro* Seahorse based assays, repeated measures one-way ANOVA was used to calculate statistical significance. For all *in vivo* mouse models, Mann-Whitney's test was used to estimate statistical significance between treatment and control groups. GraphPad Prism 7.0 software was used to generate all the graphs presented in this thesis. *, $P < 0.05$, **, $P < 0.01$, ***, $P < 0.001$, ****, $P < 0.0001$.

REFERENCES

- (1) Hanahan, D.; Weinberg, R. A. The Hallmarks of Cancer. *Cell* **2000**, *100* (1), 57–70.
- (2) Hanahan, D.; Weinberg, R. A. Hallmarks of Cancer: The next Generation. *Cell* **2011**, *144* (5), 646–674. <https://doi.org/10.1016/j.cell.2011.02.013>.
- (3) Cantor, J. R.; Sabatini, D. M. Cancer Cell Metabolism: One Hallmark, Many Faces. *Cancer Discov.* **2012**, *2* (10), 881–898. <https://doi.org/10.1158/2159-8290.CD-12-0345>.
- (4) Hsu, P. P.; Sabatini, D. M. Cancer Cell Metabolism: Warburg and Beyond. *Cell* **2008**, *134* (5), 703–707. <https://doi.org/10.1016/j.cell.2008.08.021>.
- (5) Ganapathy, V.; Thangaraju, M.; Prasad, P. D. Nutrient Transporters in Cancer: Relevance to Warburg Hypothesis and Beyond. *Pharmacol. Ther.* **2009**, *121* (1), 29–40. <https://doi.org/10.1016/j.pharmthera.2008.09.005>.
- (6) Sonveaux, P.; Végran, F.; Schroeder, T.; Wergin, M. C.; Verrax, J.; Rabbani, Z. N.; De Saedeleer, C. J.; Kennedy, K. M.; Diepart, C.; Jordan, B. F.; et al. Targeting Lactate-Fueled Respiration Selectively Kills Hypoxic Tumor Cells in Mice. *J. Clin. Invest.* **2008**, *118* (12), 3930–3942. <https://doi.org/10.1172/JCI36843>.
- (7) Gatenby, R. A.; Gillies, R. J. Why Do Cancers Have High Aerobic Glycolysis? *Nat. Rev. Cancer* **2004**, *4* (11), 891–899. <https://doi.org/10.1038/nrc1478>.
- (8) Warburg, O. On the Origin of Cancer Cells. *Science* **1956**, *123* (3191), 309–314.
- (9) Pavlides, S.; Whitaker-Menezes, D.; Castello-Cros, R.; Flomenberg, N.; Witkiewicz, A. K.; Frank, P. G.; Casimiro, M. C.; Wang, C.; Fortina, P.; Addya, S.; et al. The Reverse Warburg Effect: Aerobic Glycolysis in Cancer Associated Fibroblasts and the Tumor Stroma. *Cell Cycle Georget. Tex* **2009**, *8* (23), 3984–4001. <https://doi.org/10.4161/cc.8.23.10238>.
- (10) Witkiewicz, A. K.; Whitaker-Menezes, D.; Dasgupta, A.; Philp, N. J.; Lin, Z.; Gandara, R.; Sneddon, S.; Martinez-Outschoorn, U. E.; Sotgia, F.; Lisanti, M. P. Using the “Reverse Warburg Effect” to Identify High-Risk Breast Cancer Patients: Stromal MCT4 Predicts Poor Clinical Outcome in Triple-Negative Breast Cancers. *Cell Cycle Georget. Tex* **2012**, *11* (6), 1108–1117. <https://doi.org/10.4161/cc.11.6.19530>.
- (11) Halestrap, A. P.; Price, N. T. The Proton-Linked Monocarboxylate Transporter (MCT) Family: Structure, Function and Regulation. *Biochem. J.* **1999**, *343* (Pt 2), 281–299.
- (12) Justin A. Spanier; Lester R. Drewes. Monocarboxylate Transporters. In *Drug Transporters*.
- (13) Poole, R. C.; Sansom, C. E.; Halestrap, A. P. Studies of the Membrane Topology of the Rat Erythrocyte H⁺/Lactate Cotransporter (MCT1). *Biochem. J.* **1996**, *320* (Pt 3), 817–824.
- (14) Wilson, M. C.; Meredith, D.; Bunnun, C.; Sessions, R. B.; Halestrap, A. P. Studies on the DIDS-Binding Site of Monocarboxylate Transporter 1 Suggest a Homology Model of the Open Conformation and a Plausible Translocation Cycle. *J. Biol. Chem.* **2009**, *284* (30), 20011–20021. <https://doi.org/10.1074/jbc.M109.014217>.

- (15) Manoharan, C.; Wilson, M. C.; Sessions, R. B.; Halestrap, A. P. The Role of Charged Residues in the Transmembrane Helices of Monocarboxylate Transporter 1 and Its Ancillary Protein Basigin in Determining Plasma Membrane Expression and Catalytic Activity. *Mol. Membr. Biol.* **2006**, *23* (6), 486–498. <https://doi.org/10.1080/09687860600841967>.
- (16) Bröer, S.; Schneider, H. P.; Bröer, A.; Rahman, B.; Hamprecht, B.; Deitmer, J. W. Characterization of the Monocarboxylate Transporter 1 Expressed in *Xenopus Laevis* Oocytes by Changes in Cytosolic PH. *Biochem. J.* **1998**, *333* (Pt 1), 167–174.
- (17) Pinheiro, C.; Albergaria, A.; Paredes, J.; Sousa, B.; Dufloth, R.; Vieira, D.; Schmitt, F.; Baltazar, F. Monocarboxylate Transporter 1 Is Up-Regulated in Basal-like Breast Carcinoma. *Histopathology* **2010**, *56* (7), 860–867. <https://doi.org/10.1111/j.1365-2559.2010.03560.x>.
- (18) Hong, C. S.; Graham, N. A.; Gu, W.; Espindola Camacho, C.; Mah, V.; Maresh, E. L.; Alavi, M.; Bagryanova, L.; Krotee, P. A. L.; Gardner, B. K.; et al. MCT1 Modulates Cancer Cell Pyruvate Export and Growth of Tumors That Co-Express MCT1 and MCT4. *Cell Rep.* **2016**, *14* (7), 1590–1601. <https://doi.org/10.1016/j.celrep.2016.01.057>.
- (19) Pinheiro, C.; Longatto-Filho, A.; Scapulatempo, C.; Ferreira, L.; Martins, S.; Pellerin, L.; Rodrigues, M.; Alves, V. A. F.; Schmitt, F.; Baltazar, F. Increased Expression of Monocarboxylate Transporters 1, 2, and 4 in Colorectal Carcinomas. *Virchows Arch. Int. J. Pathol.* **2008**, *452* (2), 139–146. <https://doi.org/10.1007/s00428-007-0558-5>.
- (20) Kim, Y.; Choi, J.-W.; Lee, J.-H.; Kim, Y.-S. Expression of Lactate/H⁺ Symporters MCT1 and MCT4 and Their Chaperone CD147 Predicts Tumor Progression in Clear Cell Renal Cell Carcinoma: Immunohistochemical and The Cancer Genome Atlas Data Analyses. *Hum. Pathol.* **2015**, *46* (1), 104–112. <https://doi.org/10.1016/j.humpath.2014.09.013>.
- (21) Choi, J.-W.; Kim, Y.; Lee, J.-H.; Kim, Y.-S. Prognostic Significance of Lactate/Proton Symporters MCT1, MCT4, and Their Chaperone CD147 Expressions in Urothelial Carcinoma of the Bladder. *Urology* **2014**, *84* (1), 245.e9-15. <https://doi.org/10.1016/j.urology.2014.03.031>.
- (22) de Oliveira, A. T. T.; Pinheiro, C.; Longatto-Filho, A.; Brito, M. J.; Martinho, O.; Matos, D.; Carvalho, A. L.; Vazquez, V. L.; Silva, T. B.; Scapulatempo, C.; et al. Co-Expression of Monocarboxylate Transporter 1 (MCT1) and Its Chaperone (CD147) Is Associated with Low Survival in Patients with Gastrointestinal Stromal Tumors (GISTs). *J. Bioenerg. Biomembr.* **2012**, *44* (1), 171–178. <https://doi.org/10.1007/s10863-012-9408-5>.
- (23) Lai, Y. 1 - Membrane Transporters and the Diseases Corresponding to Functional Defects. In *Transporters in Drug Discovery and Development*; Lai, Y., Ed.; Woodhead Publishing Series in Biomedicine; Woodhead Publishing, 2013; pp 1–146. <https://doi.org/10.1533/9781908818287.1>.
- (24) Baek, G.; Tse, Y. F.; Hu, Z.; Cox, D.; Buboltz, N.; McCue, P.; Yeo, C. J.; White, M. A.; DeBerardinis, R. J.; Knudsen, E. S.; et al. MCT4 Defines a Glycolytic Subtype of

- Pancreatic Cancer with Poor Prognosis and Unique Metabolic Dependencies. *Cell Rep.* **2014**, 9 (6), 2233–2249. <https://doi.org/10.1016/j.celrep.2014.11.025>.
- (25) Di Vizio, D.; Morello, M.; Sotgia, F.; Pestell, R. G.; Freeman, M. R.; Lisanti, M. P. An Absence of Stromal Caveolin-1 Is Associated with Advanced Prostate Cancer, Metastatic Disease and Epithelial Akt Activation. *Cell Cycle Georget. Tex* **2009**, 8 (15), 2420–2424. <https://doi.org/10.4161/cc.8.15.9116>.
- (26) Witkiewicz, A. K.; Dasgupta, A.; Sammons, S.; Er, O.; Potoczek, M. B.; Guiles, F.; Sotgia, F.; Brody, J. R.; Mitchell, E. P.; Lisanti, M. P. Loss of Stromal Caveolin-1 Expression Predicts Poor Clinical Outcome in Triple Negative and Basal-like Breast Cancers. *Cancer Biol. Ther.* **2010**, 10 (2), 135–143.
- (27) Curry, J. M.; Tuluc, M.; Whitaker-Menezes, D.; Ames, J. A.; Anantharaman, A.; Butera, A.; Leiby, B.; Cognetti, D. M.; Sotgia, F.; Lisanti, M. P.; et al. Cancer Metabolism, Stemness and Tumor Recurrence: MCT1 and MCT4 Are Functional Biomarkers of Metabolic Symbiosis in Head and Neck Cancer. *Cell Cycle Georget. Tex* **2013**, 12 (9), 1371–1384. <https://doi.org/10.4161/cc.24092>.
- (28) Kumar, G. R.; Subazini, T. K.; Subha, K.; Rajadurai, C. P.; Prabakar, L. CanGeneBase (CGB) - a Database on Cancer Related Genes. *Bioinformation* **2009**, 3 (10), 422–424.
- (29) Onitilo, A. A.; Engel, J. M.; Greenlee, R. T.; Mukesh, B. N. Breast Cancer Subtypes Based on ER/PR and Her2 Expression: Comparison of Clinicopathologic Features and Survival. *Clin. Med. Res.* **2009**, 7 (1–2), 4–13. <https://doi.org/10.3121/cmr.2009.825>.
- (30) Dawood, S. Triple-Negative Breast Cancer: Epidemiology and Management Options. *Drugs* **2010**, 70 (17), 2247–2258. <https://doi.org/10.2165/11538150-000000000-00000>.
- (31) De Laurentiis, M.; Cianniello, D.; Caputo, R.; Stanzione, B.; Arpino, G.; Cinieri, S.; Lorusso, V.; De Placido, S. Treatment of Triple Negative Breast Cancer (TNBC): Current Options and Future Perspectives. *Cancer Treat. Rev.* **2010**, 36 Suppl 3, S80-86. [https://doi.org/10.1016/S0305-7372\(10\)70025-6](https://doi.org/10.1016/S0305-7372(10)70025-6).
- (32) Eralp, Y.; Derin, D.; Ozluk, Y.; Yavuz, E.; Guney, N.; Saip, P.; Muslumanoglu, M.; Igci, A.; Kücük, S.; Dincer, M.; et al. MAPK Overexpression Is Associated with Anthracycline Resistance and Increased Risk for Recurrence in Patients with Triple-Negative Breast Cancer. *Ann. Oncol. Off. J. Eur. Soc. Med. Oncol.* **2008**, 19 (4), 669–674. <https://doi.org/10.1093/annonc/mdm522>.
- (33) Martinez-Outschoorn, U. E.; Pavlides, S.; Howell, A.; Pestell, R. G.; Tanowitz, H. B.; Sotgia, F.; Lisanti, M. P. Stromal-Epithelial Metabolic Coupling in Cancer: Integrating Autophagy and Metabolism in the Tumor Microenvironment. *Int. J. Biochem. Cell Biol.* **2011**, 43 (7), 1045–1051. <https://doi.org/10.1016/j.biocel.2011.01.023>.
- (34) Wiechen, K.; Sers, C.; Agoulnik, A.; Arlt, K.; Dietel, M.; Schlag, P. M.; Schneider, U. Down-Regulation of Caveolin-1, a Candidate Tumor Suppressor Gene, in Sarcomas. *Am. J. Pathol.* **2001**, 158 (3), 833–839. [https://doi.org/10.1016/S0002-9440\(10\)64031-X](https://doi.org/10.1016/S0002-9440(10)64031-X).
- (35) Martinez-Outschoorn, U. E.; Lin, Z.; Trimmer, C.; Flomenberg, N.; Wang, C.;

- Pavlidis, S.; Pestell, R. G.; Howell, A.; Sotgia, F.; Lisanti, M. P. Cancer Cells Metabolically “Fertilize” the Tumor Microenvironment with Hydrogen Peroxide, Driving the Warburg Effect: Implications for PET Imaging of Human Tumors. *Cell Cycle Georget. Tex* **2011**, *10* (15), 2504–2520. <https://doi.org/10.4161/cc.10.15.16585>.
- (36) Lisanti, M. P.; Martinez-Outschoorn, U. E.; Chiavarina, B.; Pavlidis, S.; Whitaker-Menezes, D.; Tsigos, A.; Witkiewicz, A.; Lin, Z.; Balliet, R.; Howell, A.; et al. Understanding the “Lethal” Drivers of Tumor-Stroma Co-Evolution: Emerging Role(s) for Hypoxia, Oxidative Stress and Autophagy/Mitophagy in the Tumor Micro-Environment. *Cancer Biol. Ther.* **2010**, *10* (6), 537–542. <https://doi.org/10.4161/cbt.10.6.13370>.
- (37) Witkiewicz, A. K.; Casimiro, M. C.; Dasgupta, A.; Mercier, I.; Wang, C.; Bonuccelli, G.; Jasmin, J.-F.; Frank, P. G.; Pestell, R. G.; Kleer, C. G.; et al. Towards a New “Stromal-Based” Classification System for Human Breast Cancer Prognosis and Therapy. *Cell Cycle Georget. Tex* **2009**, *8* (11), 1654–1658. <https://doi.org/10.4161/cc.8.11.8544>.
- (38) Wu, K. N.; Queenan, M.; Brody, J. R.; Potoczek, M.; Sotgia, F.; Lisanti, M. P.; Witkiewicz, A. K. Loss of Stromal Caveolin-1 Expression in Malignant Melanoma Metastases Predicts Poor Survival. *Cell Cycle Georget. Tex* **2011**, *10* (24), 4250–4255. <https://doi.org/10.4161/cc.10.24.18551>.
- (39) Tanowitz, H. B.; Machado, F. S.; Avantaggiati, M. L.; Albanese, C. An Expanded Role for Caveolin-1 in Brain Tumors. *Cell Cycle* **2013**, *12* (10), 1485–1486. <https://doi.org/10.4161/cc.24855>.
- (40) Autophagy in cancer associated fibroblasts promotes tumor cell survival <https://www.ncbi.nlm.nih.gov/pmc/articles/PMC3047617/> (accessed Mar 14, 2019).
- (41) Witkiewicz, A. K.; Kline, J.; Queenan, M.; Brody, J. R.; Tsigos, A.; Bilal, E.; Pavlidis, S.; Ertel, A.; Sotgia, F.; Lisanti, M. P. Molecular Profiling of a Lethal Tumor Microenvironment, as Defined by Stromal Caveolin-1 Status in Breast Cancers. *Cell Cycle Georget. Tex* **2011**, *10* (11), 1794–1809. <https://doi.org/10.4161/cc.10.11.15675>.
- (42) Weinberg, S. E.; Chandel, N. S. Targeting Mitochondria Metabolism for Cancer Therapy. *Nat. Chem. Biol.* **2015**, *11* (1), 9–15. <https://doi.org/10.1038/nchembio.1712>.
- (43) Sotgia, F.; Whitaker-Menezes, D.; Martinez-Outschoorn, U. E.; Salem, A. F.; Tsigos, A.; Lamb, R.; Sneddon, S.; Hult, J.; Howell, A.; Lisanti, M. P. Mitochondria “Fuel” Breast Cancer Metabolism: Fifteen Markers of Mitochondrial Biogenesis Label Epithelial Cancer Cells, but Are Excluded from Adjacent Stromal Cells. *Cell Cycle Georget. Tex* **2012**, *11* (23), 4390–4401. <https://doi.org/10.4161/cc.22777>.
- (44) Martinez-Outschoorn, U. E.; Lin, Z.; Whitaker-Menezes, D.; Howell, A.; Lisanti, M. P.; Sotgia, F. Ketone Bodies and Two-Compartment Tumor Metabolism: Stromal Ketone Production Fuels Mitochondrial Biogenesis in Epithelial Cancer Cells. *Cell Cycle Georget. Tex* **2012**, *11* (21), 3956–3963. <https://doi.org/10.4161/cc.22136>.
- (45) Zhao, X.; He, Y.; Chen, H. Autophagic Tumor Stroma: Mechanisms and Roles in Tumor Growth and Progression. *Int. J. Cancer* **2013**, *132* (1), 1–8. <https://doi.org/10.1002/ijc.27664>.
- (46) Pavlidis, S.; Vera, I.; Gandara, R.; Sneddon, S.; Pestell, R. G.; Mercier, I.;

- Martinez-Outschoorn, U. E.; Whitaker-Menezes, D.; Howell, A.; Sotgia, F.; et al. Warburg Meets Autophagy: Cancer-Associated Fibroblasts Accelerate Tumor Growth and Metastasis via Oxidative Stress, Mitophagy, and Aerobic Glycolysis. *Antioxid. Redox Signal.* **2012**, *16* (11), 1264–1284. <https://doi.org/10.1089/ars.2011.4243>.
- (47) Lin, N.-Y.; Beyer, C.; Giessler, A.; Kireva, T.; Scholtysek, C.; Uderhardt, S.; Munoz, L. E.; Dees, C.; Distler, A.; Wirtz, S.; et al. Autophagy Regulates TNF α -Mediated Joint Destruction in Experimental Arthritis. *Ann. Rheum. Dis.* **2013**, *72* (5), 761–768. <https://doi.org/10.1136/annrheumdis-2012-201671>.
- (48) Martinez-Outschoorn, U. E.; Balliet, R. M.; Rivadeneira, D. B.; Chiavarina, B.; Pavlides, S.; Wang, C.; Whitaker-Menezes, D.; Daumer, K. M.; Lin, Z.; Witkiewicz, A. K.; et al. Oxidative Stress in Cancer Associated Fibroblasts Drives Tumor-Stroma Co-Evolution: A New Paradigm for Understanding Tumor Metabolism, the Field Effect and Genomic Instability in Cancer Cells. *Cell Cycle Georget. Tex* **2010**, *9* (16), 3256–3276. <https://doi.org/10.4161/cc.9.16.12553>.
- (49) Martinez-Outschoorn, U. E.; Curry, J. M.; Ko, Y.-H.; Lin, Z.; Tuluc, M.; Cognetti, D.; Birbe, R. C.; Pribitkin, E.; Bombonati, A.; Pestell, R. G.; et al. Oncogenes and Inflammation Rewire Host Energy Metabolism in the Tumor Microenvironment: RAS and NF κ B Target Stromal MCT4. *Cell Cycle Georget. Tex* **2013**, *12* (16), 2580–2597. <https://doi.org/10.4161/cc.25510>.
- (50) Pani, G.; Galeotti, T.; Chiarugi, P. Metastasis: Cancer Cell's Escape from Oxidative Stress. *Cancer Metastasis Rev.* **2010**, *29* (2), 351–378. <https://doi.org/10.1007/s10555-010-9225-4>.
- (51) Pavlides, S.; Tsigos, A.; Migneco, G.; Whitaker-Menezes, D.; Chiavarina, B.; Flomenberg, N.; Frank, P. G.; Casimiro, M. C.; Wang, C.; Pestell, R. G.; et al. The Autophagic Tumor Stroma Model of Cancer: Role of Oxidative Stress and Ketone Production in Fueling Tumor Cell Metabolism. *Cell Cycle Georget. Tex* **2010**, *9* (17), 3485–3505. <https://doi.org/10.4161/cc.9.17.12721>.
- (52) Liu, E. Y.; Ryan, K. M. Autophagy and Cancer--Issues We Need to Digest. *J. Cell Sci.* **2012**, *125* (Pt 10), 2349–2358. <https://doi.org/10.1242/jcs.093708>.
- (53) Durán, R. V.; Hall, M. N. Glutaminolysis Feeds MTORC1. *Cell Cycle* **2012**, *11* (22), 4107–4108. <https://doi.org/10.4161/cc.22632>.
- (54) Chen, J.-Q.; Russo, J. Dysregulation of Glucose Transport, Glycolysis, TCA Cycle and Glutaminolysis by Oncogenes and Tumor Suppressors in Cancer Cells. *Biochim. Biophys. Acta* **2012**, *1826* (2), 370–384. <https://doi.org/10.1016/j.bbcan.2012.06.004>.
- (55) Erickson, J. W.; Cerione, R. A. Glutaminase: A Hot Spot For Regulation Of Cancer Cell Metabolism? *Oncotarget* **2010**, *1* (8), 734–740.
- (56) Chiavarina, B.; Whitaker-Menezes, D.; Migneco, G.; Martinez-Outschoorn, U. E.; Pavlides, S.; Howell, A.; Tanowitz, H. B.; Casimiro, M. C.; Wang, C.; Pestell, R. G.; et al. HIF1-Alpha Functions as a Tumor Promoter in Cancer Associated Fibroblasts, and as a Tumor Suppressor in Breast Cancer Cells: Autophagy Drives Compartment-Specific Oncogenesis. *Cell Cycle Georget. Tex* **2010**, *9* (17), 3534–3551. <https://doi.org/10.4161/cc.9.17.12908>.

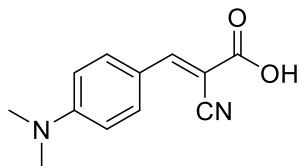
- (57) Colen, C. B.; Shen, Y.; Ghoddoussi, F.; Yu, P.; Francis, T. B.; Koch, B. J.; Monterey, M. D.; Galloway, M. P.; Sloan, A. E.; Mathupala, S. P. Metabolic Targeting of Lactate Efflux by Malignant Glioma Inhibits Invasiveness and Induces Necrosis: An in Vivo Study. *Neoplasia N. Y. N* **2011**, *13* (7), 620–632.
- (58) Miranda-Gonçalves, V.; Honavar, M.; Pinheiro, C.; Martinho, O.; Pires, M. M.; Pinheiro, C.; Cordeiro, M.; Bebiano, G.; Costa, P.; Palmeirim, I.; et al. Monocarboxylate Transporters (MCTs) in Gliomas: Expression and Exploitation as Therapeutic Targets. *Neuro-Oncol.* **2013**, *15* (2), 172–188. <https://doi.org/10.1093/neuonc/nos298>.
- (59) Zhao, Z.; Wu, M.-S.; Zou, C.; Tang, Q.; Lu, J.; Liu, D.; Wu, Y.; Yin, J.; Xie, X.; Shen, J.; et al. Downregulation of MCT1 Inhibits Tumor Growth, Metastasis and Enhances Chemotherapeutic Efficacy in Osteosarcoma through Regulation of the NF-KB Pathway. *Cancer Lett.* **2014**, *342* (1), 150–158. <https://doi.org/10.1016/j.canlet.2013.08.042>.
- (60) Araki, T.; Hayashi, M.; Saruta, T. Anion-Exchange Blocker Enhances Cytoplasmic Vacuole Formation and Cell Death in Serum-Deprived Mouse Kidney Epithelial Cells in Mice. *Cell Biol. Int.* **2006**, *30* (1), 93–100. <https://doi.org/10.1016/j.cellbi.2005.10.020>.
- (61) Poole, R. C.; Halestrap, A. P. Reversible and Irreversible Inhibition, by Stilbenedisulphonates, of Lactate Transport into Rat Erythrocytes. Identification of Some New High-Affinity Inhibitors. *Biochem. J.* **1991**, *275* (Pt 2), 307–312.
- (62) McKay, T. B.; Lyon, D.; Sarker-Nag, A.; Priyadarsini, S.; Asara, J. M.; Karamichos, D. Quercetin Attenuates Lactate Production and Extracellular Matrix Secretion in Keratoconus. *Sci. Rep.* **2015**, *5*, 9003. <https://doi.org/10.1038/srep09003>.
- (63) Nancolas, B.; Guo, L.; Zhou, R.; Nath, K.; Nelson, D. S.; Leeper, D. B.; Blair, I. A.; Glickson, J. D.; Halestrap, A. P. The Anti-Tumour Agent Lonidamine Is a Potent Inhibitor of the Mitochondrial Pyruvate Carrier and Plasma Membrane Monocarboxylate Transporters. *Biochem. J.* **2016**, *473* (7), 929–936. <https://doi.org/10.1042/BJ20151120>.
- (64) Morais-Santos, F.; Miranda-Gonçalves, V.; Pinheiro, S.; Vieira, A. F.; Paredes, J.; Schmitt, F. C.; Baltazar, F.; Pinheiro, C. Differential Sensitivities to Lactate Transport Inhibitors of Breast Cancer Cell Lines. *Endocr. Relat. Cancer* **2014**, *21* (1), 27–38. <https://doi.org/10.1530/ERC-13-0132>.
- (65) Cundy, K. C.; Branch, R.; Chernov-Rogan, T.; Dias, T.; Estrada, T.; Hold, K.; Koller, K.; Liu, X.; Mann, A.; Panuwat, M.; et al. XP13512 [(+/-)-1-[(Alpha-Isobutanoyloxyethoxy)Carbonyl] Aminomethyl)-1-Cyclohexane Acetic Acid], a Novel Gabapentin Prodrug: I. Design, Synthesis, Enzymatic Conversion to Gabapentin, and Transport by Intestinal Solute Transporters. *J. Pharmacol. Exp. Ther.* **2004**, *311* (1), 315–323. <https://doi.org/10.1124/jpet.104.067934>.
- (66) Lal, R.; Sukbuntherng, J.; Luo, W.; Vicente, V.; Blumenthal, R.; Ho, J.; Cundy, K. C. Clinical Pharmacokinetic Drug Interaction Studies of Gabapentin Enacarbil, a Novel Transported Prodrug of Gabapentin, with Naproxen and Cimetidine. *Br. J. Clin. Pharmacol.* **2010**, *69* (5), 498–507. <https://doi.org/10.1111/j.1365-2125.2010.03616.x>.
- (67) Gan, L.; Xiu, R.; Ren, P.; Yue, M.; Su, H.; Guo, G.; Xiao, D.; Yu, J.; Jiang, H.; Liu, H.; et al. Metabolic Targeting of Oncogene MYC by Selective Activation of the

- Proton-Coupled Monocarboxylate Family of Transporters. *Oncogene* **2016**, *35* (23), 3037–3048. <https://doi.org/10.1038/onc.2015.360>.
- (68) Chen, T. C.; Yu, J.; Nouri Nigjeh, E.; Wang, W.; Myint, P. T.; Zandi, E.; Hofman, F. M.; Schönthal, A. H. A Perillyl Alcohol-Conjugated Analog of 3-Bromopyruvate without Cellular Uptake Dependency on Monocarboxylate Transporter 1 and with Activity in 3-BP-Resistant Tumor Cells. *Cancer Lett.* **2017**, *400*, 161–174. <https://doi.org/10.1016/j.canlet.2017.04.015>.
- (69) Ovens, M. J.; Davies, A. J.; Wilson, M. C.; Murray, C. M.; Halestrap, A. P. AR-C155858 Is a Potent Inhibitor of Monocarboxylate Transporters MCT1 and MCT2 That Binds to an Intracellular Site Involving Transmembrane Helices 7-10. *Biochem. J.* **2010**, *425* (3), 523–530. <https://doi.org/10.1042/BJ20091515>.
- (70) Lamb, R.; Harrison, H.; Hulit, J.; Smith, D. L.; Lisanti, M. P.; Sotgia, F. Mitochondria as New Therapeutic Targets for Eradicating Cancer Stem Cells: Quantitative Proteomics and Functional Validation via MCT1/2 Inhibition. *Oncotarget* **2014**, *5* (22), 11029–11037. <https://doi.org/10.18632/oncotarget.2789>.
- (71) Marchiq, I.; Le Floch, R.; Roux, D.; Simon, M.-P.; Pouyssegur, J. Genetic Disruption of Lactate/H⁺ Symporters (MCTs) and Their Subunit CD147/BASIGIN Sensitizes Glycolytic Tumor Cells to Phenformin. *Cancer Res.* **2015**, *75* (1), 171–180. <https://doi.org/10.1158/0008-5472.CAN-14-2260>.
- (72) Bola, B. M.; Chadwick, A. L.; Michopoulos, F.; Blount, K. G.; Telfer, B. A.; Williams, K. J.; Smith, P. D.; Critchlow, S. E.; Stratford, I. J. Inhibition of Monocarboxylate Transporter-1 (MCT1) by AZD3965 Enhances Radiosensitivity by Reducing Lactate Transport. *Mol. Cancer Ther.* **2014**, *13* (12), 2805–2816. <https://doi.org/10.1158/1535-7163.MCT-13-1091>.
- (73) Polański, R.; Hodgkinson, C. L.; Fusi, A.; Nonaka, D.; Priest, L.; Kelly, P.; Trapani, F.; Bishop, P. W.; White, A.; Critchlow, S. E.; et al. Activity of the Monocarboxylate Transporter 1 Inhibitor AZD3965 in Small Cell Lung Cancer. *Clin. Cancer Res. Off. J. Am. Assoc. Cancer Res.* **2014**, *20* (4), 926–937. <https://doi.org/10.1158/1078-0432.CCR-13-2270>.
- (74) Noble, R. A.; Bell, N.; Blair, H.; Sikka, A.; Thomas, H.; Phillips, N.; Nakjang, S.; Miwa, S.; Crossland, R.; Rand, V.; et al. Inhibition of Monocarboxylate Transporter 1 by AZD3965 as a Novel Therapeutic Approach for Diffuse Large B-Cell Lymphoma and Burkitt Lymphoma. *Haematologica* **2017**, *102* (7), 1247–1257. <https://doi.org/10.3324/haematol.2016.163030>.
- (75) Wang, H.; Yang, C.; Doherty, J. R.; Roush, W. R.; Cleveland, J. L.; Bannister, T. D. Synthesis and Structure-Activity Relationships of Pteridine Dione and Trione Monocarboxylate Transporter 1 Inhibitors. *J. Med. Chem.* **2014**, *57* (17), 7317–7324. <https://doi.org/10.1021/jm500640x>.
- (76) Draoui, N.; Schicke, O.; Fernandes, A.; Drozak, X.; Nahra, F.; Dumont, A.; Douxfils, J.; Hermans, E.; Dogné, J.-M.; Corbau, R.; et al. Synthesis and Pharmacological Evaluation of Carboxycoumarins as a New Antitumor Treatment Targeting Lactate Transport in Cancer Cells. *Bioorg. Med. Chem.* **2013**, *21* (22), 7107–7117. <https://doi.org/10.1016/j.bmc.2013.09.010>.

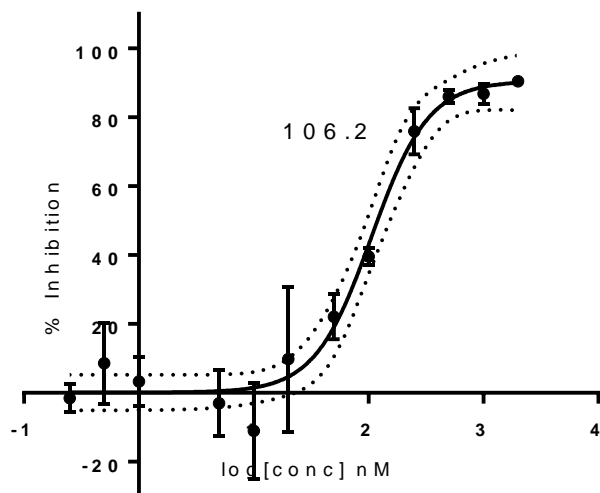
- (77) Draoui, N.; Schicke, O.; Seront, E.; Bouzin, C.; Sonveaux, P.; Riant, O.; Feron, O. Antitumor Activity of 7-Aminocarboxycoumarin Derivatives, a New Class of Potent Inhibitors of Lactate Influx but Not Efflux. *Mol. Cancer Ther.* **2014**, *13* (6), 1410–1418. <https://doi.org/10.1158/1535-7163.MCT-13-0653>.
- (78) Parnell, K. M.; McCall, J. Mct4 Inhibitors for Treating Disease. US20160362378A1, December 15, 2016.
- (79) Freeman, F. Properties and Reactions of Ylidenemalononitriles. *Chem. Rev.* **1980**, *80* (4), 329–350. <https://doi.org/10.1021/cr60326a004>.
- (80) Gurrapu, S.; Jonnalagadda, S. K.; Alam, M. A.; Nelson, G. L.; Sneve, M. G.; Drewes, L. R.; Mereddy, V. R. Monocarboxylate Transporter 1 Inhibitors as Potential Anticancer Agents. *ACS Med. Chem. Lett.* **2015**, *6* (5), 558–561. <https://doi.org/10.1021/acsmchemlett.5b00049>.
- (81) Critchlow, S. E.; Tate, L. Use of a Mct1 Inhibitor in the Treatment of Cancers Expressing Mct1 over Mct4. WO2010089580A1, August 12, 2010.
- (82) Serafimova, I. M.; Pufall, M. A.; Krishnan, S.; Duda, K.; Cohen, M. S.; Maglathlin, R. L.; McFarland, J. M.; Miller, R. M.; Frödin, M.; Taunton, J. Reversible Targeting of Noncatalytic Cysteines with Chemically Tuned Electrophiles. *Nat. Chem. Biol.* **2012**, *8* (5), 471–476. <https://doi.org/10.1038/nchembio.925>.
- (83) Gurrapu, S.; Jonnalagadda, S. K.; Alam, M. A.; Ronayne, C. T.; Nelson, G. L.; Solano, L. N.; Lueth, E. A.; Drewes, L. R.; Mereddy, V. R. Coumarin Carboxylic Acids as Monocarboxylate Transporter 1 Inhibitors: In Vitro and in Vivo Studies as Potential Anticancer Agents. *Bioorg. Med. Chem. Lett.* **2016**, *26* (14), 3282–3286. <https://doi.org/10.1016/j.bmcl.2016.05.054>.
- (84) Hidalgo, I. J.; Raub, T. J.; Borchardt, R. T. Characterization of the Human Colon Carcinoma Cell Line (Caco-2) as a Model System for Intestinal Epithelial Permeability. *Gastroenterology* **1989**, *96* (3), 736–749.
- (85) Obach, R. S.; Baxter, J. G.; Liston, T. E.; Silber, B. M.; Jones, B. C.; MacIntyre, F.; Rance, D. J.; Wastall, P. The Prediction of Human Pharmacokinetic Parameters from Preclinical and in Vitro Metabolism Data. *J. Pharmacol. Exp. Ther.* **1997**, *283* (1), 46–58.
- (86) Seshadri, M.; Ciesielski, M. J. MRI-Based Characterization of Vascular Disruption by 5,6-Dimethylxanthenone-Acetic Acid in Gliomas. *J. Cereb. Blood Flow Metab. Off. J. Int. Soc. Cereb. Blood Flow Metab.* **2009**, *29* (8), 1373–1382. <https://doi.org/10.1038/jcbfm.2009.68>.
- (87) Winkler, F.; Kienast, Y.; Fuhrmann, M.; Von Baumgarten, L.; Burgold, S.; Mitteregger, G.; Kretzschmar, H.; Herms, J. Imaging Glioma Cell Invasion in Vivo Reveals Mechanisms of Dissemination and Peritumoral Angiogenesis. *Glia* **2009**, *57* (12), 1306–1315. <https://doi.org/10.1002/glia.20850>.
- (88) Jonnalagadda, S.; Jonnalagadda, S. K.; Ronayne, C. T.; Nelson, G. L.; Solano, L. N.; Rumbley, J.; Holy, J.; Mereddy, V. R.; Drewes, L. R. Novel N,N-Dialkyl Cyanocinnamic Acids as Monocarboxylate Transporter 1 and 4 Inhibitors. *Oncotarget* **2019**, *10* (24), 2355–2368. <https://doi.org/10.18632/oncotarget.26760>.

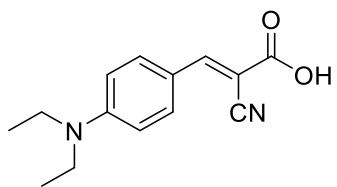
APPENDIX

Representative IC_{50} graphs for MCT1 inhibition:

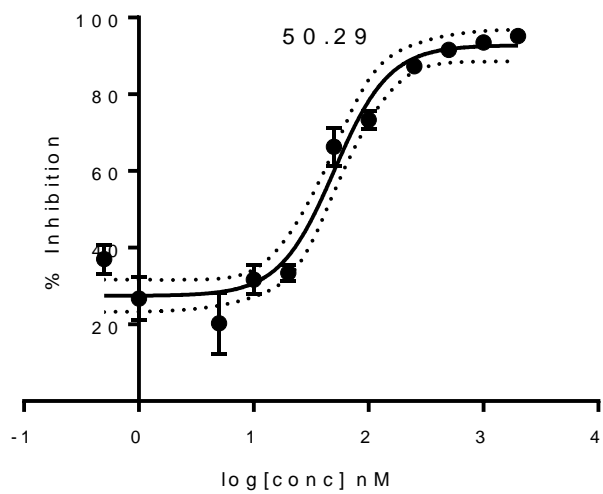


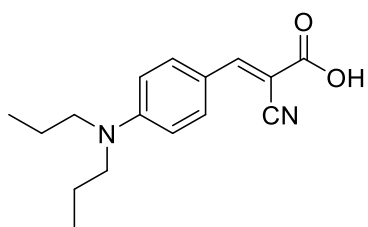
(*E*)-2-cyano-3-(4-(dimethylamino)phenyl)acrylic acid, **2m**



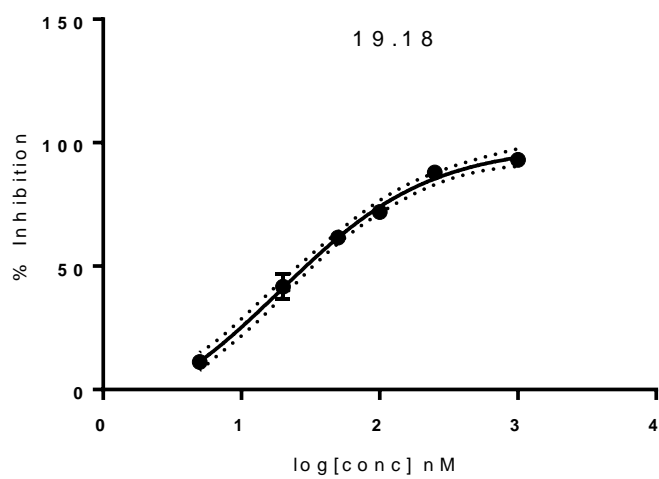


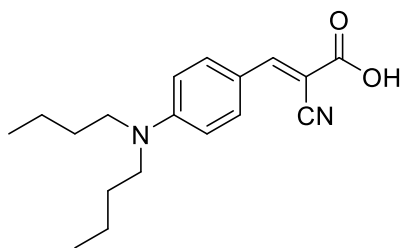
(*E*)-2-cyano-3-(4-(diethylamino)phenyl)acrylic acid, **2n**



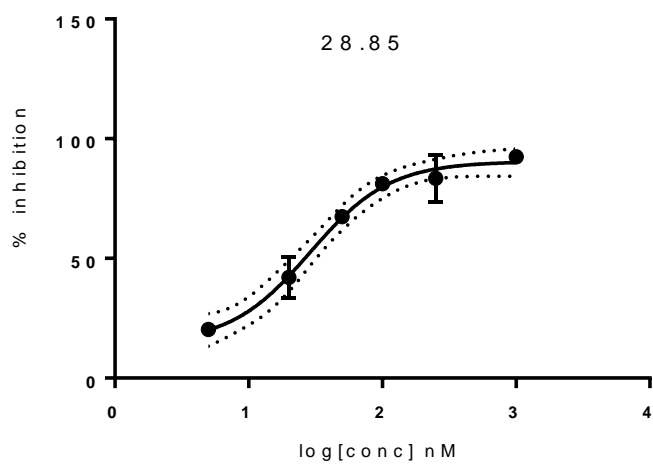


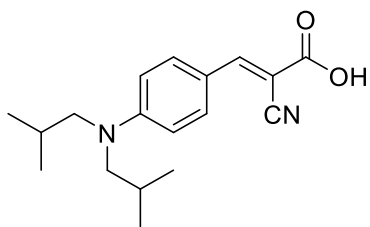
(*E*)-2-cyano-3-(4-(dipropylamino)phenyl)acrylic acid, **2o**



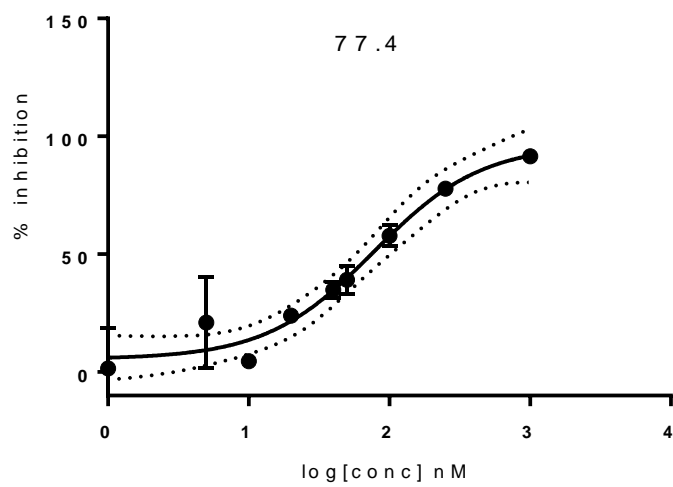


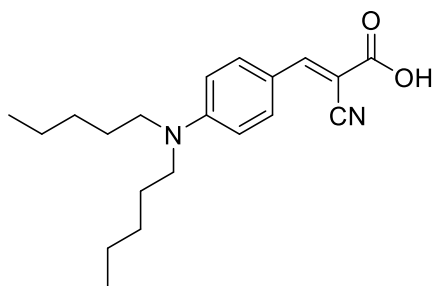
(*E*)-2-cyano-3-(4-(dibutylamino)phenyl)acrylic acid, **2p**



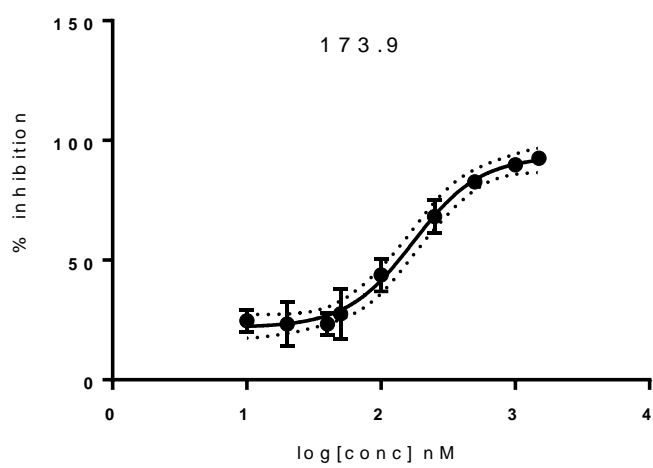


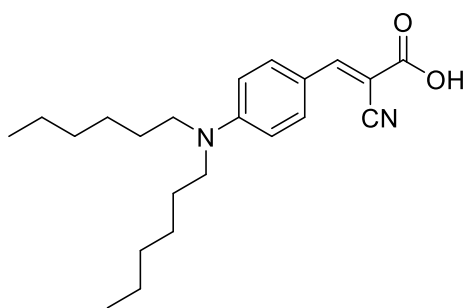
(*E*)-2-cyano-3-(4-(diisobutylamino)phenyl)acrylic acid, **2q**



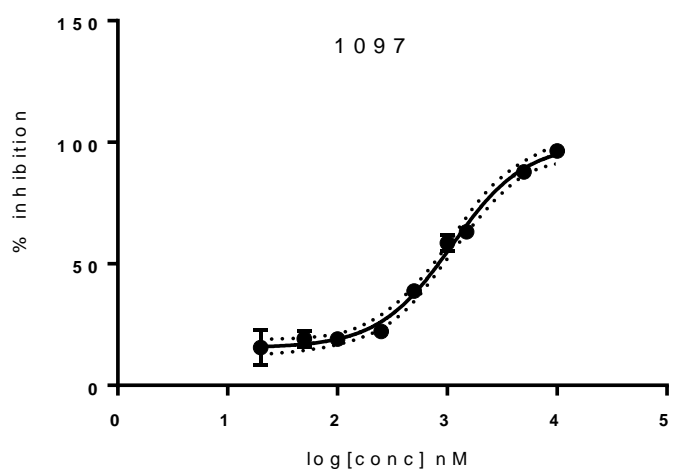


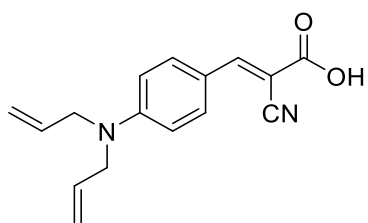
(*E*)-2-cyano-3-(4-(dipentylamino)phenyl)acrylic acid, **2r**



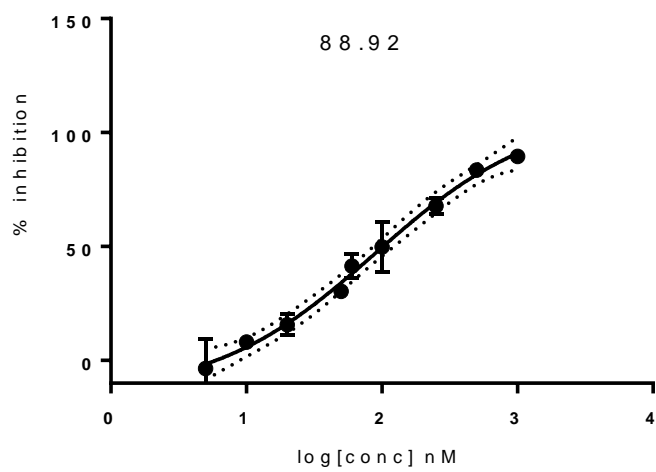


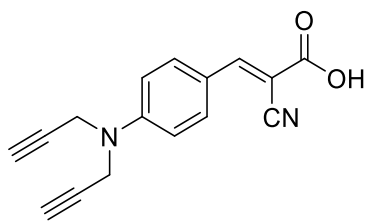
(*E*)-2-cyano-3-(4-(dihexylamino)phenyl)acrylic acid, **2s**



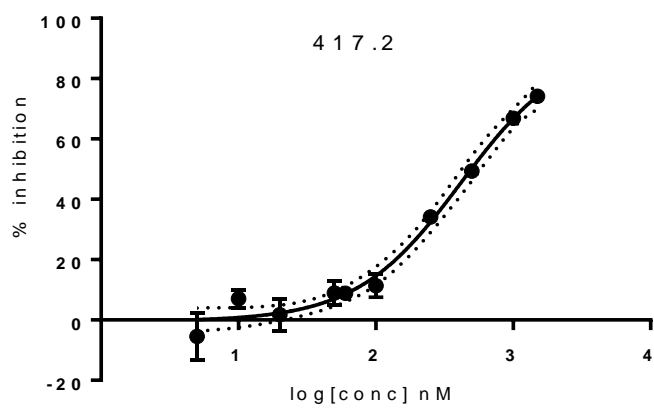


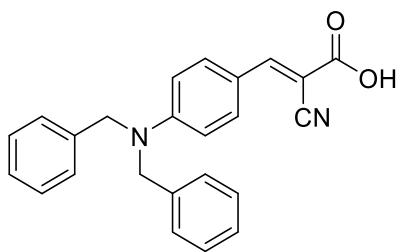
(*E*)-2-cyano-3-(4-(diallylamino)phenyl)acrylic acid, **2t**



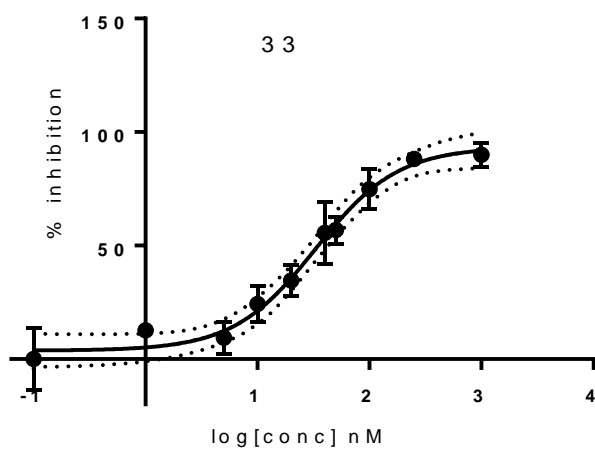


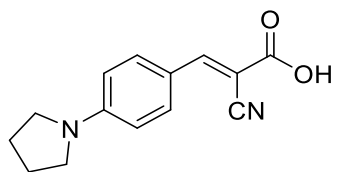
(*E*)-2-cyano-3-(4-(di(prop-2-yn-1-yl)amino)phenyl)acrylic acid, **2u**



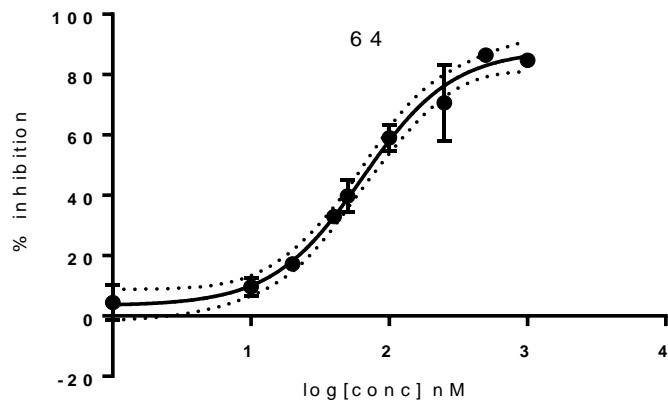


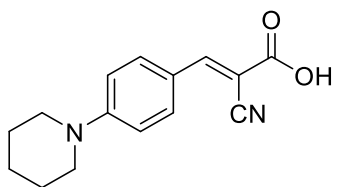
(*E*)-2-cyano-3-(4-(dibenzylamino)phenyl)acrylic acid, **2v**



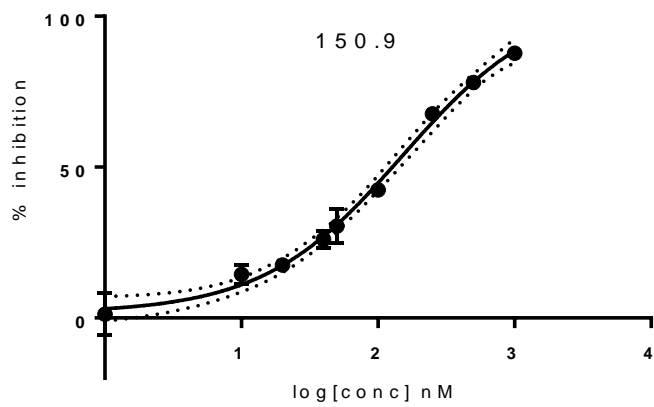


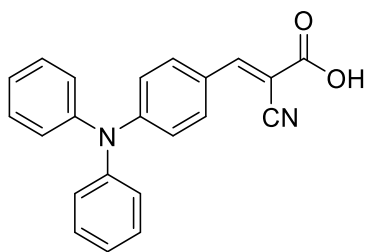
(*E*)-2-cyano-3-(4-(pyrrolidin-1-yl)phenyl)acrylic acid, **2w**



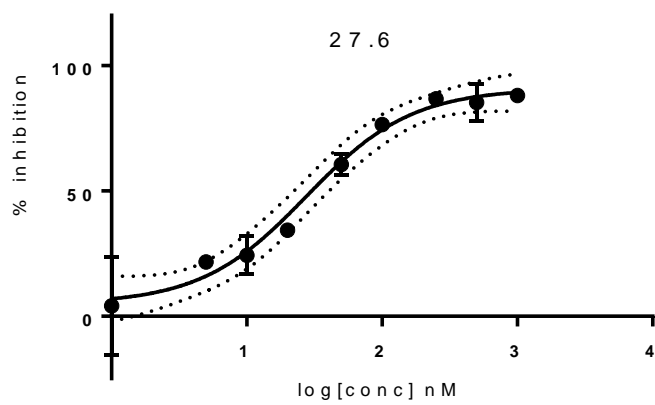


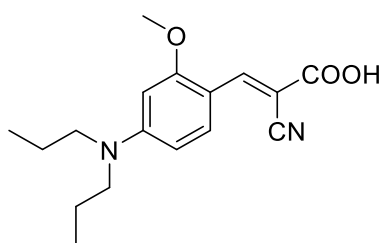
(*E*)-2-cyano-3-(4-(piperidin-1-yl)phenyl)acrylic acid, **2x**



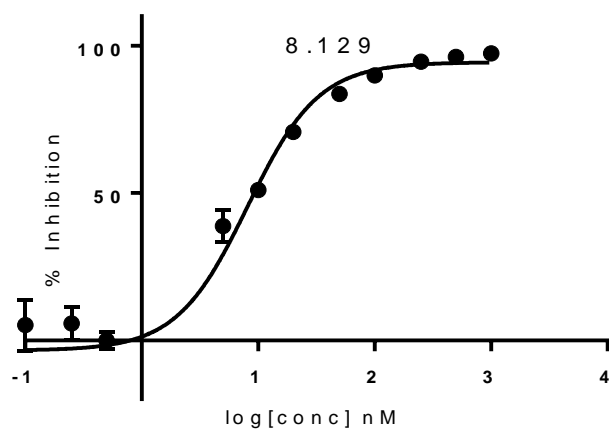


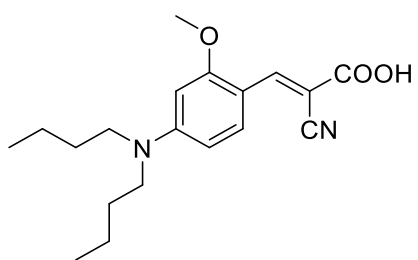
(*E*)-2-cyano-3-(4-(diphenylamino)phenyl)acrylic acid, **2y**



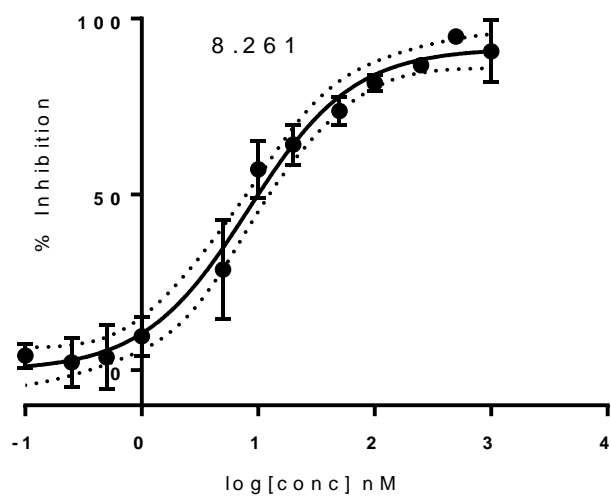


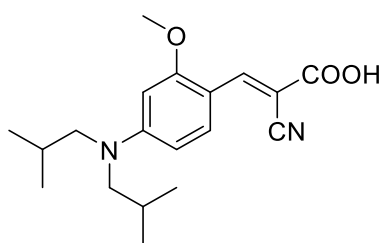
(*E*)-2-cyano-3-(4-(dipropylamino)-2-methoxyphenyl)acrylic acid, **3a**



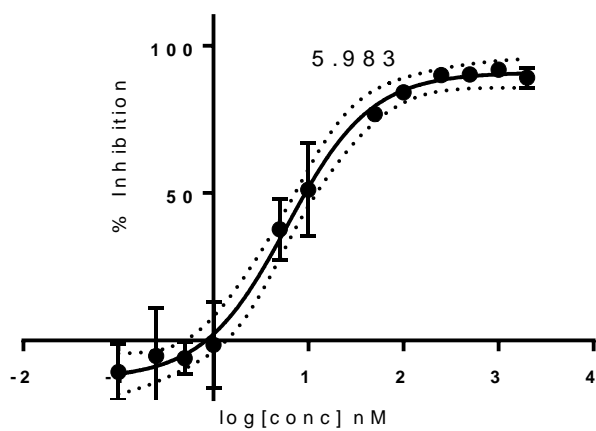


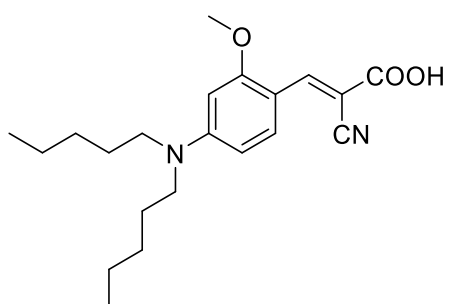
(*E*)-2-cyano-3-(4-(dibutylamino)-2-methoxyphenyl)acrylic acid, **3b**



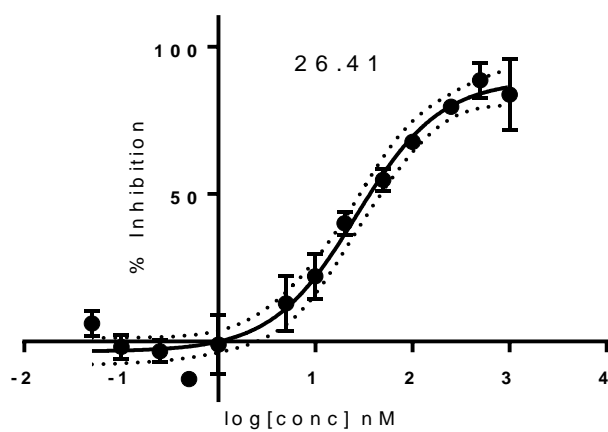


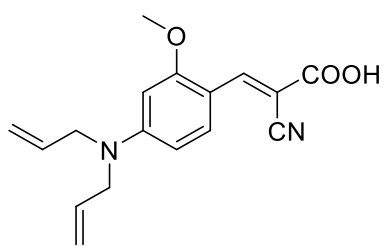
(*E*)-2-cyano-3-(4-(diisobutylamino)-2-methoxyphenyl)acrylic acid, **3c**



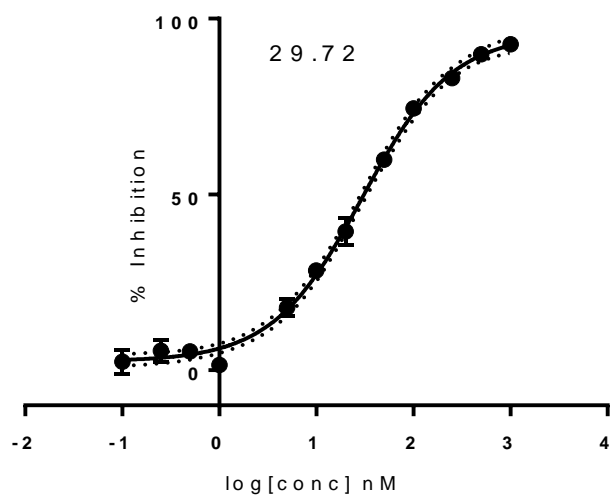


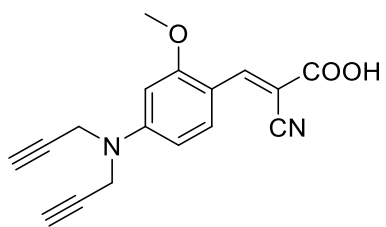
(*E*)-2-cyano-3-(4-(dipentylamino)-2-methoxyphenyl)acrylic acid, **3d**



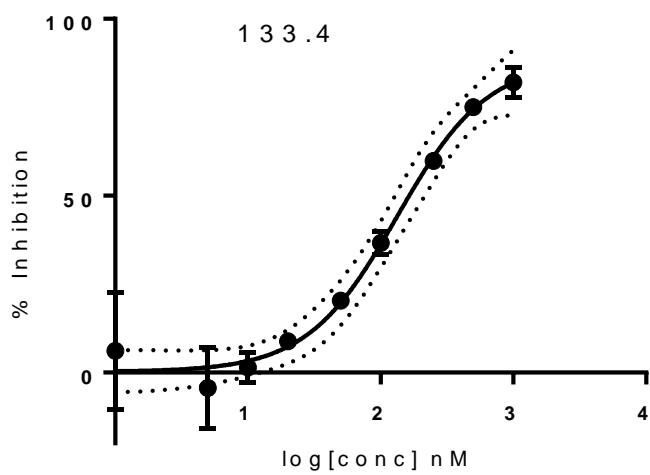


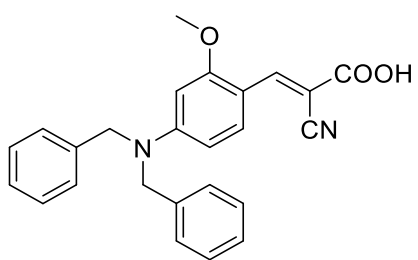
(*E*)-2-cyano-3-(4-(diallylamino)-2-methoxyphenyl)acrylic acid, **3e**



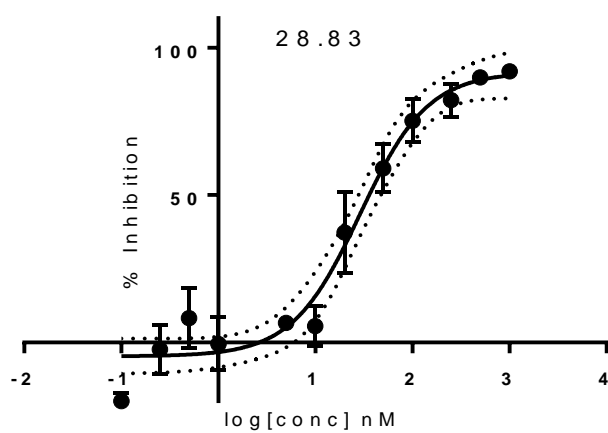


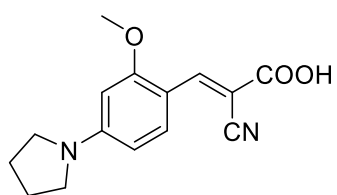
(*E*)-2-cyano-3-(4-(diallylamino)-2-methoxyphenyl)acrylic acid, **3f**



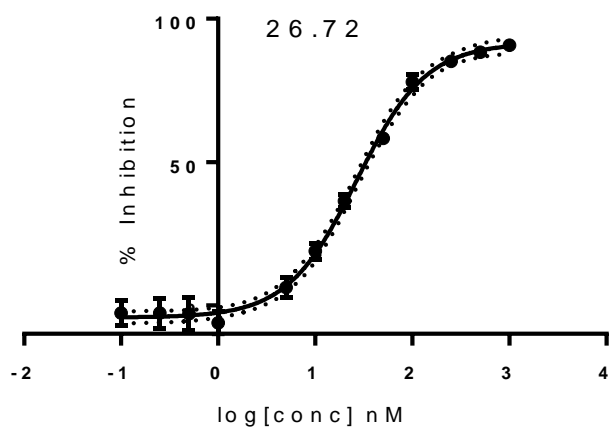


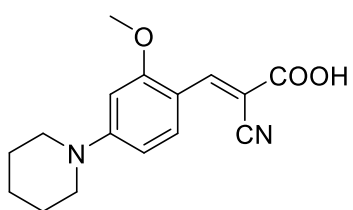
(*E*)-2-cyano-3-(4-(dibenzylamino)-2-methoxyphenyl)acrylic acid, **3g**



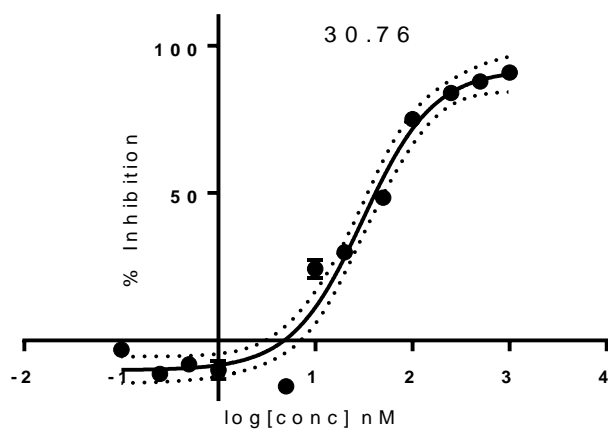


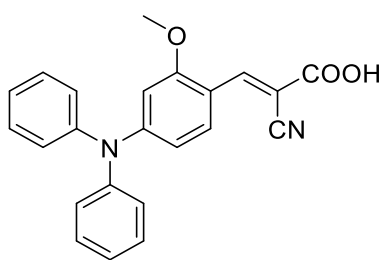
(*E*)-2-cyano-3-(2-methoxy-4-(pyrrolidin-1-yl)phenyl)acrylic acid, **3h**



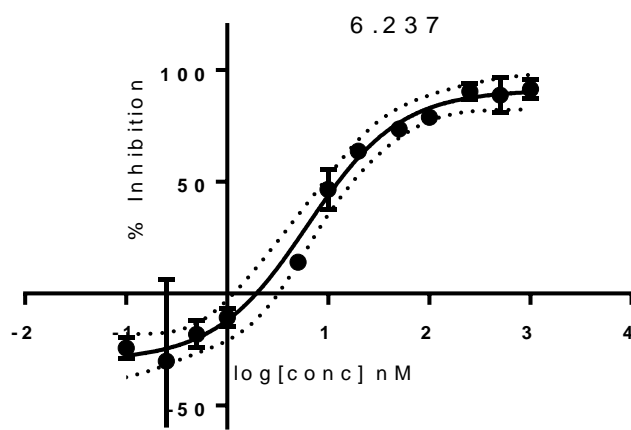


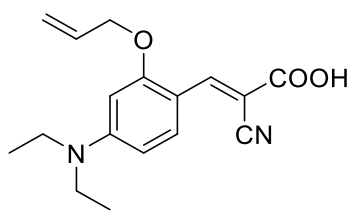
(*E*)-2-cyano-3-(2-methoxy-4-(piperidin-1-yl)phenyl)acrylic acid, **3i**



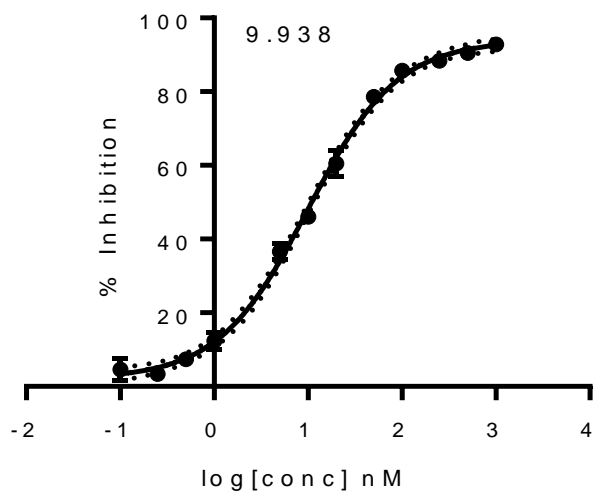


(*E*)-2-cyano-3-(4-(diphenylamino)-2-methoxyphenyl)acrylic acid, **3j**

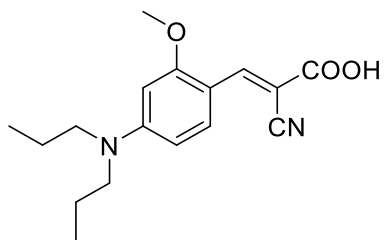




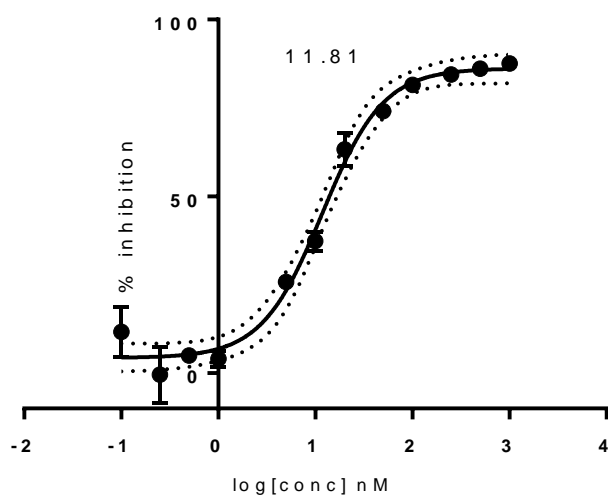
(*E*)-3-(2-(allyloxy)-4-(diethylamino)phenyl)-2-cyanoacrylic acid, **3k**

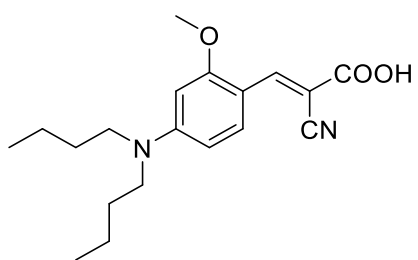


Representative IC_{50} graphs for MCT4 inhibition:

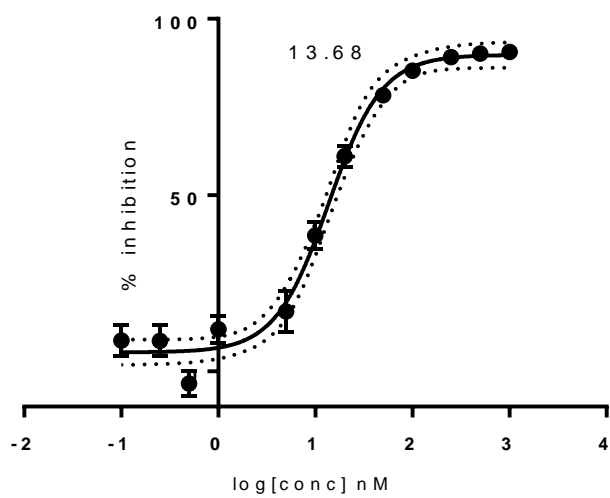


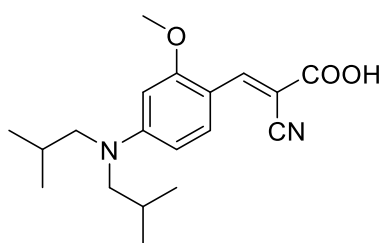
(*E*)-2-cyano-3-(4-(dipropylamino)-2-methoxyphenyl)acrylic acid, **3a**



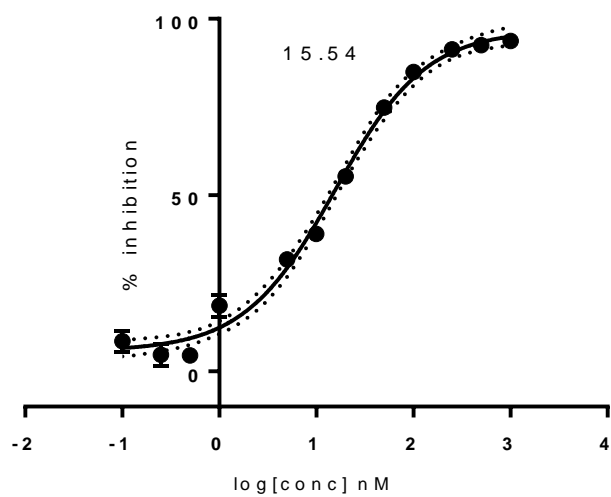


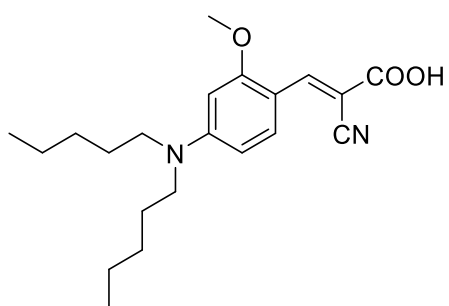
(*E*)-2-cyano-3-(4-(dibutylamino)-2-methoxyphenyl)acrylic acid, **3b**



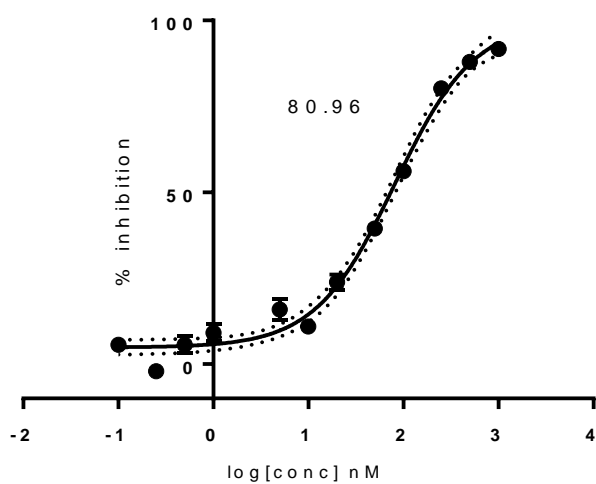


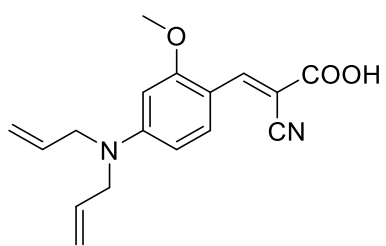
(*E*)-2-cyano-3-(4-(diisobutylamino)-2-methoxyphenyl)acrylic acid, **3c**



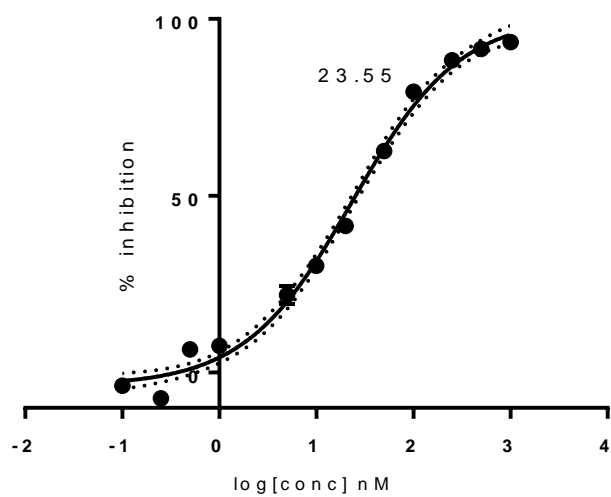


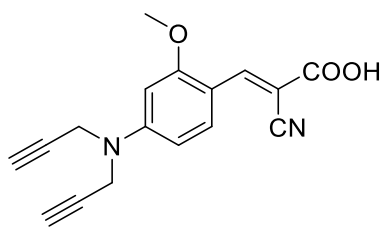
(*E*)-2-cyano-3-(4-(dipentylamino)-2-methoxyphenyl)acrylic acid, **3d**



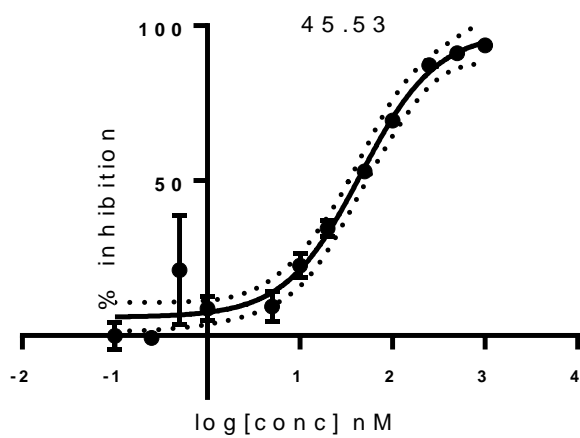


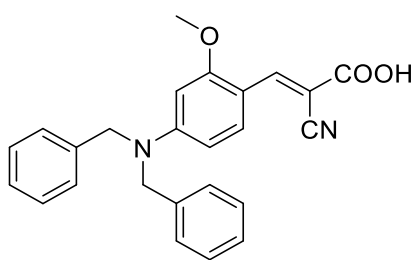
(*E*)-2-cyano-3-(4-(diallylamino)-2-methoxyphenyl)acrylic acid, **3e**



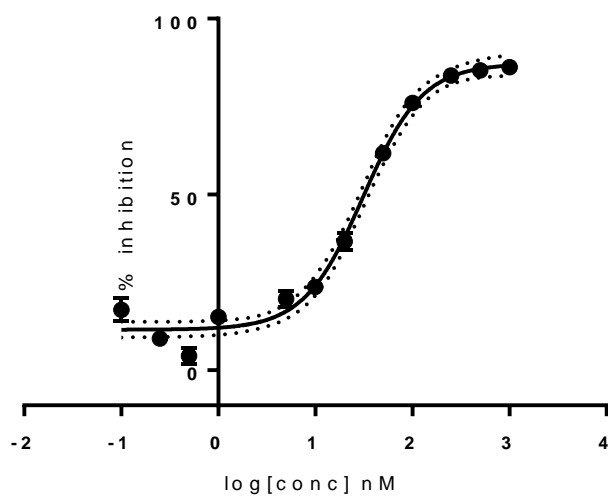


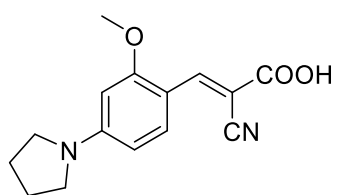
(*E*)-2-cyano-3-(4-(diallylamino)-2-methoxyphenyl)acrylic acid, **3f**



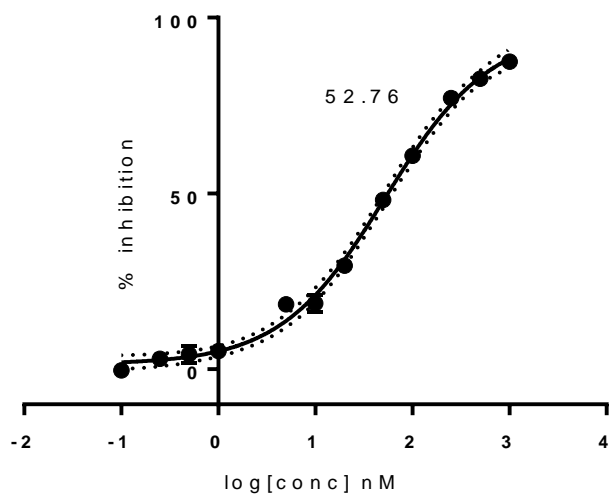


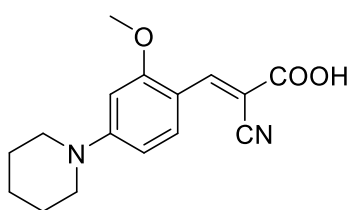
(*E*)-2-cyano-3-(4-(dibenzylamino)-2-methoxyphenyl)acrylic acid, **3g**



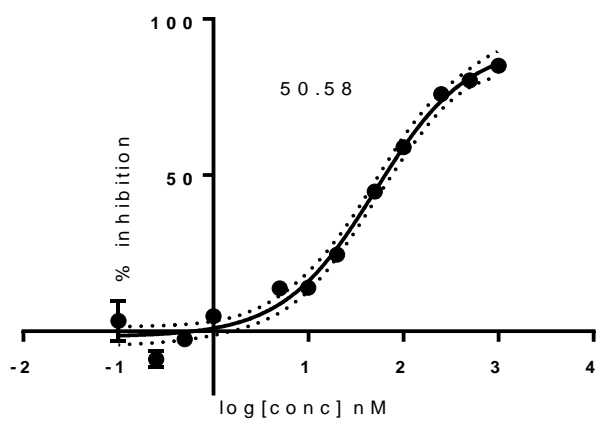


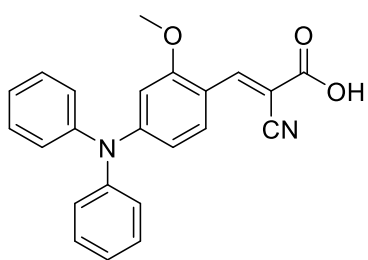
(*E*)-2-cyano-3-(2-methoxy-4-(pyrrolidin-1-yl)phenyl)acrylic acid, **3h**



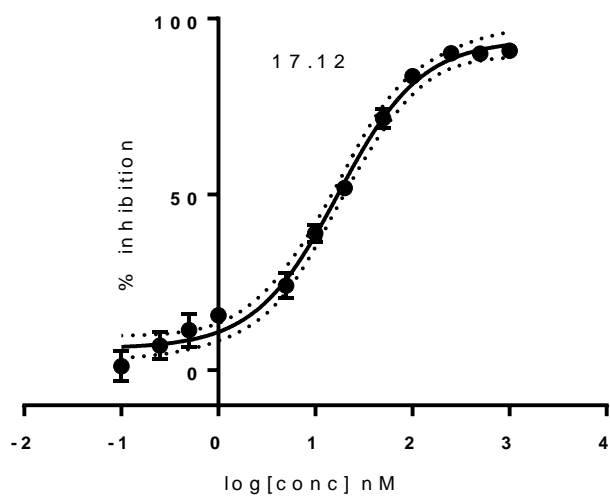


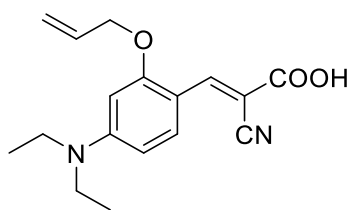
(*E*)-2-cyano-3-(2-methoxy-4-(piperidin-1-yl)phenyl)acrylic acid, **3i**



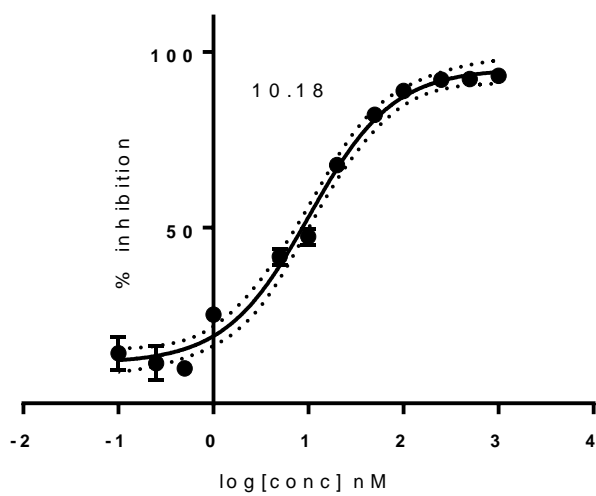


(*E*)-2-cyano-3-(4-(diphenylamino)-2-methoxyphenyl)acrylic acid, **3j**





(*E*)-3-(2-(allyloxy)-4-(diethylamino)phenyl)-2-cyanoacrylic acid, **3k**



NMR SPECTRA

